科技部補助專題研究計畫成果報告
期末報告

基材物化特性對碳分子篩選薄膜之孔洞結構及氣體分選能力之影響(第 3 年)

計 畫 類 別 ： 個別型計畫
計 畫 編 號 ： NSC 100-2221-E-040-004-MY3
執 行 期 間 ： 102 年 08 月 01 日至 103 年 07 月 31 日
執 行 單 位 ： 中山醫學大學職業安全衛生學系暨碩士班

計 畫 主 持 人 ： 曾惠馨

計畫參與人員： 碩士班研究生-兼任助理人員：江建楷
碩士班研究生-兼任助理人員：王敬婷

報 告 附 件 ： 出席國際會議研究心得報告及發表論文

處 理 方 式 ：
1.公開資訊：本計畫涉及專利或其他智慧財產權，2 年後可公開查詢
2.「本研究」是否已有嚴重損及公共利益之發現：否
3.「本報告」是否建議提供政府單位施政參考：否

中 華 民 國 103 年 10 月 31 日

中文摘要：碳分子篩選薄膜（carbon molecular sieve membrane）因具有微孔（micropore）及次微孔（sub-micropore）的雙峰孔洞分佈，而較其它薄膜材料具有高氣體通量及分選效率。然而，碳膜與鋁基材間的性質差異，使其界面易成為應力集中的地方，往往在熱處理後因收縮速率不同而形成裂縫，進而影響碳分子篩選薄膜的氣體分選行為。本計畫的研究主題即在探討基材的物化特性對碳分子篩選薄膜孔洞結構及氣體分選能力的影響。第一年以高溫燒結法自製不同孔徑分佈之鋁基材，探討鋁基材燒結溫度、升溫速率、燒結持溫時間等因子對鋁基材及碳膜孔徑分佈的影響々研究結果發現，氧化鋁基材的顆粒大小及孔隙分佈率是影響基材表面粗糙度的主要因素，亦是決定高分子鏈堆疊情形的重要因子，當基材孔隙率大且表面粗糙大時，由於高分子鏈的任意堆疊而造成空間效應，因此碳化後將產生較大的層間距而有泯於氣體的擴散，但此時氣體的分選效果較不理想。相反地，在本研究發現經 1400 oC 熱處理、升溫速率為 2 oC/min 且熱沉浸時間為 2 小時時，鋁基材因形成十四面體結構而產生粗糙度低但具氣孔之結構，因此可提供碳膜高滲透率及高選擇率的分離特性，此時 H2 滲透率為 1300 Barrer、H2/CH4 與 CO2/CH4 分沖為 174.16 與 56.44。第二年中，以水熱法及溶膠凝膠法分沖製備 MFI 與 TiO2 中間層形成矽-鋁與鈦-鋁複合基材。首先泯用 MFI 製備之矽/鋁基材 1100-MFI-1 因植種矽晶核後修飾了原氧化鋁的孔洞結構，且因高分子鏈與 Si-O 及 Si-O-Si 官能基產生交聯作用，故其所支撐之碳膜的滲透率及選擇率皆明顯增加，H2 的滲透率為 2223 Barrer，H2/CH4 的選擇率為 260。不同基材所支撐之碳膜的滲透分選效能大多都超越 Robeson’s 2008 upper bound。當塗佈含有羥基的 TiO2 做為中間層時，因可與 PEI 高分子鏈（碳膜的前驅物）產生氫鍵鍵結而增強兩相間的機械互鎖，進而有效地提升兩相間的黏附特性，並使得薄膜的機械強度由 187.4 N 增強至 215.9 N。研究第三年則以拋光技術改變基材的表面粗糙度，並同時探討高分子鑄膜液之組成、溶劑揮發動力與基材膨脹、收縮之關係。研究結果發現，隨著

基材表面粗糙度越大，中間層因
滲入較多而減少羥基與PEI高分子鏈的氫鍵鍵結，故氣體滲透率遞增，且高分子鏈層間距較大，
選擇率較差。而鑄膜液黏滯度低時，因溶液移動性高，容易滲入基材的孔洞之中，使得互鎖
效應較高，接合程度也增加，故滲透率下降。當鑄膜液溫度高時，溶劑揮發速率較快，會使
高分子鏈在伸展狀態即固化，因此形成的薄膜較為緻密，碳化後層間距值較小，滲透率會較
低，分選效率較高。

中文關鍵詞： 碳膜、基材、中間層、TiO2、粗糙度、黏度

英文摘要： iN this project, the effect of support physic-chemical characterization on the morphology and the greenhouse gas separation performance of the CMS membrane were investigated.
In the first year, several different pore size distributions of alumina supports were synthesized and used to evaluate the effect on the morphology and adhesive properties of CMS/A12O3 composite membranes. The tetradecahedral shape of the substrate achieved at the sintering temperature of 1400 °C was found to be suitable for the prepared CMS membranes, which exhibited a H2 permeability of 1300 Barrer with H2/CH4 and CO2/CH4 selectivities of 174.16 and 56.44, respectively. To optimize the substrate structure to provide a cost-effective and highly productive method for the deposition of brittle CMS membranes, this proposed procedure can be used to improve the mechanical strength of the supported membrane for enhanced manipulation.
In the second year, the MFI and TiO2 were acting as intermediate layer to modify the interfacial adhesion. After modification with MFI silica, the CMSM supported on 1100-MFI-1 substrate shows better H2 permeability of 2223 Barrer and an ideal H2/CH4 selectivity of 260 due to the crosslinking reaction between polymer chain and Si-O, Si-O-Si groups. The results indicated that the permselectivity of carbon molecular sieving (CMS) membrane fabricated in this study can exceed the 2008 Robeson’s trade-off line. Then, the alumina support was modified by TiO2 nano-

network. The surface area and the total pore volume of substrate were increased, which is benefited for mechanical interlocking with polymer chain. Further, PEI chain was bonded by the Hydroxyl groups of the TiO2 to improve the chemical bonding. The mechanical strength of the TiO2-modified Al2O3 support was enhanced from 187.4 N to 215.9 compared to the original one.
In the third year, we change the polymer solution temperature to adjust the viscosity of dopes. The low viscosity of dopes will penetrate into the substrate to improve the mechanical interlocking, but the permeability will also decrease. When increasing the polymer solution temperature, the polymer chain was rigidified due to the high volatility of solvent. Therefore, the membrane became much dense. The d-spacing was decreased after carbonization and also resulted in low permeability.

英文關鍵詞： carbon membrane； substrate； intermediate layer； TiO2； roughness； viscosity

科技部補助專題研究計畫成果報告

（□期中進度報告/☑期末報告）

基材物化特性對碳分子篩選薄膜之孔洞結構及氣體分選能力之影響

計畫類別：☑個別型計畫　□整合型計畫
計畫編號：MOST　100－2221－E－040－004－MY3
執行期間：100　年　8 月 1 日至　103　年　7 月 31 日

執行機構及系所：中山醫學大學/職業安全衛生學系

計畫主持人：曾惠馨
共同主持人：無
計畫參與人員：江建楷、王敬婷 研究生
鄭博育、張郁琪、林淑筠、詹鎮宇 專題生

本計畫除繳交成果報告外，另含下列出國報告，共 1 份：
□執行國際合作與移地研究心得報告
☑出席國際學術會議心得報告

期末報告處理方式：

1. 公開方式：
   □非列管計畫亦不具下列情形，立即公開查詢
   ☑涉及專利或其他智慧財產權，□一年☑二年後可公開查詢
2. 「本研究」是否已有嚴重損及公共利益之發現：☑否 □是
3. 「本報告」是否建議提供政府單位施政參考 ☑否 □是，____（請列舉提供之單位；本部不經審議，依勾選逕予轉送）

中　華　民　國　103年　10　月　20 日

中文摘要

碳分子篩選薄膜（carbon molecular sieve membrane）因具有微孔（micropore）及次微孔（sub-micropore）的雙峰孔洞分佈，而較其它薄膜材料具有高氣體通量及分選效率。然而，碳膜與鋁基材間的性質差異，使其界面易成為應力集中的地方，往往在熱處理後因收縮速率不同而形成裂縫，進而影響碳分子篩選薄膜的氣體分選行為。本計畫的研究主題即在探討基材的物化特性對碳分子篩選薄膜孔洞結構及氣體分選能力的影響。

第一年以高溫燒結法自製不同孔徑分佈之鋁基材，探討鋁基材燒結溫度、升溫速率、燒結持溫時間等因子對鋁基材及碳膜孔徑分佈的影響；研究結果發現，氧化鋁基材的顆粒大小及孔隙分佈率是影響基材表面粗糙度的主要因素，亦是決定高分子鏈堆疊情形的重要因子，當基材孔隙率大且表面粗糙大時，由於高分子鏈的任意堆疊而造成空間效應，因此碳化後將產生較大的層間距而有利於氣體的擴散，但此時氣體的分選效果較不理想。相反地，在本研究發現經1400 ^{o}C熱處理、升溫速率為2 ^{o}C/min且熱沉浸時間為2小時時，鋁基材因形成十四面體結構而產生粗糙度低但具氣孔之結構，因此可提供碳膜高滲透率及高選擇率的分離特性，此時H_2滲透率為1300 Barrer、H_2/CH_4與CO_2/CH_4分別為174.16與56.44。

第二年中，以水熱法及溶膠凝膠法分別製備MFI與TiO_2中間層形成矽-鋁與鈦-鋁複合基材。首先利用MFI製備之矽/鋁基材1100-MFI-1 因植種矽晶核後修飾了原氧化鋁的孔洞結構，且因高分子鏈與Si-O 及Si-O-Si 官能基產生交聯作用，故其所支撐之碳膜的滲透率及選擇率皆明顯增加，H_2 的滲透率為2223 Barrer，H_2/CH_4 的選擇率為260。不同基材所支撐之碳膜的滲透分選效能大多都超越Robeson's 2008 upper bound。當塗佈含有羥基的TiO_2做為中間層時，因可與PEI高分子鏈（碳膜的前驅物）產生氫鍵鍵結而增強兩相間的機械互鎖，進而有效地提升兩相間的黏附特性，並使得薄膜的機械強度由187.4 N增強至215.9 N。

研究第三年則以拋光技術改變基材的表面粗糙度，並同時探討高分子鑄膜液之組成、溶劑揮發動力與基材膨脹、收縮之關係。研究結果發現，隨著基材表面粗糙度越大，中間層因滲入較多而減少羥基與PEI高分子鏈的氫鍵鍵結，故氣體滲透率遞增，且高分子鏈層間距較大，選擇率較差。而鑄膜液黏滯度低時，因溶液移動性高，容易滲入基材的孔洞之中，使得互鎖效應較高，接合程度也增加，故滲透率下降。當鑄膜液溫度高時，溶劑揮發速率較快，會使高分子鏈在伸展狀態即固化，因此形成的薄膜較為緻密，碳化後層間距值較小，滲透率會較低，分選效率較高。

關鍵詞：碳膜、基材、中間層、TiO_2、粗糙度、黏度

Abstract

The CMS membrane has an amorphous construction, which consists of micrometer-to-submicrometer porous channel. This idealized bimodal pore distribution ensures high membrane separation performance. However, the selective layer (carbon) cannot be bond well to the Al_2O_3 support due to the different properties between them. In general, during thermal treatment, the interfacial stresses are relaxed by forming interfacial gap due to the shrinkage of organic phase. Thus, in this project, the effect of support physic-chemical characterization on the morphology and the greenhouse gas separation performance of the CMS membrane were investigated.

In the first year, several different pore size distributions of alumina supports were synthesized and used to evaluate the effect on the morphology and adhesive properties of CMS/Al_2O_3 composite membranes. The tetradecahedral shape of the substrate achieved at the sintering temperature of 1400 ℃ was found to be suitable for the prepared CMS membranes, which exhibited a H_2 permeability of 1300 Barrer with H_2/CH_4 and CO_2/CH_4 selectivities of 174.16 and 56.44, respectively. To optimize the substrate structure to provide a cost-effective and highly productive method for the deposition of brittle CMS membranes, this proposed procedure can be used to improve the mechanical strength of the supported membrane for enhanced manipulation.

In the second year, the MFI and TiO_2 were acting as intermediate layer to modify the interfacial adhesion. After modification with MFI silica, the CMSM supported on 1100-MFI-1 substrate shows better H_2 permeability of 2223 Barrer and an ideal H_2/CH_4 selectivity of 260 due to the crosslinking reaction between polymer chain and Si-O, Si-O-Si groups. The results indicated that the permselectivity of carbon molecular sieving (CMS) membrane fabricated in this study can exceed the 2008 Robeson's trade-off line. Then, the alumina support was modified by TiO_2 nano-network. The surface area and the total pore volume of substrate were increased, which is benefited for mechanical interlocking with polymer chain. Further, PEI chain was bonded by the Hydroxyl groups of the TiO_2 to improve the chemical bonding. The mechanical strength of the TiO_2-modified Al_2O_3 support was enhanced from 187.4 N to 215.9 compared to the original one.

In the third year, we change the polymer solution temperature to adjust the viscosity of dopes. The low viscosity of dopes will penetrate into the substrate to improve the mechanical interlocking, but the permeability will also decrease. When increasing the polymer solution temperature, the polymer chain was rigidified due to the high volatility of solvent. Therefore, the membrane became much dense. The d-spacing was decreased after carbonization and also resulted in low permeability.

Keywords: carbon membrane; substrate; intermediate layer; TiO_2; roughness; viscosity.

目錄

一、 研究緣起與目的

1.1 研究緣起

近年來由於工業及科技發展快速，大量使用石化燃料及濫砍濫伐，使得地球植披面積大量減少，造成大氣中的溫室氣體，如水蒸氣、二氧化碳、甲烷、臭氧、氧化亞氮、氟氯碳化物等產生增溫效應，其中又以二氧化碳對全球的貢獻量最多，形成地球暖化現象，如圖 1-1 所示。地球暖化同時也會使地表平均溫度上升(圖 1-2)為解決日益嚴重的地球暖化問題，限制溫室氣體排放，聯合國在 1992 年通過氣候變化綱要公約(United Nations Framework Convention on Climate Change，UNFCCC)，目標是將大氣中溫室氣體的濃度穩定在防止氣候系統受到人為干擾的水平；並於 1997 年通過京都議定書，訂出對各國二氧化碳的減量要求。

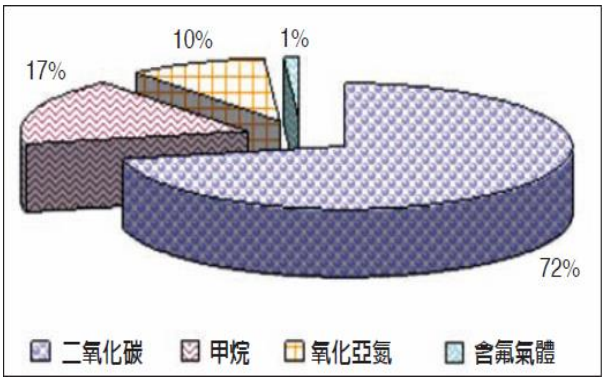

圖1-1不同溫室氣體對於全球升溫的貢獻量[1]

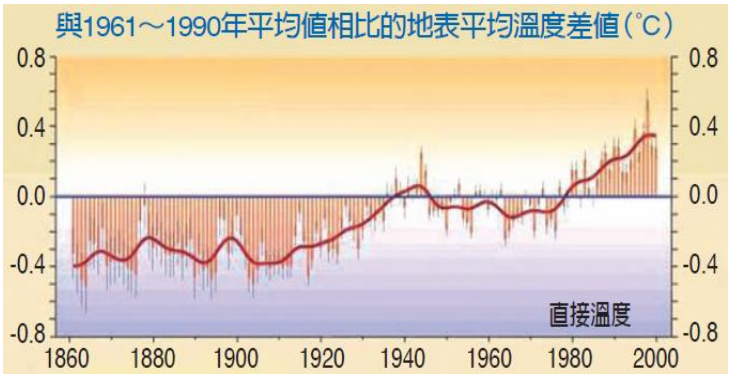

圖 1-2 歷年地表平均溫度差值[1]

根據國際能源總署 IEA/OECD 之能源燃燒二氧化碳（CO_2）排放量統計資料顯示，我國 2010 年能源燃燒二氧化碳排放總量為 270.22 百萬公噸，占全球排放總量的 0.89 %，全球排名第 20 位；每人平均排放量為 11.66 公噸[2]。該評估報告亦指出，在沒有採取任何二氧化碳排放的限制措施之下，到 2100 年前，大氣中二氧化碳濃度將升高至 490~1,200 ppm，比 1975 年

時的濃度增加 75~350%。若要使大氣中二氧化碳濃度維持在 450 ppm，必須在 2010 年前把二氧化碳排放量降至 1990 年的水準[1]。另外，能源的需求也日益劇增，使傳統燃料已不敷使用，根據永續能源國際網路機構所提出之全球未來能源趨勢[3]，如圖 1-3 所示，傳統燃料如石油、煤、天然氣及核能未來將逐漸被可再生能源及生質能所取代。另外，有學者也提出在未來的能源系統(圖 1-4)也會由過去以固態能源(如煤礦)到現在的液態(如石油)轉變為氣態能源(如潔淨能源氫氣) [4]，因此氫氣的純化技術也是一個研究的重點。

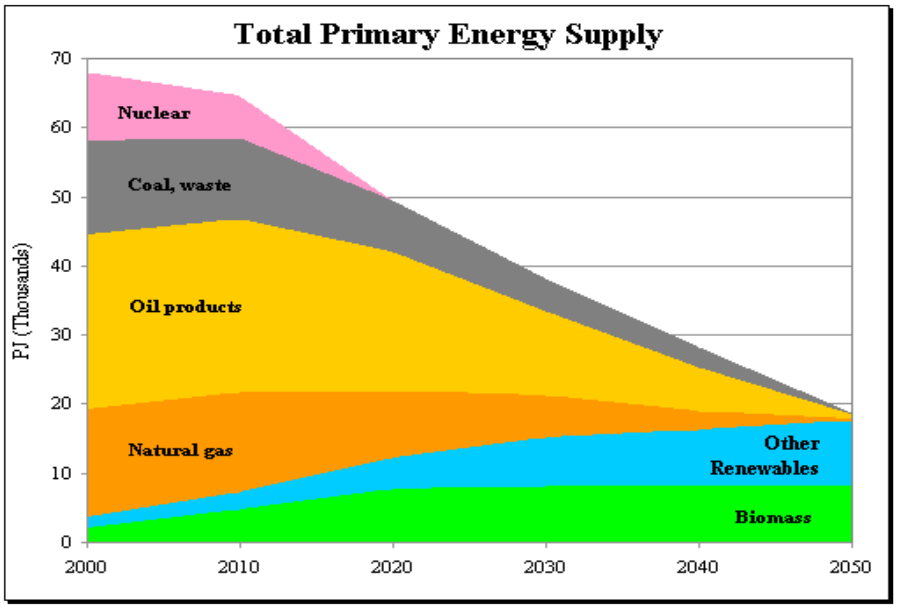

圖 1-3 INFORSE 預測未來歐盟 25 國對各種能源燃料之需求量[3]

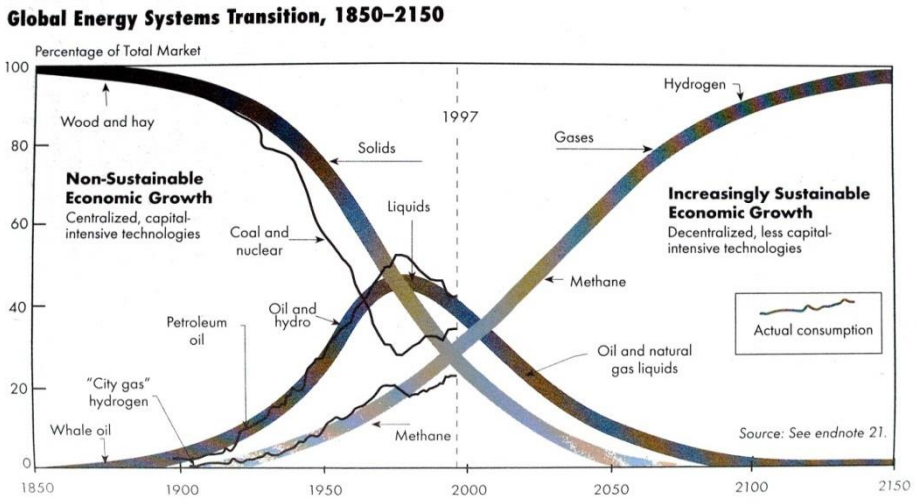

圖 1-4 未來能源系統之轉型[4]

因此，近年來發展出許多二氧化碳的控制與處理技術，二氧化碳的處理技術主要可分為物理儲存、化學分離、及生物固定化幾種，而用於分離煙氣中二氧化碳的方法一般則有化學溶劑吸收法、低溫冷凝法、薄膜分離法、物理吸收法、物理吸附法等幾種[5]。其中，應用薄膜來進行氣體分離，因為具備操作簡單、成本便宜、佔地小、高效能、低汙染等特點，更是近年來的研究趨勢。

薄膜應用於氣體分離的領域自 1980 年代以來已快速發展，而隨著技術的進步，工程應用上對於薄膜的分離及滲透效率更加要求。薄膜主要可分為有機薄膜與無機薄膜兩種，有機薄膜的原料主要為高分子前驅物，經由相轉換製備成高分子薄膜，但高分子薄膜並不適合用於惡劣環境，如高腐蝕及高溫條件下，並有機械強度不佳、化學和熱穩定性較低等等缺點。而無機薄膜，如金屬、沸石、陶瓷、碳分子篩選薄膜等具有良好的熱及化學穩定性，且結構不易被破壞，因而迅速獲得矚目，成為近年來主要的研究的方向之一[6]。

1.2. 研究目的

碳分子篩選薄膜應用於氣體分選程序時，主要由分子篩選機制所支配，高分子前驅物的選擇、氣體的動力直徑、基材與碳層間的相互作用皆為影響薄膜氣體分選效能的主要因素。在本研究室過去的研究中曾發現，當基材孔徑過大時，高分子鑄膜液將無法完整的披覆於基材表面而易生成具有缺陷的碳膜。根據先前的研究指出[7]，影響高分子與基材間黏附的主要機制為：機械互鎖、吸附作用及化學鍵結，當黏附機制較差時，極可能在兩相之間產生間隙，使得選擇性大幅下降。因此，本研究為了降低兩相之間的間隙使接合更加緊密，故將藉由不同的高溫燒結參數來改變氧化鋁基材的孔洞結構，再選擇塗佈矽沸石及 TiO_2 中間層來修飾基材表面表面物性及化性，讓薄膜與基材間的黏附效果更好、減少缺陷，提升整體的滲透選擇效能與機械強度，以增加該薄膜在實場上應用之可行性，研究流程圖如圖 1-5 所示。

研究中將以不同參數探討製備的最適化方法，並使用原子力顯微鏡(AFM)、比表面積分析儀(BET)、場發射掃描式電子顯微鏡(FE-SEM)、X-ray 粉末繞射儀(XRD)、熱重分析儀(TGA)及傅立葉紅外線光譜儀(FTIR)等儀器探討基材與薄膜間之物化特性對碳分子篩選薄膜之影響。

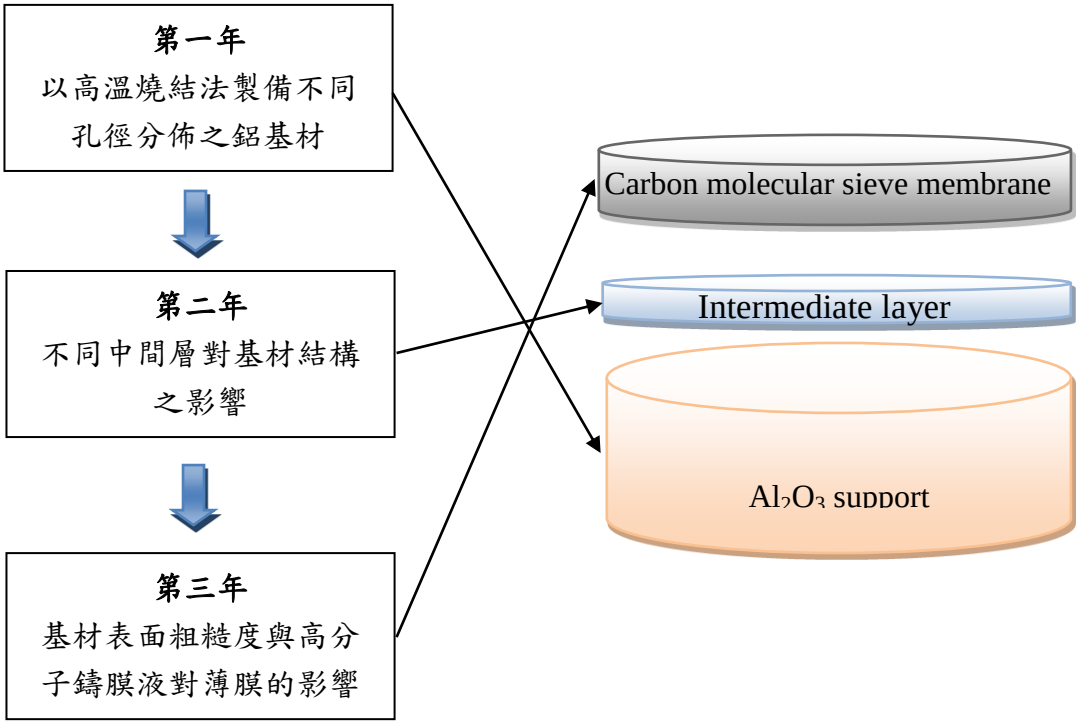
第一年
以高溫燒結法製備不同孔徑分佈之鋁基材
第二年
不同中間層對基材結構之影響
第三年
基材表面粗糙度與高分子鑄膜液對薄膜的影響
Carbon molecular sieve membrane
Intermediate layer
Al2O3 support

圖 1-5 研究流程圖

二、 文獻探討

2-1 薄膜簡介

薄膜是介於兩相之間具有滲透能力的選擇性屏障(Selective barrier)[8]，藉由驅動力及薄膜產生選擇穿透性的阻礙，對物質進行分離達到純化之目的，薄膜於氣體分離程序中的表現效能，取決於膜材本身的物理及化學特性，如：親疏水性、親和性、化性、孔洞大小、形狀...等，藉由這些材料的性質變化，就可使薄膜的性能有極大的改變，因此選擇適當之薄膜材料將可有效地提升氣體分離效率。在各種分離技術中，薄膜分離技術因具節省能源的優點，故近年來漸漸取代傳統分離技術，並廣泛應用於半導體、生物科技、化學工程及環境工程等產業上。

薄膜分離法(Membrane separation)是利用選擇性滲透膜來分離溶液中的物質，為一種被動傳遞，而要使物質通過薄膜就需要驅動力，其驅動力主要區分為(表 2-1)：(1)以壓力差為驅動力，如微過濾（Microfiltration, MF）、超過濾（Ultrafiltration, UF）、奈米過濾（Nanofiltration）；(2)以濃度差為驅動力，如氣體分離(Gas Separation)、透析(Dialysis)及滲透蒸發(Pervaporation)；(3)以溫度差為驅動力，如薄膜蒸餾(Membrane distillation)； (4)以電位差為驅動力，如電透析(Electrodialysis)[9]。而工業中薄膜分離的發展，則可分為已發展的微濾、超濾膜，發展中的氣體分離，及還未發展的壓力透析等[10]如表 2-2 所示。其中，因近年來溫室氣體濃度持續攀高，故許多研究致力於使用氣體分離法來控制及純化氣體[11-15]，使得此領域蓬勃發展。

表 2-1 薄膜分離程序常見的驅動力來源[9]

Pressure difference	Concentration (activity) difference	Temperature difference	Electrical potential difference
Microfiltration	Gas separation	Membrane distillation	Electrodialysis
Ultrafiltration	Pervaporation		
Nanofiltration	Carrier mediated transport		
Reverse osmosis	Dialysis		
Piezodialysis	Diffusion dialysis		

表 2-2 薄膜分離狀態[10]

Category	Process	Status
Developed industrial membrane separation technologies	Microfiltration, Ultrafiltration, reverse osmosis, electrodialysis	Well-established unit operations. No major breakthroughs seem imminent.
Developing industrial membrane separation technologies	Gas separation, pervaporation	A number of plants have been installed. Market size and number of applications served are expanding.
To-be- developed industrial membrane separation technologies	Carrier facilitated transport membrane, piezodialysis	Major problems remain to be solved before industrial systems will be installed on a large scale

2-2 氣體薄膜種類

薄膜可分為有機薄膜及無機薄膜兩種，有機薄膜通常泛指高分子薄膜，而無機薄膜則有金屬、陶瓷、沸石膜、碳分子篩選薄膜等。有機高分子薄膜目前已被廣泛應用工業上，用來分離、純化氣體，但仍有機械強度不佳、耐熱及化學性差及無法同時具有高滲透選擇率等缺點，因此發展受到限制。而另一方面，無機薄膜因為具有良好的化學及熱穩定性、且可同時提升滲透及選擇率，如表 2-3，所示故近年來許多研究開始致力於此[16-21]。

表 2-3 薄膜優缺點比較

	Polymeric membrane	Inorganic membrane	
		Carbon membrane	Zeolite membrane
Separation mechanism	Solution diffusion	• Knudsen diffusion>10 Å • Surface diffusion<50 Å • Capillary condensation <30 Å	
		• Similarity Molecular sieving<6 Å	
Advantages	Low production cost	• Excellent chemical stability • Surpass the trade-off between permeability and selectivity	• Create uniform pore structure at molecular Level • Exhibit catalytic property
		Similarity Excellent thermal stability	
Disadvantages	• Poor thermal resistance • Poor chemical resistance • Arduous to beach the trade-off between permeability and selectivity	• Vulnerable to adverse effect from exposure to organic contaminants and water vapor	• Difficult to operate in bulky organic environment • High material cost • Reproducibility in the synthesis method • Poor processability • Difficult to synthesis membrane with a large surface area
		Similarity Brittle High production cost	

薄膜依其橫結構型態可分為對稱型及非對稱型薄膜，如圖 2-1。

(1) 對稱型薄膜(Symmetric)

對稱型薄膜其整體的組成均為同一種分子，其孔洞結構幾乎一致，膜的厚度約在 10 ~ 200 μm 之間，通常藉由膜的厚度及孔洞大小及分布來控制其通透量大小，當厚度下降或孔洞較大時滲透通量隨之增加，常用於滲透蒸發。在製備上常使用單一高分子溶液為主原料，再以沉澱或蒸發技術來成膜。

(2) 非對稱型薄膜(Asymmetric)

通常此型態的薄膜由兩種分子所組成，孔洞較大的為基材層，負責擔持薄膜以增加其整體機械強度，而孔洞較緻密的選擇層則具有分選的功能。因其具有較好的機械強度，故此種類型的薄膜為工業界廣泛使用，非對稱膜結構的基材層厚度約為 50~150 μm 之間，而薄膜層則是由 0.1~0.5 μm 所組成。在製備上常用高分子前驅物塗佈於基材上所形成，而碳分子篩選薄膜則是將塗佈完成之高分子非對稱型薄膜再放入真空或惰性氣體高溫爐進行碳化而得。

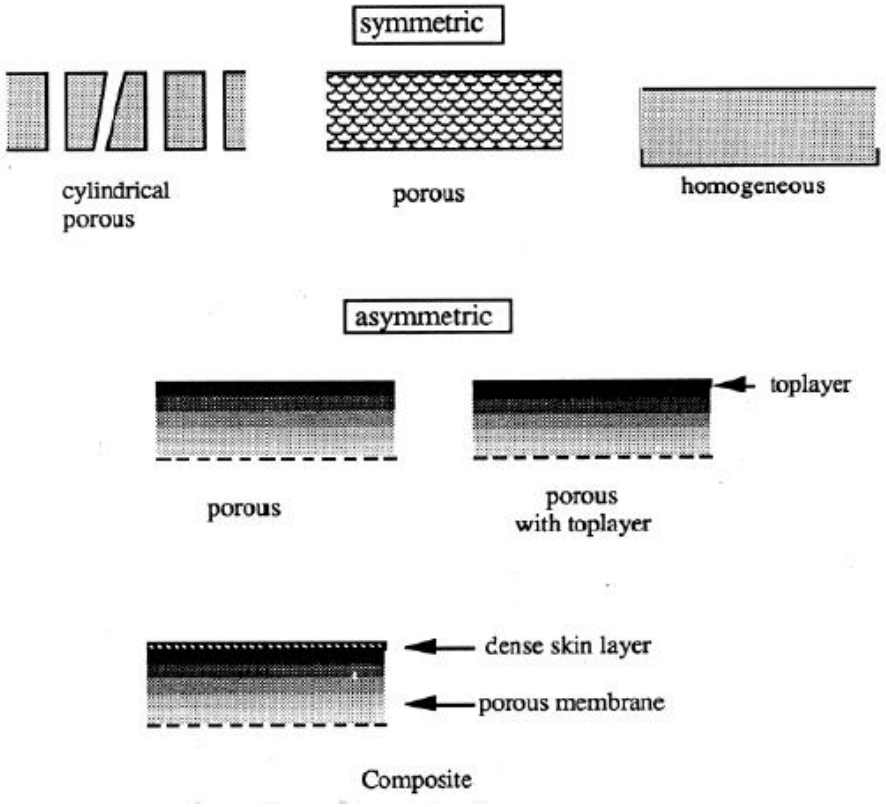

圖 2-1 薄膜橫截結構圖[8]

2-3 薄膜分離機制與原理

常見薄膜型態以緻密、微孔及巨孔這三種類型為主，(1)緻密型薄膜：主要是呈現一個孔洞非常微小或無孔的狀態，此種薄膜是利用分子在薄膜中的溶解擴散速率不同而進行分離，如鈀膜或高分子薄膜。(2) 微孔型薄膜：這種薄膜孔洞比緻密型大，是利用孔洞大小來進行分離，當分子小於孔徑時可快速通過，若大於孔徑則無法，因此可藉此分離兩種不同物質，如碳分子篩選薄膜。(3)巨孔型薄膜：因孔洞極大，無分選能力，固常被用來作為基材層，以提升薄膜整體機械強度，擔持微孔或緻密型的薄膜，如氧化鋁基材。

薄膜在氣體的分離機制主要可分為(1) Poiseuille flow (2) 紐森擴散(Knuden diffusion) (3) 毛細管冷凝(capillary condensation) (4) 分子篩(molecular sieving) (5) 表面擴散(surface diffusion) (6) 溶解擴散(solution-diffusion)等六種，如圖 2-2 [22]。

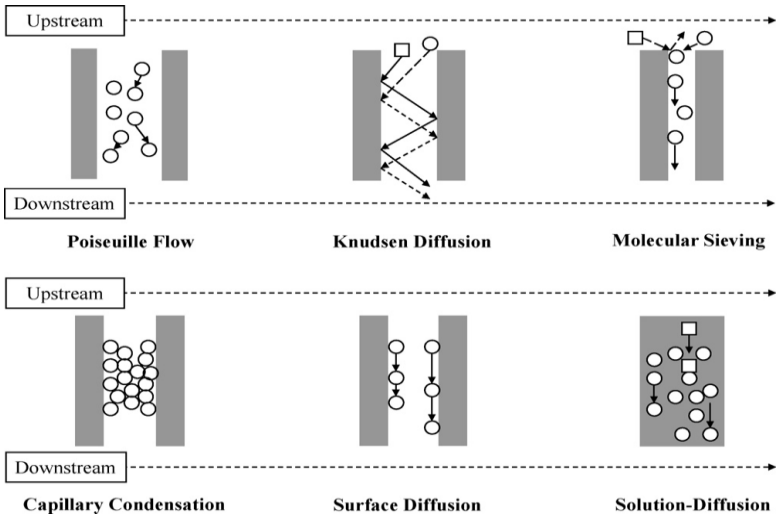

圖 2-2 氣體於薄膜的傳輸機制[23]

(1) 普以士流(Poiseuille flow) :

發生於當薄膜自身的孔洞半徑(r)大於氣體分子之動力直徑(λ)時(即 r/λ＞1)，薄膜兩側存在壓力差，氣體分子即藉由彼此互相碰撞前進，而因孔壁間距過大而無篩選性能，因此無法分離通入之氣體混合物，故於薄膜分離行為中一般不期望發生，常發生在巨孔型薄膜的傳輸機制。

(2) 紐森擴散(Knudsen diffusion):

此種傳輸機制與 Poiseulle flow 相反，當分子的動力直徑(λ)大於薄膜自身的孔洞半徑(r)時(即 r/λ＜1)，會發生紐森擴散機制，薄膜兩側存在壓力差，氣體分子主要藉由與孔壁之間的碰撞前進，相較於上述機制，其薄膜孔洞半徑降低，當薄膜具有中孔結構時，紐森擴散即為主要支配機制，在此種機制下，薄膜的選擇性主要與氣體分子量有關。

(3) 毛細管冷凝(Capillary condensation):

當薄膜孔洞屬於微孔型(20~30Å)時發生，主要利用氣體的穿透時與孔壁間存在的相互作用力，使氣體冷凝薄膜孔洞內部。此種機制可藉由氣流及控制壓力的方式得到冷凝於孔壁中的氣體，因此具有相當高的選擇率。

(4) 分子篩選(Molecular sieving)

當薄膜的孔洞屬於次微孔型，可利用薄膜本身孔徑與分離物質的動力直徑(kinetic diameter)的相對大小而達到分離的效果。動力直徑較大的氣體會被阻擋在薄膜外側，而動力直徑較小的氣體分子則可快速通過，藉此達到氣體分離效果。但分子篩選機制對於大小相似的氣體較無法有效的分離，因此現今許多學者利用添加其他材料或化學改質，來達到提升分選能力的目的。

(5) 表面擴散 (Surface diffusion)

當氣體分子被吸附於孔洞表面上，此時產生之氣體傳輸機制即稱為表面擴散機制。在具有壓力梯度的環境下，優先吸附於孔洞表面的物質將會快速於孔洞表面遷移並擴散出薄膜。

(6) 溶解擴散(Solution-diddusion):

當薄膜孔洞屬於緻密型時，其傳輸機制是利用溶解擴散來進行氣體分離，根據高壓側到低壓側其步驟為: (1)氣體分子擴散至薄膜表面。(2) 氣體分子解離為原子。(3)原子溶入薄膜。(4)原子擴散於膜表面。(5)原子在膜的表面結合成氣體分子。(6) 氣體分子在薄膜的表面上進行脫附[20]。此機制利用不同氣體在薄膜材料中的擴散速率不同來達到分離的目的。

使物質由上游端至下游端進行擴散，其內部濃度分佈現象，可由Fick的第二擴散定律(Fick's second law of diffusion)表示，如式(1)。

$$\frac{\partial C}{\partial t} = D_g \frac{\partial^2 \mathrm{C}}{\partial \mathrm{x}^2} \qquad (1)$$

起始條件式(I.C)，式(2)，與邊界條件(B.C.)，式(3)

I.C： t=0, C=0 (2)

B.C：x=0, $C=C_1$; x=l, $C=C_2$ (3)

當系統處於擬穩定狀態(Pseudo-steady-state)，即($\frac{\partial C}{\partial t}=0$)，假設$D\ g$ 為一常數，則式(1)成為式(4)

$$\frac{d^2C}{dx^2} = 0 \qquad (4)$$

利用邊界條件可解出氣體分子在薄膜中的濃度分佈現象，結果如式(5)所示。

$$\frac{C-C_1}{C_2-C_1} = \frac{x}{\ell} \qquad (5)$$

由Fick的第一擴散定律(Fick's first law of diffusion)知，氣體的通量如式(6)所示。

$$J = -D_g\left[\frac{\partial C}{\partial x}\right]_{x=0} = D_g\frac{(C_1 - C_2)}{\ell} \tag{6}$$

隨著時間的變化，氣體分子的擴散量在薄膜中與下游區介面，為相同的傳送量(J)，以式(7)表示

$$J = \frac{1}{A}\frac{dn}{dt} \tag{7}$$

其中

n：氣體分子擴散的莫耳數

A：薄膜面積

由於在擬穩定狀態下，薄膜中各處氣體的傳送量(J)都相同，因此由式(6)與式(7)可得式(8)

$$\frac{1}{A}\frac{dn}{dt} = D_g\frac{(C_1 - C_2)}{\ell} \tag{8}$$

再經由亨利定律(Henry's law)，C =Sp

及在定溫下$S_1=S_2=S_g$ (10)

可得式(11)

$$\frac{1}{A}\frac{dn}{dt} = D_g\frac{(S_1p_1 - S_2p_2)}{\ell} = D_gS_g\frac{(p_1 - p_2)}{\ell} = \frac{P_g\Delta p}{\ell} \tag{11}$$

另外，假設薄膜下游區的氣體為理想氣體狀態(pV =nRT)，則經移項後得式(12)及式(13)

$$n = \frac{pV}{RT} \tag{12}$$

$$dn = \left[\frac{V}{RT}\right]dp \tag{13}$$

將式(13)代入式(11)得式(14)

$$\frac{1}{A}\left[\frac{V}{RT}\right]\frac{dp}{dt} = \frac{P_g\Delta p}{\ell} \tag{14}$$

經移項整理後可表示為式(15)

$$P_g = \left[\frac{dp}{dt}\right]\frac{\ell}{A\Delta p}\frac{V}{RT} \tag{15}$$

再整理為(16)

$$P_g = \left[\frac{dp}{dt}\right]\frac{\ell\cdot T_0\cdot V}{A\cdot\Delta p\cdot T\cdot p_0} \tag{16}$$

其中

($\frac{dp}{dt}$)：為薄膜下游壓力隨著時間的變化。

Δp：為薄膜兩端上游區與下游區的壓力差(cm-Hg)。

l：為薄膜的厚度(cm)。

A：為薄膜的面積(cm^2)。

V：滲透端體積(cm^3)。

T：操作溫度(K)。

因此，我們可經由實驗獲得壓力隨時間的變化曲線，將直線部分的斜率代入式(16)，可求得穩定狀態時氣體的滲透係數(P_g)，其單位為 Barrer

($1\times10^{-10}\frac{cm^3(STP)cm}{cm^2\cdot s\cdot cmHg}$)，若無膜厚度其單位為 Gas Permeation Unite, GPU

($1\times10^{-6}\frac{cm^3(STP)}{cm^2\cdot s\cdot cmHg}$)，由圖 2-3 可判讀擬穩態之斜率並代入公式。

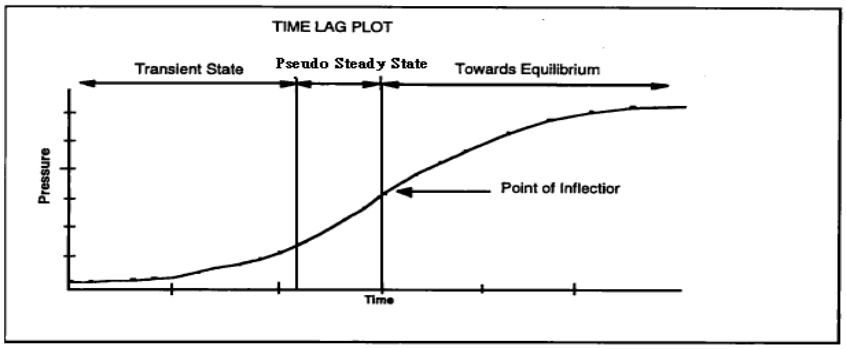

圖 2-3 下游端壓力變化圖

而兩種氣體(A、B)之滲透係數比值，則以選擇係數(Selectivity coefficient, $\alpha_{A/B}$)則以 P_A/P_B 來表示。

2-4 碳分子篩選薄膜

碳分子篩選薄膜（carbon molecular sieve membrane，CMSM）是一種無機薄膜，由熱固性高分子前趨物於真空或是惰性環境下熱裂解而成，其顯著優勢是，具有耐高壓、高溫及化學安定性等優點。此外，碳膜具有分子篩能力，認為可改善滲透率及選擇率互相抗衡的現象，同時提升氣體滲透率及選擇率。碳膜通常以非對稱型式存在，並使用氧化鋁作為基材層，塗佈一層高分子材料後再進行碳化而得。而理想化的碳膜孔洞為一狹縫狀結構[24]，如圖 2-4，是由一連串的微孔及超微孔所組成，其中微孔主要負責增加氣體在薄膜中的擴散能力，而超微孔則是使薄膜有分選氣體的能力。

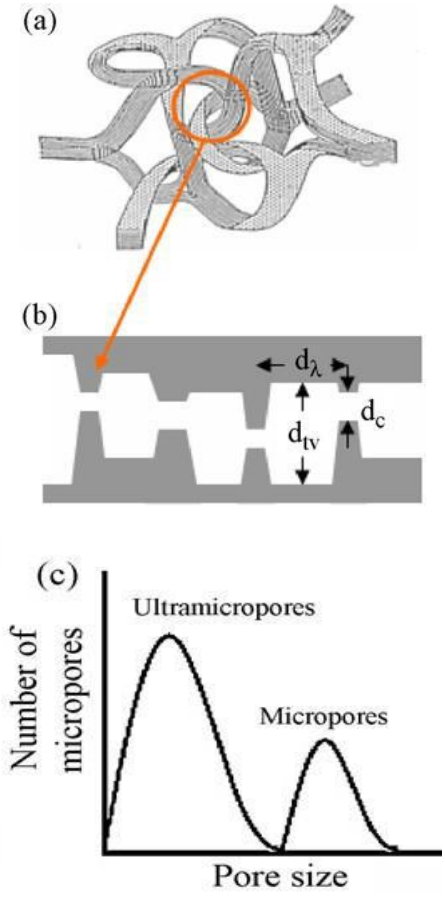

圖 2-4 碳分子篩選薄膜的理想孔洞結構示意圖：(a)碳結構、(b)孔洞結構、 (c)孔洞分佈。[24]

碳分子篩選薄膜的製備程序主要分為六大步驟[25]，如圖 2-5 所示，首先會選擇適當的前驅物，製備成高分子薄膜，再經過預處理的步驟，使高分子於碳化前的結構穩定，最後進行碳化，而有些研究還會對薄膜做後處理，例如表面修飾等，得到碳分子篩選薄膜後，就薄膜形式設計適合的氣體滲透模組結構進行測試。

(1) 前驅物選擇：

為了得到高品質的碳分子篩選薄膜，前驅物的選擇就是一個很重要的關鍵，不同的高分子前驅物可製備出不同物性、化性的薄膜，因此我們可藉由選擇不同薄膜前趨物來改變薄膜之微孔結構、薄膜的組成方式與碳化條件等參數[26]，使氣體滲透選擇效率提高。製備碳膜所選擇之高分子前驅物大多以熱固性材料為主，因其較可操作在高溫下且於熱裂解過程中不會產生液化(liquefy)或軟化(soften)的現象，可避免熱裂化後產生缺陷及裂縫[27]。而高分子前驅物因本身化學結構及裂解形式不同，明顯改變碳膜的結構進而影響氣體分選效果，因此有學者針對不同前驅物，探討其所製備成之碳分子篩選薄膜氣體滲透效果的差異[24, 28]。

(2) 高分子薄膜之製備：

高分子膜之製備需在一個適當的條件下進行,若製備的方法不適合所選擇的高分子性質，碳化後則無法達到預期的分選效果。將高分子塗佈於基材上的方法有很多種，以旋轉塗佈法(Spin coating)操作方便、設備簡單，且較容易得到一均勻的薄膜，故被廣泛應用於製備高分子薄膜。其方法為將過量之高分子溶液置於基材上，再由高速旋轉將多餘溶液甩出，而得到一均勻的薄膜[29]。

(3) 薄膜前處理：

薄膜的前處理主要當碳分子篩選薄膜碳化裂解時，確保前驅物之穩定性，並保有前驅物之結構特性，提升薄膜整體之穩定性與分離特性。如 Kisuki 等學者提到特定前驅物若沒經過前處理步驟，於熱解/碳化時會造成軟化現象，進而影響薄膜氣體分離效率[30]。前驅物處理方式又可分為物理及化學法，所謂物理法：包括拉伸法，通常使用於中空纖維式薄膜之前驅物上，是為了增強保留熱處理前的分子排列。化學法：使用化學試劑處理的方法，主要於熱裂化過程中增加微孔之均勻性

(4) 前驅物裂解/碳化：

薄膜的熱解/碳化為形成薄膜之關鍵步驟，其方法為將前驅物於真空或惰性環境下進行熱解/碳化而得，正確的選擇前驅物及熱裂解條件就可以定製出理想的微孔大小及形狀。熱裂解條件大致可分為這幾個:溫度、升溫速率、環境和熱浸泡時間、氣體流量、壓力和濃度等等[31]。

(5) 薄膜後處理：

此階段雖已得到碳分子篩選薄膜之結構,但亦可藉由其高溫處理程序進一步利用熱化學的方式針對不同分離應用之需求修飾薄膜孔洞大小及分布。後氧化及活化為常用來改變碳膜孔洞結構的後處理程序。當薄膜於熱裂解後暴露於氧化環境時，其孔徑及微孔體積均會增加， 而不同材料有不同的活化時間和停滯時間，因此，會應用這兩個因素來於獲得所需的孔洞結構。另外可使用化學氣相沉積法來增加碳膜的選擇性，利用有機物種進入膜孔洞中，再進行熱裂解而形成。而後熱解則是可以縮小薄膜的孔洞，通常可藉由後氧化跟後熱解這兩個步驟來調整所需的孔洞大小。

(6) 氣體滲透模組設計：

製備完成後的薄膜，需藉由氣體滲透測試來瞭解薄膜之性能。因此需參考過去之文獻，設計一個適合的模組來進行實驗，同時也必須將所得之數據做整合計算，方便與文獻中的數據作一性能的比較探討。

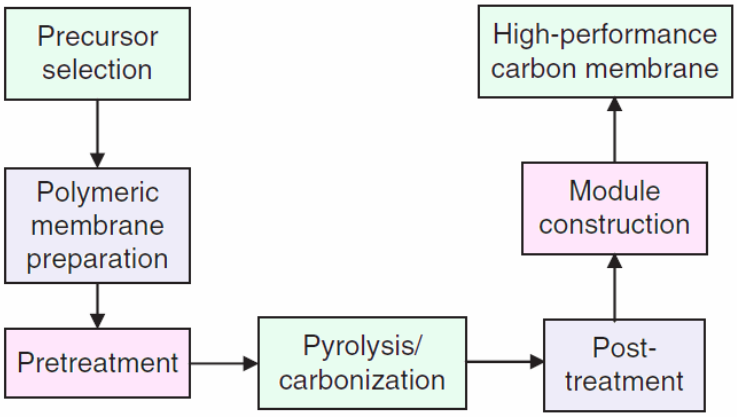

圖 2-5 碳分子篩選薄膜的製備程序[27]

2-5 薄膜改質技術

2008 年 Robeson 整理出薄膜氣體分離性能的資料提出 upper bound trade-off line，如圖 2-6。upper bound 代表薄膜對氣體分離效能的上限，也是目前學者所希望超越的目標，因此各方研究人員無不盡全力利用各種方法來達到此目的，不管是合成新的高分子材料、摻合、表面改質等方法，皆希望能製備出超越 upper bound 的薄膜。

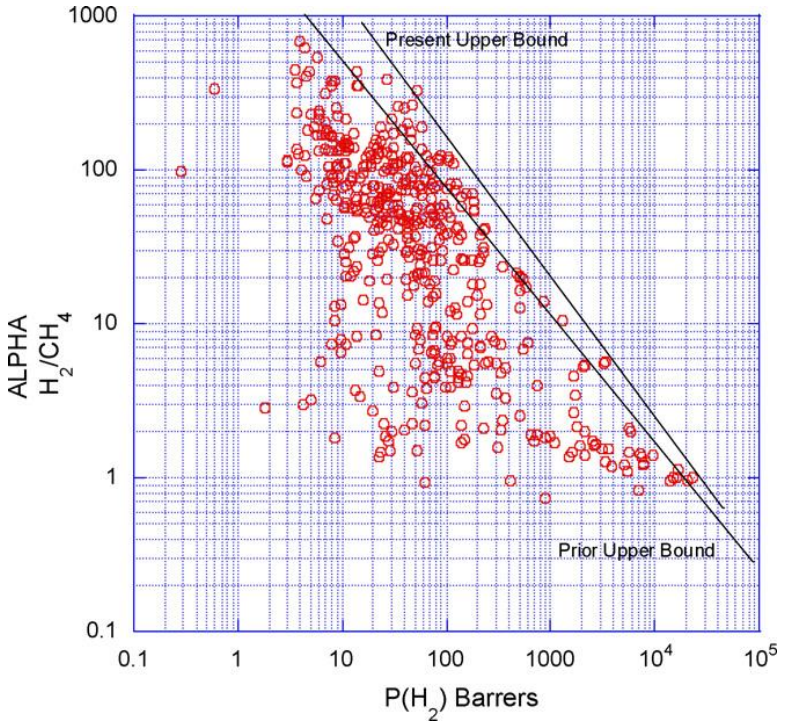

圖 2-6 高分子與無機薄膜之 H_2/CH_4 選擇率與 H_2 滲透率 Robeson 曲線

2-5-1 添加奈米無機材料

近年來，許多學者不再僅是改變高分子材料的物性或化學結構，也亦嘗試添加具有分子篩結構之奈米材料如二氧化矽(silica)、沸石(zeolite)或奈米碳管等，進而增加氣體之滲透能力，並透過無機材之官能基對特定氣體之吸附能力，來提高選擇能力，故許多學者以此種複合方法獲得高滲透率和選擇率的氣體分離薄膜。如表2-4所示，如Nik等人[32]添加具有胺基的沸石材料進入薄膜後，可以明顯提升CO_2的通透量及CO_2/CH_4的氣體分選能力；Liu等人[17]則是將不同尺寸的T型沸石添加到高分子溶液中，再經高溫碳化製備成複合碳膜，而研究結果指出，體積較大的沸石容易造成顆粒與碳膜間產生較大的間隙而導致薄膜的通透率增加、選擇率降低，而顆粒較小的沸石則有相反的趨勢，而這些研究結果都顯示出添加具有分子篩結構之材料可以明顯改善氣體滲透選擇之權衡關係。

表 2-4 添加奈米無機材之碳分子篩選薄膜的相關文獻彙整

Polymer	Material	Performance		Rrf.
		Permeability	Selectivity	
Polyimide	MWCNT	PCO_2=866(Barrer)	CO_2/O_2=4.1	[33]
PAA	Zeolite T	--	--	[17]
PSF	3A zeolite	PH_2=1121 (GPU)	$\alpha H_2/CO_2$=1.53	[34]
PPO	SBA-15	PCO_2=2420(Barrer)	$\alpha CO_2/CH_4$=63.8	[35]
PEI	SBA-15	PH_2=667.5(Barrer)	$\alpha H_2/CH_4$=75.0	[20]
PSF	MWCNT	PH_2=290(Barrer)	$\alpha H_2/N_2$=6	[36]

2-5-2 非對稱型薄膜之改質

相較於對稱型複合基材薄膜具有較低的機械強度，非對稱型則利用多孔基材層作為支撐材，以提升薄膜的機械強度[37, 38]，並可藉由降低選擇層厚度達到提升薄膜通量[39-41]的目的，因此將選擇性薄膜塗佈於多孔性基材層已漸漸取代一般常見之對稱型緻密薄膜。而一般的支撐材料可分為有機及無機種類，常見的有機支撐材如聚苯醚砜(PES)、聚砜(PSF)等，而無機支撐材則有氧化鋁、陶瓷、不鏽鋼等材料，目前已有許多學者成功以非對稱式薄膜應用於氣體分離，如表2-5所示。然而研究指出，一般有機支撐材能提供的機械強度有限，隨著操作壓力提高，多孔的有機基材層型態開始改變，相對而言無機支撐材能提供足夠的化學、熱穩定性和機械強度，因此被廣為使用。但其缺點是，這些材料的表面非常粗糙，往往會使沉積在上方的薄膜產生缺陷，因此，過去的文獻也往往會在兩相之間加入中間層進行修飾，如表2-6所示。

而碳分子篩選薄膜通常以非對稱型式呈現，過去學者認為，基材的目的只是增加薄膜的機械強度，而其孔洞並不會干擾薄膜的滲透選擇率，但經過研究發現，當基材孔徑或粗糙度過大時，高分子鑄膜液將無法完整披覆於基材表面而易生成具有缺陷的碳膜，且基材表面的粗糙度會影響薄膜層的分子排列情形[20, 42]，孔洞大小也會使的鑄模時鑄造液的滲入量不同[43]，對薄膜的性能影響極大，因此，基材的性質也是製造薄膜的成敗關鍵。碳分子篩選薄膜目前未能商業化使用的最大原因，是其整體機械強度不足、易碎，因此也開始有許多研究開始致力於提

升整體機械強度，如Hong等學者[44] 藉由在氧化鋁基材中混合小顆粒的TiO_2粉末，讓這兩種複合物在燒結時同時產生緻密化與固化兩種作用，生成強度更高的鈦酸鋁，從一開始鍛燒溫度為1400°C，氧化鋁/二氧化鈦混合比95/5的18.2 MPa到提升混合比為70/30時得到最高的機械強度(49.4MPa)。Gaiye等學者[45]則是提到氧化鋁被普遍使用來做為薄膜基材，這是因為它有極高的穩定性，在高溫及惡劣的化學環境下也能保持其效能。然而，其易脆的本質會大大縮短壽命，並限制在商業的應用及發展。因此，為了有效的改善氧化鋁的斷裂韌性，故利用混合YSZ粉末來改質基材，使其具有最高的抗折強度和斷裂韌性，實驗結果也證實添加YSZ粉末的基材可以比未添加的基材在1400℃的鍛燒溫度下斷裂韌性提高了10倍，1600 ℃下則提高了3倍，而抗彎強度在YSZ添加量為2wt%時有最大的強度，約140MPa，這比未添加YSZ的基材在1400 ℃時提高5倍，1600 ℃提高了1.4倍。其綜合比較如表2-7所示。

表 2-5 非對稱式薄膜應用於氣體分離

Selective layer	Polymer precursor	Supported materials	Application	Ref.
Polymer	Polydimethylsiloxane (PDMS)	Polyethersulfone (PES)	H_2, CH_4, CO_2 and C_3H_8	[46]
CMSM	polyetherimide (PEI)	Alumina disk	H_2,CO_2,O_2, N_2, CH_4	[47]
CMSM	BPDA-pPDA polyimide	Macroporous carbon support	Pure He, CO_2, O_2, N_2, CH_4	[48]
Polymer	Matrimid	polysulfone (PSF)	Pure O_2, N_2	[41]
Palladium	--	Porous stainless steel	Pure N_2, H_2	[42]
Polymer	Poly(vinyl acetate) (PVAc) blend with poly(vinyl pyrrolidone) (PVP)	Alumina tube	Methanol/MTBE mixtures	[38]
CMSM	Poly(2,6-dimethyl-1,4-phenylene oxide) (PPO)	Alumina tubular ceramic support	H_2, CO_2, N_2 and CH_4	[49]

表 2-6 添加中間層之非對稱式薄膜

基材	結果	Ref.
氧化鋁	在基材上塗上二氧化矽層，二氧化矽提供了平滑表面及吸附作用使其於上方長出b軸取向的MFI薄膜。	[50]
玻璃	藉由改變基材表面羥基的密度及反應活性與使用溶膠-凝膠法生成Ti-OH基團，可促進生成沸石晶體。	[51]
氧化鋁	透過溶膠-凝膠法在基材上塗佈二氧化矽中間層，並透過二次生長法合成b軸取向的silicalite-1型沸石膜。	[52, 53]
氧化鋁	塗佈氧化鋯(YSZ)中間層因為可解除在燒結過程中應力引起的裂紋，因此可提高MFI薄膜的穩定性	[54]
不銹鋼	使用不銹鋼做為silicalite-1沸石薄膜的基材，並發現鐵的氧化物可以促進沸石成核。	[55]

表 2-7 基材改質方法比較表

基材	研究方法	結果	文獻
不銹鋼管	利用添加氧化鋯中間層減少基材表面粗糙度。	成功利用氧化鋯修飾基材，讓其孔洞明顯縮小，製備出非常薄且均勻的薄膜。	[42]
氧化鋁	比較粒徑尺寸為0.3μm與0.2μm的氧化鋁其粗糙度與孔洞對薄膜的影響。	使用0.3μm所製備出的薄膜會因氧化鋁孔洞過大造成薄膜而有氣體洩漏情形。	[43]
氧化鋁	將氧化鋁基材混合小顆粒的TiO_2粉末，讓這兩種複合物在燒結時同時產生緻密化與固化作用。	成功將機械強度由原本的18.2 MPa提升為49.4 MPa。	[44]
氧化鋁	混合YSZ粉末來改質基材，使其具有最高的抗折強度和斷裂韌性	其最佳參數可將抗折強度提高5倍，斷裂韌性提高了10倍。	[45]
氧化鋁	利用低溫燒結法使改變氧化鋁晶粒排列成長情形	當溫度增加時，晶粒成長行為會提供粗糙度較低的表面，增加黏附性，減少缺陷產生。	[20]
氧化鋁	利用高溫燒結法使氧化鋁結構越趨使其緻密化。	經過高溫燒結後的基材其孔隙率與表面粗糙度的綜合效應能增加氣體分選能力	[47]

2-6 基材與薄膜的界面黏接現象

Wang 等學者[7]在其研究中提到：一般用於黏附力的五個黏附機制為：(1) 機械互鎖、(2) 擴散、(3) 化學鍵、(4) 電子和(5) 吸附力。其中，機械互鎖，吸附能力和化學鍵是被普遍認為在高分子/陶瓷界面上常見的黏附機制。吸附能力的產生是由於陶瓷基材具有比高分子溶液還高的表面能量，因此塗佈的高分子層可以黏附在基材表面。化學鍵的產生則是緣自於基材及高分子鑄膜液之間鍵結的產生，機械互鎖則是指基材孔洞和鑄模液之間因孔洞產生的鑲嵌結構。故也有許多學者針對以上三種不同黏附能力對基材進行改質，如表 2-8 所示。

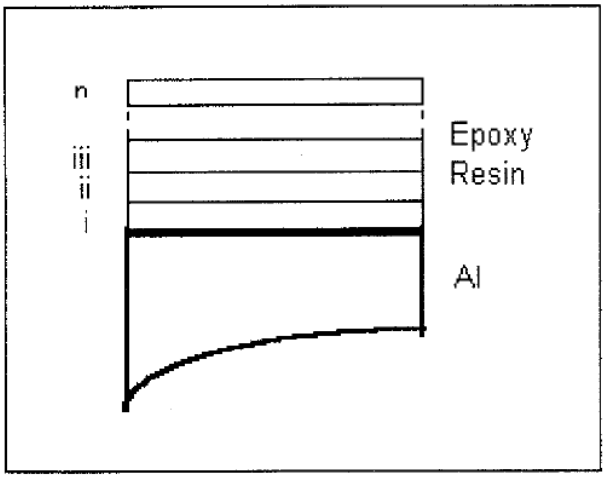

圖 2-8 高分子與鋁基材界面示意圖[56]

表 2-8 應用不同黏附機制進行薄膜改質

主要作用機制	改質方法	結果	文獻
機械互鎖	在薄膜與基材之間塗佈一層氧化鋁做為中間層	氧化鋁可以減少基材層之粗糙度及表面孔徑，並使薄膜層能牢固粘附於基材上。	[42]
	對基材做預濕潤之前處理	經預濕潤的基材可以使塗佈之高分子液滲入較少，能更完整的覆蓋在基材上，減少缺陷。	[57]
化學鍵結	在薄膜與基材之間添加一層 MFI 沸石中間層。	高分子膜與矽基材產生化學性鍵結，使得高分子結構變的更為緊密，並同時提升氣體的滲透率與選擇率。	[58]
吸附	在薄膜與基材間加入TiO_2中間層	TiO_2提供了平滑表面及可吸附之 OH基，於上方生成高度b-軸取向的 ZSM-5薄膜。	[59]
	利用不同的前處理方法使氧化鋁基材表面含有高濃度的官能基團	改質後的氧化鋁表面含有高濃度的 O^-和OH^-，這些非常活躍的表面可以吸附高量金屬鑄膜液的陽離子，使兩相接合緊密，結果也顯現出非常高的烴類/氧選擇率。	[60]

為了讓薄膜與基材接合更加緊密，不易在兩相之間產生些許間隙而降低整體的選擇率，有研究在薄膜及基材之間添加中間層[42, 59, 61, 62] ，藉由改善粗糙度或增加化學吸附力，使其接合性更好。如 Meiling 等學者[59]利用塗佈 TiO_2 中間層讓其其在薄膜與基材之間扮演三個重要的角色，如圖 2-9 所示，第一個是形成一個平滑的表面，有利於 b-軸取向的沸石生長，第二個是提供一個沸石晶體與基材之間的吸引力，使兩相接和更緊密，第三個則是提供一個高密度的羥基基團在基材表面上，這三個重要的特點使得此研究可以合成出高度 b-軸取向的 ZSM-5 分子篩薄膜。Lin 等學者[62]在研究中也提到，在製備具有優良的分離性能的支撐型碳膜時，基材的孔洞結構和表面粗糙度也會嚴重影響頂層薄膜，故利用旋轉塗佈法在基材表面塗佈有序中孔中間層， 其結果也指出與過去文獻相比具備中間層的碳膜的整體效能較好，且有序中孔結構與蠕蟲狀結構的中間層相比，在不損失選擇能力的情況下，滲透率更是提升了四倍，故指出藉由模板法合成的有序中孔中間層可以提高基材與薄膜之間的黏附性與結構穩定性，並可以提高氣體滲透率，此方法也提供了製備高氣體滲透率與減少表面缺陷的薄膜，有助於加快碳膜在氣體分離中的商業化的應用

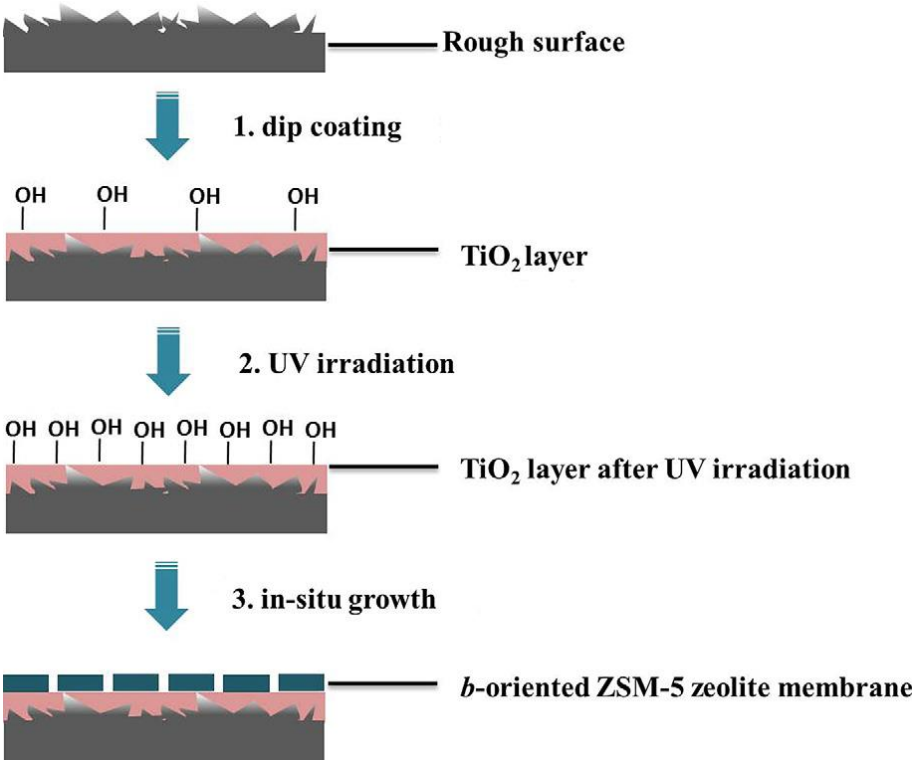

圖 2-9 b-軸取向的 ZSM-5 分子篩薄膜合成示意圖[59]

另外，也有學者在鑄膜前先對基材做化學前處理[43, 60]，藉由化學反應讓薄膜與基材之間發生交互作用，使薄膜可更完整披覆於基材上。改質後的氧化鋁表面含有高濃度的O^-和OH^-，這些非常活躍的表面可以吸附高量金屬鑄膜液的陽離子，使兩相接合緊密，結果也顯現出非常高的烴類/氧選擇率。Wang等學者[7]則改變拋光時間來得到不同粗糙度之基材。當高分子塗佈於不同粗糙度的基材後，製備出來的薄膜對氣體篩選能力也有明顯不同，拋光程度較高之基材，因為拋光而降低陶瓷表面的缺陷，有助於提高複合膜的完整性，進而使選擇率增加。

2-7 氧化鋁基材孔洞結構影響因子

氧化鋁為一種廣泛利用於各個領域的陶瓷材料，如研磨材、生醫材料、薄膜技術等。在薄膜技術中，氧化鋁常被當做薄膜支撐基材使用，因氧化鋁陶瓷材料具備良好的機械強度及化學穩定性，因此於許多研究中多選用氧化鋁陶瓷材料做為薄膜基材。 [63-65]一般平板型氧化鋁支撐基材為利用擠壓成型的方式製備，而製備流程為球磨、造粒、煅燒、過篩、加壓成型、燒結(sinter)等。氧化鋁經燒結處理後，結構與械械強度也會受到許多不同因素所影響，如生胚(Green Body)之型式、粉末之型態、燒結條件等。

一般陶瓷材料為符合商業化之需求，多使用燒結方式進行處理，燒結意指藉由熱能使得粉末或胚體緻密化的技術。陶瓷燒結過程會有一系列的變化，如粒子粗化(coarsening)、晶粒成長(grain growth)、胚體緻密化(densification)等，此三種變化之活化能不同，且於動力學過程中於不同溫度下會有不同的變化，因此可藉由控制受熱溫度讓氧化鋁產生粗化、晶粒成長、緻密化，以獲得不同機械強度、及孔隙結構之基材。[66]

一般而言，燒結過程可分為前期、中期、末期三個階段，茲分述如下：

(1) 前期：

於燒結前期，粉末顆粒與顆粒間之接觸面將會慢慢轉變為頸狀。其主要之驅動力是顆粒間頸部周圍的曲率會使得物質進行流動，此時孔洞皆是相互開通的狀態。

依據 1974 年 Ashby 學者所提出燒結理論模型[67]，燒結的前期階段，原子會由六種不同路徑來進行傳送，包括：晶界擴散、表面擴散、蒸發-凝結、體擴散(來自晶界處原子、來自表面處原子、差排處原子)等。藉由不同之擴散機制，進而讓顆粒成長或緻密化，如圖 2-10 所示。而六種傳送路徑中只有體傳送之機制有收縮及緻密化之現象。

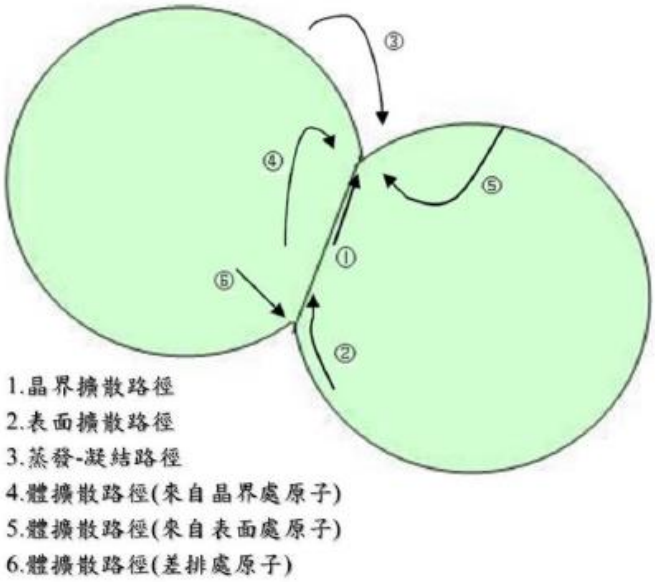

圖2-10 顆粒燒結初期之擴散路徑[68]

(2) 中期：

經前期顆粒轉變為頸狀型態後，進入中期階段時所有燒結前期之擴散機制將會持續的進行。此階段中所有顆粒間孔隙之位置將落在所有晶粒之邊緣及角落，此能有效的防止晶界移動，且在燒結中期晶粒成長較不明顯，但孔洞結構會慢慢的崩解並漸漸趨於平滑狀，並且形變為相互連接之柱狀體。此時燒結之理論密度約為 90%，顆粒並會開始快速的成長，並轉變為十四面之柱狀體型態如圖 2-11(a)所示。

(3) 末期：

當燒結進入末期時，狀態如圖 2-11(b)，緻密化之速度將會變的非常緩慢，且僅依賴孔洞與界面面積做為驅動力。孔洞也會轉變為不連續的封閉球狀型態，且於此皆段孔洞將變小且較孤立，進而使得晶界之阻力變小，顆粒成長也變的較為明顯。

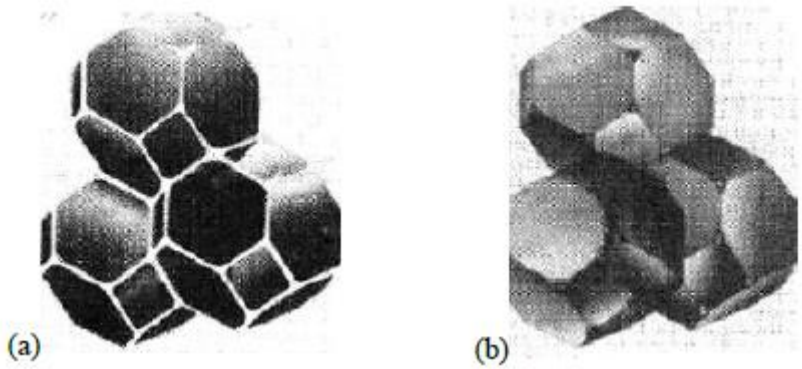

圖 2-11 燒結階段顆粒型態(a)中期(b)末期[68]

Chen 等學者也提出奈米尺度之顆粒比起一般尺度燒結較容易產生晶粒重排及晶界移動等機制。並由此理論推估於燒結前期顆粒較小的粒子因表面活性較大，有著較高的趨動能力，使得粒子會快速粗化，粗化後之顆粒將會引發再堆疊而重新排列，以利後序顆粒之緻密化如圖 2-12。

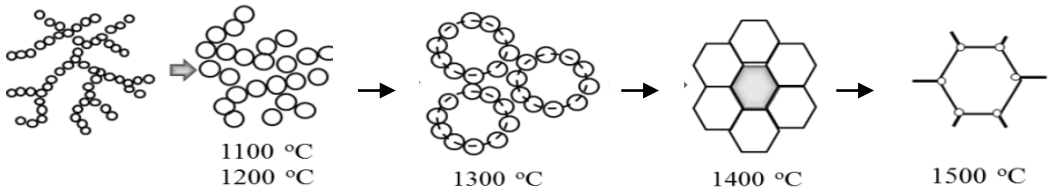

圖 2-12 奈米顆粒燒結示意圖[68]

先前亦有學者利用微米尺寸之氧化鋁粉末進行燒結，以觀察氧化鋁顆粒形變及晶相隨燒結溫度的變化情況，由結果指出氧化鋁顆粒經燒結後，前期會經歷顆粒粗化之步驟，進而使得孔隙有變大之情況，而隨著溫度提升至1400℃，氧化鋁之顆粒將轉變為蠕蟲形狀(亦為十四面體)，此時結構較為鬆散，整體之孔隙量也會有上升的情況，溫度提升至 1500℃時，氧化鋁顆粒與顆粒間會趨於緻密化現象，整體孔洞結構也會急劇減少與下降，而當溫度上升至 1600℃將會完整的達到緻密化型態，此時孔洞結構也會完全消失。氧化鋁密度或收縮率及顆粒粒徑隨燒結溫度之變化情形如圖 2-13 所示。[69]

薄膜所選用之多孔性支撐基材其質傳阻力不可影響到薄膜傳輸能力，因此本研究將燒結溫度控制於 1600℃以下，以防止氧化鋁基材於燒結時因高溫而產生的緻密化行為，影響了氣體的傳輸現象。

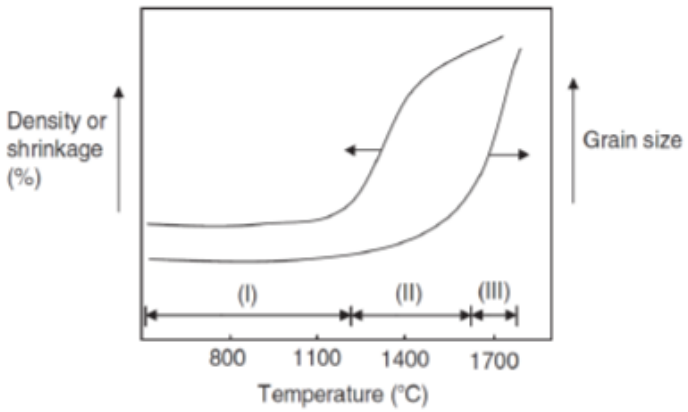

圖 2-13 氧化鋁粉燒結過程中密度及晶粒尺寸變化曲線圖

2-8 矽/鋁基材結構

矽/鋁結構俗稱為沸石，係由氧化矽與氧化鋁以規則方式排列所組成，沸石材料最為重要之物化性質為Si/Al比、孔洞尺寸與連接之氧原子數、結構之陽離子。一般沸石化學結構為 $Ay/m^{m+}[(SiO_2)\cdot(AlO_2^-)_y]\cdot zH_2O$，而A表示陽離子，m+表示陽離子之價數，y/m則是不同之陽離子數量[70]，而孔洞尺寸約分佈在3-13，並可依不同之結晶方向與結構進行區分[71, 72]。沸石本身之結構常會含有Si-O-Si、Si-O、Si-OH等化學官能基。常見之沸石結構為LTA、FAU、MFI、LTL 及AFI 結構等，表2-9 及圖2-14所示，為常見的沸石結構及其孔徑尺寸、陽離子種類。

表2-9 不同結構之沸石特性[73, 74]

種類	型態	孔徑大小	矽鋁比	陽離子
FAU	X 型沸石	4.1Å	1-1.5	Na^+
	Y 型沸石	7.4Å	1.5-3	Na^+
MFI	ZSM-5	5.6×5.4Å 5.1×5.5 Å	>5	Na^+
	Silicalite-1	5.6×5.4 Å 5.1×5.5 Å	無限大	-
LTL	L 型沸石	7.1 Å	3	Na^+ K^+
LTA	A 型沸石	4.1 Å	0.7-1.2	Na^+
AFI	AlPO4-5	7.3 Å	-	磷酸鹽類

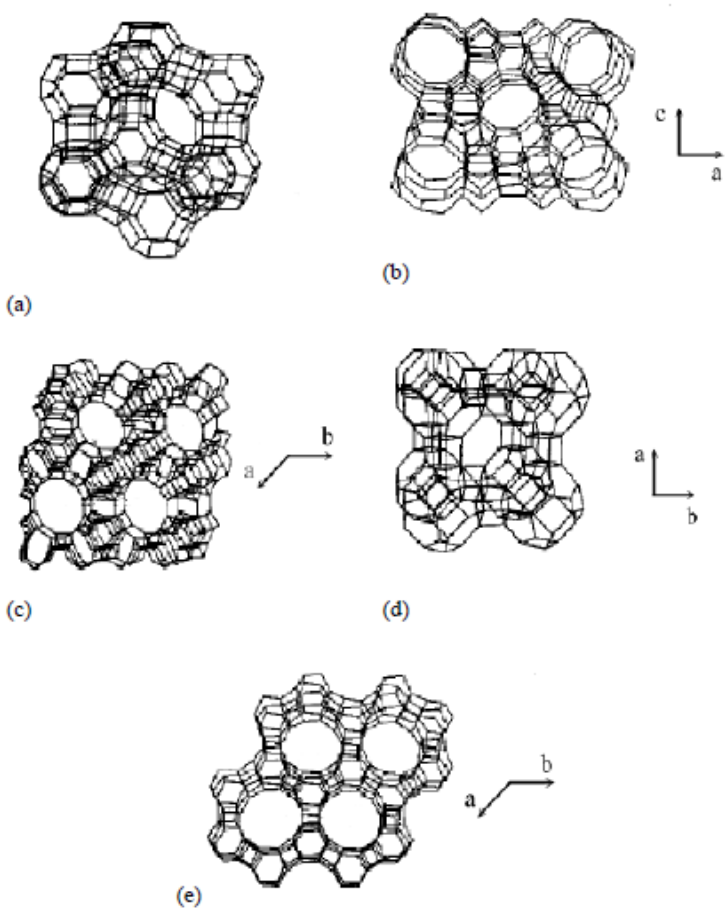

圖2-14 不同沸石結構圖(a)FAU、(b)MFI、(c)LTL、(d)LTA、(e)AFI

較常見之沸石結構為A型與X型，因結構中鋁含量較多，較常應用在離子交換的領域；Y型則因具備催化活性則常應用在石化工業之觸媒；MFI結構中的ZSM-5及Silicalite-1型沸石。因矽鋁比之範圍較大可微調沸石之孔徑，且MFI沸石本身可承受900℃之高溫，於pH=4-10之環境下也較穩定。[74]因此於本研究中選擇MFI的Silicalite-1沸石材料做為修飾鋁基材之矽層結構。

MFI沸石之矽鋁比範圍為5至無限大，其中Silicalite-1沸石之矽鋁比為無限大，故本身為純矽沸石，也因成份中不含鋁，所製備出之沸石材料並沒有催化活性。MFI沸石屬於一斜面晶體，相貌為六角柱狀體，孔徑大小約介於0.51 nm-0.56 nm間，如圖2-15(a)所示。由圖中顯示之結晶方向，b方向用(0 1 0)表示、a方向用(1 0 0)表示、c方向為為一斜面因而用(1 0 1)表示。

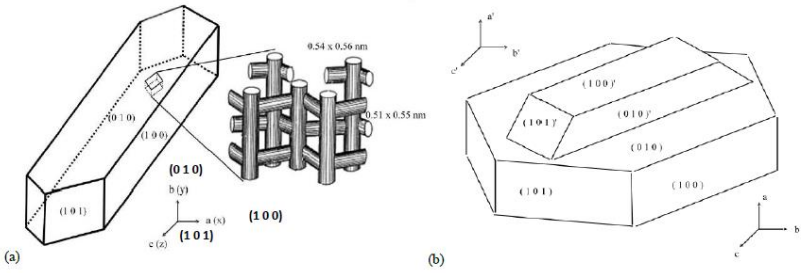

圖2-15 MFI 晶體結構(a)單一晶體結構(b)孿生晶體結構

較為常見的沸石製備法為使用水熱合成方式，製備內容物包含矽鋁源、結構導向劑、稀釋溶液、陽離子反應物等。製備可分為三個階段，(1)誘導期、(2)成核、(3)結晶生長[75]等。如圖2-16 所示，於誘導期時矽源(一般為四乙基矽酸鹽，TEOS)會水解於水中，也因溶液中加入了結構導向劑，使得矽酸鹽與結構導向劑間產生了疏水驅動力，於水解後矽酸鹽會排列於結構導向劑之周圍[76]，此時所型成之矽酸鹽類膠體將懸浮在溶液中，膠體將成為預核，經高溫高壓後，預核將會生長成核並在聚集的地方進行有順序之排列、並結晶生長[75, 77]。

水熱合成之方法為將氧化鋁基材放置浸含有矽源之前驅溶液中，並放至於高壓高溫之環境後，以固定溫度之方式進行水熱合成。合成之示意圖如圖2-17 所示，首先會於基材上成核，此時為異相與勻相同時發生，於此狀態下除基材之核種外，溶液相中也會慢慢形成沸石顆粒，緊接著藉由於基材上已成核之晶體，進行結晶成長，接著則為結晶晶體與核同時生長，直至覆蓋了基材表面[78]。

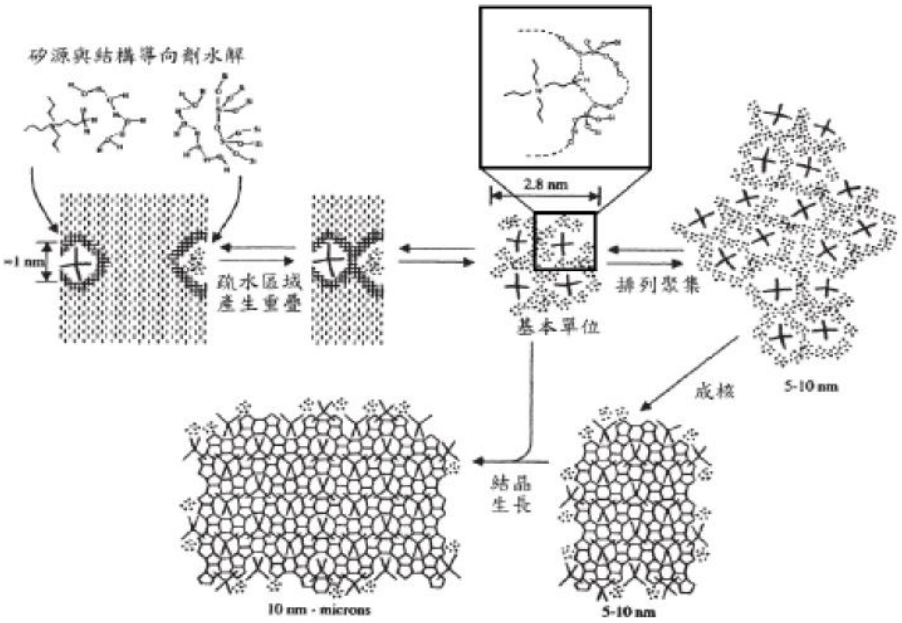

圖2-16 MFI 沸石結晶示意圖

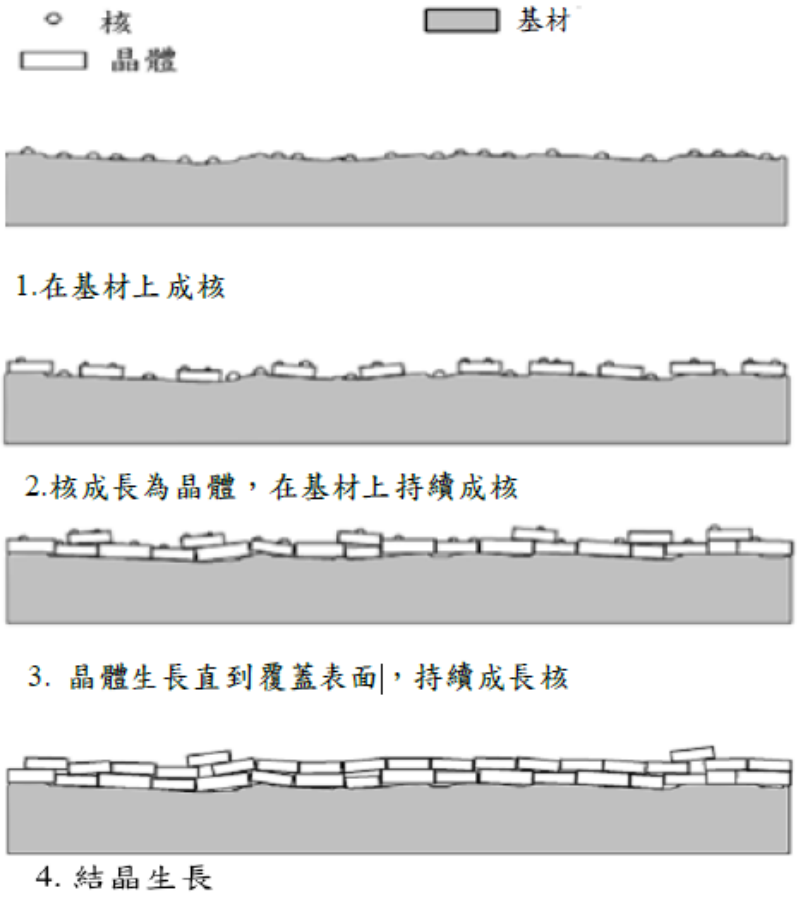

圖2-17 水熱合成示意圖[82]

2-9 TiO_2 製備與特性結構

溶膠-凝膠(Sol-Gel)是兩種物理化學狀態間的轉化過程，其反應式如2-1~2-3，為一種溼式化學合成技術。製備方法大多利用將金屬醇鹽或無機鹽類進行水解及縮合反應形成溶膠[79-81]，而後隨著水的蒸發轉變為凝膠，再於低溫中乾燥得到疏鬆的乾凝膠，或進行高溫煅燒處理以得到奈米粉體或利用含浸法將其鍍在基材上形成薄膜的方法。水解與聚縮合反應的速率受起始原料種類與濃度、溶劑、觸媒、pH 值、溫度以及化學添加劑等因素所影響，可藉此控制溶膠粒子的大小及微結構[82, 83]。

溶膠(Sol)是屬於膠狀體(Colloid)的一種，由大小約1~100 nm 膠體粒子均勻安定的分散於一連續相中。因為分散粒子很微小，因此可以忽略重力效應。凝膠(gel)的定義為經過凝膠化(Gelation)反應後，分子單體形成兩個或兩個以上的鍵結，而經縮合後逐漸形成大分子乃至於高分子之半固態[84]。故溶凝膠法即泛指將均勻分散的膠體粒子交鏈化或將金屬前驅物經水解、聚縮合產生網狀結構物的製程，如圖2-18所示[85]。

(1) Hydrolysis

$$\equiv Ti\text{-}OR + H_2O \rightarrow \equiv Ti\text{-}OH + ROH \quad (2\text{-}1)$$

(2) Alcohol condensation

$$\equiv Ti\text{-}OR + OH\text{-}Ti\equiv \rightarrow \equiv Ti\text{-}O\text{-}Ti\equiv + ROH \quad (2\text{-}2)$$

(3) Water condensation

$$\equiv Ti\text{-}OH + OH\text{-}Ti\equiv \rightarrow \equiv Ti\text{-}O\text{-}Ti\equiv + H_2O \quad (2\text{-}3)$$

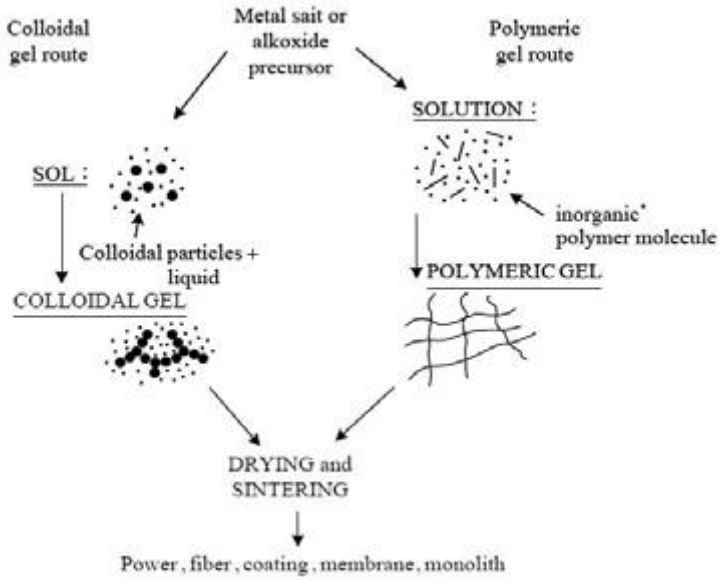

圖 2-18 溶膠-凝膠製程示意圖[85]

TiO_2具有三種晶體結構，分別為正方晶系(tetragonal)的銳鈦礦(Anatase, A type)和金紅石(Rutile, R type)及斜方晶系(orthorhombic)的板鈦礦(Brookite, B type)。一般在低溫的情況下，TiO_2是以銳鈦礦(Anatase)晶相存在，而當溫度高於約600℃時則會轉變成熱力學較穩定的金紅石(Rutile)晶相。圖2-19為此兩種晶格結構。

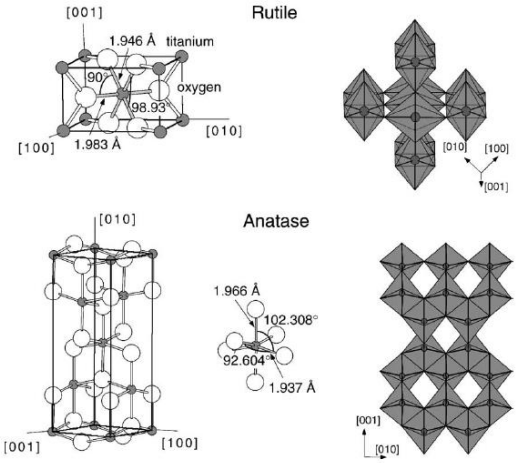

圖 2-19 銳鈦礦(Anatase)和金紅石(Rutile)之結構[86]

一般而言，TiO_2多使用 Sol-Gel 法製備，Sol-Gel 反應在酸性、中性、鹼性下均能進行水解反應與縮合反應，但在不同的 pH 條件中水解縮合的速率也不同。在鹼性條件下水解速率較慢，但縮合速率較快，所形成的粒子以顆粒大的居多；在酸性條件下水解速率較快，但縮合速率較慢，而反應所產生的粒子則是以小顆粒居多而成串長成如圖 2-20 所示[87]。由此可知調整反應的 pH 值大小對反應的水解和縮合速率有著決定性的影響，而反應的速率快慢關係著產物的結構與型態。

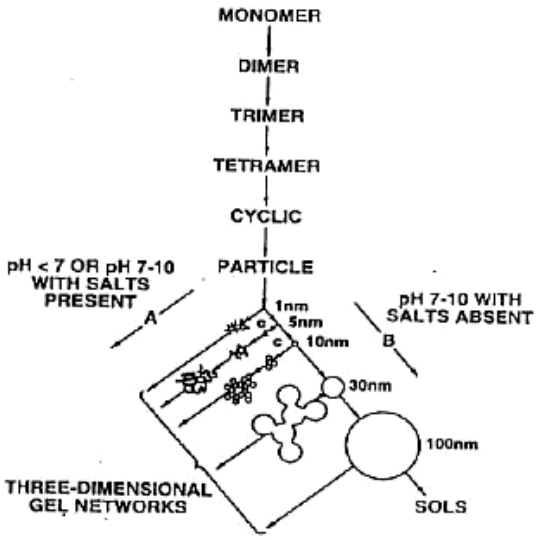

2-20 Sol-Gel 反應在不同酸鹼條件下之顆粒大小[87]

2-10 文獻總結

經由上述文獻可得知，碳分子篩選薄膜（carbon molecular sieve membrane）因具有耐高壓、高溫及化學安定性等優點，且能同時兼具高滲透率及高選擇率，近年來備受重視。一般而言，碳分子篩選薄膜之合成多以基材支撐型態製備，因碳分子篩選薄之機械強度較低，可藉由製備非對稱型薄膜讓碳膜完整的沉積於基材上方，提升薄膜的機械強度。過去研究大多藉由前驅物選擇、製備高分子薄膜、薄膜之預處理、熱解/碳化、薄膜之後處理等五步驟及添加奈米無機材料等進行改質。

此外，近來由文獻中得知，碳分子篩選薄膜之滲透分選現象確實會受到基材的影響，因此也開始有學者針對添加中間層或基材前處理進行改質。基材與薄膜間的接合行為亦會影響薄膜的分選能力，而其黏附機制主要為機械互鎖、化學鍵結與吸附作用三者，但其個別的作用力大小卻難以判別。

因此，在本研究中，將會先利用不同燒結溫度自製不同孔徑分佈之鋁基材找出最佳參數後再製備矽-鋁與鈦-鋁複合基材，探討中間層對結構的影響，最後將以拋光技術改變基材的表面粗糙度，並同時探討高分子鑄膜液之組成。另外也將薄膜進行一系列的特性分析(如:氣體滲透試驗、AFM、SEM、XRD等)，以了解基材對薄膜型態、結構之影響。並藉由本研究之結果，評估出黏附機制主要作用力大小與影響之情形。

三、 實驗設備及方法

3.1. 實驗藥品

1. polyetherimide (PEI)，Sigma-Aldrich Chemical Co. USA。
2. N-Methyl-2-pyrrolidone (NMP)，Mallinckrodt Chemical Co. USA
3. 四異丙烷氧化鈦，Sigma-Aldrich Chemical Co. USA
4. 硝酸，Sigma-Aldrich Chemical Co. USA
5. 無水酒精，島久藥品株式會社，Japan
6. 四乙氧矽烷 Tetraethyl orthosilicate (TEOS，$C_8H_2OSiO_4$) 藥品級，純度 99%，Fluka，Germany
7. 丙基氫氧化銨溶液 Tetrapropylammonium hydroxide (TPAOH，$(C_3H_7)_4N^+ \cdot OH^-$) 1 M ，Aldrich，America
8. 氫氧化納 Sodium Hydroxide 藥品級，純度 95%，島久藥品株式會社，日本。
9. 生坯，氧化鋁粉末加壓成型之坯體，鋼亞精密陶瓷股份有限公司，台灣。
10. 氧氣，純度 99.99%，東洋氣體儀器行，台灣。
11. 氮氣，純度 99.99%，東洋氣體儀器行，台灣。
12. 二氧化碳，純度 99.99%，東洋氣體儀器行，台灣。
13. 甲烷，純度 99.99%，東洋氣體儀器行，台灣。
14. 氫氣，純度 99.99%，東洋氣體儀器行，台灣。

3.2. 基材燒結前處理

本研究所用之生胚係由氧化鋁粉經研磨、造粒及1噸壓力加壓成型。取得生胚(Green body)後即以高溫爐進行高溫燒結處理。本研究設定之條件為燒結溫度(1100,1200, 1300, 1400, 1500^{o}C)、升溫速率(1,2,5,10^{o}C/min)、熱沉浸時間(2,3 hr)，並於燒結後降至室溫，將其燒結完成基材做為本研究之薄膜基材。

3.3. 矽/鋁基材製備程序

根據第一年計畫的研究結果，選擇最佳參數之氧化鋁燒結參數後，再利用一次水熱合成之矽/鋁基材(MFI-1)。係以模板法製備矽晶核並將其植種於鋁基材，以獲得研究所需之基材。首先將 TPAOH 溶解於去離子水中，再適當的加入 TEOS(矽源)，並放置烘箱以 100oC、24 小時進行一次水熱合成。取出並經過濾清洗後，放入烘箱乾燥。取適量乾燥後之晶核與無水酒精混合，並以超音波振盪 30 分鐘，使其沸石晶核可分散於酒精中。以玻璃滴管將晶核植種於氧化鋁擔體上後，再經 400 ^{o}C 鍛燒即可得一次水熱合成之矽/鋁基材(MFI-1)。

二次水熱合成矽/鋁基材之製備，為將前述步驟完成之基材放置於已配製好之適當濃度之 TPAOH:TEOS:NaOH:H_2O 混合溶液中，並再次以 110 ^{o}C、48 小時進行二次水熱合成，經 600 ^{o}C 鍛燒，即可得二次水熱合成之矽/鋁基材(MFI-2)。

3.4. TiO_2/鋁基材製備程序

根據第一年計畫的研究結果，選擇最佳參數之氧化鋁燒結參數後，再採用溶膠凝膠法製備TiO_2中間層。首先，將14.65 ml的TTIP緩緩加入100 ml的無水酒精中混合，充分攪拌30分鐘使其溶解後，再分別加入0.1、0.3、0.5 ml等三種不同配比的硝酸及1ml去離子水，其組成莫耳比如表3-1所示。經磁石持續攪拌2小時後，設定旋轉塗佈機轉數為2400轉，再將凝膠均勻塗佈於基材表面，分別塗佈2、3或4次。乾燥隔夜，放入高溫爐進行鍛燒，以每分鐘5 ℃的升溫速率，升至400℃，再持溫2小時，即可得到所需的中間層

根據第一年計畫的研究結果，選擇PEI高分子前驅物做為碳支撐材之前驅材料。首先將PEI高分子配製10%混合溶液，再利用旋轉塗佈法，將高分子溶液均勻塗佈在氧化鋁擔體上以600℃與升溫速率5℃/min進行碳化程序。

3.5. 基材拋光處理

將基材利用14μ、8μ之水砂紙與3μ之鑽石液拋光基材表面，拋光時將砂紙固定於研磨輪上，將基材置於固定位置，並施予一固定下壓力，拋光2分鐘後即可。

3.6. 製備碳分子篩選薄膜

將製備好之基材置於烘箱中避免水氣干擾，並配置10% 聚醚醯亞胺(PEI)前驅體。將PEI高分子與N-Methyl-2-pyrrolidone(NMP)溶劑加熱攪拌一天使其均勻混合後，以旋轉塗佈法(spin coating)將高分子均勻塗布於基材上，並重複進行5次塗佈製備成高分子薄膜。將塗佈好的薄膜置於室溫下乾燥一天後，將薄膜置於管狀爐並抽真空，並控制溫度為240℃持溫6小時作前處理，再升溫至600℃進行碳化，持溫兩小時後，降至室溫，即得到碳分子篩選薄膜。

3.7. 薄膜特性分析

(1) 場發射掃描式顯微鏡(FESEM)

本研究利用場發射掃描式電子顯微鏡分析樣品表面形態，探討基材及薄膜表面及側面結構變化，了解基材於不同燒結溫度操作下結構之變化及對薄膜所造成之影響。

(2) 原子力顯微鏡(AFM)

本研究利用此種顯微分析儀器，針對不同基材及所製備成之碳分子篩選薄膜表面進行掃描，主要觀察表面形態及高低差(以粗糙係數表示)，此類顯微技術都是利用特製的微小探針，來偵測探針與樣品表面之間的交互作用，本研究利用AFM分析基材及薄膜之表面高低形態及粗糙係數，藉以討論基材表面粗糙係數對於薄膜長成之影響。

(3) 紅外線吸收光譜儀(FTIR)

特定官能基(functional group)於IR光譜途中具特定之吸收頻率。判斷IR之官能基後，再配合其他儀器(如X-ray)即可判斷出化合物之結構。

(4) 黏度計

本研究利用年度計測試不同混合無機材高分子溶液之黏滯係數，膠體溶液中黏滯係數與顆粒之擴散係數的關係可透過Stokes-Einstein方程式獲得[88]:

$$D = \frac{KT}{6\pi\eta R} \quad (3\text{-}2)$$

其中 R: 水力半徑 ,m

K: 波茲曼常數 ,J/K

T: 溫度 ,K

η: 溶液黏滯係數 ,c.p.

D: 顆粒之擴散係數 ,m^2/s

(5) 高解析X光繞射分析儀(XRD)

本研究所使用分析儀器為(XRD)Bruker D8 SSS，將樣品置於儀器中以CuKa (λ=1.5418 Å)進行繞射分析，若量測結果有結晶的波峰出現時，以 Scherrer's equation 計算結晶大小，公式為:

$$D=0.9\lambda/\triangle 2\theta\cos\theta \quad (3.1)$$

上式中d 為結晶大小單位為nm，κ為係數通常為0.94，λ為X 光波長0.054nm，β為半高寬，θ為繞射峰最高值的角度，將得到的繞射強度作分峰，得到半高寬的值再帶入式3.1 中，即可得結晶大小值(grain size)。

本研究亦利用XRD以低掠角方式進行碳膜分析，所得到非晶相繞射波峰結果以布拉格定律計算，將X光的繞射現象視為入射光被結晶體的晶面反射，在某些散射角下，由相鄰晶面所散射出的X光波有相同的相位，光程差是波長的整倍數，產生建設性干涉，公式如下：

$$2d\sin\theta = n\lambda \quad (3.2)$$

d為碳膜層間距，θ為繞射角，λ為波長，當X光入射薄膜表面時，只有某些入射角會產生繞射波，因此可計算出薄膜層間距。

(6) BET 比表面積分析

利用比表面積分析儀(high resolution surface area and porosimetry analyser)分析基材內部孔洞體積及孔徑分布做為基材結構之參考依據。本研究選擇氮吸附測定法(nitrogen surface area)進行比表面積之測定，以-196℃(77K)之氮氣等溫吸附/脫附進行測量，樣品進行分析前需先經110℃以上加熱10小時之前處理以移除水氣與雜質。

本研究係於定容下利用氮氣做物理吸附，藉由重複升高或降低系統之壓力或溫度，使基材發生循環之吸附，並帶入 Brunauer Emmett Teller method總比表面積分析法來獲知樣品之總孔洞體積、比表面積、孔洞型態分析、及平均孔洞大小等數據，該方法係Langmuir 吸附為基礎，然後將其推廣為多層吸附。微孔表面積係使用t-plot分析法所得；中孔洞體積分佈則依據Barrett-Johner-Halenda所發展之BJH方法，基於脫附模式可計算求得8.5至1500.0孔徑範圍內之累積孔洞體積;微孔孔洞體積分佈係根據MP法，可求得小於20 Å 孔徑範圍內之累積孔洞體積。

3.8. 薄膜氣體滲透測試設備

薄膜氣體滲透測試，是評估薄膜對於氣體分離效率的主要依據，圖3-1為本研究的氣體滲透測試圖，將製備好薄膜，放入中央的薄膜槽體中，並利用真空幫浦維持系統真空狀態1小時，之後將利用高壓氣體鋼瓶，控制氣體壓力，當上游端壓力穩定到定值之後，開啟上游端壓力控制閥，使氣體穿透薄膜，下游端壓力偵測器記錄壓力變化以電子信號電壓輸出，並紀錄壓力隨時間變化。

以下流端壓力差與時間作圖中求得擬穩定區域的斜率值，代入以下公式計算出各別的氣體滲透率數值:

$$P = \left[\frac{dp}{dt}\right]\frac{l}{A\Delta p}\frac{VT_0}{P_0T}$$

P ：氣體滲透率(barrer) (1barrer = $10^{-10}\,\frac{cm^3\ (STP)\ cm}{cm^2\ cm\ Hg\ s}$)

($\frac{dp}{dt}$)：為薄膜下游壓力隨著時間的變化。(kg/cm^2 s)

ΔP ：為薄膜兩端上游區與下游區的壓力差。(cm Hg)

l ：為薄膜的厚度(cm)

A ：為薄膜的面積(cm^2)

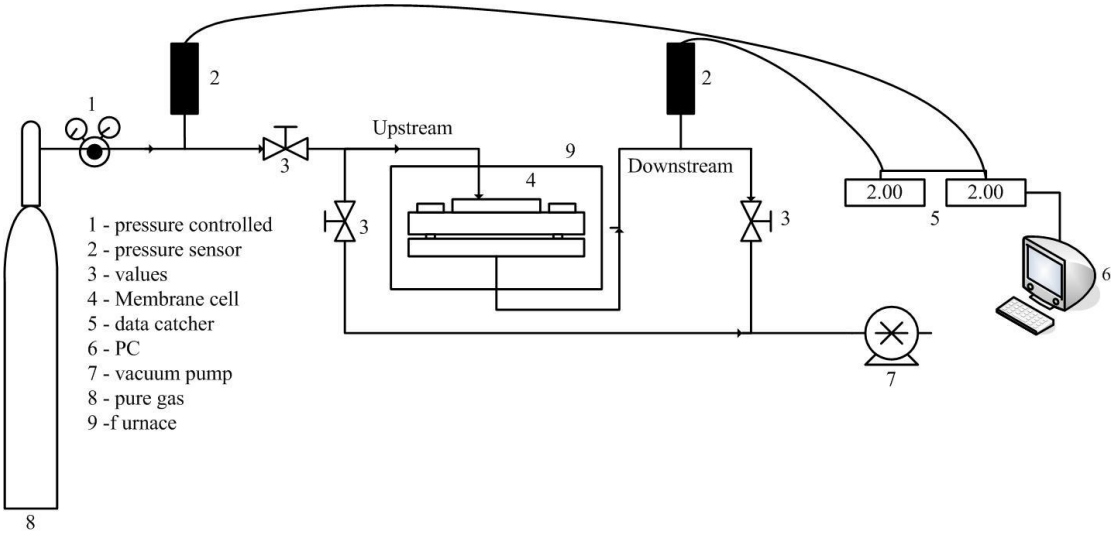

圖3-1 氣體滲透率設備圖 (自組設備)

四、 結果與討論

4.1. 氧化鋁生胚基本特性

本研究所使用之氧化鋁基材，為利用α-氧化鋁粉末壓錠成型之圓盤，直徑約為18 mm，厚度約為1.25 mm其外觀如圖4-1所示，基材之微結構分析圖如圖4-3所示，由圖可發現氧化鋁顆粒之粒徑分佈範圍約為0.1-2 μm。圖4-2為氧化鋁生胚XRD分析圖譜，經標準圖譜(JPCD 46-1212)比對後確定為氧化鋁之特徵峰，其特徵峰分別為25.58^{o}(0 1 2)、35.12^{o} (1 0 4)、37.76^{o} (1 1 0)、43.34^{o} (1 1 3)、52.52^{o} (0 2 4)、57.52^{o} (1 1 6)。經Scherrer's equation計算晶粒大小為29.54 nm。

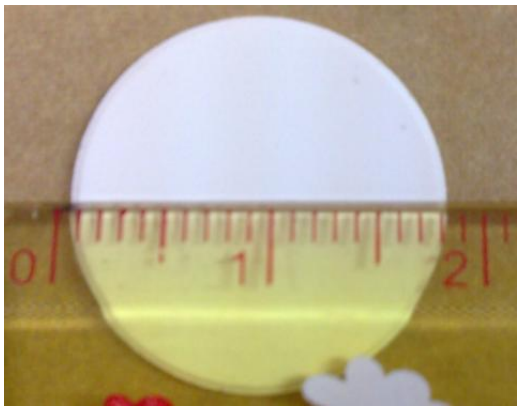

圖4-1氧化鋁生胚型貌

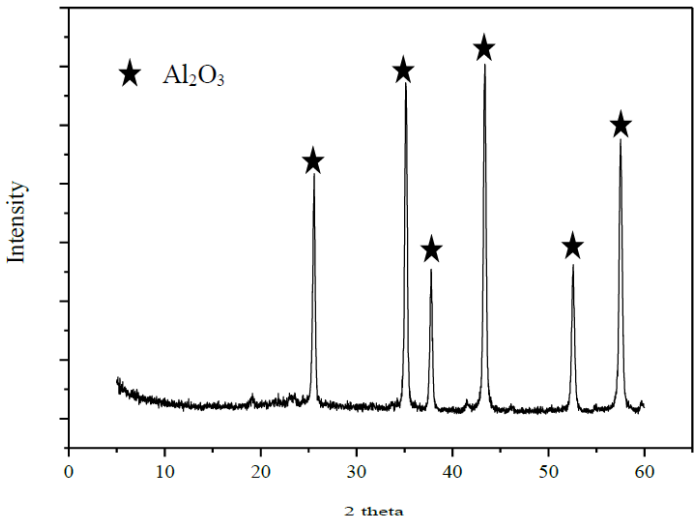

圖4-2氧化鋁粉末XRD分析圖譜

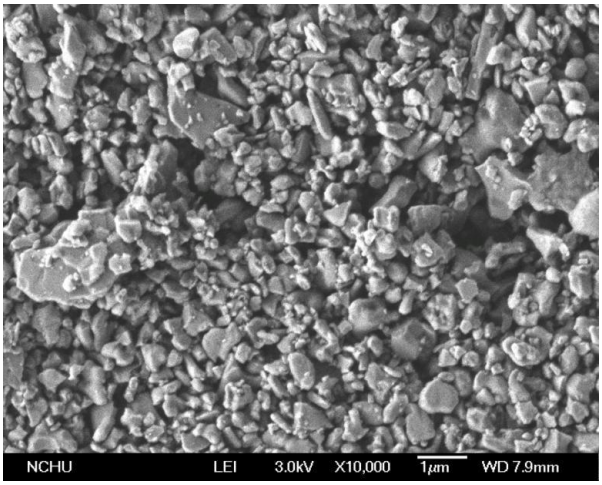

圖4-3生胚微結構分析

4.2. 燒結條件對氧化鋁基材物化特性之影響

表4-1為本研究中使用不同製程參數(燒結溫度、升溫速率、熱沉浸時間)製備之基材代碼。

表4-1不同製程處理之基材

Support code	Sintering condition		
	Sintering Temperature(^{o}C)	Hearting Rate(^{o}C/min)	Soaking time(hr)
S1100-1-2	1100	1	2
S1200-1-2	1200	1	2
S1300-1-2	1300	1	2
S1400-1-2	1400	1	2
S1500-1-2	1500	1	2
S1400-2-2	1400	2	2
S1400-5-2	1400	5	2
S1400-10-2	1400	10	2
S1400-2-3	1400	2	3

4.2.1.基材特性分析

4.2.1.1.基材晶相分析

不同燒結參數對基材晶相及晶粒之變化情況，對基材物理特性之影響，將藉由XRD(X-ray diffraction)進行分析。

不同燒結參數對氧化鋁基材之晶相及晶粒尺寸的影響，如圖4-4及表4-2所示。由分析圖譜(以不同燒結溫度為例)及Schere公式所計算之晶粒尺寸的結果得知，圖譜形態及晶粒尺寸無太大變化，各基材之晶粒尺寸約介於34.08-37.98 nm間，並未因燒結條件之不同而有明顯變化。此可能為本研究訂定之燒結溫度並未大於原氧化鋁粉末的煆燒處理溫度，因此燒結條件之不同而產生較顯著之變化。

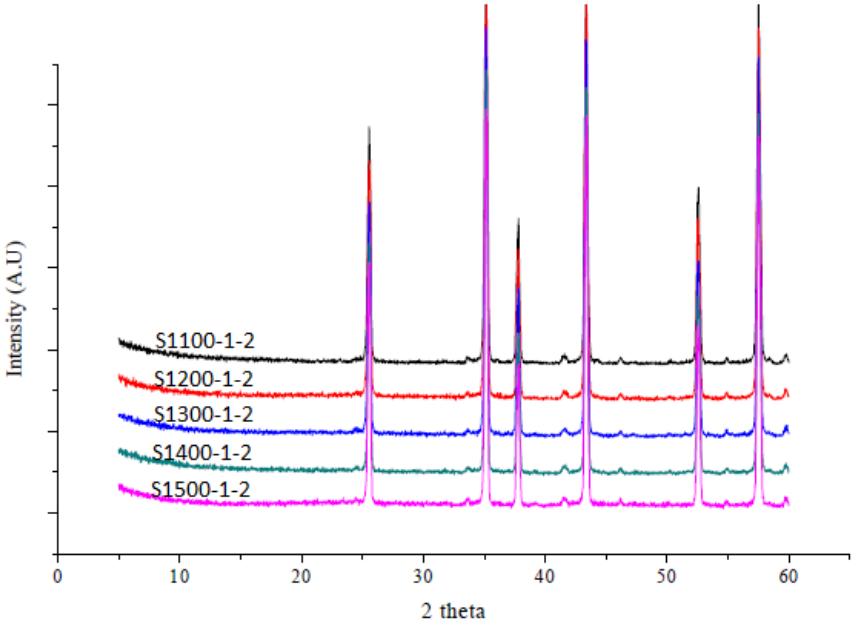

圖4-4氧化鋁基材經不同燒結溫度處理後之XRD繞射圖譜

表4-2不同燒結溫度對氧化鋁晶粒尺寸之影響

Support	晶粒大小(nm)
S1100-1-2	34.08
S1200-1-2	35.85
S1300-1-2	35.85
S1400-1-2	37.50
S1500-1-2	37.98
S1400-2-2	36.82
S1400-5-2	36.33
S1400-10-2	36.49
S1400-2-3	36.01

4.2.1.2基材微結構變化

本研究所使用之基材為未經過燒結處理之氧化鋁錠片，為將α-Al_2O_3粉末加壓成型之生胚體，因生胚體本身為物理性的接合，機械強度相對較低且顆粒與顆粒間無法達到理想的結合，因此必須藉由高溫燒結的方式，使氧化鋁顆粒產生一系列的顆粒成長及緻密化行為，進而改變基材內部結構及提升基材之機械強度。

圖4-2為經不同燒結溫度之處理基材的表面形態。如圖4-5 (a)及(b)所示當燒結溫度上升1100及1200^{o}C時，基材顆粒增大，而有粗化現象發生[89]，但顆粒與顆粒間仍有著較多之間隙，此時仍較容易受到外力破壞。當燒結溫度提升至1300^{o}C時(如圖4-5(d))可看出顆粒與顆粒間較為緊密，此因顆粒重新堆疊使得顆粒之間隙有明顯減少之現象[89]。圖4-5 (e)為燒結溫度1400 ^{o}C時之基材表面形態，可發現與圖4-5(a)(b)(c)基材相較起來，結構更為緊密，由文獻[67]得知當燒結溫度提升至1400 ^{o}C顆粒將轉變為十四面體之結構，顆粒與顆粒間會更為緊密，孔洞也會急劇減少。當溫度提升至1500^{o}C(如圖4-5 (f))時，可發現顆粒與顆粒間更為緊密，此為氧化鋁顆粒趨近於緻密化[68]，因此顆粒間之間隙有大幅遞減的現象。

圖4-5(f)~(h)為經1400 ^{o}C、不同升溫速率處理之氧化鋁基材的表面形態顯微圖。如圖所示，當升溫速率由10 ^{o}C/min減緩至1 ^{o}C/min時，氧化鋁顆粒有明顯增大之趨勢；此可能是升溫速率慢而導致氧化鋁顆粒歷經較長的熱處理程序，而使其顆粒粗化。圖4-5(f)與(i)分別為氧化鋁基材經1400 ^{o}C熱處理2及3小時後的表面形態顯微圖，如圖所示當熱沉浸時間增加時顆粒尺寸有明顯增加的現象，此可能由於提供氧化鋁顆粒轉變為十四面體之時間較長，因而導致顆粒粗化。

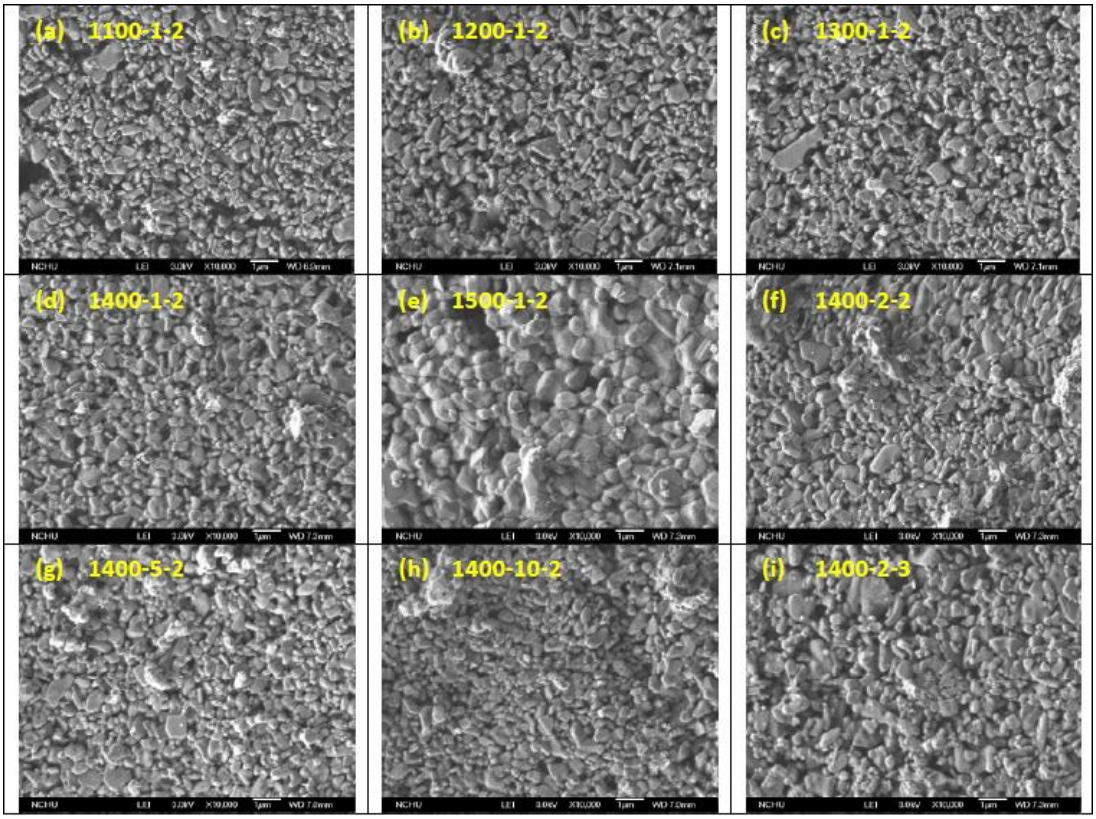

圖 4-5 經不同燒結條件處理之氧化鋁基材的表面形態顯微圖

4.2.1.3基材孔洞結構與體積收縮率分析

如表4-3所示，隨著燒結溫度由1100 °C上升至1400 °C時，氧化鋁基材的比表面積由5.9 cm^2/g下降至1.6 cm^2/g，平均孔徑由78.63增加至107.4 Å，孔洞體積則由0.0116 cm^3/g減少至0.0043 cm^3/g；整體而言，孔洞結構隨著燒結溫度上升而有收縮的情形產生(如圖4-6(a)所示)。此現象可能為氧化鋁顆粒因受高溫處理，而有明顯的顆粒粗化及重新堆疊的現象發生，進而造成顆粒及顆粒之間因重新排列而相互擠壓，使得顆粒接合面增加而壓縮孔洞體積，因為導致基材之比表面積及總孔體積下降。此外，由文獻得知，當Al_2O_3經燒結處理至1400 °C時，將開始產生形變現象，轉變為十四面體之形態，此時Al_2O_3顆粒已有逐漸轉變緻密化之行為，導致顆粒與顆粒間更為緊密使得比表面積及總孔洞體積有急劇下降之情況;故當溫度提升至1500 °C時，Al_2O_3基材已趨近於緻密化，而無法測得其孔洞結構。上述結果與FESEM結果相吻合。

由表4-3得知，基材於1400 °C進行燒結處理時，當升溫速率由10°C減少至1°C，氧化鋁基材的比表面積、總孔洞體積及巨孔、中孔及微孔的孔體積皆有損失的趨勢，此結果顯示，當升溫速率減緩時，鋁基材歷經熱處理的總時間較長，故有較充足的時間進行行態轉變，而有利於十四面體的形成；因此，孔洞結構損失較多(如圖4-6(b)所示)。而當升溫速率為1 °C/min時，其比表面積、孔洞體積最小而平均孔徑最大。

熱沉浸時間對氧化鋁基材的孔洞結構及孔徑分佈之影響，如表4-3所示。當熱沉浸時間由2小時增加至3小時時，比表面積、孔洞體積及孔徑分佈並無明顯之差異(如圖4-6(c)所示)。此可能為2小時或3小時的熱沉浸時間太相近，而無法反應出熱沉浸時間的效應。綜合燒結溫度、升溫速率及熱沉浸時間的影響結果，可推測燒結溫度及升溫速率的高低，對氧化鋁基材孔洞結構之影響較為顯著。

表 4-3 不同燒結參數對基材比表面積、孔洞半徑及孔洞體積之影響

Code	S_{BET} (m^2/g)	D_{pore} (Å)	BJH adsorption cumulative Pore Volume of pores between 3.5Å and 1000 micros Radius (cm^3/g)			
			V_{total}	V_{micro}	V_{meso}	V_{macro}
S1100-1-2	5.9	78.63	0.0116	0.0021	0.0082	0.0011
S1200-1-2	4.3	76.54	0.0084	0.0017	0.0058	0.0008
S1300-1-2	3.1	80.16	0.0061	0.0011	0.0044	0.0005
S1400-1-2	1.6	107.4	0.0043	0.0005	0.0033	0.0003
S1500-1-2	N.D.	N.D.	N.D.	N.D.	N.D.	N.D.
S1400-2-2	4.3	74.22	0.0080	0.0011	0.0063	0.0005
S1400-5-2	5.2	66.48	0.0087	0.0012	0.0062	0.0005
S1400-10-2	5.2	66.00	0.0086	0.0012	0.0068	0.0005
S1400-2-3	4.3	74.10	0.0080	0.0011	0.0062	0.0005

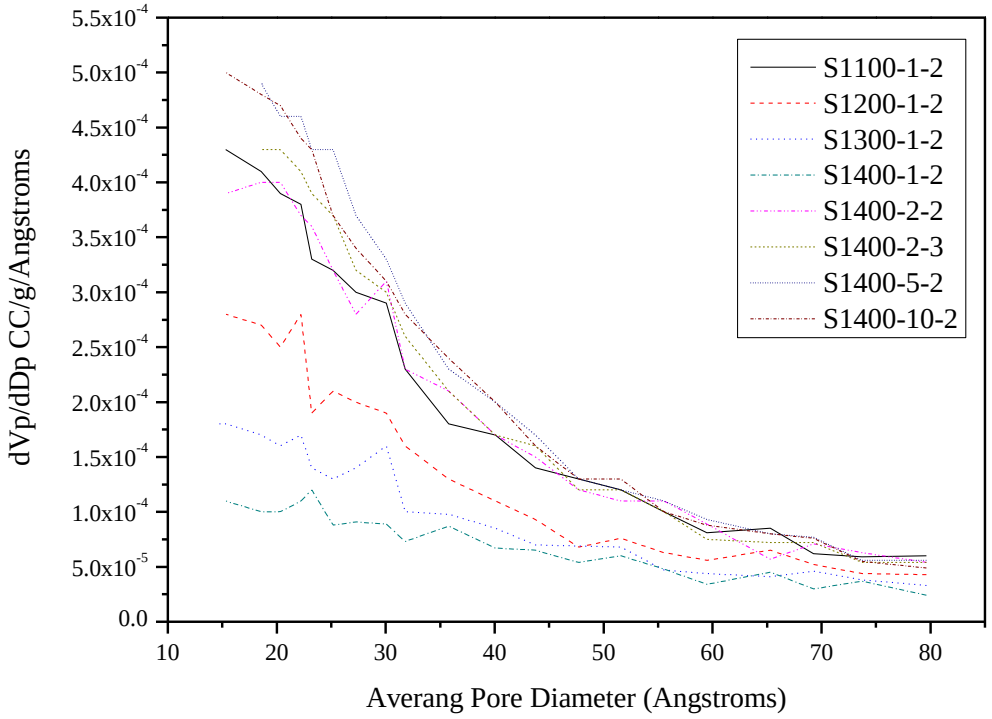

圖 4-6 不同燒結溫度之基材平均孔徑分佈圖

4.2.1.4基材真密度與體積收縮率分析

本研究利用真密度測量儀，分析經不同燒結溫度處理的基材真密度變化情形，如表4-4所示，發現當基材燒結溫度由1100 °C提升至1500 °C時，密度由5.174 g/cm^{3}遞增至6.932 g/cm^3。此趨勢與文獻之結果相符合，因氧化鋁燒結時會有顆粒緻密化而產生一系列的成長與變化機制，進而導緻密度會有明顯上升之現象[68]。

表 4-4 基材真密度變化

Sample code	Density(g/cm^3)
Green body	4.280
S1100-1-2	5.174
S1200-1-2	5.576
S1300-1-2	5.604
S1400-1-2	5.827
S1500-1-2	6.932

圖4-7為經不同燒結溫度處理之基材的體積收縮率分析圖，由圖可得知收縮曲線可分為兩階段，一為1100 ^{o}C-1400 ^{o}C，此階段氧化鋁顆粒因粗化與重新堆疊之現象，進而造成體積收縮為14.44 %。而第二階段則為1400 ^{o}C-1500 ^{o}C，此階段顆粒產生形變之狀態，體積收縮率有較為明顯上升之現象，體積收縮率可達16.55 %。

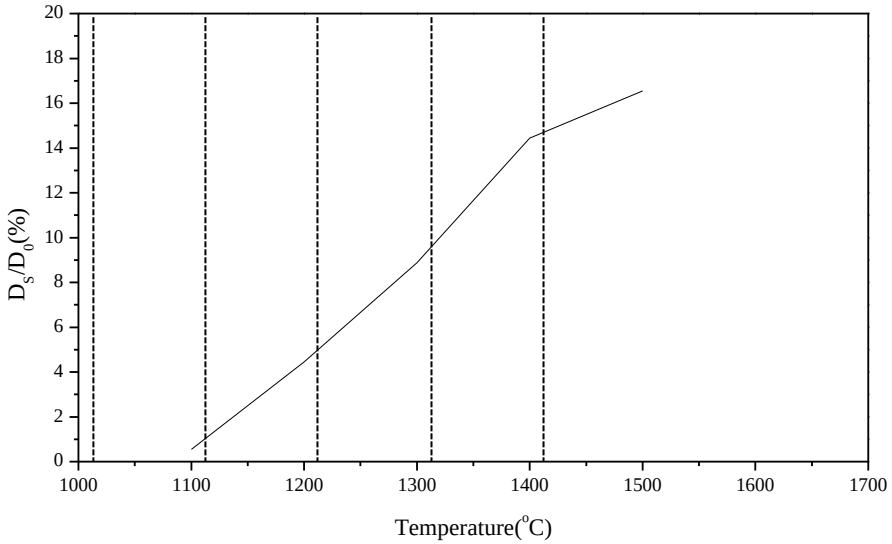

圖 4-7　不同燒結溫度基材體積收縮率分析圖

4.2.1.5基材表面粗糙度分析

本研究藉由生物原子力顯微鏡(AFM)分析基材的表面粗糙係數Ra、Rq、Rz，其中，Ra為中心線平均粗糙度，Rq為粗糙度幾何平均值(又稱為均方根粗糙度，Rms)，而Rz為十點平均粗糙度。結果如表4-5所示，當基材的燒結溫度由1100 ^{o}C上升至1500 ^{o}C時，基材表面的粗糙係數Rq由55.4 nm增加至136.0nm。這是由於當氧化鋁的熱處理溫度由1100 ^{o}C上升至1500 ^{o}C時，氧化鋁顆粒將經歷：顆粒粗化、重新堆疊、轉變為十四面體…等顆粒粒徑增加的過程，進而使得基材表面粗糙係數增加。此結果與前述FE-SEM分析結果相吻合。

表4-5亦同時顯示了，升溫速率對氧化鋁基材表面粗糙度的影響。如表所示，當升溫速率由10 ^{o}C/min減緩至2 ^{o}C/min時，鋁基材的表面粗糙係數將由67.6 nm減少至42.8 nm，並於升溫速率為1 ^{o}C/min時再提升至69.7 nm。此結果與之前所示之顆粒大小的變化趨勢並不吻合，因此可推測影響鋁基材表面粗糙度之因素，除了氧化鋁的顆粒大小外，氧化鋁基材的孔徑及孔洞體積亦為重要的影響因子。如表4-5所示，當升溫速率由10 ^{o}C/min減緩至2 ^{o}C/min時，氧化鋁因受熱時間較長，因此，除了有顆粒粗化之現象發生，亦使得孔洞結構有些微損失。孔洞體積減少，意謂著基材的高低差將會減小。因此可推測，在本研究所設計的升溫速範圍內，當升溫度速率為10 ^{o}C/min至2 ^{o}C/min時，孔洞體積及其分佈為支配粗糙係數的主要因子；而當升溫速率為1 ^{o}C/min時，顆粒粗化的現象較孔體積收縮現象顯著，因而導致粗糙係數又再次增加。

表4-5為不同熱沉浸時間之基材粗糙係數，由表中可發現當熱沉浸時間由2小時增加至3小時時，粗糙係數由53.1 nm增加至75.5 nm，此可能與較長的熱沉浸時間會導致氧化鋁顆粒有粗化之現象，進而使得基材的表面粗糙係數增加。

表4-5 不同燒結條件之基材表面粗糙係數

Surface Roughness(nm)			
	Ra	Rq	Rz
S1100-1-2	38.8	55.4	102.0
S1200-1-2	57.2	72.1	149.0
S1300-1-2	60.4	76.4	160.0
S1400-1-2	69.7	89.6	171.0
S1500-1-2	103.0	136.0	231.0
S1400-2-2	42.8	53.1	112.0
S1400-5-2	61.0	77.8	156.0
S1400-10-2	67.6	117.0	187.0
S1400-2-3	59.4	75.5	155.0

綜合XRD、BET及FE-SEM分析結果得知，鋁基材的孔洞結構會因燒結參數不同而有所改變。燒結溫度對孔洞結構影響之示意圖如圖4-8所示：當升溫速率固定為1 ^{o}C/min，而燒結溫度上升至1100-1200 ^{o}C時，氧化鋁基材會有顆粒粗化及孔體積減少之現象發生；當溫度上升至1300 ^{o}C時，氧化鋁顆粒產生重新堆疊狀態，使得顆粒相互擠壓而導致孔洞體積有下降的趨勢；而當溫度提升至1400 ^{o}C時氧化鋁顆粒開始轉變為十四面體，接觸面增加、導致孔洞體積急劇下降；隨溫度提升至1500^{o}C時，顆粒與顆粒間已近似完全的聚集，孔洞結構趨近緻密化。

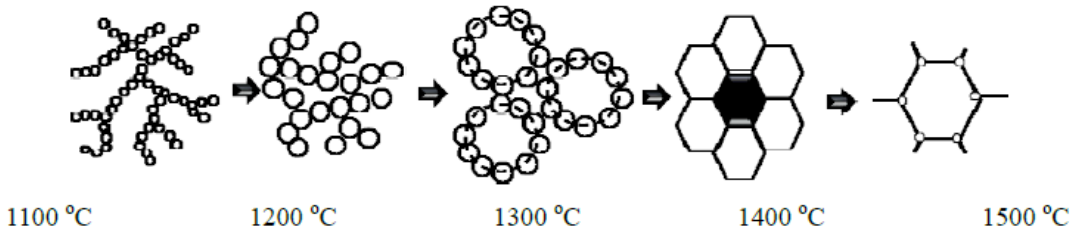

圖4-8 氧化鋁基材隨不同燒結溫度處理之形變情形

在此升溫處理的過程中，顆粒粗化將使鋁基材表面高低差增加，粗糙係數上升；而孔洞結構損失，則會使得鋁基材表面高低差減少，粗糙係數下降。由以上實驗結果可推測，當升溫速率為1^{o}C/min時，顆粒粗化是支配粗糙係的主要因子；而燒結溫度為1400 ^{o}C，升溫速率為10^{o}C/min~2^{o}C/min時，孔體積的收縮率則為影響粗糙度的支配因子。

4.2.2.碳分子篩膜特性分析

4.2.2.1碳膜表面型態分析

本研究將製備好之碳分子篩選薄膜進行表面及側面分析，其因PEI屬緻密型之結構，由圖4-9可發現無論基材經過不同之前處理方式，其碳膜表面都相當的緻密且較無缺陷。而側面型態則可看出碳膜是完整的沉積於基材上方，且內部屬緻密結構，其碳膜之膜厚約為3-4 μm，最厚之膜厚為1500^{o}C之基材，膜厚可達4.815 μm。此外，可觀察出氧化鋁基材與碳膜之接合非常的完整，為一無缺陷之非對稱型態的碳分子篩選薄膜。

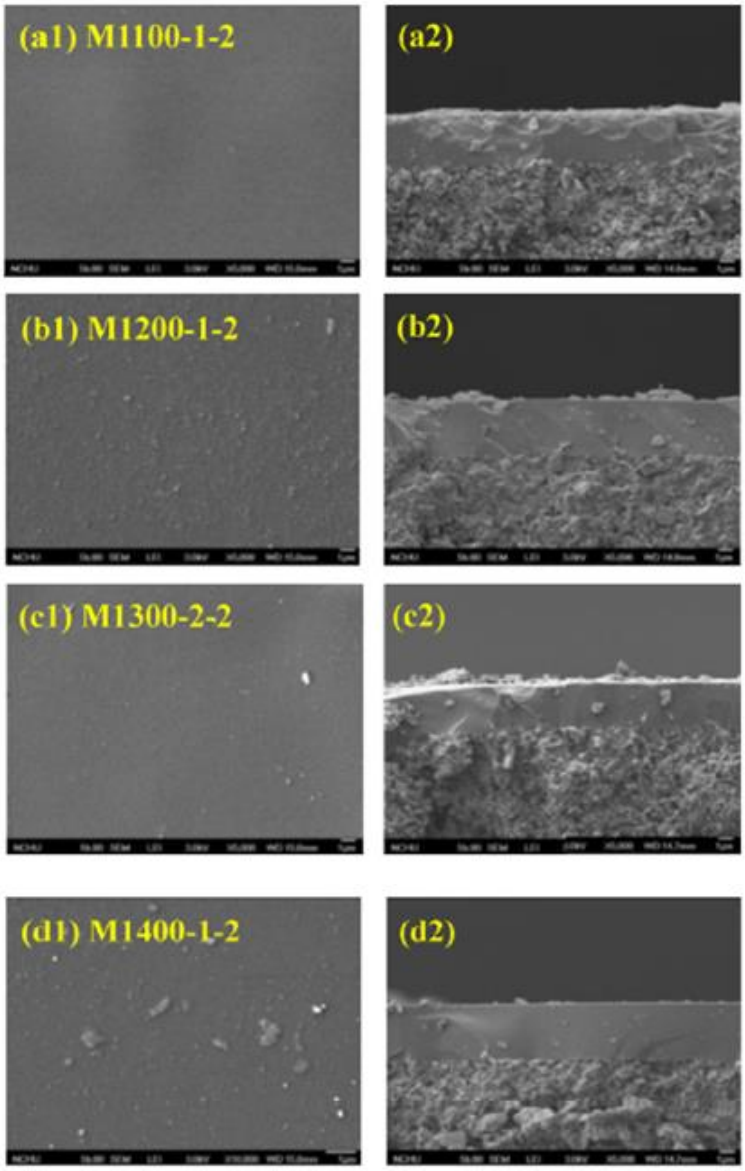

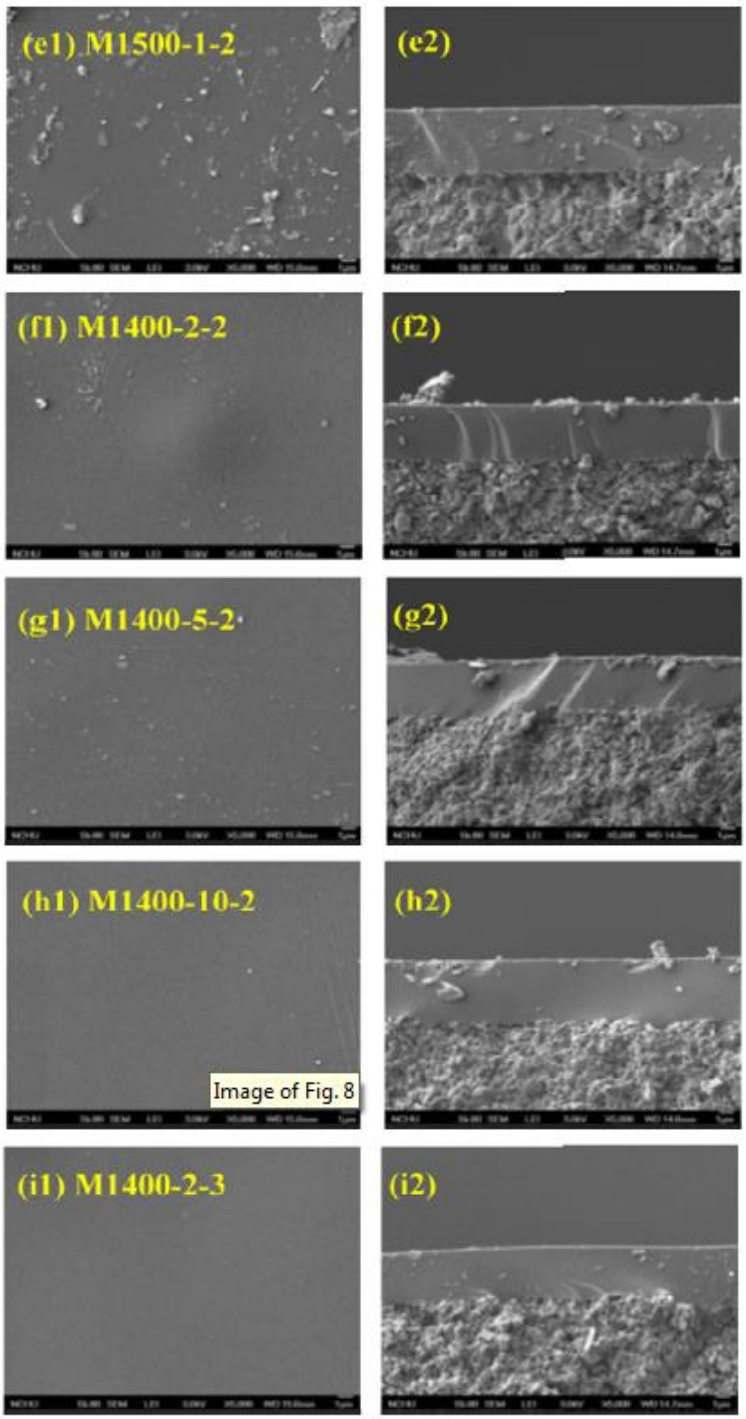

圖4-9碳分子篩薄膜之表面及側面型態顯微圖(a) M1100-1-2、(b)M1200-1-2、(c)M1300-1-2、(d)M1400-1-2、(e)M1500-1-2、(f)M1400-2-2、(g)M1400-5-2、(h)M1400-10-2、(i)M1400-2-3，(1)表面、(2)側面。

4.2.2.2碳膜層間距與表面粗糙度分析

層間距(d-spacing)即碳層與碳層間的距離，數值大小可做為判斷碳膜孔徑大小的依據。由X-ray以低略角入射方式分析，所得的圖譜可發現，在2θ= 20˚~26˚有一非晶相波鋒，經布拉格公式Bragg’s Law :nλ=2dsinθ計算後，即可得碳膜的d-spacing值。

如表4-6所示，碳膜的層間距隨著燒結溫度的增加，呈現規則性的”增加-減少-增加-減少”的趨勢，此趨勢與前述的氧化鋁基材特性趨勢，如比表面積、平均孔徑、孔洞體積及表面粗糙係數並不吻合。由此可見，碳膜層的層間距，應為前述因子的綜合效應。由於碳膜的層間距，係為高分子前驅物經熱裂解後，不規則芳香族任意堆疊所產生的間隙；因此，高分子鑄膜液於基材上的披附情形，將會影響碳膜的層間距。一般而言，基材表面愈粗糙，高分子鏈的堆疊將會愈不具規則性，鏈與鏈的立體空間效應亦愈顯著，因此碳化後所得的層間距值將會愈大。

此外，基材的孔隙率亦是影響高分子鏈堆疊的另一重要因子。一般而言，孔隙率愈大，高分子鏈於旋轉塗佈過程中，較容易滲入基材的孔隙結構中，而導致鏈的不規則堆積；反之，當孔隙率縮小時，高分子鏈將會於基材表面產生較規則的排列，而不會滲入孔洞中，此時膜厚也較厚。因此，綜合比較基材平均孔徑、孔洞體積、基材表面粗糙度及碳膜層間距可發現，當鋁基材經高溫燒結處理至1300^{o}C/min時，由於氧化鋁顆粒的重新堆疊，造成孔隙率的損失，高分子鏈無法滲入基材孔隙，而較規則地堆積於基材表面，使得碳膜層間距值較低，膜厚也較厚(如圖4-9所示，以M1300-1-2為例)。

表4-6 碳膜層間距與擔體孔洞結構、擔體粗糙係數及碳膜表面粗糙係數之關係

Sample code	d-spacing (Å)	V_{total} of support (cm^3/g)	Rq of support (nm)	Rq of membranes (nm)	Membrane Thickness (μm)
M1100-1-2	4.47	0.0116	55.4	81.2	4.237
M1200-1-2	4.51	0.0084	72.1	112.0	4.219
M1300-1-2	4.32	0.0061	76.4	61.3	3.722
M1400-1-2	4.64	0.0043	89.6	88.7	4.144
M1500-1-2	4.02	N.D.	136.0	203.0	5.550
M1400-2-2	4.32	0.0080	53.1	62.2	4.800
M1400-5-2	4.62	0.0087	77.8	120.0	4.500
M1400-10-2	4.76	0.0086	117.0	150.0	4.313
M1400-2-3	4.64	0.0080	75.5	81.5	2.981

4.2.3氣體分選試驗結果

本研究使用不同氧化鋁基材藉由不同之燒結條件前處理後，製備成擔體型態之碳分子篩選薄膜，進行單一氣體滲透測試，探討不同基材結構對於氣體滲透分選效能之影響。圖4-10(a)為不同燒結溫度處理之基材對薄膜滲透率影響，可發現當基材由1100 ^{o}C上升至1200 ^{o}C時滲透率有些微增加，其中H_2由2112.2增加至2304.8 Barrer，CH_4則由376.96增加至543.57Barrer；而隨溫度上升至1300 ^{o}C時，滲透率則有下降趨勢，H_2由2304.8下降385.71 Barrer，CH_4從543.57下降至276.07 Barrer；溫度上升至1400 ^{o}C時，H_2由385.71上升至1232.34 Barrer，CH_4從276.07下降至22.76 Barrer；溫度上升至1500 ^{o}C時，整體滲透通量則有大幅下降情況，H_2由1232.34 下降至102.67 Barrer，CH_4從22.76下降至15.33 Barrer。上述滲透趨勢可由氧化鋁顆粒成長過程說明，顆粒之轉變過程分為三個部份：首先當溫度上升至1100-1200 ^{o}C時顆粒會有粗化及重新堆疊狀態，此皆段顆粒因粗化會有較大之孔係結構，因而使得滲透通量有較高之現象；而當溫度提升至1300 ^{o}C時氧化鋁顆粒此時有著重新堆疊及開始轉變為十四面體之狀況，兩種狀態共存使得薄膜生成較平滑之表面進而使得滲透通量有大幅下降之情況；溫度提升至1400 ^{o}C時，顆粒轉化至十四面體之顆粒，基材之孔洞較為一致使得滲透通量因而提升；隨溫度提升至1500 ^{o}C時顆粒與顆粒間已完整的聚集在一起，使得基材本身有著極少的孔洞結構，也因顆粒與顆粒間完整聚集而使材表面粗粗糙係數有大幅提升的趨勢，但因顆粒與顆粒間的聚集為緻密化之相態，進而導致薄膜彼覆於基材後滲透通量急劇下降。

圖4-10(b)則為不同升溫速率處理之基材對碳分子篩薄膜滲透率影響，可看出當升溫速率由1 ^{o}C增加至2 ^{o}C時，H_2由為1232.24增加至1300.3 Barrer，CH_4從22.76下降至7.74Barrer；升溫速率由2 ^{o}C增加至10 ^{o}C時，各種氣體的滲透率皆有上升之趨勢，如H_2由1300.3上升至1796.89Barrer，CH_4則從7.74上升至33.22 Barrer；上述滲透率結果可由SEM及AFM分析結果說明之，升溫速率由1 ^{o}C增加至2 ^{o}C時因顆粒之大小差異較為明顯因而生成較小之基材粗糙係數(由89.6下降至53.1 nm)而當薄膜彼覆至基材上後薄膜表面之粗糙係數(分別為88.7及81.5 nm)並無太大之差異，由此堆測薄膜之內部結構較為緻薄無缺限，造成較大直徑之氣體較不易通過薄膜使得滲透通量下降;而升溫速率由2 ^{o}C增加至10 ^{o}C時，可發現基材(由53.1上升至117.0 nm)及薄膜表面(81.5上升至150 nm)之粗糙係數都有明顯提升之現象，因而得到較大之滲透通量。

圖4-10(c)為不同熱沉浸時間基材對碳分子篩薄膜滲透率影響，由圖可發現隨著熱沉浸加長至3小時H_2由1300.3下降至1069.74 Barrer，CH_4從7.74上升至14.55 Barrer。此趨勢可藉由XRD及AFM結果說明，因較長之熱沉浸會使得氧化鋁顆粒粗化

(a)

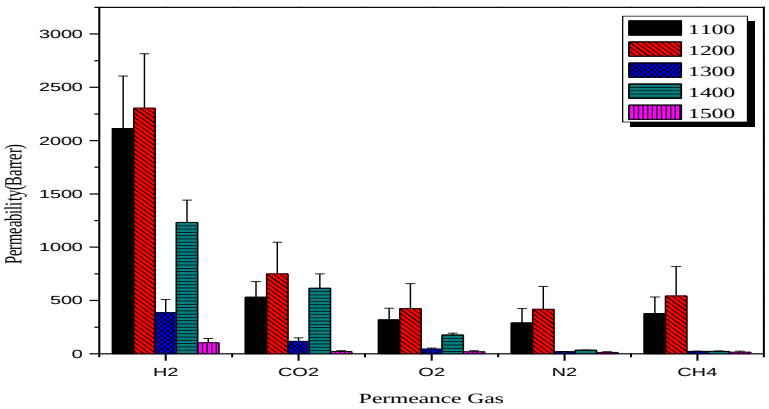

(b)

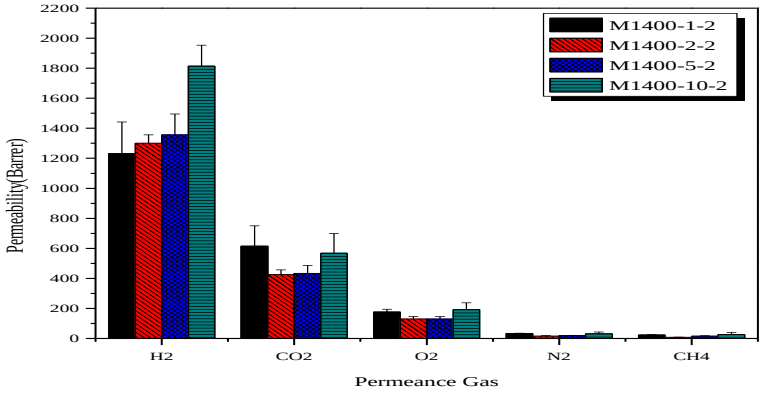

(c)

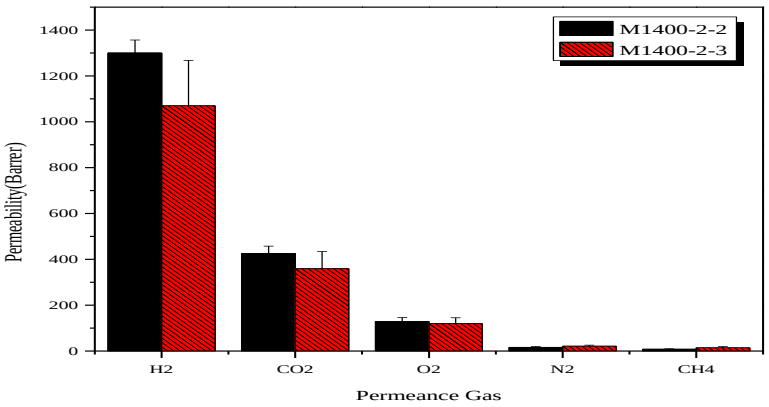

圖4-10 不同基材對碳分子篩薄膜滲透率影響(a)不同溫度 (b)升溫速率 (c)熱沉浸時間

本研究藉由2008年Robenson學者提出Upper bound之概念[90]，做為薄膜氣體之滲透選擇效能之篩選，進而選擇具備高滲透選擇效能之薄膜。比較結果如圖4-11所示，並發現薄膜於滲透選擇較能皆有相互抗衡之現象，當滲透通量高時選擇率則會減少;由此可知，當滲透通量降低時選擇率則會提升。由本研究之實驗中可發現大多有此現象。另外，不同燒結條件製備之薄膜H_2/CH_4之滲透選擇效能除M1100-1-2、M1200-1-2、M1300-1-2、M1500-1-2之薄膜外皆能達到H_2/CH_4之標準。而於CO_2/CH_4亦可發現只有M1400-1-2、M1400-2-2、M1400-5-2之薄膜達到CO_2/CH_4之標準。由上述結果可發現本研究之M1400-2-2具備高滲透選擇效能，可同時超越2008年Robenson學者提出H_2/CH_4及CO_2/CH_4之標準，因此本研究選定M1400-2-2之基材做為後續矽/鋁基材之實驗基材。

(a)

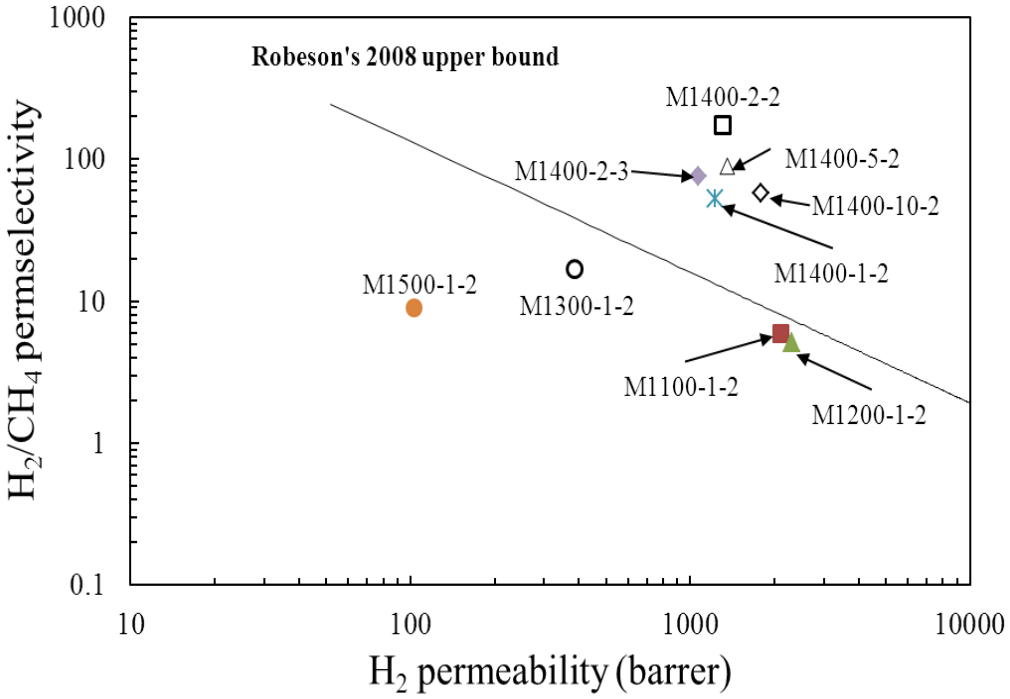

(b)

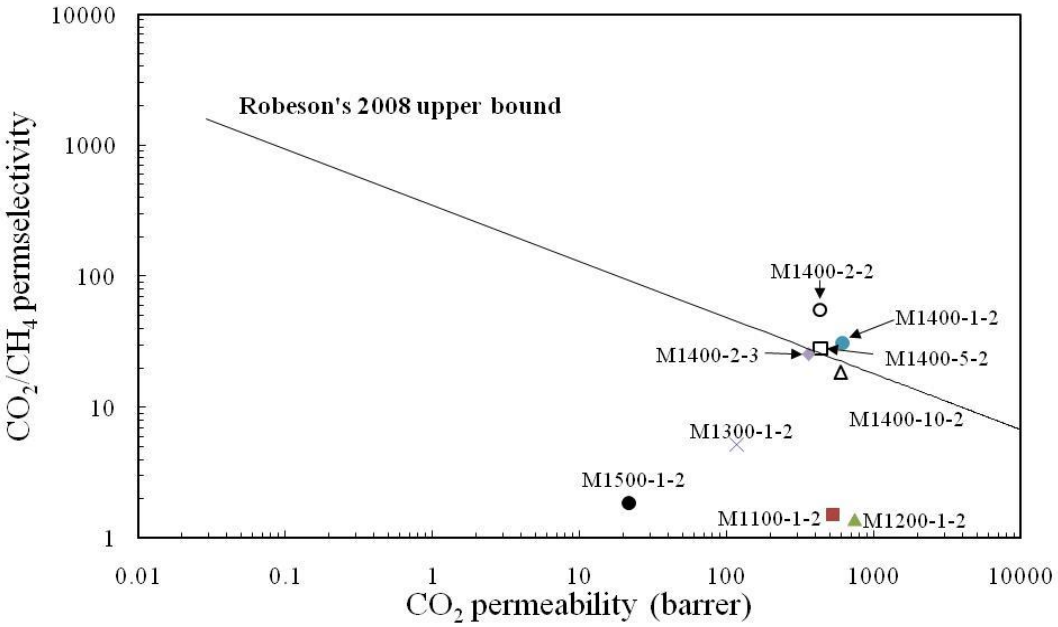

圖4-11不同燒結條件製備之薄膜比較Robeson's 2008 upper bound比較圖(a) H_2/CH_4 (b) CO_2/CH_4

4.2.4. 小結

本計畫的研究主題係在探討基材的物化特性對碳分子篩選薄膜之孔洞結構及氣體分選能力的影響。計畫第一年，為自製不同孔徑分佈之鋁基材，探討鋁基材燒結溫度、升溫速率、熱沉溫時間等因子對鋁基材及碳膜孔徑分佈的影響。實驗共設計五組不同燒結溫度、四組不同升溫速率及二組不同熱沉浸時間等燒結條件，並對氧化鋁基材及碳分子篩選薄膜進行XRD、BET、FESEM及AFM等特性分析。研究結果發現，氧化鋁基材的顆粒大小及孔隙分佈率是影響基材表面粗糙度的主要因素，亦是決定高分子鏈堆疊情形的重要因子，當基材孔隙率大且表面粗糙大時，由於高分子鏈的任意堆疊而造成空間效應，因此碳化後將產生較大的層間距而有利於氣體的擴散，但此時氣體的分選效果較不理想。相反地，在本研究發現經1400 ^{o}C熱處理、升溫速率為2且熱沉浸時間為2小時時，鋁基材因形成十四面體結構而產生粗糙度低但具氣孔之結構，因此可提供碳膜高滲透率及高選擇率的分離特性。

4.3. 添加MFI中間層之效應

4.3.1矽/鋁基材結構分析

本研究中選用MFI純矽之沸石製備成矽/鋁基材，而矽/鋁基材除沸石表面富有化學官能基外，本身也能夠提供氣體之擴散通道，因此用於做為碳分子篩選薄膜的基材，除可改善兩相之接合性，亦可以提供薄膜氣體擴散通道，進而提升薄膜滲透分選效能。表4-7為不同矽/鋁基材的製備條件之樣品編碼。

表 4-7 矽/鋁基材的製備條件

	Preparation conditions			
Support code	Sintering Temperature (°C)	Hearting Rate (°C/min)	Soaking time (hr)	Hydrothermal growth
S1100	1100	2	2	--
S1100-MFI-1	1100	2	2	Primary
S1100-MFI-2	1100	2	2	Secondary
S1200	1200	2	2	--
S1200-MFI-1	1200	2	2	Primary
S1200-MFI-2	1200	2	2	Secondary
S1300	1300	2	2	--
S1300-MFI-1	1300	2	2	Primary
S1300-MFI-2	1300	2	2	Secondary
S1400	1400	2	2	--
S1400-MFI-1	1400	2	2	Primary
S1400-MFI-2	1400	2	2	Secondary

4.3.1.1 矽鋁基材微結構分析

本研究選用1100-1400 °C燒結前處理之氧化鋁基材，進行矽的表面修飾，圖4-12為矽/鋁基材微結構分析圖。如圖所示，當氧化鋁基材經晶核植種後，於基材表面可發現有矽晶核的存在，粒徑最大可達1 μm，而當基材進行二次水熱後，可發現基材表面有較大顆粒的晶體覆蓋於氧化鋁表面，晶體之粒徑約為2-3 μm。

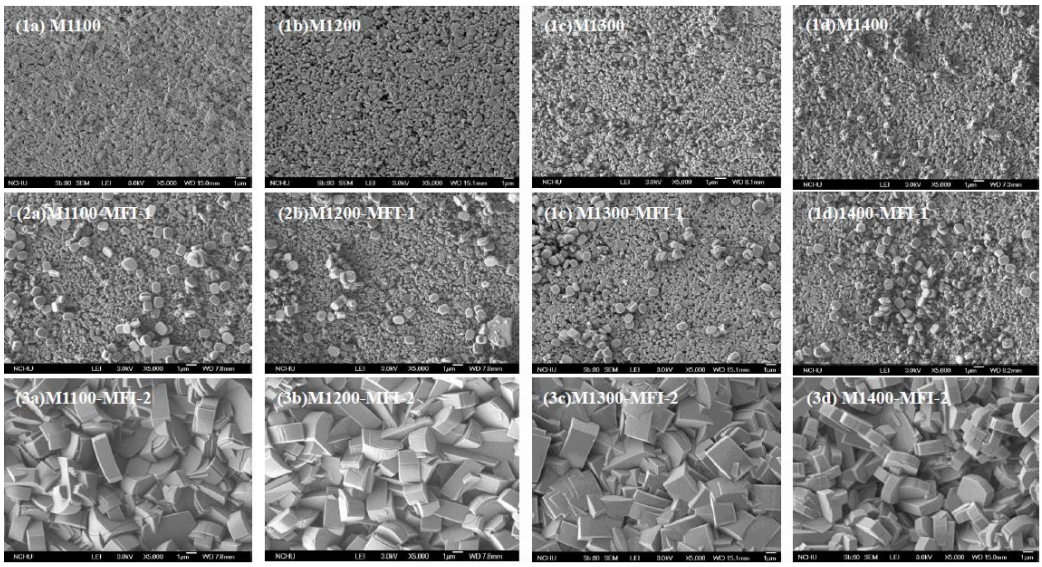

圖 4-12 矽/鋁基材微結構分析:(1)Al_2O_3、(2)MFI-1、(3)MFI-2，不同燒結溫度(a)1100 ^oC、(b)1200 ^oC、(c)1300 ^oC、(d)1400 ^oC

4.3.1.2 矽/鋁基材晶相分析

為了解基材經不同水熱合成條件修飾後，所生成之結晶相態，本研究藉由 X-ray 繞射儀進行晶相分析。如圖 4-13 所示，分別為：(a)未經改質之氧化鋁基材，及(2)經晶核植種、(3)二次水熱合成之矽/鋁基材的 XRD 繞射圖。經比對氧化鋁標準圖譜後，發現繞射圖除保有原來的氧化鋁特徵波峰外，另外也可由圖 4-13(b)、(c)中發現於 2θ=7.906^o(1 0 1)、8.856^o(2 0 0)、23.029^o(5 0 1)時有新特徵峰的出現，經比對圖譜資料庫後確定此三組特徵波峰為 MFI 純矽之特徵波峰[17]。三個特徵峰分別代表不同晶體之生長方向，藉由倒置晶格向量的米勒指標(h、k、l)分別代表三個方向，(1 0 1)為 a 與 c 軸方向的斜面，(2 0 0)為 a 軸面之晶面，(5 0 1)為 a 與 c 軸方向的斜面，但其中 c 軸之晶面間距較長，由圖 4-13(c)中也可發現，當基材經二次水熱合成後 2θ 於 7.906^o、8.856 ^{o}、23.029 ^{o}之 MFI 純矽特徵波峰有明顯增強之現象，此與 Hasegawa 等學者於 2006 年[13]的研究結果相符合。

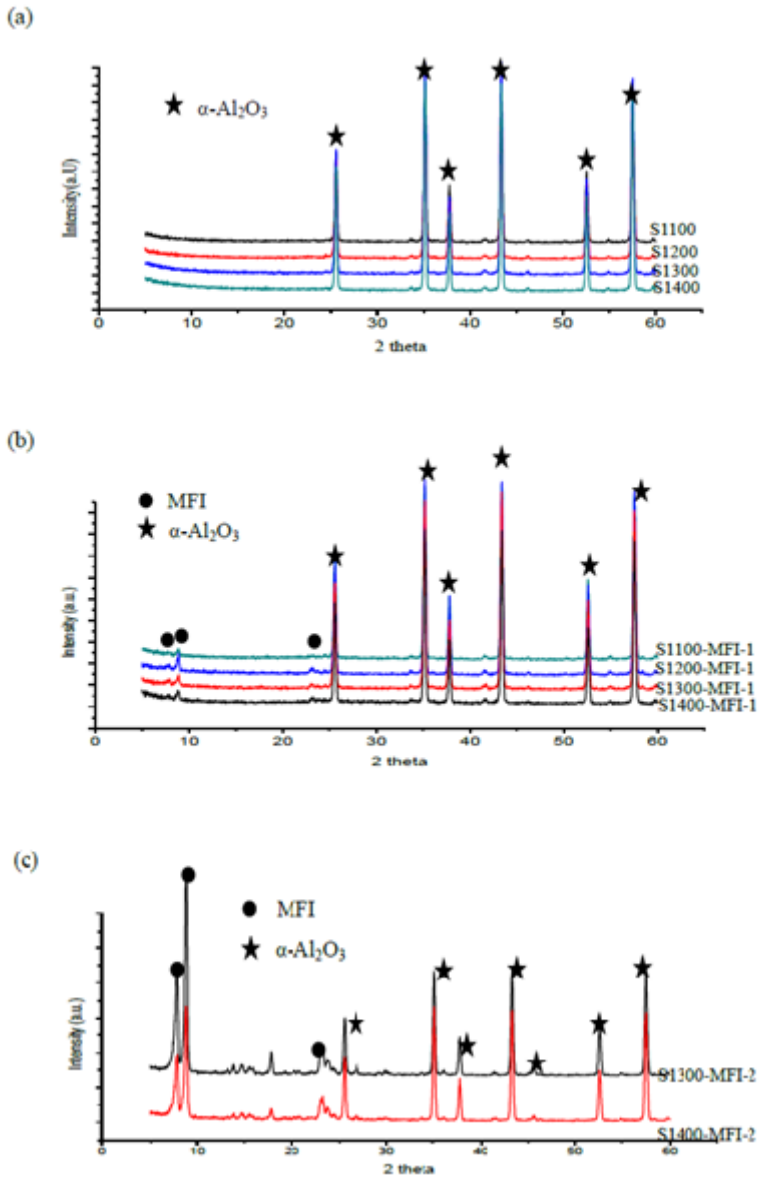

圖 4-13 矽/鋁基材 XRD 分析圖(a)Al_2O_3、(b)MFI-1、(c)MFI-2

4.3.1.3. 矽/鋁基材結構孔洞結構分析

表4-8為矽/鋁基材之比表面積、孔洞半徑及孔洞體積分析結果。如表所示，可發現當基材經植種矽晶核後，基材之表面積及總孔洞體積有明顯下降的趨勢，1100 ^oC基材之比表面積由8.0 m^2/g下降至5.6 m^2/g，平均孔徑從65.16 Å 上升至74.41 Å ，總孔洞體積則由0.0131 cm^3/g下降至0.0105 cm^3/g，使用1200 ^oC -1300 ^oC基材時，亦有相同之趨勢。此由SEM分析結果可得知：植種於鋁基材表面之晶核的粒徑，除1 μm的大尺寸外，基材表面也存在無數細小晶核，小尺寸之晶核可能阻塞中孔、微孔之孔洞而造成總孔洞體積有減少之趨勢。

表4-8不同矽/鋁基材比表面積、孔洞半徑、孔洞體積

Code	S_{BET} (m^2/g)	D_{pore} (Å)	BJH adsorption cumulative Pore Volume of pores between 3.5Å and 1000 micros Radius (cm^3/g)			
			V_{total}	V_{micro}	V_{meso}	V_{macro}
S1100	8.0	65.16	0.0131	0.0026	0.0096	0.0008
S1100-MFI-1	5.6	74.41	0.0105	0.0020	0.0074	0.0010
S1200	6.4	70.63	0.0115	0.0021	0.0084	0.0008
S1200-MFI-1	4.2	80.46	0.0086	0.0016	0.0060	0.0009
S1300	6.9	69.88	0.0122	0.0020	0.0094	0.0006
S1300-MFI-1	3.6	82.20	0.0074	0.0012	0.0053	0.0007
S1300-MFI-2	4.9	70.90	0.0087	0.0017	0.0061	0.0007
S1400	4.3	74.22	0.0080	0.0011	0.0063	0.0005
S1400-MFI-1	6.1	61.13	0.0094	0.0012	0.0075	0.0005
S1400-MFI-2	5.1	70.24	0.0091	0.0014	0.0070	0.0005

此外，由表中也可發現：使用1400 °C基材進行一次水熱合成後，基材之比表面積由4.3 m^2/g上升至6.1 m^2/g，平均孔徑從74.22 Å下降至61.13 Å，總孔洞體積則由0.0080上升至0.0094 cm^3/g，顯現出使用此溫度之基材經水熱合成後，並不會造成基材孔洞阻塞之現象，此可能為1400 °C之基材較為緻密故晶核不會阻塞孔洞，使得本身富有孔洞結構之矽晶核貢獻了孔洞體積，進而導致總孔洞體積有提升之現象。

二次水熱合成之矽/鋁基材的孔洞結構，如表4-8所示，可知當基材經二次水熱合成後(S1300-MFI-2)基材之比表面積由3.6 m^2/g上升至4.9 m^2/g，平均孔徑從82.20 Å下降至70.90 Å，總孔洞體積則由0.0074 cm^3/g上升至0.0087 cm^3/g，此可能因結晶生長之MFI純矽結構本身富有孔洞結構，進而導致基材之孔洞體積、比表面積有上升之趨勢。而於使用1400 °C基材進行二次水熱合成時，比表面積由6.1 m^2/g下降升至5.1 m^2/g，平均孔徑從61.13 Å上升至70.24 Å，總孔洞體積則無太大的差異。此可能因披覆於鋁基材表面的晶核較多(未滲入孔洞結構中)，成形的沸石粒徑變小，使得顆粒與顆粒間的間隙增加，而增加了平均孔徑[14]。

4.3.1.4.矽/鋁基材表面粗糙度分析

由表4-9矽/鋁基材表面粗糙度分析可發現，當使用不同溫度處理之基材經一次水熱合成後，基材之表面粗糙係數皆有明顯上升之趨勢如S1400-MFI-1基材的粗糙係數Rq由53.1 nm上升至209.0 nm，而當基材經二次水熱合成處理後，基材表面粗糙係數也有顯著遞增趨勢，如S1400-MFI-2基材的粗糙係數Rq由209.0 nm上升至342.0 nm，其餘樣品也有相同之趨勢。此分析結果由上述SEM微結構分析可得知，當基材經晶核植種後表面會披覆著一層純矽晶核，晶核尺寸最大可達1 μm，進而導致基材之表面粗糙係數有所提升。而當基材經二次水熱合成後表面

粗糙係數有遞增情況，原因為基材表面之矽晶核已完整的結晶成長，而由SEM微結構分析圖可發現，表面之型態較為不平整，使得粗糙係數有提升的趨勢。

表4-9 矽/鋁基材表面粗糙度分析

Surface Roughness(nm)			
	Ra	Rq	Rz
S1100	22.7	28.9	58.7
S1100-MFI-1	87.5	145.0	191.0
S1200	29.3	38.1	83.2
S1200-MFI-1	157.0	212.0	380.0
S1300	30.5	39.5	65.0
S1300-MFI-1	210.0	270.0	655.0
S1300-MFI-2	272.0	339.0	825.0
S1400	42.8	53.1	112.0
S1400-MFI-1	158.0	209.0	363
S1400-MFI-2	279.0	342.0	1013.0

4.3.2 支撐於矽/鋁基材之薄膜特性分析

4.3.2.1高分子薄膜FT-IR官能基分析

支撐於矽/鋁基材之高分子薄膜的化學結構變化，可藉由FT-IR觀察，其結果如圖4-14所示。圖4-14(a)顯示MFI粉末有三個特徵波峰，出現在1066 cm-1、800 cm-1及547 cm-1，分別為MFI純矽之主要結構Si-O-Si、Si-O官能基及MFI典型結構；圖4-2-1(b)觀察出，PEI高分子主要特徵峰出現於1775 cm-1、1717 cm-1、1353 cm-1等三個位置，分別為C=O半對稱、C=O對稱及C-N官能基[15]。

由圖4-14(c-h)中，雖未發現MFI粉末之特徵波峰，但可由圖中發現PEI高分子原有之特徵波峰半對稱C=O、對稱C=O及C-N等波峰的強度都有減弱，此可能為因高分子膜與矽基材產生化學性鍵結，使得PEI高分子原有的特徵波峰強度減弱，此現象亦可能使得高分子結構變的更為緊密。

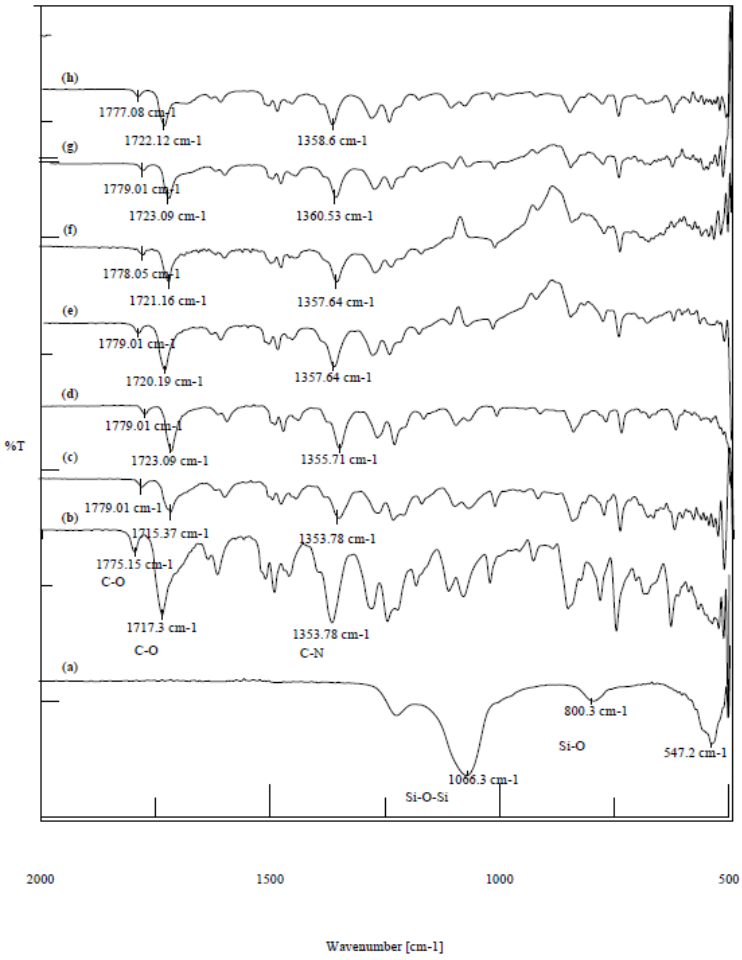

圖 4-14 不同基材製備之薄膜 FTIR 圖譜(a)MFI powder、(b)Pure PEI、(c)1100-MFI-1、(d)1200-MFI-1、(e)1300-MFI-1、(f)1300-MFI-2、(g)1400-MFI-1、(h)1400-MFI-2

4.3.2.2 碳膜層間距分析

本研究進一步的將不同條件合成之 表4-9不同矽/鋁基材碳膜的d-spacing值矽/鋁基材，做為薄膜的支撐材料以製備成碳分子篩選薄膜，並利用XRD、AFM等特性分析，探討基材對碳分子篩選薄膜表面粗糙係數及層間距等特性之影響。圖4-15為支撐於矽/鋁基材之碳膜的XRD分析圖譜，由圖中可發現於2θ=18^{o}-23^{o}有一非結晶之波峰，本研究利用布拉格公式，計算碳膜d-spacing值，如表4-9所示。由表中可發現除了M1400-MFI-1外，其餘碳膜的層間距都因矽沸石修飾而有下降之趨勢，比對前述矽/鋁基材AFM與BET分析結果發現，碳膜的d-spacing值並未因粗糙係數增加而增加。此可能為基材與高分子鏈間因化學性的鍵結而產生交聯作用，使得高分子鏈排列較為緊密，故經碳化後將使得碳層間距離縮小，使得
d-spacing值變小。

表4-9 披覆於不同矽/鋁基材之碳膜的d-spacing值

CMSM	d-Spacing (Å)
	(2θ=18-23°)
M1100	3.99
M1100-MFI-1	3.88
M1200	3.93
M1200-MFI-1	3.89
M1300	3.82
M1300-MFI-1	3.61
M1400	4.04
M1400-MFI-1	4.08

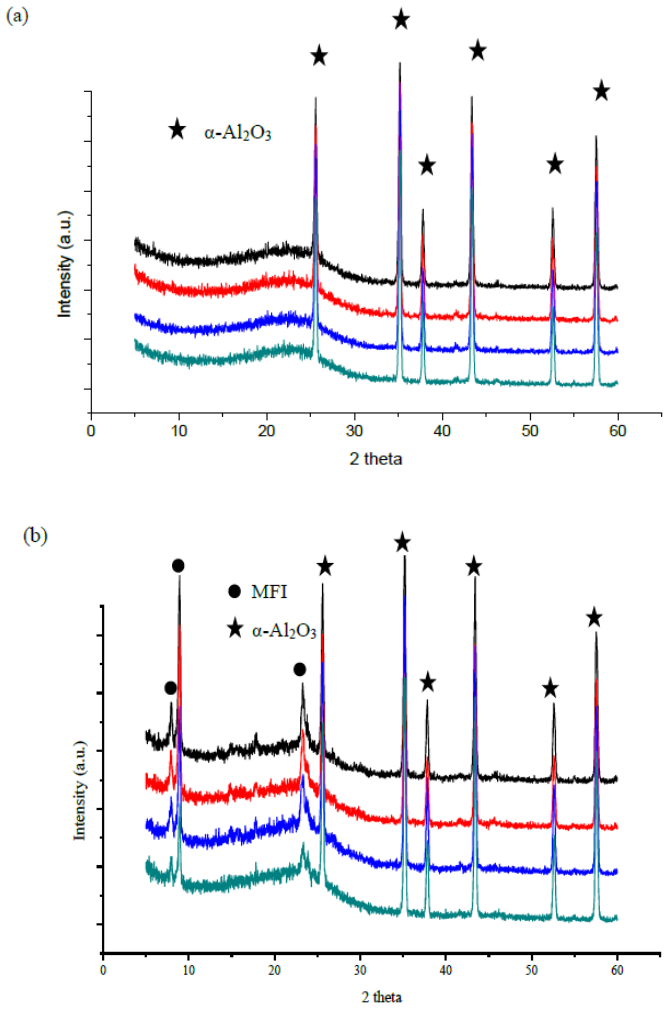

圖4-15支撐矽/鋁基材之碳分子篩選薄膜的XRD繞射圖譜

4.3.2.3 碳膜粗糙係數分析

本研究將支撐於矽/鋁基材的碳膜表層，進行表面粗糙係數分析，分析結果如表4-10所示，可發現使用矽晶核植種後及經二次水熱處理之基材所製備的碳膜，其粗糙係數有明顯上升之趨勢，如M1400-MFI-1的Rq值由10.9 nm上升至15.2 nm，經二次水熱處理後則再增加至64.1 nm；其餘碳膜也都有相同之現象。此結果可能與基材因矽沸石修飾導致粗糙度增加，進而提升了碳膜表面的粗糙度[16]。當高分子鏈被沉積於基材表面時，若基材的表面較粗糙，將造成高分子鏈產生了連續性且雜亂的折疊，薄膜於熱裂解後，將產生較大的高低起伏，造成粗糙係數有遞增的趨勢。

此外，相較於d-Spacing分析結果可發現，碳膜表面的高粗糙係數與碳膜層間距值並沒有互為因果關係，即高粗糙係數係緣自於基材的粗糙度，而與碳膜層間距無關。因此，如4.2.2.2節所述，支撐於矽/鋁基導致碳膜層間距變小，則是因為高分子鏈與矽基材產生化學鍵結的關係。

表4-10 矽/鋁基材製備之碳膜表面粗糙係數分析

	Surface roughness (nm)		
Sample Code	Ra	Rq	Rz
M1100	3.4	6.5	19.9
M1100-MFI-1	19.5	24.6	84.8
M1200	2.9	3.6	3.1
M1200-MFI-1	14.9	18.9	29.1
M1300	3.5	4.9	9.0
M1300-MFI-1	11.1	14.8	66.8
M1300-MFI-2	42.0	52.0	154.0
M1400	6.8	10.9	22.6
M1400-MFI-1	11.3	15.2	33.7
M1400-MFI-2	50.8	64.1	110.0

4.3.2.4 碳膜微結構分析

本研究將製備完成之矽/鋁基材支撐型碳膜進行表面及側面之微結構分析，由圖4-16可發現，薄膜之表面有完整的碳層沉積於基材表面，與圖4-17、4-18相比較可發現，經一次及二次水熱合成之薄膜表面及側面隱約可看到矽晶核及晶體之存在，且由薄膜側面可發現碳膜層完整的沉積於基材表面，並無間隙產生，為一完整的非對稱型薄膜。

此外本研究進一步探討基材結構對碳膜膜厚之影響，如表4-11所示，當基材經一次水熱與二次水熱合成並製備成碳膜後，碳膜膜厚與使用鋁基材之膜厚相比較，有明顯增厚之現象，推測此現象可能為晶核修飾過孔洞後，進而影響了高分子之流動性，使得高分子鑄膜液不易滲入

基材內部；另一原因為矽/鋁基材的Si-O-Si與Si-O官能基與高分子鏈產生鍵結，使得高分子鏈與鏈間更為緊密，導致鑄膜液於塗佈時，不易受到離心力影響而甩出。而由膜厚分析也可發現厚度最厚可達4.987μm。

表4-11 MFI薄膜之膜厚分析

	Membrane thickness(μm)			
Substrate	1100 °C	1200°C	1300°C	1400°C
Al_2O_3	3.994	4.05	2.794	3.188
MFI-1	4.519	4.969	3.975	4.106
MFI-2	---	----	4.987	4.837

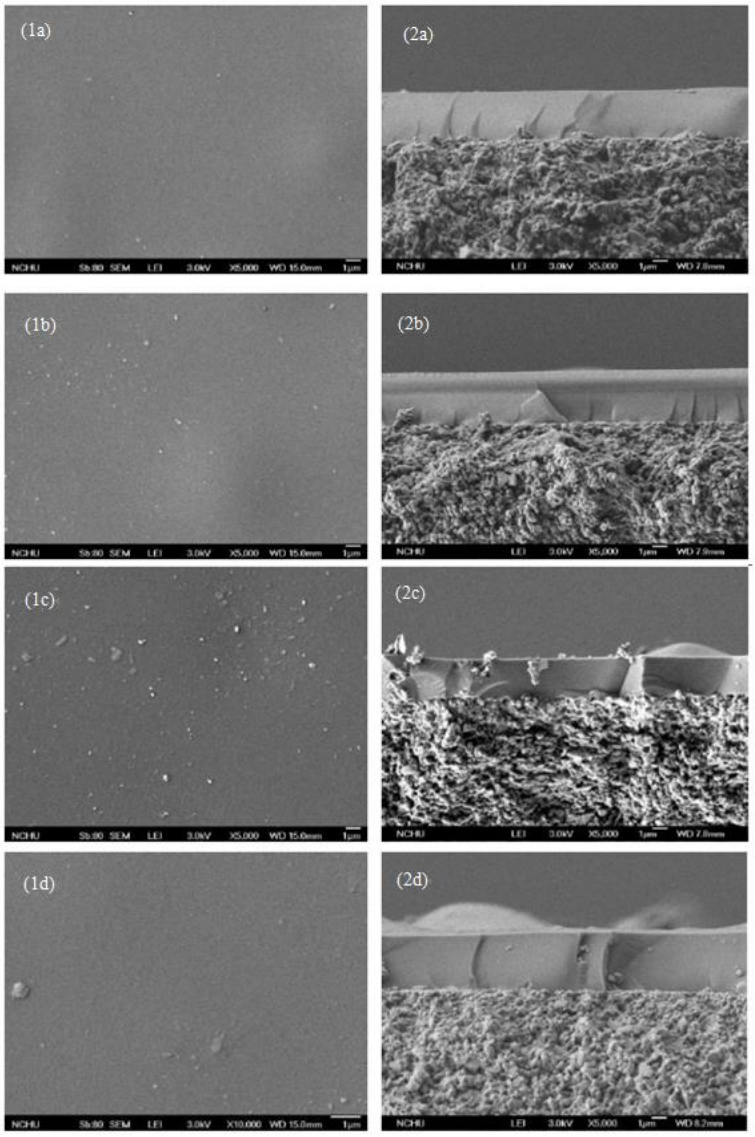

圖 4-16 支撐於鋁基材之碳分子篩選薄膜表面及側面微結構圖：(1)表面、(2)側面，(a)1100 °C、(b)1200 °C、(c)1300 °C、(d)1400 °C。

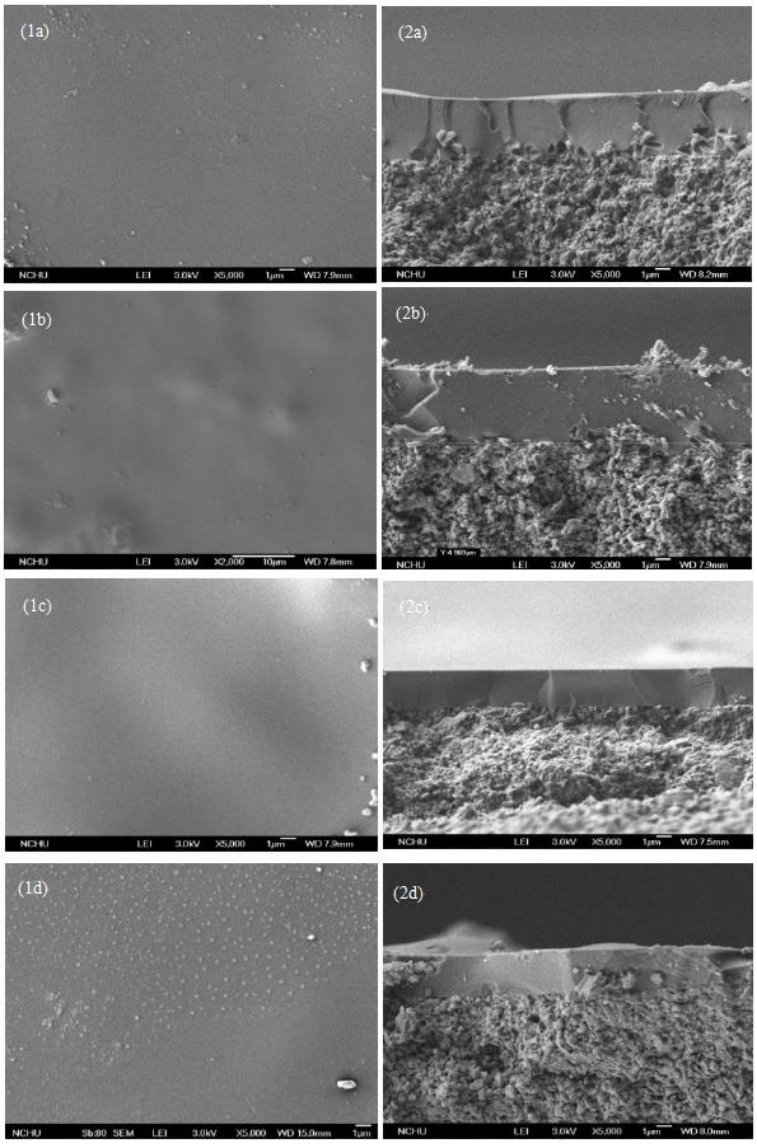

圖 4-17 支撐於矽/鋁基材 MFI-1 之碳分子篩選薄膜表面及側面微結構圖: (1)表面、(2)側面，(a)1100^{o}C、(b)1200^{o}C、(c)1300^{o}C、(d)1400^{o}C。

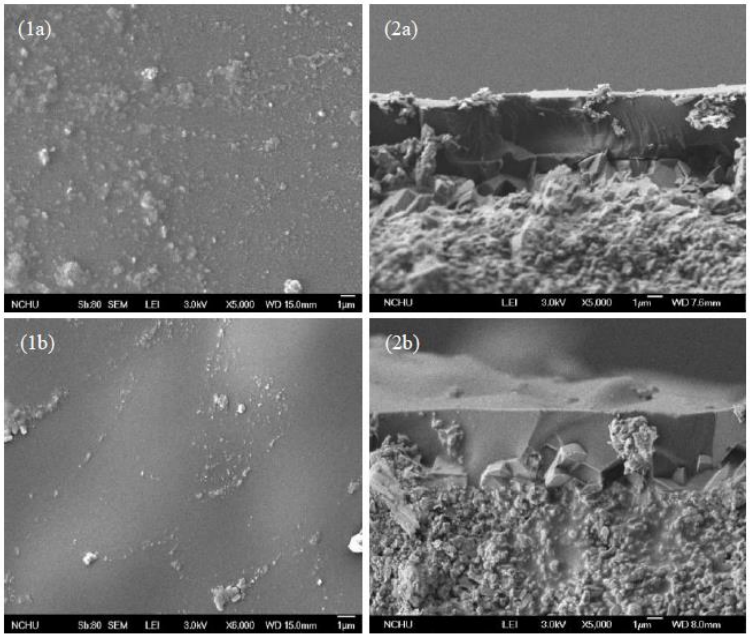

圖4-18支撐於矽/鋁基材MFI-2之碳分子篩選薄膜表面及側面微結構圖：(1)表面、(2)側面，(a)1300^{o}C、(b)1400^{o}C

4.3.3.碳膜氣體分選效能之探討

4.3.3.1. 滲透分選特性

圖4-19為使用MFI矽/鋁基材製備之碳膜滲透率，由圖可發現，當經過一次水熱合成之基材所製備碳分子篩選薄膜與未經基材改質製備之碳分子篩選薄膜滲透效率相比，滲透效能除了M1400-MFI-1薄膜有上升趨勢外H_2 由1267.25上升至1346.19 Barrer，CH_4則從15.83上升至17.32，其餘都有明顯下降之趨勢。此可能因碳膜層間距值變小，導致滲透通量減少。

此外，圖4-19亦顯示MFI-2矽/鋁基材製備之碳膜滲透率，由圖中可發現當基材經二次水熱改質後所製備之碳分子篩選薄膜，其滲透率皆有上升的情況。其中使用1300 ^{o}C矽/鋁基材製備之薄膜，增加的滲透通量最為顯著，H_2的滲透率由1297.88 Barrer上升至3066.70 Barrer，CH_4則從5.39上升至89.33Barrer。此可能因二次水熱所生成之晶體較為完整，結晶生長之晶體具有5.3x5.6 Å之直管孔道及5.1x5.1 Å鋸齒狀孔道[17,18]，導致薄膜產生更多氣體傳輸之通道，使得滲透率有上升的現象。

本研究亦針對H_2/CH_4、H_2/N_2、O_2/N_2、CO_2/CH_4進行選擇率探討，圖4-20為MFI-1矽/鋁基材製備之碳膜的選擇率，由圖得知經改質後選擇率除M1400-MFI-1有下降之現象，H_2/CH_4從115.14下降至77.48外，其餘氣體分子對的選擇率皆有遞增之現象。此可能因高分子鏈與矽基材產生交聯作用，使得薄膜之結構更為緊密，導致選擇率有大幅提升趨勢。反之，當使用1400^{o}C進行改質時，由BET結果可發現整體之孔洞體積及比表面積都有明顯上升的趨勢，此現象可能為1400^{o}C基材經植種後因基材較為緻密，使得矽晶核無法達到阻塞孔洞之現象，導致矽晶核本

身之孔洞結構提供了薄膜更多氣體傳輸的通道，使得選擇率有下降的現象。

此外，由圖4-20發現MFI-2矽/鋁基材製備之碳膜選擇率，由圖得知基材經改質後所製備之碳膜的選擇率，發現與MFI-1矽/鋁基材製備之碳相比較M1300-MFI-2選擇率有明顯下降之情況外(H_2 /CH_4從251.55下降至39.91)，而M1400-MFI-2之H_2 /CH_4選擇率從115.14上升至120.87，此為官能基鍵結能，導致結構更為緊密使得選擇率有遞增的現象。

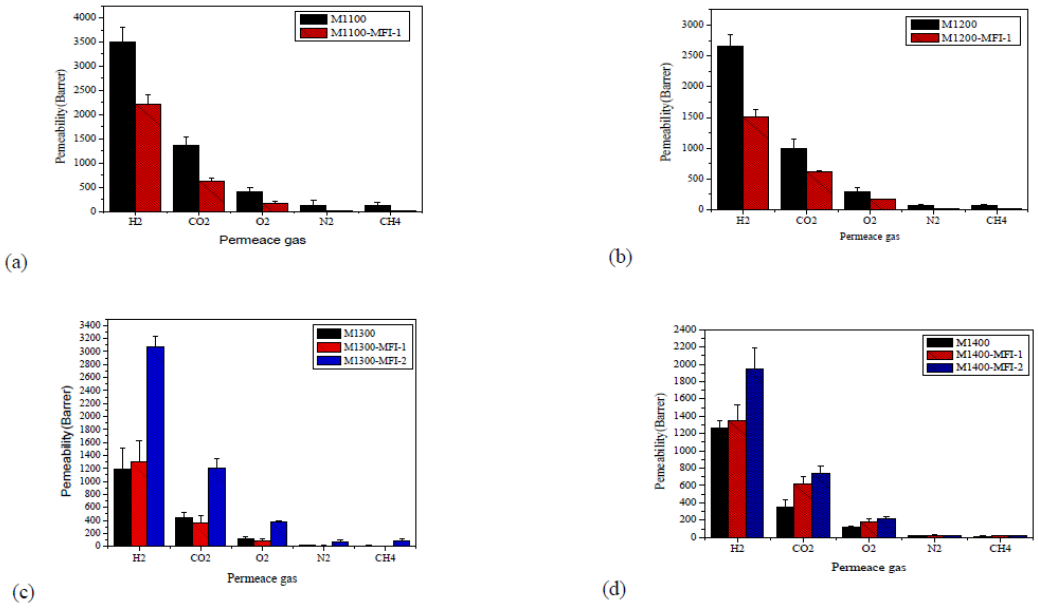

圖4-19 MFI矽/鋁基材對碳膜氣體滲透之影響(a)1100 ℃、(b)1200 ℃、(c)1300 ℃、(d)1400 ℃

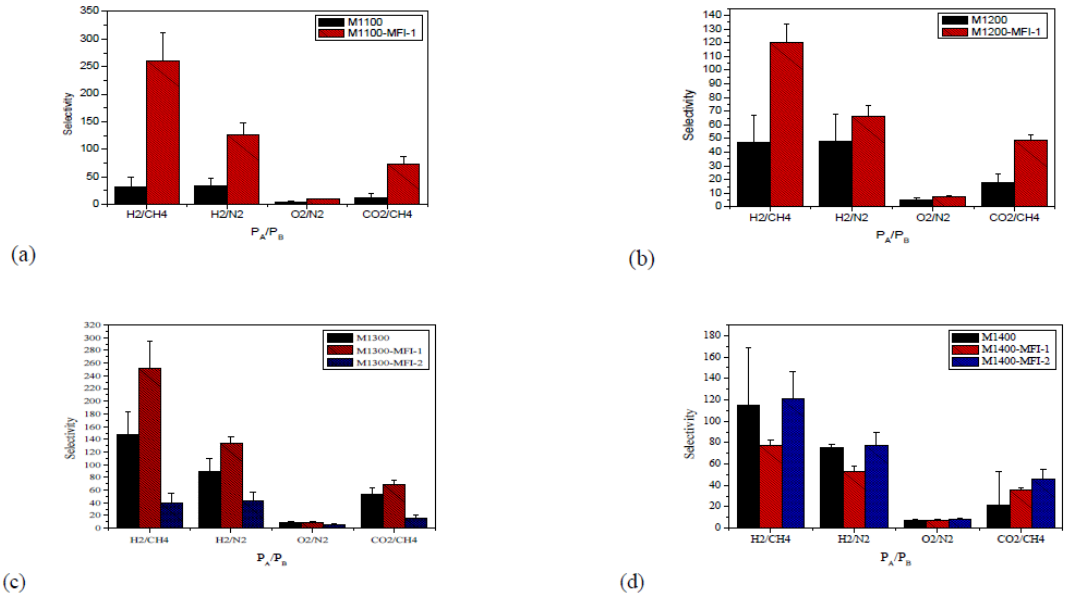

圖4-20 MFI矽/鋁基材對薄膜氣體選擇率之影響(a)1100 ℃、(b)1200 ℃、(c)1300 ℃、(d)1400 ℃

4.3.3.2. 碳膜氣體分選效能比較

綜合上述之基材的物化特性與氣體滲透率及選擇率的結果，如表4-12所示，可發現碳膜的氣體滲透率與基材之總孔洞體積與d-spacing值有關。此為比表面積、孔洞體積與化學官能基鍵結之綜合效應，導致大部份薄膜之滲透選擇效能有大幅提升的現象。因此，鋁基材以二次水熱法進行矽沸石之修飾後，明顯地可同時提升氣體的滲透率與選擇率。

表4-12 不同燒結條件燒結之基材及薄膜分析結果

Sample Code	Support (Dpore)	Support (Vtotal)	Rq of support	Rq of membrane	D-spacing	P_{H2}	$P_{H2/CH4}$
M1100	8.0	0.0131	28.9	6.5	3.99	3503	32
M1100-MFI-1	5.6	0.0105	145.0	24.6	3.88	2223	260
M1200	6.4	0.0115	38.1	3.6	3.93	2653	47
M1200-MFI-1	4.2	0.0086	212.0	18.9	3.89	1501	119
M1300	6.9	0.0122	39.5	4.9	3.82	1192	147
M1300-MFI-1	3.6	0.0074	270.0	14.8	3.61	1297	251
M1300-MFI-2	4.9	0.0087	339.0	52.0	N.D.	3066	39
M1400	4.3	0.0080	53.1	10.9	4.04	1267	115
M1400-MFI-1	6.1	0.0094	209.0	15.2	4.08	1346	77
M1400-MFI-2	5.1	0.0091	342.0	64.1	N.D.	1947	120

本研究進一步地將實驗結果與 2008 年 Robeson 學者所提出之 Upper bound 高分子膜的滲透選擇上限，進行比較，結果如圖 4-21 所示，可發現本研究利用不同燒結溫度基材進行植種與二次水熱合成之矽/鋁基材所製備之碳分子篩選薄膜，其 H_2/CH_4 滲透及選擇效能皆超越 2008 Robeson's Upper bound，表示本研究所製備之碳膜皆以超越高分子膜的滲透率-選擇率平衡得失之限制。

圖4-22為不同製備條件基材製備之碳分子篩選薄膜Robeson line CO_2/CH_4比較圖，發現除了M1100、M1200、M1300-MFI-2、M1400外其餘基材所製備之碳分子篩選薄膜CO_2/CH_4，皆能超越2008 Robeson's Upper bound標準。

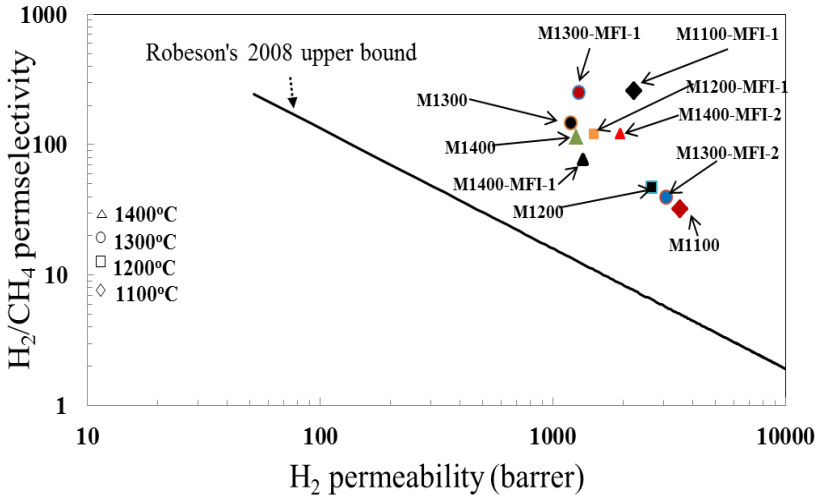

圖 4-21 不同製備條件基材之碳分子篩選薄膜 Robeson line H_2/CH_4 比較圖

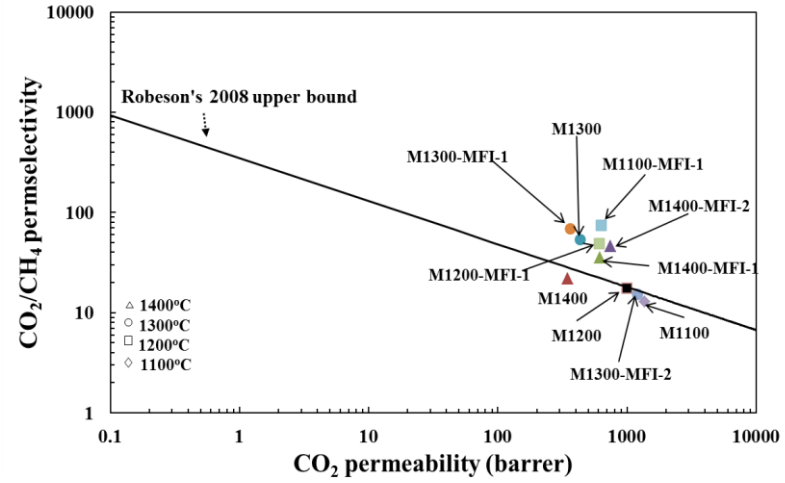

圖 4-22 不同製備條件製備之碳分子篩選薄膜 Robeson line CO_2/CH_4 比較圖

4.3.4.小結

本計畫的研究主題係在探討基材的物化特性對碳分子篩選薄膜之孔洞結構及氣體分選能力的影響。計畫第二年，為探討不同之燒結條件與利用模板製備法，製備矽/鋁基材結構，並利用基材製備成非對稱式碳膜，進一步的探討基材物化特性對碳膜氣體分選效率之影響，並探討鋁基材燒結溫度、升溫速率、熱沉溫時間等因子對鋁基材及碳膜孔徑分佈的影響。

研究結果發現，碳膜的氣體滲透率與基材之總孔洞體積與 d-spacing 值有關，鋁基材以二次水熱法進行矽沸石之修飾後，因可產生交聯作用而明顯地可同時提升氣體的滲透率與選擇率。而本研究藉由 2008 年 Robenson 學者提出 Upper bound 相比較，矽/鋁基材之 H_2/CH_4 滲透及選擇效能皆超越 2008 Robeson's Upper bound，表示本研究所製備之碳膜皆以超越高分子膜的滲透率-選擇率平衡得失之限制。

4.4. 添加TiO_2中間層之效應

4.4.1 TiO_2/Al_2O_3基材物化特性分析

4.4.1.1 TiO_2粉末的表面形態與晶相

本研究利用 Sol-gel 程序製備不同硝酸添加量，調整溶液 pH 值分別為 5(TiN5)、4(TiN4)、3 (TiN3)之 TiO_2 作為中間層，因在 Sol-gel 的製備程序中 pH 值會影響水解縮合速率及晶相組成，在鹼性條件下水解速率較慢，但縮合速率較快，所形成的粒子以顆粒大的居多；在酸性條件下水解速率較快，但縮合速率較慢，而反應所產生的粒子則是以小顆粒居多[87]。為了了解本研究所製備 TiO_2 實際形態，故以高解析度之場發射掃描式電子顯微鏡(FE-SEM)，觀察 TiO_2 粉末外觀形態及粒徑大小。圖 4-23 為透過 SEM 觀察之 TiO_2，發現所合成之 TiO_2 微粒的外觀形態極為相似，且均為網狀結構，但從圖中可發現整體顆粒大小有因添加的硝酸增加而使顆粒粒徑變小，而添加 0.3 ml (pH=3)硝酸的結構較為完整。

(a) TiN5　(b) TiN4　(c) TiN3

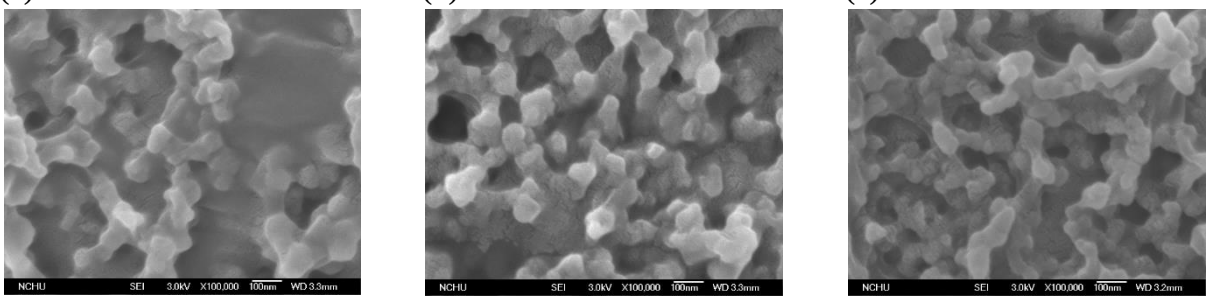

圖 4-23　不同硝酸添加量合成之 TiO_2 粉末 FE-SEM 圖：(a) TiN5、(b) TiN4、(c) TiN3

製備而成的 TiO_2 在經高溫鍛燒後，通常可觀察到兩種晶相，一個是銳鈦礦(Anatase)晶相，另一個為金紅石(Rutile)晶相，根據 JCPDS 資料庫，Anatase 晶相較強，繞射峰出現於 25.3°、37.8°、48.0°、53. 9°、55.1°、62.2°、68.8°與 75.0°，而本研究所製備出來的 TiO_2 波鋒與其符合，如圖 4-24 所示。從圖中可以發現，不同 sol-gel 溶液的 pH 值，其所呈現的波鋒強度與顯示的晶相位置皆為一致。

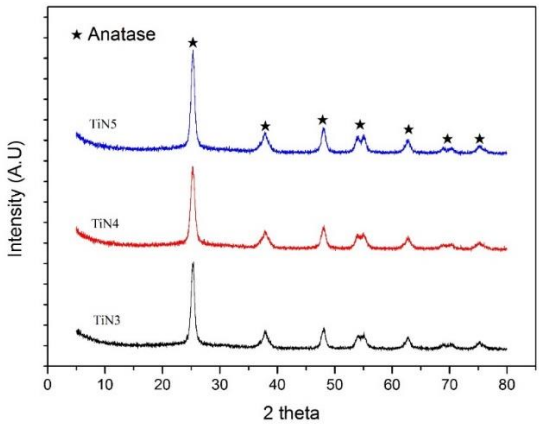

圖 4-24 不同硝酸添加量合成之 TiO_2 粉末 XRD 圖譜 (a) TiN5、(b) TiN4、(c) TiN3。

4.4.1.2 TiO_2/Al_2O_3基材表面形態

本研究選用 1400 ℃燒結前處理之氧化鋁基材，並使用 TiO_2 作為中間層進行表面修飾，圖 4-25 為 TiO_2/Al_2O_3 基材微結構分析圖。由圖 4-25(a)可以看到，原始的氧化鋁基材表面顆粒之間有較大之間隙，經過 TiO_2 修飾之後，其表面形態有明顯的改變。如圖 4-25(b)-(d)所示，塗佈 pH 值為 5 的 sol-gel 溶液經鍛燒後會在表面形成明顯的 TiO_2 層(非顆粒狀)，且隨著 TiO_2 塗佈層數增加，此薄層厚度愈趨增加，但也逐漸產生裂縫。而觀察塗佈 pH 值為 4 的 sol-gel 溶液之 TiO_2 表面狀態(圖 4-25(e)~ (g))，發現其形態與圖 4-25(a)的原始基材表面較為類似，都是呈現顆粒狀，只有塗佈四層之表面有 TiO_2 薄膜層的存在。另外 pH 值為 3 之 TiO_2 所呈現的樣貌也與原始基材表面相似，可以明顯看到氧化鋁基材顆粒且並無 TiO_2 薄膜層存在，而氧化鋁顆粒間的間隙也漸為微小的 TiO_2 顆粒所填充。推測基材表面會有不同型態是因為在 pH 較高的環境下縮合速率較快，故塗佈於基材表面後還未滲入基材孔隙就快速產生縮合效應而形成明顯 TiO_2 層，再經乾燥後於表面產生裂痕，故可由圖 4-25(b)~(d)發現塗佈的厚度越厚，因為應力的增加而 TiO_2 薄膜層破裂情況越明顯。而當添加之硝酸量增加時，因為在 pH 較低的環境下縮合速率較慢，故在塗佈時較易滲入基材孔隙中進行修飾，因此基材表面大多呈現原 Al_2O_3 顆粒狀，唯有塗佈層數增加至四層時表面有較薄之 TiO_2 薄膜層形成。

(a) Al_2O_3

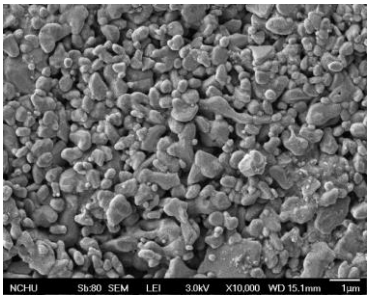

(b) TiN5-2 (c) TiN5-3 (d) TiN5-4

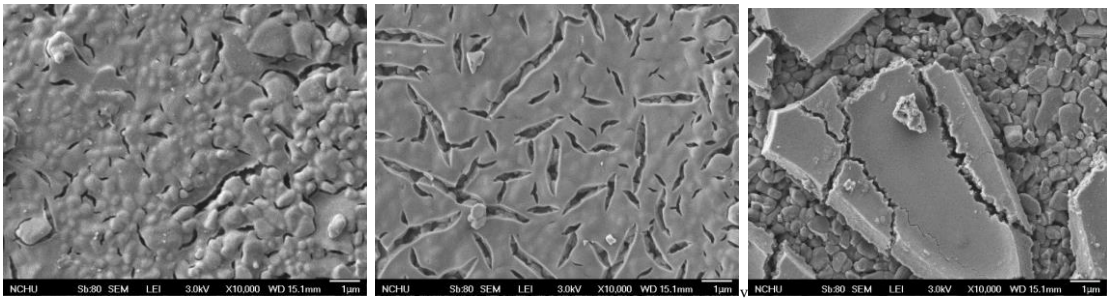

(e) TiN4-2 (f) TiN4-3 (g) TiN4-4

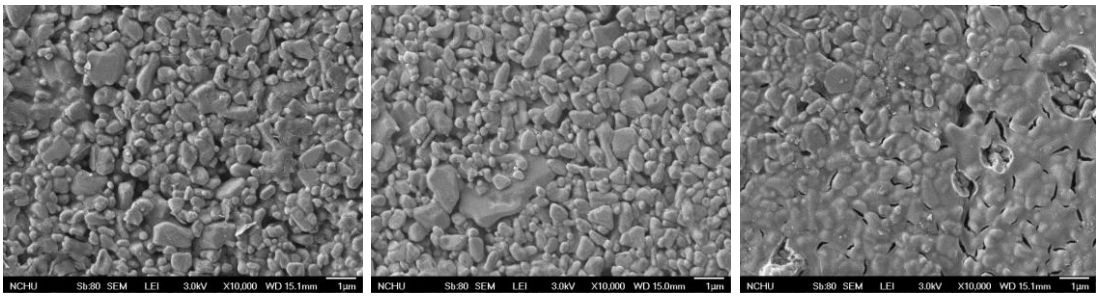

(h) TiN3-2 (i) TiN3-3 (j) TiN3- 4

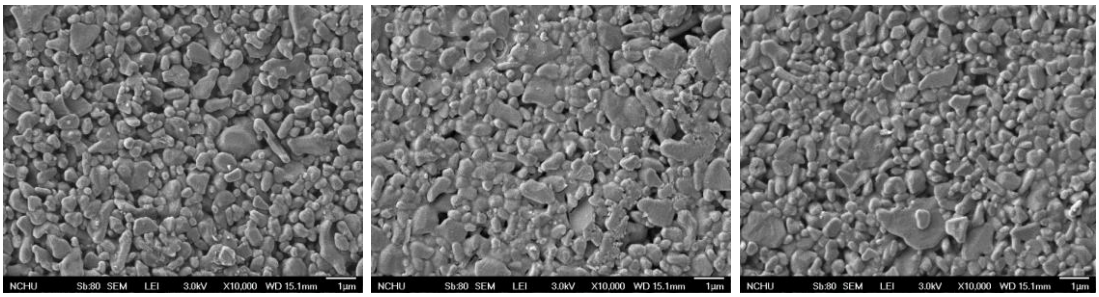

圖 4-25 塗佈不同配比之 TiO_2 中間層基材表面樣貌圖 (a) Al_2O_3、(b) TiN5-2、(c) TiN5-3、(d) TiN5-4、(e) TiN4-2、(f) TiN4-3、(g) TiN4-4、(h) TiN3-2、(i) TiN3-3、(j) TiN3-4

4.4.1.3 TiO_2/Al_2O_3基材表面化學組成分析

為瞭解基材塗佈 TiO_2 溶液後，留存於基材表面的 Ti 含量，故進行 XPS 表面分析。從分析結果得知，在所有的基材表面確實可以檢測出 Ti 的訊號，經換算 Al 與 Ti 的比例，如表 4-13 所示，可發現基材表面的 Ti 含量確實隨著塗佈層數的增加而遞增，另外，我們也可看到不同 pH 值的 sol-gel 溶液得到的表面 Ti / Al 也不同，其中以塗佈 TiN5 中間層可以得到比例較高的 Ti，主要是因為 pH 較高的環境下縮合速率較快，故塗佈於基材表面後還未滲入基材孔隙就快速產生縮合效應而產生明顯 TiO_2 層；而降低其 pH 值後，縮和速度較慢，就會在塗佈時滲入基材中進行修飾，使得表面所殘留的 Ti 比例較低，這與 SEM 所觀察到的現象相同。

表 4-13 塗佈不同配比之 TiO_2 中間層基材表面 Ti 含量分析

	Concentration (%)		Ti / Al
	Al	Ti	
TiN5-2	4.7	95.3	20.27
TiN5-3	2.9	97.1	33.48
TiN5-4	2.3	97.7	42.47
TiN4-2	59.7	40.3	0.67
TiN4-3	51.7	48.3	0.93
TiN4-4	43.3	56.7	1.30
TiN3-2	55.4	44.6	0.80
TiN3-3	54.6	45.4	0.83
TiN3-4	47.2	52.8	1.11

4.4.1.4 TiO_2/Al_2O_3基材孔洞結構分析

表 4-14 為不同基材比表面積、孔洞半徑及孔洞體積分析結果。如表所示，可發現經過 TiO_2 中間層修飾過後均有比表面積及總孔洞體積上升的情形，推測由於 TiO_2 顆粒具有網絡狀孔洞結構(圖 4-23)，使得添加於基材後可提升其整體的比表面積及孔洞體積。另外可以發現塗佈相同 pH 值不同層數的基材，其比表面積呈現先增加再減少的趨勢，而平均孔徑則與比表面積成反比，推測 TiO_2 塗佈層數由 2 層增加至 3 層時，這些增加的 TiO_2 顆粒進入孔洞之中進行填補的量增加，故產生比表面積上升、平均孔徑下降的情形，而當我們將塗佈層數增加至 4 層時因孔洞先被 TiO_2 顆粒填補完畢，此時多數顆粒在外部進行堆積，使得產生比表面積下降，平均孔徑上升的情形。另外，已知當 pH 值遞增，TiO_2 顆粒將逐漸縮小，因此可進入修飾的孔洞的 TiO_2 量將增加，會產生較大的比表面積，

因此從這邊也可以明顯看到隨著塗佈的中間層 pH 值增加，整體比表面積有逐漸上升的情形。而從各孔徑的孔體積的含量分佈可以知道，其增加的孔洞以 2~50 nm 的中孔及>50 nm 巨孔為主，<2 nm 的微孔增加的趨勢不大，這顯示添加的 TiO_2 大部分填補於氧化鋁顆粒之間的間隙中，僅有少部分會進入孔洞之中，因此可以修飾原本基材過大的間隙。

表 4-14 不同基材比表面積、孔洞半徑及孔洞體積

Code	S_{BET} (m^2/g)	D_{pore} (nm)	BJH adsorption cumulative Pore Volume of pores between 3.5 Å and 1000 micros Radius (cm^3/g)			
			V_{total}	V_{micro}	V_{meso}	V_{macro}
Al_2O_3	4.3	74.2	0.0080	0.0011 (13.75%)	0.0063 (78.75%)	0.0005 (6.25%)
TiN5-2	9.3	38.5	0.0902	0.0017 (1.88%)	0.0445 (50.44%)	0.0438 (48.55%)
TiN5-3	13.0	27.1	0.0885	0.0024 (2.71%)	0.0487 (55.02%)	0.0372 (42.03%)
TiN5-4	3.8	176.3	0.1686	0.0010 (0.59%)	0.1071 (63.52%)	0.0603 (35.76%)
TiN4-2	10.6	81.1	0.2150	0.0018 (0.83%)	0.1295 (60.23%)	0.0836 (38.88%)
TiN4-3	18.2	62.2	0.2833	0.0032 (1.12%)	0.1998 (70.52%)	0.0801 (28.27%)
TiN4-4	16.4	60.6	0.2489	0.0025 (1.00%)	0.1471 (59.10%)	0.0992 (39.85%)
TiN3-2	13.0	29.6	0.0970	0.0024 (2.47%)	0.0500 (51.54%)	0.0445 (45.87%)
TiN3-3	31.0	9.6	0.0746	0.0046 (6.16%)	0.0420 (56.30%)	0.0278 (37.26%)
TiN3-4	19.2	46.5	0.2238	0.0029 (1.29%)	0.1093 (48.83%)	0.1114 (49.77%)

4.4.1.5 TiO_2/Al_2O_3基材表面粗糙度分析

圖 4-26 所示為利用原子力顯微鏡(AFM)分析基材表面之粗糙係數(Ra)結果。由圖可以觀察到，AFM 所顯現出來 3D 樣貌圖與實際所拍攝到的 SEM 圖相似，原始未塗 TiO_2 前的氧化鋁(圖 4-26(a))粗糙度為 56.8 nm，而因為硝酸添加量較低時，基材表面雖然會被 TiO_2 薄膜層所覆蓋，但會因為縮合反應而逐漸產生明顯裂紋，因此整體看來粗糙度有增加的趨勢。而塗佈 pH 值為 4 的 TiO_2 後，與原始基材比其粗糙度開始降低(圖 4-26(e)(f))，其原因為 TiO_2 開始填補氧化鋁基材中凹陷的地方，使得其表面起伏較為平緩。最後，塗佈 pH 值為 3 的 TiO_2 後，所得到的基材表面結構與 pH=4 較為相似，從 3D 圖中看到都是接近原始的顆粒狀結構，並同樣有隨著塗佈層數增加而粗糙度有下降的趨勢。

而基材表面的型態會影響塗佈薄膜後兩相的接合情形，尤其是表面孔隙與粗糙度更是直接影響機械互鎖的主要關鍵之一。與粗糙度較高的表面相比，當基材表面呈現平滑狀態時，鑄膜液與基材的接觸範圍降低，嵌附效果變差，薄膜層就容易剝落，使得薄膜的缺陷增加，造成薄膜分選效果降低。但是另一方面，當粗糙度太高時，容易使披覆在上面的高分子鏈折疊而呈現不規則性，鏈與鏈間所產生之折疊會愈為明顯，進而使得碳化後所得之層間距變大，這也會使氣體選擇率下降。因此，良好的薄膜基材其表面粗糙度應適中，才能使薄膜黏附完整且不致於使高分子鏈折疊呈現不規則性。

(a) Ra= 56.8 nm

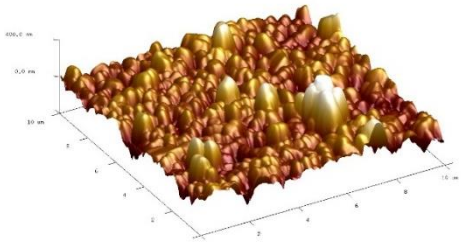

(b) Ra=26.2 nm

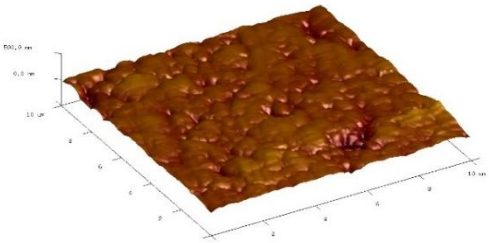

(c) Ra=56.3 nm

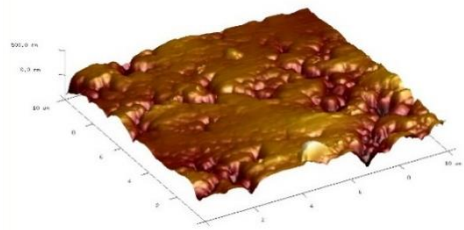

(d) Ra=99.1 nm

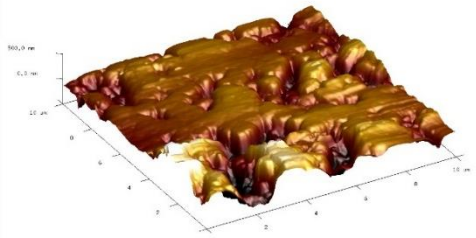

(e) Ra= 49.4 nm

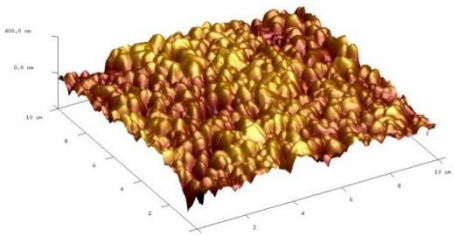

(f) Ra=45.9 nm

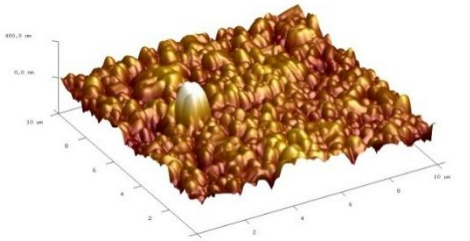

(g) Ra= 36.1 nm

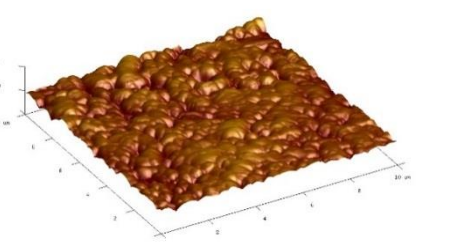

(h) Ra=49.8 nm

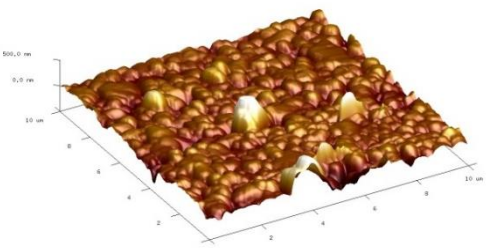

(i) Ra=47.2 nm (j) Ra=40.7 nm

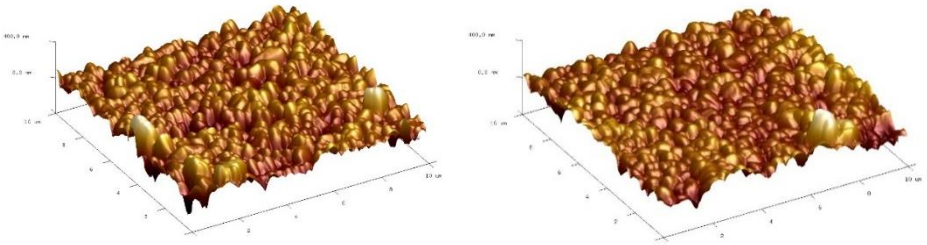

圖 4-26 不同 TiO_2 塗佈層數之基材表面粗糙度分析 (a) Al_2O_3、(b) TiN5-2、(c) TiN5-3、(d) TiN5-4、(e) TiN4-2、(f) TiN4-3、(g) TiN4-4、(h) TiN3-2、(i) TiN3-3、(j) TiN3-4。

4.4.2 TiO_2中間層對CMSM分選效能的影響

4.4.2.1 碳膜膜厚與層間距

碳分子篩選薄膜擔持於 Al_2O_3 及 TiO_2/Al_2O_3 基材的 SEM 圖與膜厚分析，如圖 4-27 與表 4-15 所示。因 PEI 衍生性碳膜屬緻密型之結構，故表面圖中可以發現所製備的薄膜皆為完整無缺陷的緻密型薄膜。而從側視圖中看到原始 Al_2O_3 基材所擔持的碳膜與其他已塗佈 TiO_2 中間層的碳膜相比，膜厚明顯較薄，其原因為基材尚未經過修飾，顆粒間的間隙過大而使高分子鑄膜液滲入所致。經塗佈 TiO_2 中間層後，則可從圖中看到膜厚明顯增加，且完整沉積於基材表面。而從圖 4-28 接合處放大圖也可以清楚看到未塗佈 TiO_2 時，薄膜與氧化鋁之間滲入情形嚴重，薄膜與基材間無明顯分層，經而塗佈 TiO_2 中間層後，因奈米 TiO_2 填補原始基材的間隙，可以將基材表面修飾成較平緩粗糙面，使高分子液不易滲入，經高溫碳化後碳選擇層可以穩定的堆疊沉積於基材上，故可以得到較清楚分層且膜厚較厚的薄膜。

表 4-15 碳膜膜厚分析

Code	Membrane thickness (μm)
Al_2O_3	2.13
TiN5-2	3.01
TiN5-3	4.20
TiN5-4	4.50
TiN4-2	2.62
TiN4-3	3.60
TiN4-4	3.64
TiN3-2	2.27
TiN3-3	3.09
TiN3-4	3.60

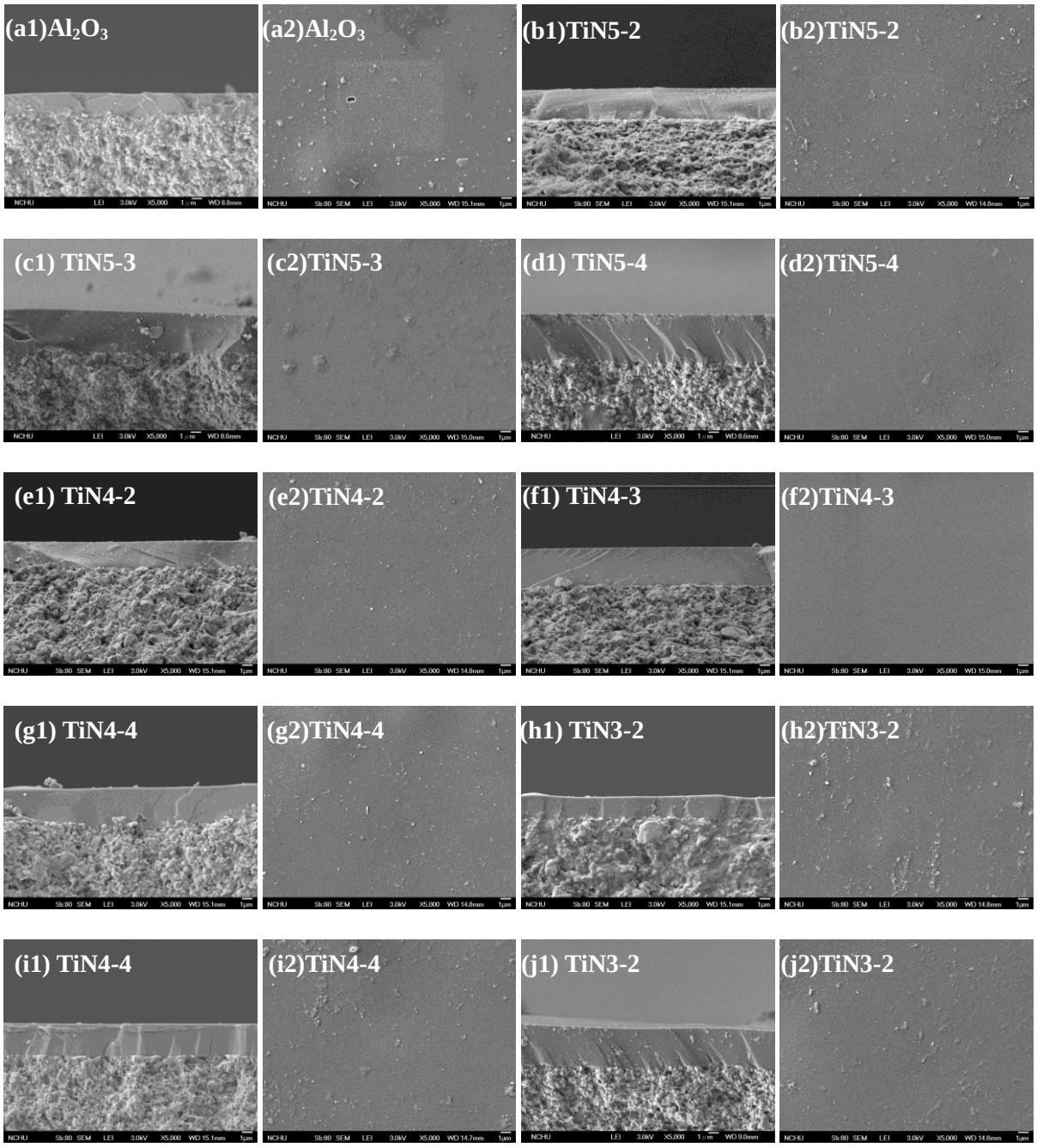

圖 4-27 塗佈不同 TiO_2 中間層的基材表面(1)及剖面(2)FESEM 圖：(a) Al_2O_3、(b) TiN5-2、(c) TiN5-3、(d) TiN5-4、(e) TiN4-2、(f) TiN4-3、(g) TiN4-4、(h) TiN3-2、(i) TiN3-3、(j) TiN3-4。

(a) Al_2O_3

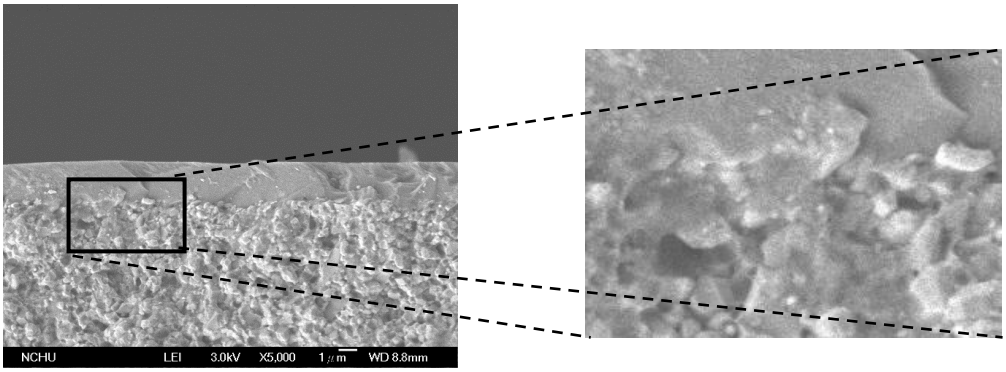

(b) TiN4-3

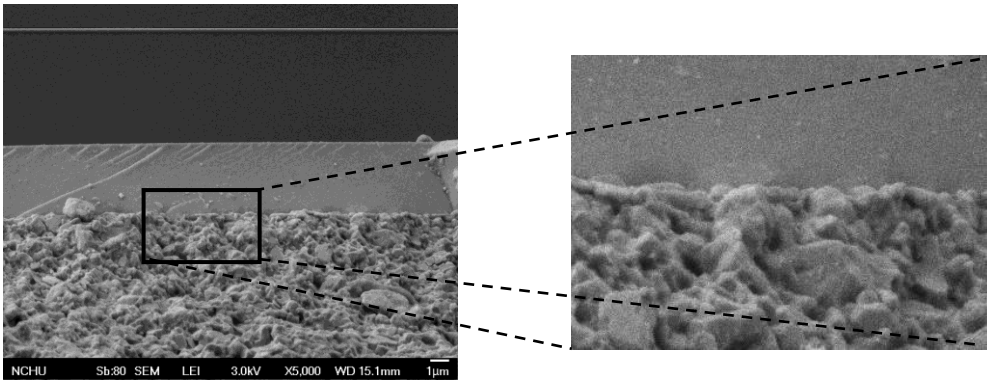

圖 4-28 塗佈中間層之基材所製備碳分子篩選薄膜接合介面放大圖(a) Al_2O_3 基材薄膜剖面、(b) TiN4-3 基材薄膜剖面。

4.4.2.2 機械互鎖能力評估

本研究利用 EDS 的 line scan 掃描薄膜側面圖，如圖 4-29 所示，我們將所檢測到的碳與鋁的相交範圍視為薄膜滲入深度，也就是機械互鎖範圍。從圖可以明顯觀察到未經修飾的 Al_2O_3 機械互鎖深度最深，而 TiN5 互鎖深度明顯較 TiN4、TiN3 低，這是因為前述所提到的 TiN5 因為縮合速度較快，在基材表面形成明顯中間層，因此塗佈高分子溶液時，較難滲入，故也造成兩項機械互鎖範圍較低，而 TiN4 與 TiN3 因為塗佈的 TiO_2 中間層會滲入基材中，僅修飾了氧化鋁顆粒間的間隙，故在進行旋轉塗佈法時塗佈的高分子鑄膜液容易滲入，因此可以看到機械互鎖範圍較高。而另一方面可以看到，塗佈不同層數但相同 pH 值的 TiO_2 中間層對機械互鎖深度影響並不大，因此可以知道塗佈上去 TiO_2 顆粒大小與型態是影響機械互鎖範圍的主要原因。另外可以從表 4-16 的膜厚與滲入深度比較中發現，滲入深度較大的樣品其量測到的膜厚也會較薄。我們可以由以上分析發現，機械互鎖能力為 Al_2O_3 > TiN3 ≒ TiN4 > TiN5。

(a)

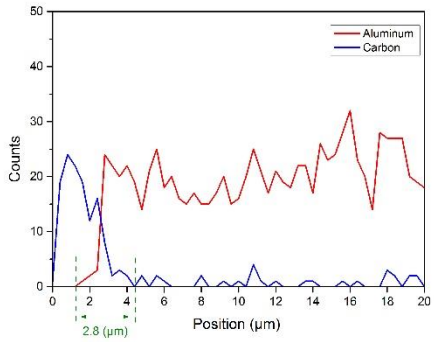
Aluminum
Carbon
Counts
Position (μm)
2.8 (μm)

(b)

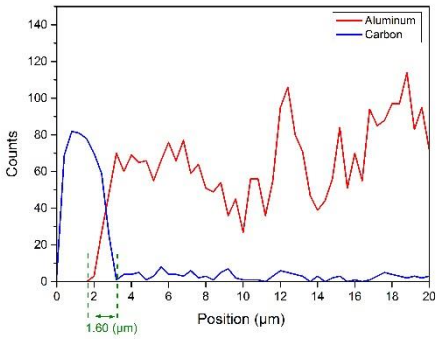
Aluminum
Carbon
Counts
Position (μm)
1.60 (μm)

(c)

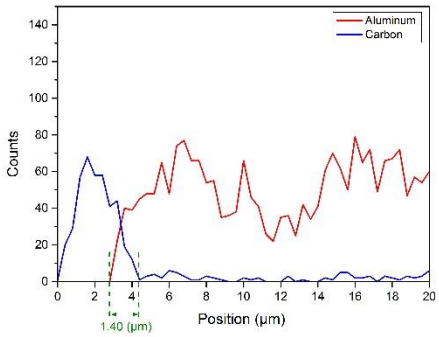
Aluminum
Carbon
Counts
Position (μm)
1.40 (μm)

(d)

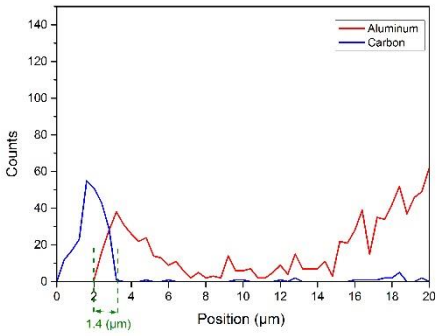
Aluminum
Carbon
Counts
Position (μm)
1.4 (μm)

(e)

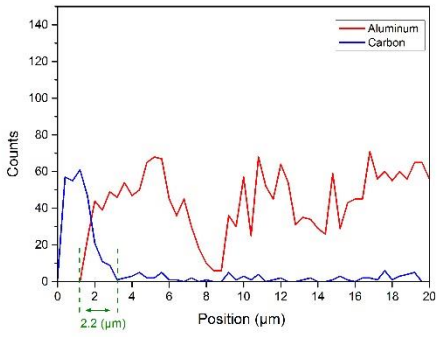
Aluminum
Carbon
Counts
Position (μm)
2.2 (μm)

(f)

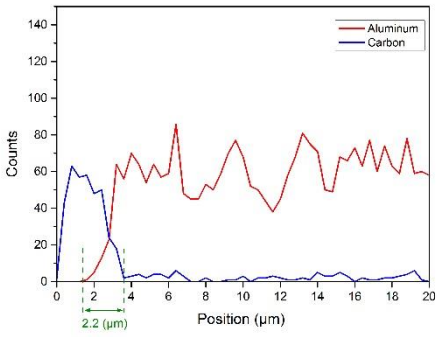
Aluminum
Carbon
Counts
Position (μm)
2.2 (μm)

(g)

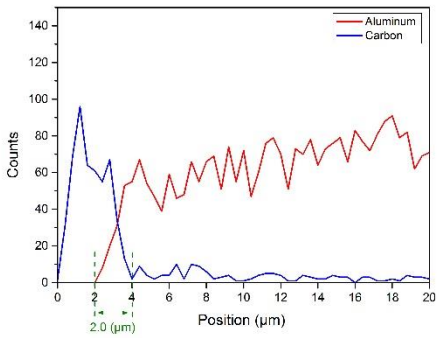
Aluminum
Carbon
Counts
Position (μm)
2.0 (μm)

(h)

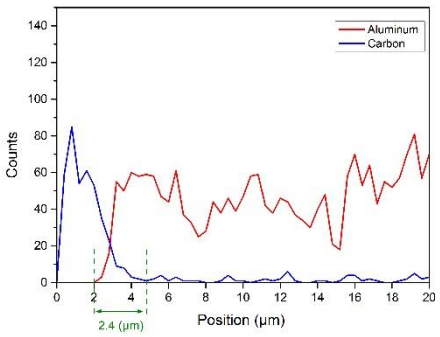
Aluminum
Carbon
Counts
Position (μm)
2.4 (μm)

(i) (j)

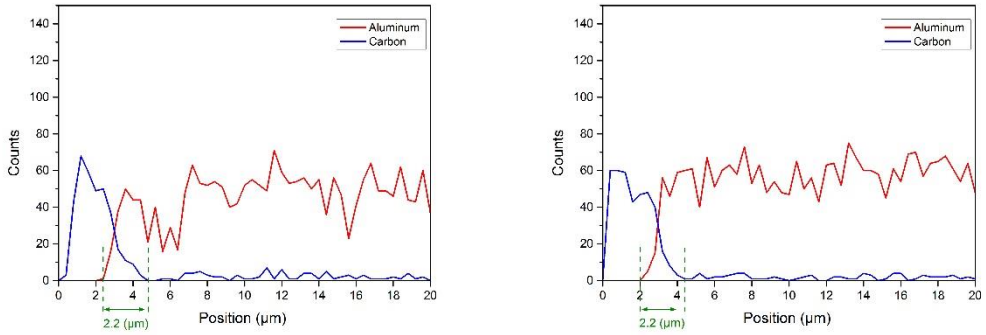

圖 4-29 不同基材製備之薄膜 EDS 側面掃描圖：(a) Al_2O_3、(b) TiN5-2、(c) TiN5-3、(d) TiN5-4、(e) TiN4-2、(f) TiN4-3、(g) TiN4-4、(h) TiN3-2、(i) TiN3-3、(j) TiN3-4

表 4-16 薄膜機械互鎖深度與膜厚

Code	Preparation conditions	
	Membrane Thickness (μm)	Interlocking Depth (μm)
Al_2O_3	2.13	2.80
TiN5-2	3.01	1.60
TiN5-3	4.20	1.40
TiN5-4	4.50	1.40
TiN4-2	2.62	2.20
TiN4-3	3.60	2.20
TiN4-4	3.64	2.00
TiN3-2	2.27	2.40
TiN3-3	3.09	2.20

4.4.2.3 化學鍵結能力評估

支撐於基材之高分子薄膜的化學結構變化，可藉由 FT-IR 觀察，其結果如圖 4-30 所示。PEI 高分子主要特徵峰出現於 1775 cm^{-1}、1717 cm^{-1}、1353 cm^{-1} 等三個位置，分別為 C=O 半對稱、C=O 對稱及 C-N 官能基[89]。由圖 4-30 中看到，原始未經修飾的 Al_2O_3 特徵峰較強，而觀察經過 TiO_2 修飾的基材，雖未發現 TiO_2 粉末之特徵波峰，但可由圖中發現 PEI 高分子原有之特徵波峰半對稱 C=O、對稱 C=O 及 C-N 等波峰的強度有減弱趨勢，尤其是 TiN5 的樣品，圖 4-30(b)-(d)，可以看到特徵峰明顯隨著塗佈層數增加而減弱，推測為高分子膜與基材產生化學性鍵結，使得 PEI 高分子原有的特徵波峰強度減弱，此現象亦可能使得薄膜與基材間更為緊密。另外，TiN4 及 TiN3 的樣品雖然波峰減弱的幅度較不明顯，但也是隨著塗佈層數增加而遞減，這符合前述所看到的 SEM 圖與 XPS 表面分析，pH 為 5 的 TiO_2 中間層因為快速縮合現象可以殘留較多於基材表面，因此有較多 TiO_2 與 PEI 高分子鍵結，故 FT-IR 圖譜中波峰的強度減弱明顯，而 pH 為 3 及 4 的 TiO_2 則因殘存於表面的量較少，故減弱的強度較不明顯。因此由 FT-IR 圖譜可以推估高分子膜與基材間產生化學性鍵結，這會使薄膜與基材兩相之間因化學鍵的力量而接合較為緊密。我們可以由以上分析發現，化學鍵結強度與溶液 pH 值及塗佈層數有關，分別為 TiN5 > TiN4> TiN3 > Al_2O_3 且塗佈 4 層> 3 層> 2 層。

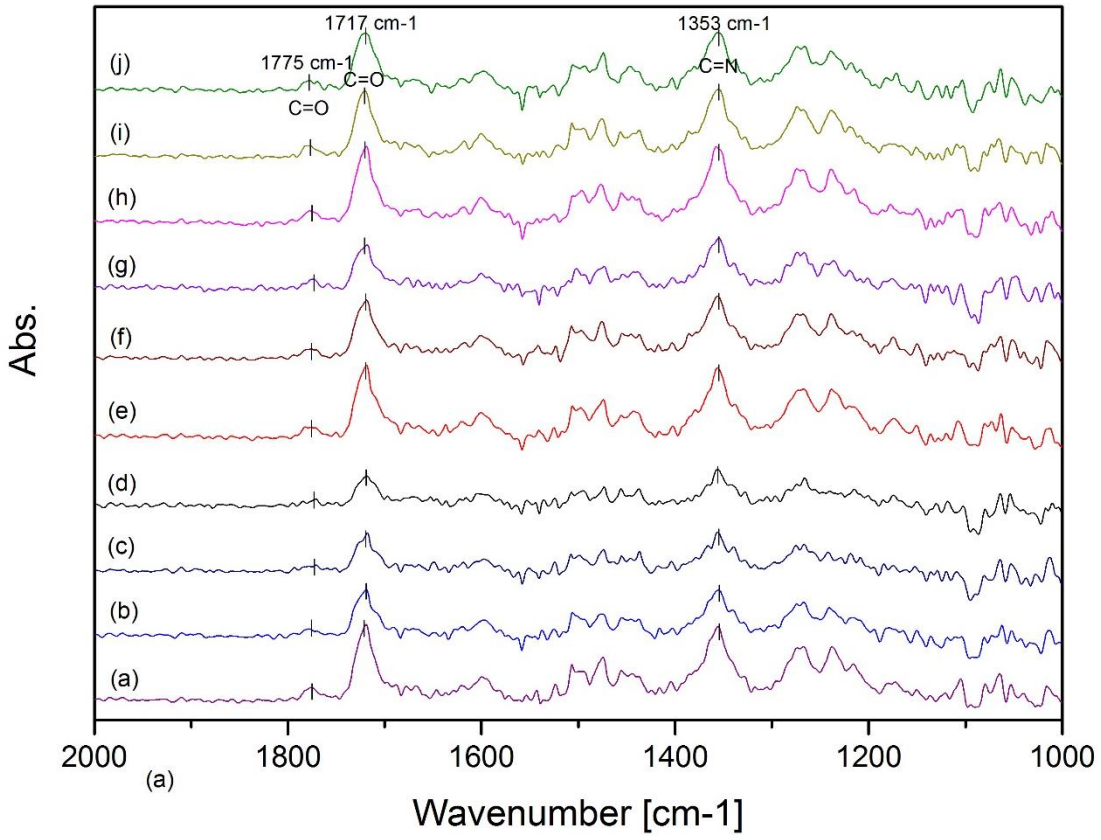

圖 4-30 不同基材製備之薄膜 FT-IR 圖譜(a) Al_2O_3、(b) TiN5-2、(c) TiN5-3、(d) TiN5-4、(e) TiN4-2、(f) TiN4-3、(g) TiN4-4、(h) TiN3-2、(i) TiN3-3、(j) TiN3-4。

4.4.2.4 吸附作用能力評估

過去文獻曾提到當基材表面具有比高分子溶液還高的表面能量，塗附的高分子層可以較完整黏附在基材表面[7]。因此，為了了解製備 TiO_2/Al_2O_3 基材表面能之差異，故對其進行接觸角測試。接觸角是一個在液體與氣體界面接觸於固體表面所形成的夾角，若固體表面上的液滴受固體表面之作用力甚強，液滴將會完全攤平在固體表面上，反之則會顯現出所謂的蓮花效應，故本研究將以實際高分子鑄膜液與基材之接觸角來判斷基材表面吸附能大小。從圖 4-31 可以發現原始的氧化鋁基材的接觸角為較小($\theta=10.5^o$)經過修飾後的基材反而會增加其接觸角($\theta=12.6^o$ ~21.0^o)，這是因為當 Al_2O_3 基材塗佈 TiO_2 層後，極性基材與非極性溶劑間的親和性不佳，故塗佈中間層後皆會增加其接觸角；此外，塗佈後的接觸角增減趨勢與所測得的粗糙度成正比，原因為當粗糙度越大時，將阻礙鑄膜液的流動性，使溶液不易擴散，此現象亦會增加高分子鏈的彎曲程度、提高高分子鏈與基材間的折點，使 d-spacing 值增加。故我們可以由以上分析發現，吸附能力以 Al_2O_3 > 塗佈 TiO_2 中間層後之基材。

(a) **Contact angle**：10.5^o (b)**Contact angle**：12.6^o

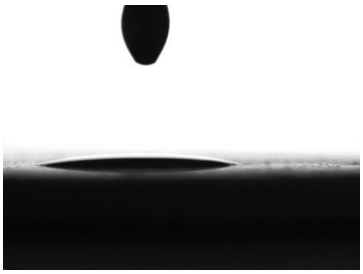

(c) **Contact angle**：20.7^o (d)**Contact angle**：21.0^o

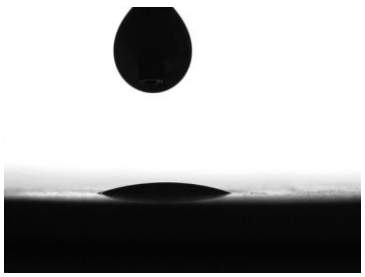

(e) **Contact angle**：17.3^o (f)**Contact angle**：16.2^o

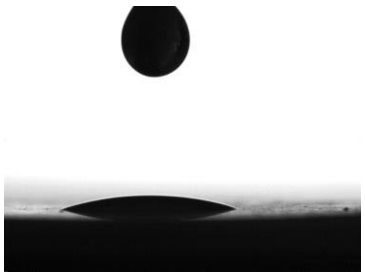

(g) **Contact angle**：13.4 ^{o} (h)**Contact angle**：18.5^{o}

(i) **Contact angle**：16.7 ^{o} (j)**Contact angle**：16.2 ^{o}

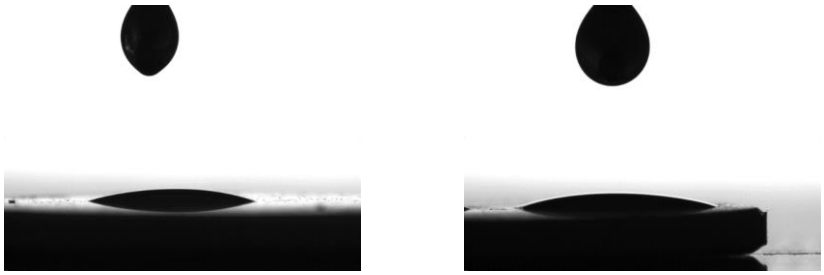

圖 4-31 基材表面接觸角度分析(a)Al_2O_3、(b)TiN5-2、(c)TiN5-3、(d)TiN5-4、(e)TiN4-2、(f)TiN4-3、(g)TiN4-4、(h)TiN3-2、(i)TiN3-3、(j)TiN3-4。

4.4.2.5 接合應力評估

從文獻中可以知道[56]，兩相的界面會因為膨脹係數不同產生應力集中的地方，故可能因為應力大增造成斷裂或裂縫進而產生相分離，影響碳膜之分選能力。而應力的大小可以由高分子膜的 Tg 點來判斷，當應力增加時，高分子膜的 Tg 點會下降，反之亦然，這是因為壓力會降低薄膜的熔點，進一步使 Tg 點下降。

因此本研究也測量塗佈於不同基材的高分子薄膜 Tg 點，如表 4-17 所示。從表中我們可以看到，塗佈於原始未添加中間層的 Al_2O_3 基材薄膜，其 Tg 為 212.5 ^{o}C，加入 pH 為 4 的 TiO_2 後，Tg 點的確有增加趨勢，其中又以塗佈三層的 TiN4-3 升高至 218.26 為最多，因此可以知道，塗佈 TiO_2 中間層的確可以降低兩相接合應力，讓薄膜在進行操作時，不易因應力造成斷裂或裂縫進而產生兩相分離的現象。觀察整體接合應力大小為：Al_2O_3 > 4 層 > 2 層 > 3 層。故塗佈 3 層 TiO_2 中間層所製備的薄膜，綜合所有影響參數後可以得到較小的基材與薄膜之間的應力，可有助於兩相的最佳黏附效果。

表 4-17 塗佈不同層數 TiO_2 的高分子薄膜玻璃轉化溫度(Tg)

Sample code	Tg (^{o}C)
Al_2O_3	212.5
TiN4-2	216.65
TiN4-3	218.26
TiN4-4	216.37

4.4.3 碳基材薄膜分選效能

4.4.3.1 黏附機制對滲透率的影響

本研究使用不同之燒結條件前處理後之氧化鋁基材，製備成支撐型態之碳分子篩選薄膜，進行單一氣體滲透測試，探討不同基材結構對於氣體滲透分選效能之影響。圖 4-32 為不同參數下薄膜的整體滲透效能，整體而言，各氣體於不同薄膜中之滲透通量大小皆為 $H_2 > CO_2 > O_2 > N_2 > CH_4$，符合分子篩選機制。此外，從圖中也可發現整體滲透率隨著硝酸的添加量增加，而有下降的趨勢。首先我們可以發現經三種不同 pH 值的製備出的 TiO_2 修飾後的薄膜，其滲透率也不相同，從這邊可以明顯看到 TiN5，其滲透率明顯大於 TiN4 與 TiN3，而 TiN4 又小幅高於 TiN3，即滲透率大小為 TiN5 >> TiN4 > TiN3。而對應其三個黏附機制，發現與機械互鎖效應及化學鍵結強度有關，即當機械互鎖範圍愈小、化學鍵結愈弱時，氣體的滲透通量愈大。但另一方面我們可以看到，原始未經修飾之 Al_2O_3 因孔隙較大，滲入深度最高，如果照此推斷，滲透率應該為最低，但是我們可以從圖中看到，Al_2O_3 並不是所有參數中滲透率最低的，這是因為就如同文獻回顧所提到的，粗糙度或孔隙太大時，會造成鑄模液大量滲入，雖然機械互鎖範圍很高，但也會形成不連續薄膜，故因此產生微小缺陷使滲透有小幅上升的情形。

另外我們還可以發現且隨著 TiO_2 塗佈層數增加，滲透也呈現遞減的現象，但是對比相同 pH 值塗佈不同層數的 TiO_2，其機械互鎖深度並無太大變化，因此對應另外兩個黏附機制，發現與化學鍵結效應相關。因為當殘留在基材表面的 TiO_2 越多，因鍵結形成會造成 PEI 特徵峰減弱，而相同 pH 值下，的確隨著塗佈層數增加有明顯減弱的趨勢，因此可以知道中間層塗佈層數較多時，鍵結能力較強，黏附效果增加，進而影響整體滲透力。

最後，若以吸附能力來看，原始未經修飾的 Al_2O_3 基材吸附能力優於經過 TiO_2 中間層修飾後的基材，但是從薄膜滲透率卻無發現此趨勢，因此推斷薄膜與基材間的吸附能力對基材與薄膜的影響遠小於機械互鎖與化學鍵結作用。

(a) pH=5

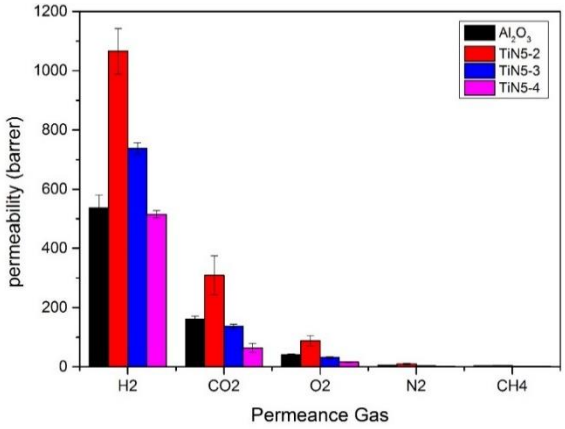

(b) pH=4

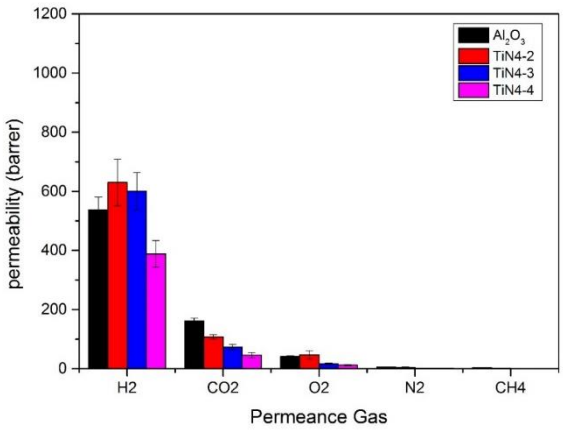

(c) pH=3

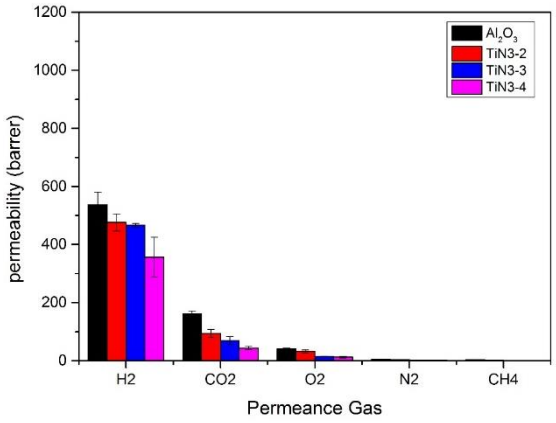

圖 4-32 塗佈不同層數之 sol-gel 溶液所製備之碳膜滲透率 pH=5、(b) pH=4、(c) pH=3。

4.4.3.2碳膜氣體分選效能比較

本研究進一步與 Robenson 學者於 2008 年所提出之 Upper bound limit 進行比較[90]，其結果如圖 4-33 所示，發現本研究所製備之薄膜在 H_2/CH_4、H_2/CO_2 之滲透選擇效能上皆能超越 Robeson's 2008 upper bound 之限制。觀察不同參數之基材製備而得的碳膜的滲透選擇效能分佈後發現，經過 TiO_2 中間層修飾後皆可提升其效能，未經修飾的 Al_2O_3 選擇率皆是所有參數中最低的，這是因為 Al_2O_3 雖然有最大的機械互鎖範圍，但是由前面文獻所提：當大量高分子鑄膜液滲入時，容易形成缺陷，且 Al_2O_3 的化學鍵結能力最低，因此造成選擇率較低。

而比較 H_2/CH_4 中 TiN5、TiN4 及 TiN3 的位置發現，TiN4 及 TiN3 位於 TiN5 的左上方，也就是整體較為損失其滲透但增加其選擇能力，此現象主要與機械互鎖效應有關，因 TiN5 的互鎖範圍較低，容易產生缺陷，因此會比互鎖較高的 TiN4 及 TiN3 有較高的滲透較低選擇率。另外比較 TiN4 及 TiN3 的位置發現，發現整體來說 TiN4 會比 TiN3

有較高的選擇率，此現象主要與化學鍵結效應有關，因 TiN4 的化學鍵結強度較 TiN3 高因此可以些微提升其選擇效能。

另一方面，比較 H_2/CO_2 中 TiN5、TiN4 及 TiN3 的位置發現，TiN4 及 TiN3 位於 TiN5 的上方，也就是會增加其選擇能力，此現象主要還是與機械互鎖效應有關，當機械互鎖範圍增加，會進而得到較高的選擇率，而比較 TiN4 及 TiN3 的位置發現， TiN4 同樣會比 TiN3 有較高的選擇率，此現象主要與 TiN4 的化學鍵結強度較 TiN3 高有關。

因此綜合以上比較，黏附效應對薄膜的影響為：機械互鎖>化學鍵結>吸附能力。

(a) H_2/CH_4

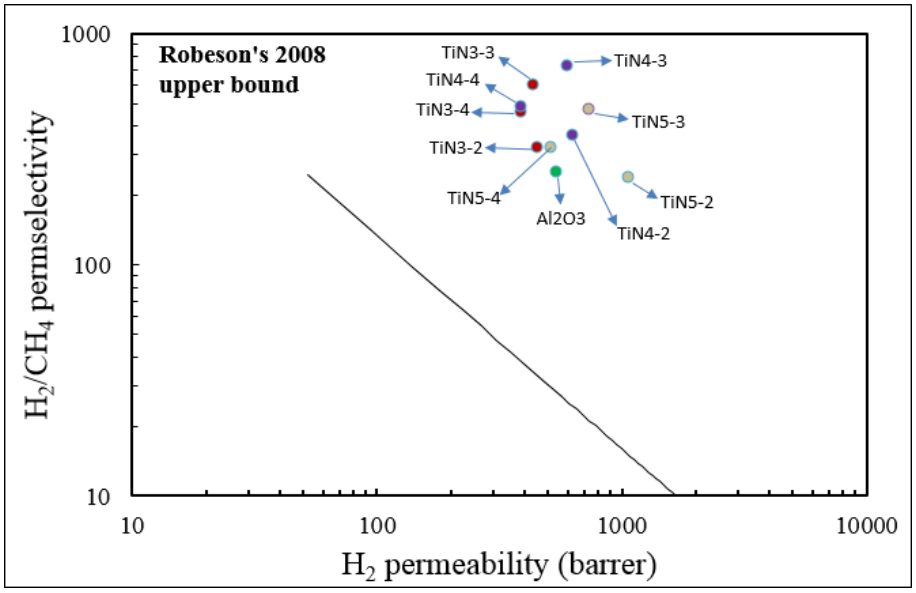

(b)H_2/CO_2

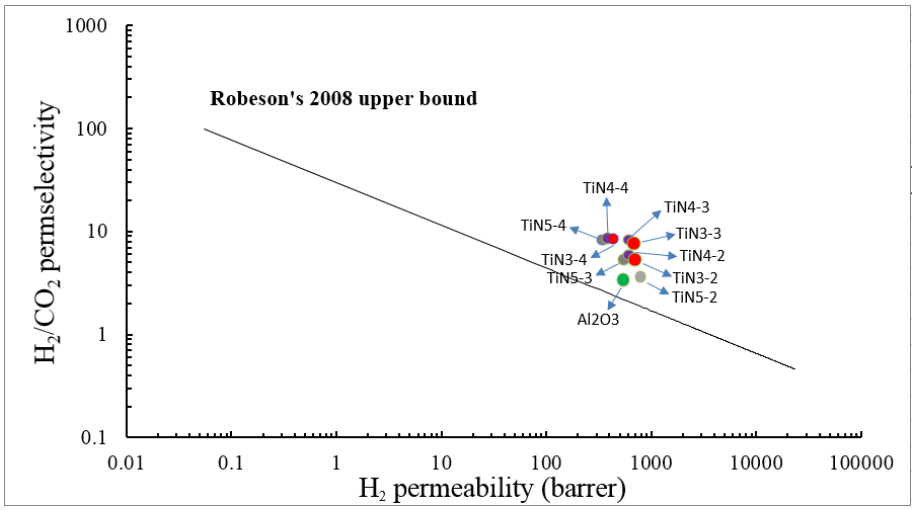

圖 4-33 不同製備條件之薄膜與 Robeson's 2008 upper bound 比較 (a) H_2/CH_4、(b) H_2/CO_2。

4.4.3.3 薄膜機械強度測試

最後，為了瞭解所製備的薄膜是否可操作在高壓環境下，因此將實驗參數中整體效率較佳之薄膜進行高壓滲透測試，從圖 4-34 可以看到當碳膜操作在進氣壓分別為 2、4 及 6 atm 的情況下，其整體滲透速率皆無太大改變，表示碳膜是可以操作在高壓的環境下而保持一定效能。另外也利用雙軸彎曲試驗了解薄膜整體耐受強度，而從圖 4-35 中可以發現原始基材不但有較差的抗壓強度 187.45 N，且在下壓力約為 50 N 時，就有一個應力突然下降的位置，這是因為在此時薄膜已經出現裂痕產生力量釋放，故此時偵測到的應力較小，最後再繼續累積，直到 187.45 N 時整體斷裂。而反觀經過修飾的薄膜，並無出現此情形，並且可以大幅提升整體的抗壓強度至 215.99 N，故所塗佈的 TiO2 中間層確實可以增加整體的機械強度。

(a) Al_2O_3 (b)TiN4-2

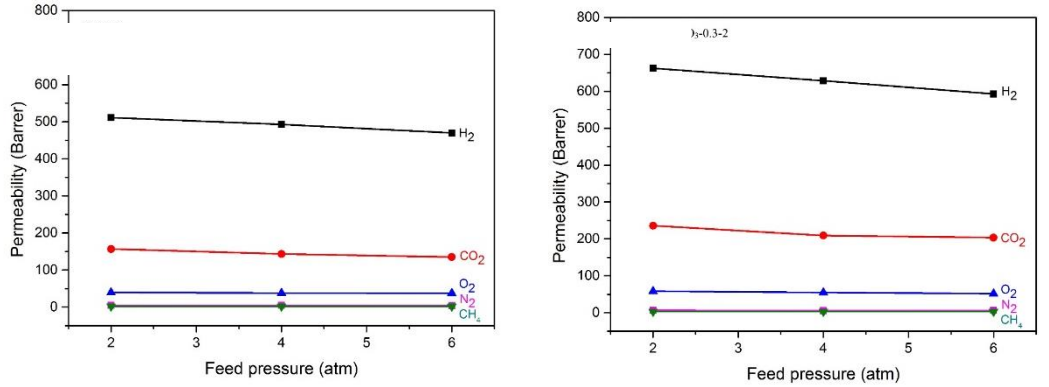

(c)TiN4-3 (d)TiN4-4

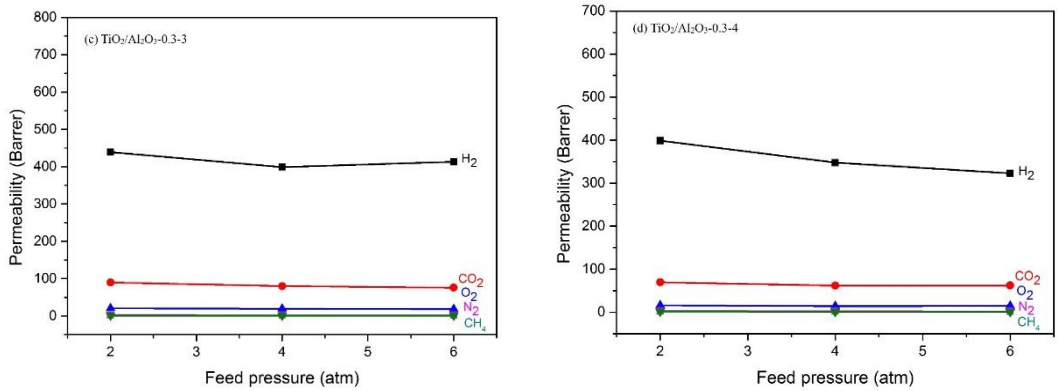

圖 4-34 薄膜在不同進氣壓對薄膜滲透率的影響(a) Al_2O_3、(b)TiN4-2、(c)TiN4-3、(d)TiN4-4。

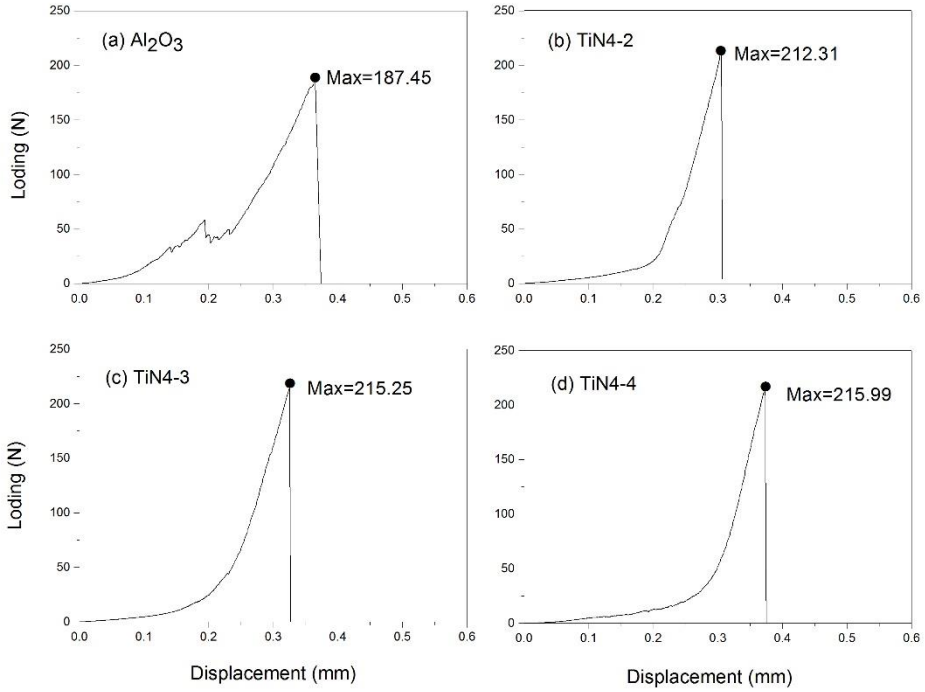

圖 4-35 不同基材製備之薄膜抗壓強度 (a) Al_2O_3、(b) TiN4-2、(c) TiN4-3、(d) TiN4-4

4.4.4 小結

本計畫的研究主題係在探討基材的物化特性對碳分子篩選薄膜之孔洞結構及氣體分選能力的影響。為探討不同中間層對薄膜的影響，並製備TiO_2/鋁基材結，進一步的探討基材物化特性對碳膜氣體分選效率之影響，並探討不同TiO_2添加量、顆粒大小等因子對碳膜的影響。

研究結果發現，TiO_2 中間層除了可有效修飾基材表面粗糙度，防止高分子鑄膜液大量滲入基材外，也可增加基材與高分子鍵間氫鍵的形成，進而改變高分子前驅物與基材的機械互鎖範圍、化學鍵結、吸附作用大小而影響薄膜與基材之間的黏附特性。透過調整 TiO_2 sol-gel 溶液 pH 值發現，當 pH 值較低時，會使水解反應較快速而造成塗佈之中間層溶液較易滲入基材孔隙中進行修飾，故可獲得較佳的機械強度，雖損失些微滲透率、但選擇率較佳。而當中間層層數增加，殘留在基材表面的 TiO_2 數量也隨之遞增，而使得化學鍵結強度上升，增強黏附效果，雖然滲透率下降，但可提升選擇率。由以上研究結果可知道，滲透選擇率主要受機械互鎖、化學鍵結兩個主要黏附機制影響，而當薄膜之間的機械互鎖範圍相似時，再由化學鍵結多寡影響滲透選擇率，而吸附特性對基材與薄膜之間的黏附貢獻是非常微弱的，以至於對滲透選擇並無影響。並發現 TiO_2 有較 MFI 中間層更佳的滲透選擇效果，故第三年延用 TiO_2 做為中間層探討粗糙度與鑄膜液黏度的影響。

4.5. 基材粗糙度對薄膜分選效能的影響

4.5.1基材物化特性分析

4.5.1.1基材表面型態分析

圖 4-36 為基材拋光後塗佈 TiN4 中間層的微結構分析圖。從圖中可以明顯看出原始未拋光 TiN4 基材表面呈現顆粒狀結構(圖 4-36(a)),但基材先經過 14μ 的砂紙研磨過後(圖 4-36(b))，表面開始呈現顆粒被磨平的現象，當再使用 8μ 之砂紙研磨，可以看到有更多的顆粒被磨掉，表面越趨平整。最後再使用更小粒徑尺寸的鑽石液進行研磨，已經觀察不到原始基材的顆粒狀結構，轉變成較平整的表面。

(a) TiN4　　(b) TiN4-14μ

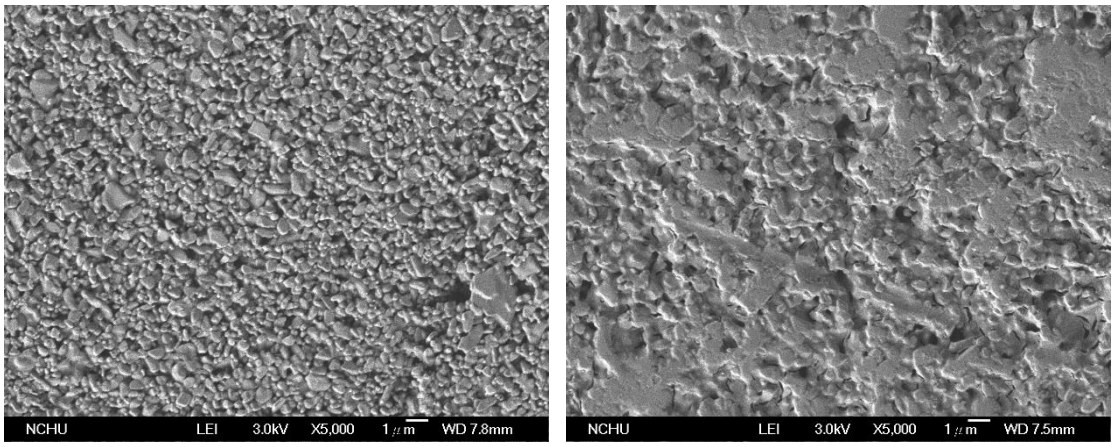

(c) TiN4-8μ　　(d) TiN4-3μ

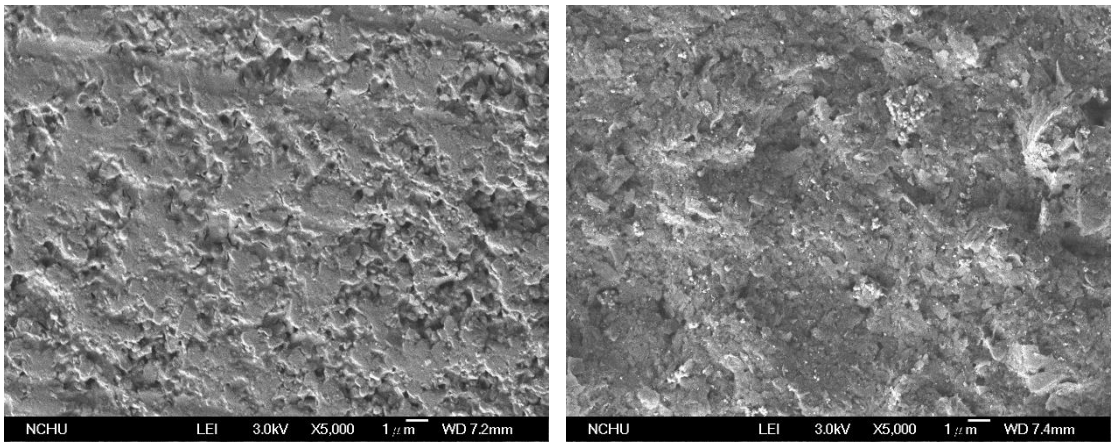

圖 4-36 利用不同粒徑之砂紙進行研磨之基材表面樣貌圖 TiN4、TiN4-14μ、(c) TiN4-8μ、(d) TiN4-3μ

4.5.1.2基材表面粗糙度分析

本實驗藉由不同粒徑的砂紙研磨來改變基材表面粗糙度，並利用原子力顯微鏡(AFM)分析基材之表面粗糙係數(Ra)。從圖 4-37 發現所測得的表面 3D 圖相當類似上述 SEM 圖所拍攝的基材實際表面圖，且表面粗糙度也如所使用的砂紙粒徑一樣呈現遞減，其粗糙度分別為使用 14μ 的 Ra = 99.1 nm、8μ 的 Ra = 74.9 nm 及 3μ 的 Ra = 29.1 nm。

(a) Ra= 45.9 nm　　(b) Ra= 99.1 nm

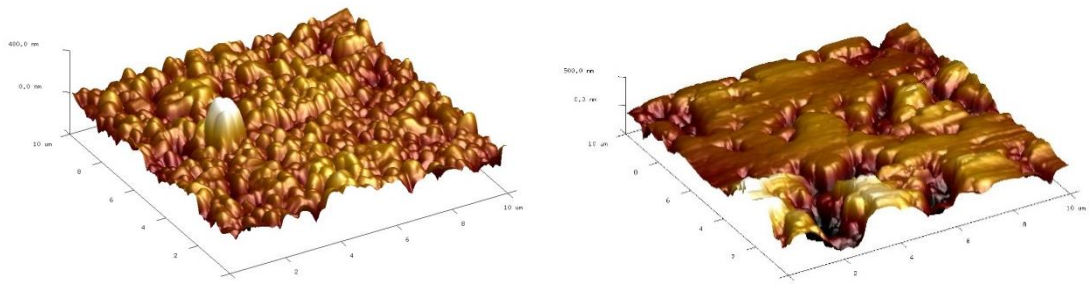

(c) Ra=74.9 nm　　(d) Ra= 29.1 nm

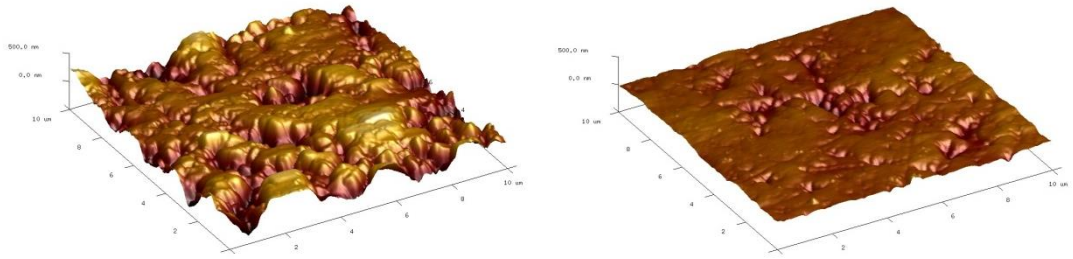

圖 4-37 以不同粒徑之砂紙研磨之基材表面粗糙度分析 (a) TiN4、(b) TiN4-14μ、(c) TiN4-8μ、(d) TiN4-3μ

4.5.1.3 基材孔洞結構分析

表 4-18 為不同粗糙度基材的比表面積、平均孔徑及孔洞體積分析結果。如表所示，可發現經 14μ 及 8μ 砂紙研磨後的基材，其粗糙度上升，會使比表面積降低、平均孔徑增加，因為當粗糙度太高時，TiO_2 容易滲入基材間隙中進行填補，故比表面積降低，而另外留在孔洞外部的 TiO_2 顆粒，則因為粗糙度太高故排列凌亂，使得平均孔徑大增、巨孔數量也較多。而粗糙度較低的基材因為 TiO_2 僅有少部分會進入孔洞之中，故本身多孔性材質使比表面積上升，而較平整的表面也使顆粒排列整齊，讓平均孔徑降低，較小孔洞的微孔及中孔增加，巨孔減少。

表 4-18 不同粗糙度基材比表面積、孔洞半徑及孔洞體積

Code	Roughness (nm)	S_{BET} (m^2/g)	D_{pore} (nm)	BJH adsorption cumulative Pore Volume of pores between 3.5 Å and 1000 micros Radius (cm^3/g)			
				Vtotal	V_{micro}	V_{meso}	V_{macro}
TiN4-3	45.9	18.2	62.2	0.2833	0.0032 (1.12%)	0.1998 (70.52%)	0.0801 (28.27%)
TiN4-3-14μ	99.1	13.0	296.4	0.0970	0.0024 (2.47%)	0.0500 (51.54%)	0.0445 (45.87%)
TiN4-3-8μ	74.9	18.2	286.8	0.1309	0.0032 (2.44%)	0.0689 (52.63%)	0.0586 (44.76%)
TiN4-3-3μ	29.1	37.0	65.1	0.0604	0.0048 (7.94%)	0.0406 (67.21%)	0.0149 (24.66%)

4.5.2 薄膜特性分析

4.5.2.1 碳膜層間距與膜厚分析

碳分子篩選薄膜擔持於經過不同粗糙度研磨過後的基材的表面及側面顯微圖，如圖 4-38 所示，經過研磨後的碳膜膜厚約在 2-3 μm。我們也可以從表 4-19 中看到，經過研磨後的基材粗糙度越大，所得的膜厚也會越薄。

另外，可以從表中發現薄膜的粗糙度亦會影響薄膜的 d-spacing 值，如 TiN4-14μ 的粗糙度為 99.1 nm，所對應的 d-spacing 值也最大，粗糙度與層間距明顯成正比。從前述分析中可以知道利用 14μ 砂紙研磨後，其粗糙度有大幅增加的趨勢，而因基材表面愈粗糙時，高分子鏈的折疊會呈現不規則性，鏈與鏈間所產生之折疊會愈為明顯，故粗糙度會明顯影響層間距的大小。

表 4-19 基材粗糙度、膜厚與碳膜層間距之關係

code	Ra of support (nm)	Membrane thickness (μm)	d-spacing (Å)
TiN4-3	45.9	3.60	4.34
TiN4-14μ	99.1	2.90	4.77
TiN4-8μ	74.9	3.09	4.49
TiN4-3μ	29.1	3.18	4.29

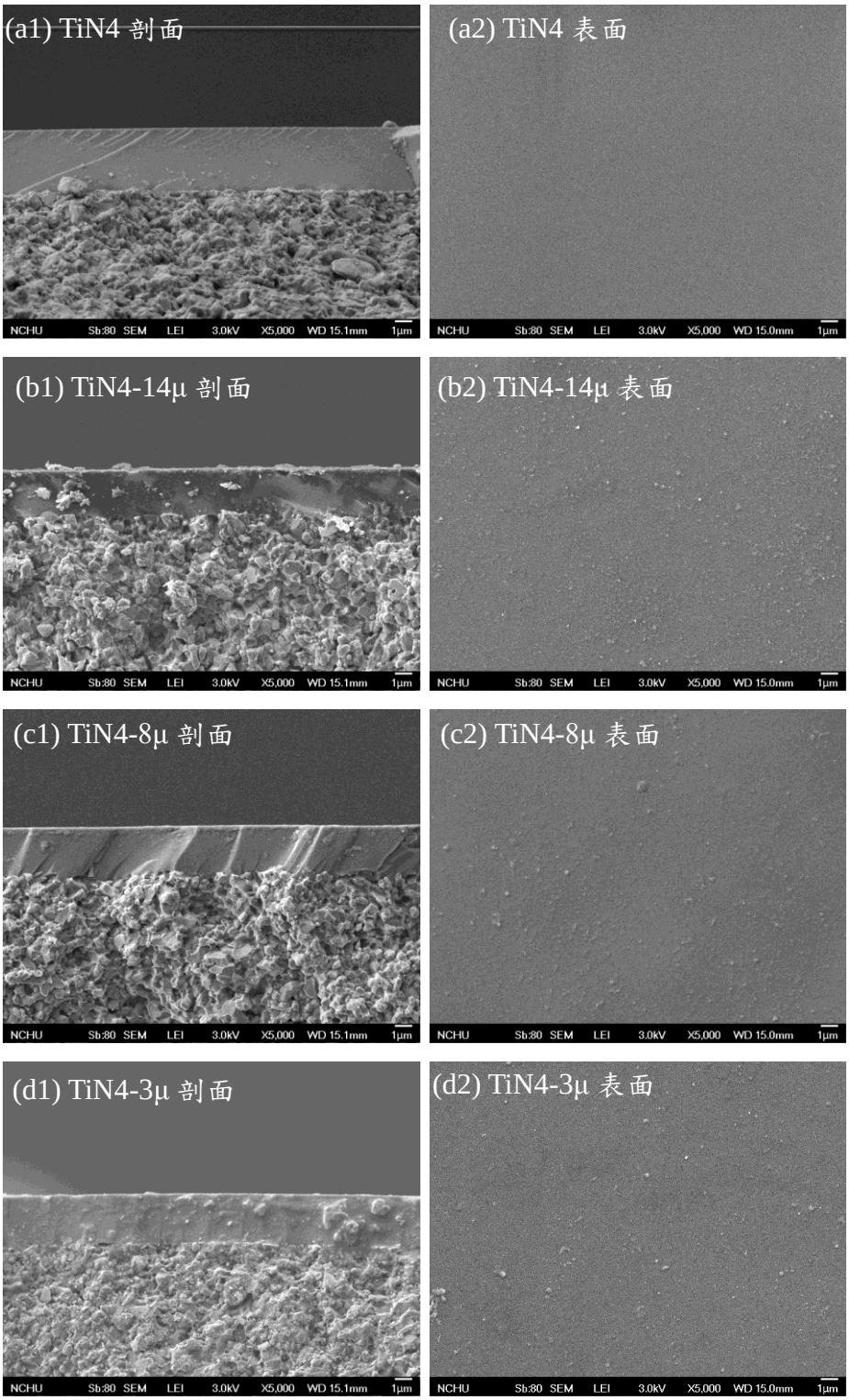

圖 4-38 以不同粗糙度之砂紙研磨後製備而成的薄膜表面(1)及剖面(2)FESEM 圖 (a) TiN4、(b) TiN4-14μ、(c) TiN4-8μ、(d) TiN4-3μ。

4.5.2.2 機械互鎖能力評估

本研究利用 EDS 的 line scan 掃描薄膜側面圖，如圖 4-39 所示，我們將所檢測到的碳與鋁的相交範圍視為薄膜滲入深度，也就是機械互鎖範圍。

從圖中可以明顯看到各基材的整體機械互鎖深度依序為 TiN4-14μ (4.6 μm)> TiN4-8μ (2.4 μm)> TiN4 (2.2 μm)> TiN4-3μ (2.0 μm)，這與前面利用 AFM 所測得粗糙度大小及 d-spacing 大小的趨勢一致，基材 TiN4-14μ 的粗糙度最大為 99.1 nm，互鎖深度高達 4. 6 μm，TiN4-3μ 粗糙度最低為 29.1 nm，互鎖深度則降為 2.0 μm，證明粗糙度也是影響滲入範圍的一個重要的因素，粗糙度較高時，得到的互鎖範圍也較大。

(a) TiN4　　(b) TiN4-14μ

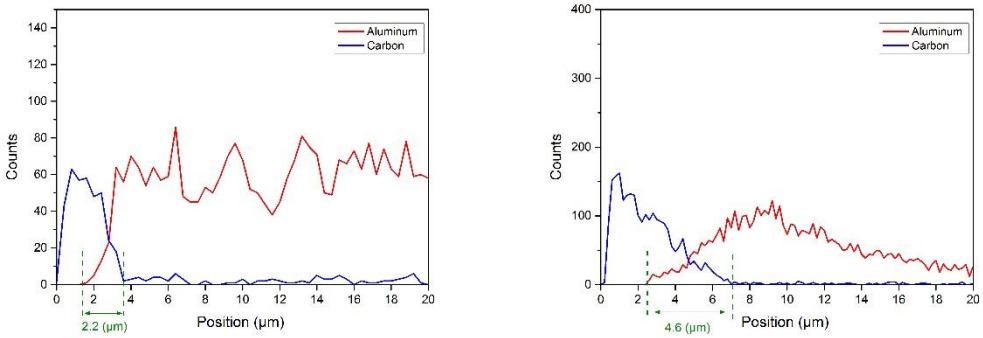

(c) TiN4-8μ　　(d)TiN4-3μ

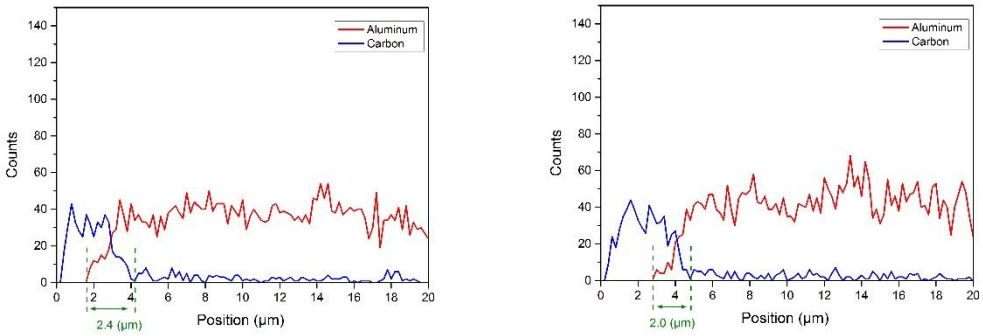

圖 4-39不同基材製備之薄膜EDS側面掃描圖 (a)TiN4、(b) TiN4-14μ、(c) TiN4-8μ、(d) TiN4-3μ。

4.5.2.3 化學鍵結能力評估

對於擔持於基材上方之高分子薄膜的化學結構變化，藉由 FT-IR 觀察得知， PEI 高分子主要特徵峰位置為 1775 cm^{-1}、1717 cm^{-1}、1353 cm^{-1} 等三個位置，利用 PEI 高分子原有之特徵波峰半對稱 C=O、對稱 C=O 及 C-N 等波峰的強度減弱趨勢，了解薄膜與基材間的化學鍵結強度。由圖 4-40 中發現 TiN4-14μ 的特徵峰強度最高，故推測其化學鍵結強度最弱，而 TiN-3μ 特徵峰減弱幅度最多，薄膜與基材間的鍵結強度最高，故薄膜與基材間的鍵結強度依序為 TiN4-3μ > TiN4 > TiN4-8μ > TiN4-14μ。而這也與粗糙度的趨勢相

同，因此當粗糙度較低時，塗佈的中間層較不易滲入基材孔隙中，使表面可提供鍵結的 TiO_2 量增加，讓薄膜與基材兩相之間接合較緊密。

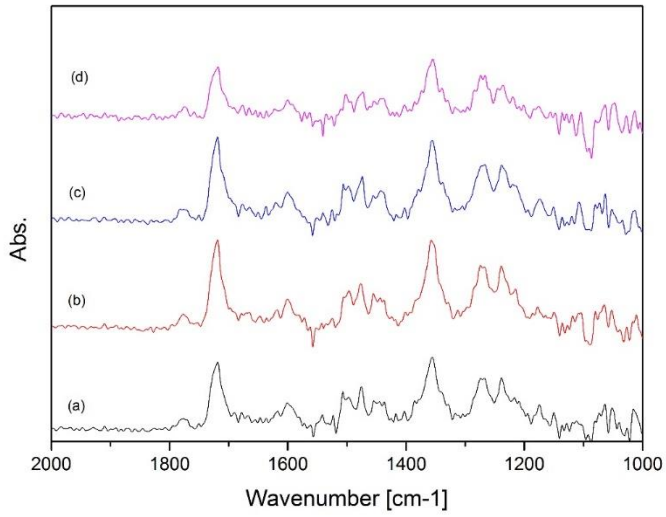

圖 4-40 不同基材製備之薄膜 FT-IR 圖譜 (a)TiN4、(b) TiN4-14μ、(c) TiN4-8μ、(d) TiN4-3μ。

4.5.3 碳膜氣體滲透選擇效能與主要黏附機制評估

由圖 4-41 可以發現，各氣體的滲透通量仍符合分子篩選機制，即 $P_{H2}>P_{CO2}>P_{O2}>P_{N2}>P_{CH2}$，且碳膜擔持於不同基材的氣體滲透率大小依序為 TiN4-14μ > TiN4 > TiN4-8μ > TiN4-3μ，此趨勢與 d-spacing、機械互鎖強度、吸附強度的趨勢並不吻合，推測應該為各作用機制的綜合效應所導致。

如表 4-20 所示，因 TiN4-14μ 的高粗糙度使薄膜滲入範圍非常大，雖然增加互鎖機制，但也可能使其發生前述文獻所提到的會在此形成缺陷，使氣體從此處通過，造成滲透增加。而使用 8μ 的砂紙研磨後，雖然 TiN4-8μ 表面粗糙度也較原始 TiN4 基材高，層間距較大，但因機械互鎖深度較深，黏附效果較好，故可以看到其滲透率略小於原始基材 TiN4 之滲透率。最後，使用平均粒徑為 3μ 之鑽石液進行研磨，從之前所進行的 SEM 表面分析也可看到，其結構已無原始基材的顆粒狀結構，大致已趨於一個較平整的狀態，因此塗佈在上方之高分子鏈的折疊也會趨於平整，因此所測得的層間距降低，使滲透率減少，因此我們可以從以上結果得知滲透率會受層間距與機械互鎖範圍影響。由此可推測，薄膜的滲透能力大小為機械互鎖與化學鍵結的綜合效應，但以機械互鎖為主要影響因素，當機械互鎖效應較為相似時，才會看出次要因素-化學鍵結的影響。

而從以上分析得知，粗糙度在此又為影響這兩個機制強弱的主要原因，故基材粗糙度應該控制在一定的範圍內，太大或太小皆會使其對薄膜產生不良效應。

此外我們也將所得到的選擇率與 2008 年的 Robeson's upper bound 做比較，如圖 4-42 所示。發現本研究所製備之薄膜在 H_2/CH_4、H_2/CO_2 之滲透選擇效能上皆能超越 Robeson's 2008 upper bound 之限制。而比較各個參數在圖中的位置發現，所有經過研磨的基材在製備成薄膜後，其選擇率皆有下降的情形，推測其原因為經過研磨後基材表面顆粒狀結構有些仍存在，但有些會被磨平，甚至因研磨的砂紙顆粒太大而有下凹情形，使得表面結構並非一致性，而是有顆粒狀、平坦狀、下凹狀結構。因此塗佈鑄膜液後，高分子鏈會因為基材表面不一致的結構，使得排列非常凌亂造成形成之超微孔較少，且會導致層間距較大(TiN4-14μ= 4.77、TiN4-8μ= 4.49)，故選擇率會較差。

表 4-20 碳膜粗糙度、機械互鎖深度、碳膜層間距與滲透率之關係

code	Ra of support (nm)	Mechanical interlock position (μm)	d-spacing (Å)	P_{H2} (barrer)
TiN4	45.9	2.2	4.34	600.74
TiN4-14μ	99.1	4.6	4.77	966.06
TiN4-8μ	74.9	2.4	4.49	529.01
TiN4-3μ	29.1	2.0	4.29	391.69

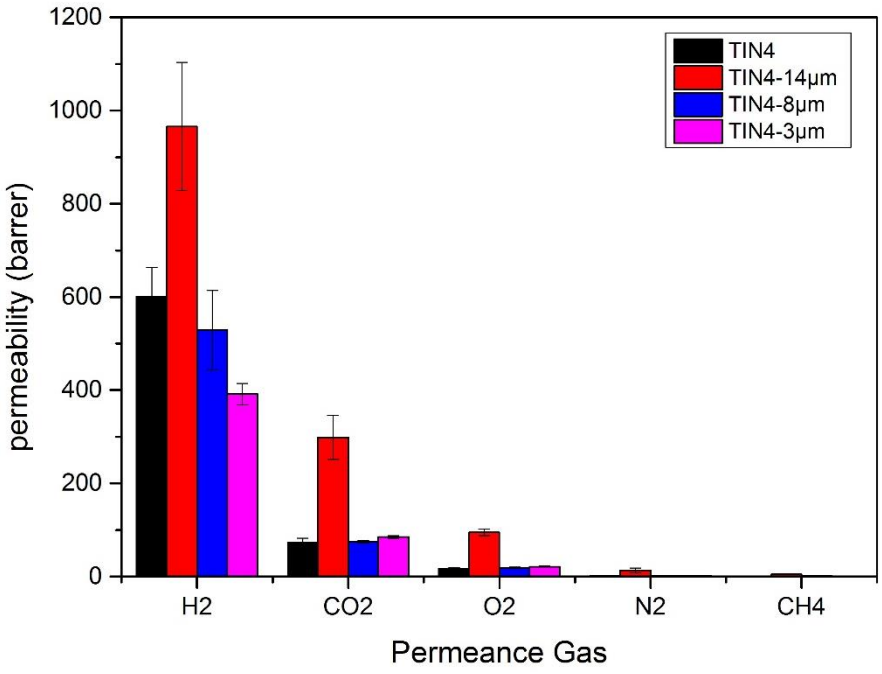

圖 4-41 不同粗糙度所製備的碳膜氣體滲透率

(a) H_2/CH_4

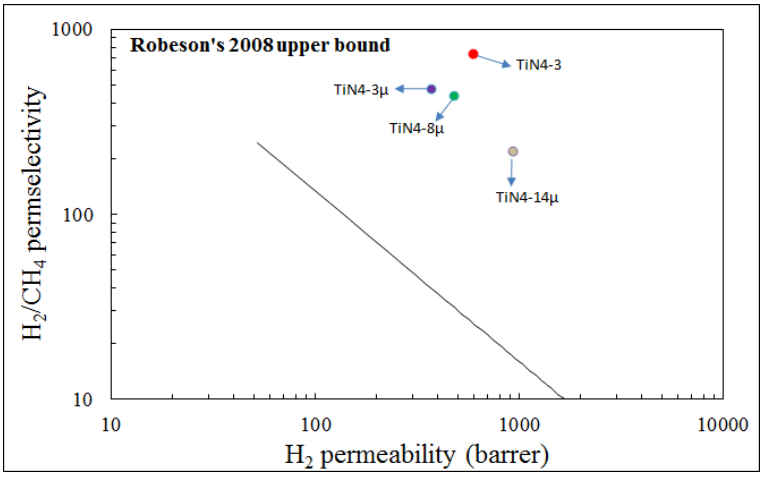

(b) H_2/CO_2

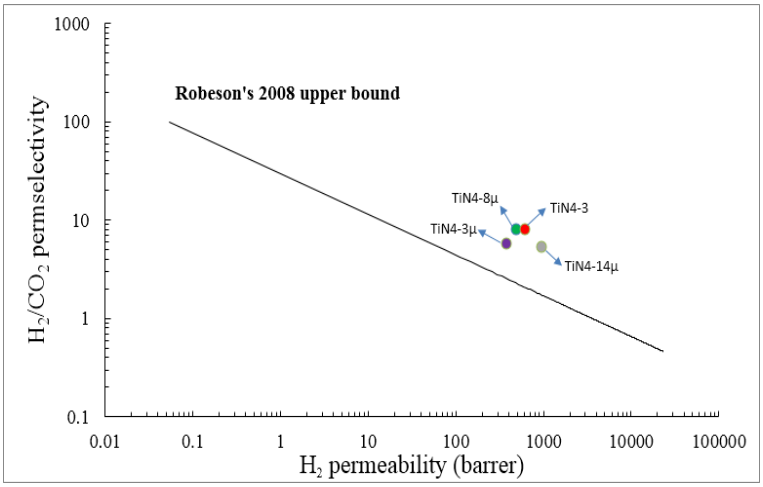

6

圖 4-42 不同製備條件之薄膜與 Robeson's 2008 upper bound 比較 (a)H_2/CH_4、(b)H_2/CO_2。

4.5.4. 小結

本計畫的研究主題係在探討基材的物化特性對碳分子篩選薄膜之孔洞結構及氣體分選能力的影響。為探討基材粗糙度對薄膜造成之效應，故利用拋光技術改變基材中間層的粗糙度，進而了解其對薄膜層間距、機械互鎖及化學鍵結效應之影響。

研究結果發現，當粗糙度過大時，高分子鏈會因為基材表面高低起伏的結構，而排列凌亂導致層間距較大，選擇率較低；且較高的粗糙度亦會使 TiO_2 微粒滲入，減少與 PEI 高分子鍵氫鍵的形成，使得化學鍵結效應減少，最後因薄膜前趨液大量滲入形成缺陷，使滲透率上升、選擇率減少。因此，粗糙度為影響機械互鎖機制強弱的主要原因，故基材粗糙度應該控制在一定的範圍內，太大或太小皆會使其對薄膜產生不良效應。

4.6. 鑄膜液黏滯度對薄膜的影響

由以上實驗發現，機械互鎖是主要影響薄膜黏附性進而改變整體滲透選擇效能的機制，而薄膜前趨液黏滯度亦是影響滲入情形的一大原因，故本小節沿用前述之最佳參數 TiN4-3 製備中間層，再以不同溫度控制前趨液黏滯度塗佈於基材上，了解鑄膜液黏度對機械互鎖能力的影響。表 4-21 為 TiN4 基材塗佈不同黏滯度前趨液之樣品編碼。

表 4-21　TiN4 基材應用不同鑄模液黏度製備條件

Code	Preparation conditions
	Dope temperature (℃)
TiN4-10℃	10
TiN4-30℃	30
TiN4-50℃	50

4.6.1 鑄模液黏度分析

液體的黏度隨溫度的升高而下降（反之亦然），隨著溫度的升高，液體中分子運動的平均速度會增大，且與臨近分子的接觸時間變短。故本實驗控制鑄膜液的溫度以調整其黏度，探討不同黏度在進行旋轉塗佈時鑄膜液殘留於基材上的多寡與滲入情形對薄膜滲透選擇率的影響。從圖 4-43 可以看到，鑄膜液的黏度的確隨著溫度的增加而遞增，分別為 10℃時的 135.2 c.p.、30℃的 72.3 c.p.及 50℃的 31.6 c.p.。

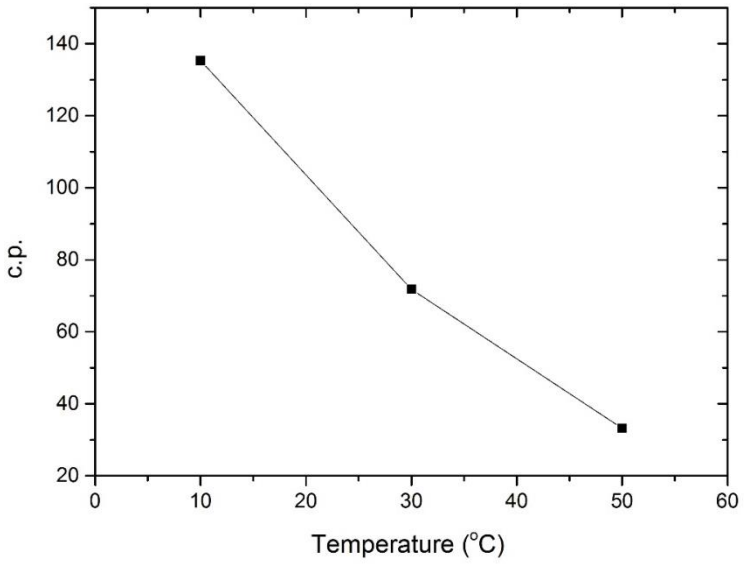

圖 4-43 不同控制溫度與鑄模液黏度的關係

4.6.2碳膜結構分析

4.6.2.1 膜層間距與膜厚分析

在本實驗中，是利用前述之最佳參數 TiN4-3 製備基材中間層，再以旋轉塗佈法塗佈高分子鑄膜液於基材上。在旋鍍時，高分子溶液滴在基材上，當啟動旋轉塗佈機時，在最初的短短 1~2 秒內，旋轉所產生的離心力與高分子溶液的黏滯力彼此互相抗衡，決定多少量的高分子溶劑會殘留在基材表面,因此當黏滯度高時,在進行塗佈的旋轉過程中，鑄膜液所含的溶劑也會隨之從表面開始揮發，而溶劑的揮發速率將影響薄膜的結構。當鑄膜液的溫度較高時，溶劑揮發速率較快，會使高分子被快速固化，造成薄膜會有厚薄不均勻的狀況，如圖 4-44(c)所示。反之當鑄膜液溫度較低時，溶劑揮發速率較慢，高分子鏈可以有較長的時間排列與形成較大的 nodule 後再固化,因此可以從表 4-22 中看到，其薄膜整體較為平整且 10℃形成的薄膜層間距也較高。

表 4-22 碳膜層間距與膜厚分析

code	Viscosity (c.p.)	Membrane thickness (μm)	d-spacing (Å)
TiN4-10℃	135.2	3.33	4.57
TiN4-30℃	72.3	3.60	4.34
TiN4-50℃	31.6	3.17	4.14

(a) TiN4-10^{o}

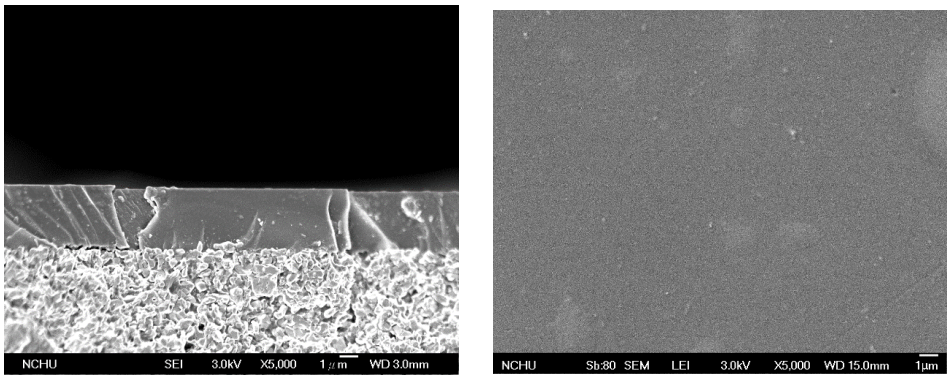

(b) TiN4-30^{o}

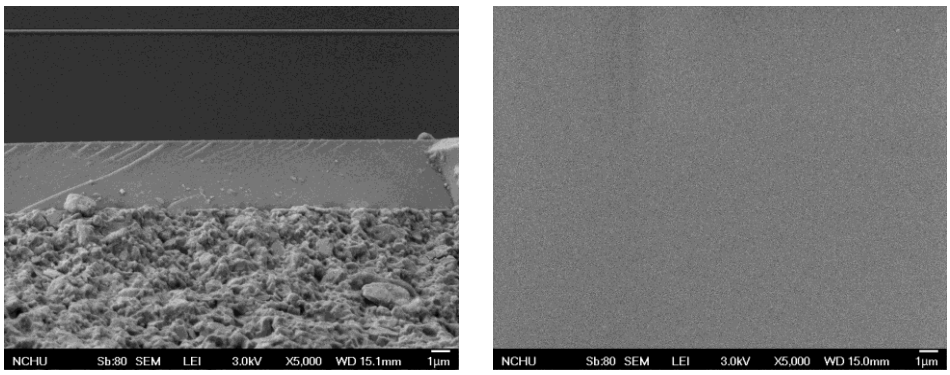

(c) TiN4-50^{o}

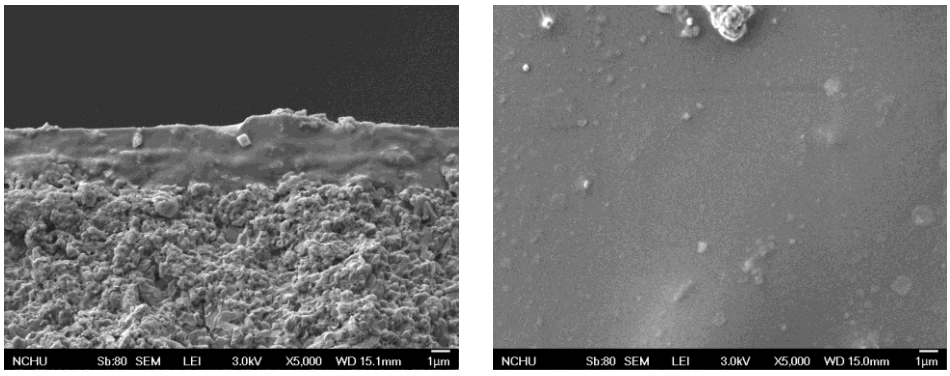

圖 4-44 以不同黏滯度之高分子前驅液製備而成的薄膜剖面及表面圖(a) TiN4-10^{o}、(b) TiN4-30^{o}、(c) TiN4-50^{o}。

4.6.2.2 機械互鎖能力評估

本研究利用 EDS 的 line scan 掃描薄膜側面圖，如圖 4-45 所示， 可明顯看到機械互鎖深度為 TiN4-50 ^{o} > TiN4-30^{o} > TiN4-10 ^{o}，這與前述所測得的黏滯度相關，當前趨液黏度越小，塗佈在基材時就容易滲入基材原始的孔洞中，而黏滯度越大時，因為溶液移動性降低，故滲入範圍會較低，而從圖 4-23 也可觀察到此情形。

(a)

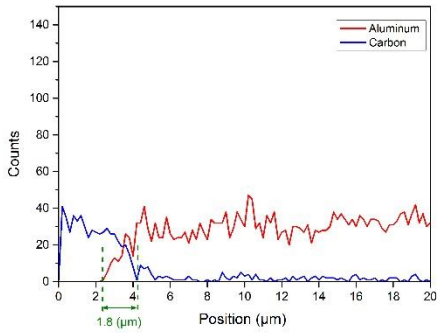

(b)

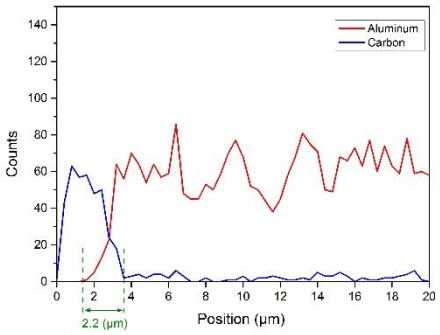

(c)

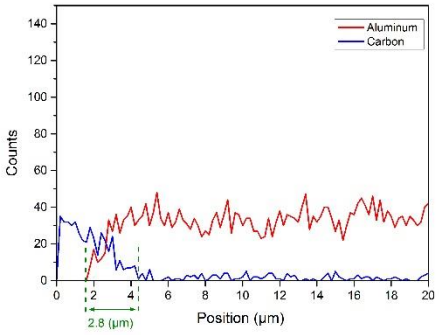

圖 4-45 不同基材製備之薄膜 EDS 側面掃描圖(a) TiN4-10^{o}、(b) TiN4-30 ^{o}、(c) TiN4-50^{o}。

4.6.3 氣體滲透選擇效能

我們可以從圖4-46觀察到，滲透率是隨著黏度增加而增加，而在本實驗中，是利用旋轉塗佈法進行鍍膜的動作，故在旋鍍過程中鑄膜液所含的溶劑也會隨之從表面開始揮發，Strawhecker [91]等學者也認為溶劑的揮發速率將影響薄膜的結構。當鑄膜液的溫度較高時，溶劑揮發速率較快，會使高分子鏈在伸展狀態即固化，因此形成的薄膜較為緻密，碳化後層間距值較小(如表4-22所示)，滲透率會較低，相反若溶劑揮發速率較慢，高分子之分子鏈有充分時間形成較大的nodule後再固化，因此製備出的薄膜會有較高的滲透率。另一方面，高分子溶液滴在基材上，當啟動旋轉塗佈機時，在最初的短短1~2 秒內，旋轉而產生的離心力與高分子溶液的黏滯力彼此互相抗衡，影響高分子鑄膜液在基材表

面的殘留量。因此當黏滯度高時，在進行塗佈的旋轉過程中，留在基材表面的鑄膜液較多，且較不容易滲入基材的孔洞之中。反之，則因為黏滯度過低而使溶液在旋轉時就被甩掉，也易滲入基材中。另外，滲透率也符合機械互鎖趨勢，當機械互鎖程度增加，接合程度也提高，使滲透率有逐漸下降的情形。

而在選擇率方面，我們進一步將所得到的選擇率與2008年的 Robeson's upper bound做比較，如圖4-47所示。從圖中發現TiN4-10°選擇率較低，這是因為鑄膜液處於低溫的情況下，溶劑揮發速率較慢，雖有較多的時間可以自我調整溶劑揮發產生的不穩定性，但因分子的流動性較低，一條分子鏈不易與另一條的分子鏈緊密的穿插、交纏在一起，再交纏的程度較低，經過碳化後產生可篩選氣體的超微孔含量較低，因此其分選效果較差。另外，TiN4-50°的選擇率也較30 °時低，此可能因碳膜層間距值較小，整體限制氣體的滲透率，因而使選擇率亦隨之損失。

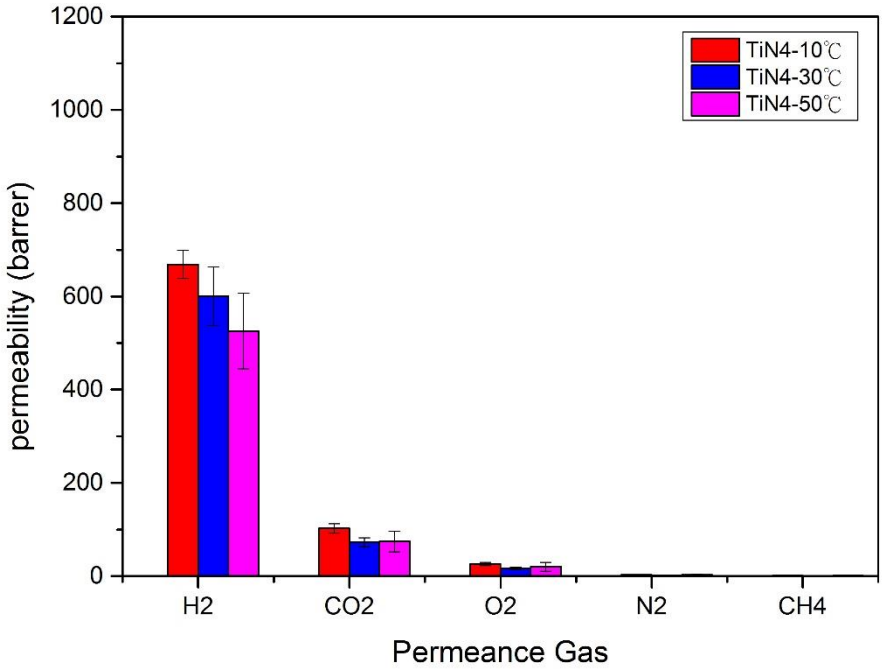

圖 4-46 不同黏滯度所製備之碳膜的氣體滲透率

(a) H_2/CH_4

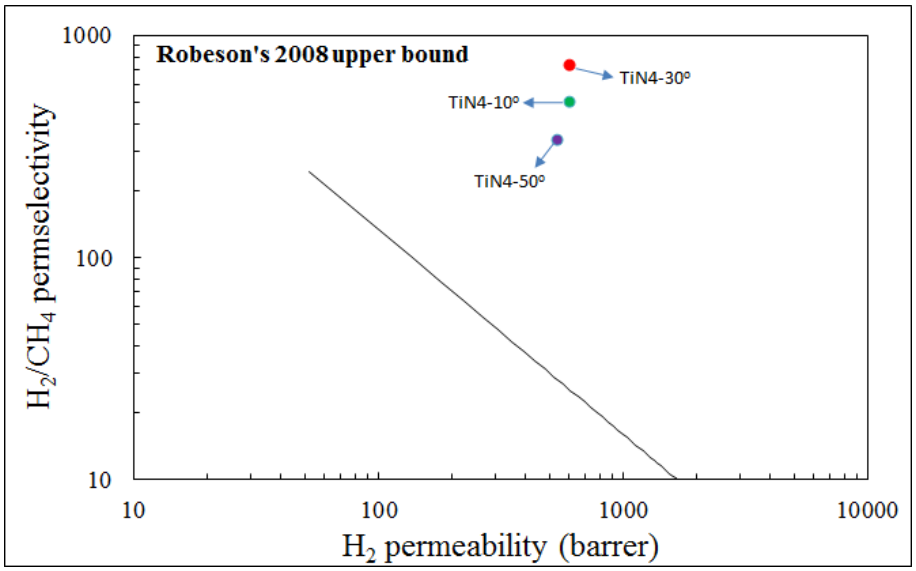

(b) H_2/CO_2

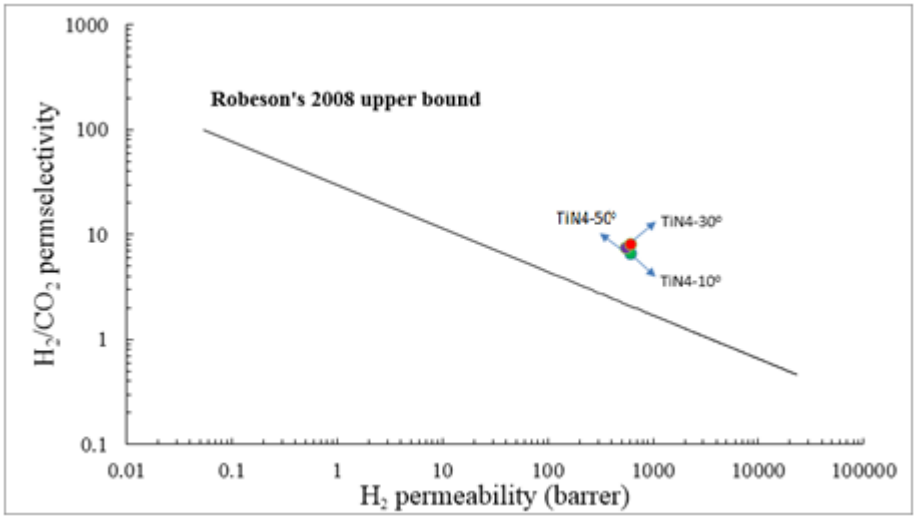

圖 4-47 不同製備條件之薄膜與 Robeson's 2008 upper bound 比較 (a)H_2/CH_4、(b)H_2/CO_2

4.6.4. 小結

本研究利用調整鑄膜液溫度，改變其黏滯度。在進行塗佈的旋轉過程中，旋轉所產生的離心力會與高分子溶液的黏滯力彼此互相抗衡，影響高分子鑄膜液在基材表面的殘留量。因此當黏滯度較低時，在進行塗佈的旋轉過程中，留在基材表面的鑄膜液較少，且因溶液移動性較高，容易滲入基材的孔洞之中，故滲入範圍會較多，使得互鎖效應較高，接合程度也增加，使滲透率有下降，反之當鑄膜液的溫度較高時，溶劑揮發速率較快，會使高分子鏈在伸展狀態即固化，因此形成的薄膜較為緻密，碳化後層間距值較小，滲透率會較低。綜合比較其選擇率，發現是在 30°C 有最好之效果，因為此時不會因為黏度太高使得無法平均披覆於基材表面，也不會因為鑄膜液在高溫下而使溶劑揮發太快，而造成缺陷。

五、 計畫總結

本研究計畫成功製備出具有良好分選效能的碳分子篩選膜，並在計畫第一年，探討鋁基材燒結溫度、升溫速率、熱沉溫時間等因子對鋁基材及碳膜孔徑分佈的影響。結果發現，氧化鋁基材的顆粒大小及孔隙分佈率是影響基材表面粗糙度的主要因素，亦是決定高分子鏈堆疊情形的重要因子，當基材孔隙率大且表面粗糙大時，由於高分子鏈的任意堆疊而造成空間效應，因此碳化後將產生較大的層間距而有利於氣體的擴散，但此時氣體的分選效果較不理想。相反地，在本研究發現經 1400 ^{o}C 熱處理後，鋁基材因形成十四面體結構而產生粗糙度低但具氣孔之結構，因此可提供碳膜高滲透率及高選擇率的分離特性。

另外，利用，MFI及TiO_2做為中間層進行修飾基材的表面。結果發現鋁基材以二次水熱法進行矽沸石之修飾後，碳膜的氣體滲透率與基材之總孔洞體積與d-spacing 值有關，導致大多數薄膜之滲透選擇效能有大幅提升的現象。因此，鋁基材以二次水熱法進行矽沸石之修飾後因可產生交聯作用而明顯地可同時提升氣體的滲透率與選擇率。而添加TiO_2後則可滲入基材孔隙中進行修飾，故可獲得較佳的機械強度，並隨著中間層層數增加，殘留在基材表面的TiO_2數量也隨之遞增，而使得化學鍵結強度上升，增強黏附效果，雖然滲透率下降，但可提升選擇率。增加兩相之間的黏附特性，讓披覆後的結構完整性提高，使得整體選擇率大幅增加，皆能超越Upper bound 標準，表示本研究所製備之碳膜皆以超越高分子膜的滲透率-選擇率平衡得失之限制。

研究中再利用拋光技術改變基材的粗糙度，進而了解其對薄膜層間距、機械互鎖及化學鍵結效應之影響。 研究結果發現，當粗糙度過大時，高分子鏈會因為基材表面高低起伏的結構，而排列凌亂導致層間距較大，選擇率較低；且較高的粗糙度亦會使TiO_2微粒滲入，減少與PEI高分子鍵氫鍵的形成，使得化學鍵結效應減少，最後因薄膜前趨液大量滲入形成缺陷，使滲透率上升、選擇率減少。因此，粗糙度為影響機械互鎖機制強弱的主要原因，故基材粗糙度應該控制在一定的範圍內，太大或太小皆會使其對薄膜產生不良效應。

最後，調整鑄膜液溫度，改變其黏滯度。結果發現在進行塗佈的旋轉過程中，旋轉所產生的離心力會與高分子溶液的黏滯力彼此互相抗衡，影響高分子鑄膜液在基材表面的殘留量。因此當黏滯度較低時，在進行塗佈的旋轉過程中，留在基材表面的鑄膜液較少，且因溶液移動性較高，容易滲入基材的孔洞之中，故滲入範圍會較多，使得互鎖效應較高，接合程度也增加，使滲透率有下降，反之當鑄膜液的溫度較高時，溶劑揮發速率較快，會使高分子鏈在伸展狀態即固化，因此形成的薄膜較為緻密，碳化後層間距值較小，滲透率會較低。綜合比較其選擇率，發現是在 30^{o}C 有最好之效果，因為此時不會因為黏度太高使得無法平均披覆於基材表面，也不會因為鑄膜液在高溫下而使溶劑揮發太快，而造成缺陷。

六、計畫結果自評

本研究成功的將利用高溫燒結與添加中間層的方式修飾基材，並製備出具有高效能的碳分子篩選薄膜。研究也證明添加中間層可有效地提升兩相間的黏附特性，確實能夠降低有機無機兩相因相分離產生的分選擇性間隙出現,使得分離效能能夠有良好的提升,符合本研究所預期的。另外,目前本研究也有部分成果已成功於 SCI 國際期刊發表 2 篇，另有 2 準備中，另投稿至 AMS7、AMS8、2012 環工年會、2012、2013、2014 環境保護與奈米科技學術研討會、ICOM2014 與 ICIM2014 共 8 篇。故已達到計畫預期目標，成功發展出高效能的碳分子篩選薄膜，期未來能應用於實廠。

七、 參考文獻

[1] 黃啟峰, 二氧化碳與地球暖化, 科學發展, 413 (2007) 6~12.
[2] I.E. Agency, Key World Energy Statistics, (2012).
[3] I.N.f.S. Energy, VISION 2050.
[4] R.A. Hefner Iii, The age of energy gases, International journal of hydrogen energy, 27 (2002) 1-9.
[5] A. Wolsky, E. Daniels, B. Jody, CO2 capture from the flue gas of conventional fossil-fuel-fired power plants, Environmental Progress, 13 (1994) 214-219.
[6] W. Salleh, A. Ismail, T. Matsuura, M. Abdullah, Precursor selection and process conditions in the preparation of carbon membrane for gas separation: A review, Separation & Purification Reviews, 40 (2011) 261-311.
[7] W. Wei, S. Xia, G. Liu, X. Gu, W. Jin, N. Xu, Interfacial adhesion between polymer separation layer and ceramic support for composite membrane, AIChE journal, 56 (2010) 1584-1592.
[8] M. Mulder, Basic Principles of Membrane Technology, Kluwer Academic Publishers, (1991).
[9] M. Mulder, Basic Principles of Membrane Technology Second Edition, Kluwer Academic Pub, 1996.
[10] W.B. Richard, Membrane technology and applications, John Wiley & Sons Ltd, (2004).
[11] A.A. Olajire, CO_2 capture and separation technologies for end-of-pipe applications–A review, Energy, 35 (2010) 2610-2628.
[12] Y. Xiao, B.T. Low, S.S. Hosseini, T.S. Chung, D.R. Paul, The strategies of molecular architecture and modification of polyimide-based membranes for CO_2 removal from natural gas—A review, Progress in Polymer Science, 34 (2009) 561-580.
[13] G. Lu, J. Diniz da Costa, M. Duke, S. Giessler, R. Socolow, R. Williams, T. Kreutz, Inorganic membranes for hydrogen production and purification: a critical review and perspective, Journal of colloid and interface science, 314 (2007) 589-603.
[14] A.S. Augustine, Y.H. Ma, N.K. Kazantzis, High pressure palladium membrane reactor for the high temperature water–gas shift reaction, International journal of hydrogen energy, 36 (2011) 5350-5360.
[15] C.-Y. Liang, P. Uchytil, R. Petrychkovych, Y.-C. Lai, K. Friess, M. Sipek, M. Mohan Reddy, S.-Y. Suen, A comparison on gas separation between PES (polyethersulfone)/MMT (Na-montmorillonite) and PES/TiO_2 mixed matrix membranes, Separation and Purification Technology, 92 (2012) 57-63.
[16] H.-J. Lee, H. Suda, K. Haraya, Characterization of the post-oxidized carbon membranes derived from poly (2, 4-dimethyl-1, 4-phenylene oxide) and their gas permeation properties, Separation and Purification Technology, 59 (2008) 190-196.

[17] Q. Liu, T. Wang, H. Guo, C. Liang, S. Liu, Z. Zhang, Y. Cao, D.S. Su, J. Qiu, Controlled synthesis of high performance carbon/zeolite T composite membrane materials for gas separation, Microporous and Mesoporous Materials, 120 (2009) 460-466.
[18] T.-H. Weng, H.-H. Tseng, M.-Y. Wey, Preparation and characterization of multi-walled carbon nanotube/PBNPI nanocomposite membrane for H_2/CH_4 separation, International journal of hydrogen energy, 34 (2009) 8707-8715.
[19] C. Zeng, L. Zhang, X. Cheng, H. Wang, N. Xu, Preparation and gas permeation of nano-sized zeolite NaA-filled carbon membranes, Separation and Purification Technology, 63 (2008) 628-633.
[20] H.-H. Tseng, P.-T. Shiu, Y.-S. Lin, Effect of mesoporous silica modification on the structure of hybrid carbon membrane for hydrogen separation, International journal of hydrogen energy, 36 (2011) 15352-15363.
[21] K. Briceño, D. Montané, R. Garcia-Valls, A. Iulianelli, A. Basile, Fabrication variables affecting the structure and properties of supported carbon molecular sieve membranes for hydrogen separation, Journal of Membrane Science, 415 (2012) 288-297.
[22] L. Shao, B.T. Low, T.-S. Chung, A.R. Greenberg, Polymeric membranes for the hydrogen economy: contemporary approaches and prospects for the future, Journal of Membrane Science, 327 (2009) 18-31.
[23] L. Shao, B.T. Low, T.-S. Chung, A.R. Greenberg, Polymeric membranes for the hydrogen economy: Contemporary approaches and prospects for the future, Journal of Membrane Science, 327 (2009) 18-31.
[24] M. Kiyono, P.J. Williams, W.J. Koros, Effect of polymer precursors on carbon molecular sieve structure and separation performance properties, Carbon, 48 (2010) 4432-4441.
[25] A.F. Ismail, 1.13 - Preparation of Carbon Membranes for Gas Separation, in: E. Drioli, L. Giorno (Eds.) Comprehensive Membrane Science and Engineering, Elsevier, Oxford, 2010, pp. 275-290.
[26] H. Yang, Z. Xu, M. Fan, R. Gupta, R.B. Slimane, A.E. Bland, I. Wright, Progress in carbon dioxide separation and capture: A review, Journal of Environmental Sciences, 20 (2008) 14-27.
[27] A.F. Ismail, L. David, A review on the latest development of carbon membranes for gas separation, Journal of membrane science, 193 (2001) 1-18.
[28] K.G.W. Jung C. H. , Han S. H., Lee Y. M., Gas Separation of Pyrolyzed Polymeric Membranes:Effect of Polymer Precursor and Pyrolysis Conditions, Macromolecular Research, 15 (2007) 565-574.
[29] S. Saufi, A. Ismail, Fabrication of carbon membranes for gas separation—a review, Carbon, 42 (2004) 241-259.

[30] Y. Kusuki, H. Shimazaki, N. Tanihara, S. Nakanishi, T. Yoshinaga, Gas permeation properties and characterization of asymmetric carbon membranes prepared by pyrolyzing asymmetric polyimide hollow fiber membrane, Journal of membrane science, 134 (1997) 245-253.
[31] M. Kiyono, P.J. Williams, W.J. Koros, Effect of pyrolysis atmosphere on separation performance of carbon molecular sieve membranes, Journal of Membrane Science, 359 (2010) 2-10.
[32] O.G. Nik, X.Y. Chen, S. Kaliaguine, Amine-functionalized zeolite FAU/EMT-polyimide mixed matrix membranes for CO2/CH4 separation, Journal of Membrane Science, 379 (2011) 468-478.
[33] H.-H. Tseng, I.A. Kumar, T.-H. Weng, C.-Y. Lu, M.-Y. Wey, Preparation and characterization of carbon molecular sieve membranes for gas separation—the effect of incorporated multi-wall carbon nanotubes, Desalination, 240 (2009) 40-45.
[34] A.L. Khan, A. Cano-Odena, B. Gutiérrez, C. Minguillón, I.F. Vankelecom, Hydrogen separation and purification using polysulfone acrylate–zeolite mixed matrix membranes, Journal of Membrane Science, 350 (2010) 340-346.
[35] A.K. Itta, H.-H. Tseng, M.-Y. Wey, Fabrication and characterization of PPO/PVP blend carbon molecular sieve membranes for H_2/N_2 and H_2/CH_4 separation, Journal of Membrane Science, 372 (2011) 387-395.
[36] S. Kumar, S. Srivastava, Y.K. Vijay, Study of gas transport properties of multi-walled carbon nanotubes/polystyrene composite membranes, International journal of hydrogen energy, 37 (2012) 3914-3921.
[37] F. Hamad, K. Khulbe, T. Matsuura, Comparison of gas separation performance and morphology of homogeneous and composite PPO membranes, Journal of membrane science, 256 (2005) 29-37.
[38] W. Yoshida, Y. Cohen, Ceramic-supported polymer membranes for pervaporation of binary organic/organic mixtures, Journal of membrane science, 213 (2003) 145-157.
[39] M. Rezac, W. Koros, Preparation of polymer–ceramic composite membranes with thin defect-free separating layers, Journal of applied polymer science, 46 (1992) 1927-1938.
[40] U. Beuscher, C. H Gooding, The influence of the porous support layer of composite membranes on the separation of binary gas mixtures, Journal of membrane science, 152 (1999) 99-116.
[41] X. Ding, Y. Cao, H. Zhao, L. Wang, Q. Yuan, Fabrication of high performance Matrimid/polysulfone dual-layer hollow fiber membranes for O_2/N_2 separation, Journal of Membrane Science, 323 (2008) 352-361.
[42] Y. Huang, R. Dittmeyer, Preparation of thin palladium membranes on a porous support with rough surface, Journal of Membrane Science, 302 (2007) 160-170.

[43] P. Kumar, J. Ida, S. Kim, V. Guliants, J. Lin, Ordered mesoporous membranes: Effects of support and surfactant removal conditions on membrane quality, Journal of Membrane Science, 279 (2006) 539-547.
[44] H. Qi, Y. Fan, W. Xing, L. Winnubst, Effect of TiO_2 doping on the characteristics of macroporous Al_2O_3/TiO_2 membrane supports, Journal of the European Ceramic Society, 30 (2010) 1317-1325.
[45] G. Li, H. Qi, Y. Fan, N. Xu, Toughening macroporous alumina membrane supports with YSZ powders, Ceramics International, 35 (2009) 1641-1646.
[46] M. Sadrzadeh, M. Amirilargani, K. Shahidi, T. Mohammadi, Gas permeation through a synthesized composite PDMS/PES membrane, Journal of Membrane Science, 342 (2009) 236-250.
[47] M.-Y. Wey, H.-H. Tseng, C.-k. Chiang, Improving the mechanical strength and gas separation performance of CMS membranes by simply sintering treatment of α-Al2O3 support, Journal of Membrane Science, 453 (2014) 603-613.
[48] A. Fuertes, T. Centeno, Preparation of supported asymmetric carbon molecular sieve membranes, Journal of membrane science, 144 (1998) 105-111.
[49] H.-J. Lee, M. Yoshimune, H. Suda, K. Haraya, Gas permeation properties of poly (2, 6-dimethyl-1, 4-phenylene oxide)(PPO) derived carbon membranes prepared on a tubular ceramic support, Journal of membrane science, 279 (2006) 372-379.
[50] F.-Z. Zhang, M. Fuji, M. Takahashi, In situ growth of continuous b-oriented MFI zeolite membranes on porous α-alumina substrates precoated with a mesoporous silica sublayer, Chemistry of materials, 17 (2005) 1167-1173.
[51] J. Di, C. Zhang, W. Yan, X. Wang, J. Yu, R. Xu, Direct in situ crystallization of highly oriented silicalite-1 thin films on a surface sol–gel process modified substrate, Microporous and Mesoporous Materials, 145 (2011) 104-107.
[52] Z. Lai, G. Bonilla, I. Diaz, J.G. Nery, K. Sujaoti, M.A. Amat, E. Kokkoli, O. Terasaki, R.W. Thompson, M. Tsapatsis, Microstructural optimization of a zeolite membrane for organic vapor separation, Science, 300 (2003) 456-460.
[53] J. Choi, S. Ghosh, Z. Lai, M. Tsapatsis, Uniformly a-Oriented MFI Zeolite Films by Secondary Growth, Angewandte Chemie, 118 (2006) 1172-1176.
[54] M. Kanezashi, J. O'Brien, Y. Lin, Thermal stability improvement of MFI-type zeolite membranes with doped zirconia intermediate layer, Microporous and mesoporous materials, 103 (2007) 302-308.
[55] J.L. Hang Chau, C. Tellez, K.L. Yeung, K. Ho, The role of surface chemistry in zeolite membrane formation, Journal of Membrane Science, 164 (2000) 257-275.
[56] H.W.a.K.S. Siow, Effects Of Interfacial Residual Stress On Tg Of Epoxy Resin, IEEWCPMT Electronic Packaging Technology Conference, (1997).

[57] G. LIU, W. WEI, W. JIN, N. XU, Polymer/ceramic composite membranes and their application in pervaporation process, Chinese Journal of Chemical Engineering, 20 (2012) 62-70.
[58] M.-Y. Wey, H.-H. Tseng, C.-k. Chiang, Effect of MFI zeolite intermediate layers on gas separation performance of carbon molecular sieve (CMS) membranes, Journal of Membrane Science, 446 (2013) 220-229.
[59] M. Ji, G. Liu, C. Chen, L. Wang, X. Zhang, Synthesis of highly b-oriented ZSM-5 membrane on a rough surface modified simply with TiO2 by in situ crystallization, Microporous and Mesoporous Materials, 155 (2012) 117-123.
[60] C. Constantin, V. Parvulescu, A. Bujor, G. Popescu, B.-L. Su, Mesoporous nickelsilicate membranes on porous alumina supports: I. Effect of nature and surface pretreatment of alumina supports on the catalytic membrane formation, Journal of Molecular Catalysis A: Chemical, 208 (2004) 245-252.
[61] H. Qi, S. Niu, X. Jiang, N. Xu, Enhanced performance of a macroporous ceramic support for nanofiltration by using α-Al2O3 with narrow size distribution, Ceramics International, 39 (2013) 2463-2471.
[62] L. Li, C. Song, H. Jiang, J. Qiu, T. Wang, Preparation and gas separation performance of supported carbon membranes with ordered mesoporous carbon interlayer, Journal of Membrane Science, 450 (2014) 469-477.
[63] W. Wei, G. Qin, H. Hu, L. You, G. Chen, Preparation of supported carbon molecular sieve membrane from novolac phenol–formaldehyde resin, Journal of Membrane Science, 303 (2007) 80-85.
[64] C. Song, T. Wang, H. Jiang, X. Wang, Y. Cao, J. Qiu, Gas separation performance of C/CMS membranes derived from poly (furfuryl alcohol)(PFA) with different chemical structure, Journal of Membrane Science, 361 (2010) 22-27.
[65] D.M. K. Briceño, R. Garcia Valls, A. Iuianelli, A. Basile, Fabrication Variables Affecting the Structure and Properties of Supported Carbon Molecular Sieve Membranes for Hydrogen Separation, Journal of Membrane Science, In press (2012).
[66] 汪建民, 陶瓷技術手冊, 粉末冶金協會出版, (1999).
[67] M. Ashby, A first report on sintering diagrams, Acta Metallurgica, 22 (1974) 275-289.
[68] 楊宸宇, 奈米級 α 相氧化鋁粉末燒結之研究, 成功大學資源工程學系學位論文, (2007) 1-81.
[69] 王一峰, α-Al2O3 微粉燒結行為的觀察, 成功大學資源工程學系學位論文, (2003) 1-61.
[70] J. Weitkamp, Zeolites and catalysis, Solid State Ionics, 131 (2000) 175-188.
[71] M. Gualtieri, Synthesis and characterization of zeolite films and membranes, (2006).
[72] M.E. Davis, R.F. Lobo, Zeolite and molecular sieve synthesis, Chemistry of Materials, 4 (1992) 756-768.

[73] T. Bein, Synthesis and applications of molecular sieve layers and membranes, Chemistry of materials, 8 (1996) 1636-1653.
[74] 徐政業, 粒徑均一之分散 silicalite-1 奈米結晶製備與鑑定; Synthesis of dispersed uniform-size silicalite-1 nanocrystals and its characterization, (2005).
[75] C.S. Cundy, P.A. Cox, The hydrothermal synthesis of zeolites: Precursors, intermediates and reaction mechanism, Microporous and Mesoporous Materials, 82 (2005) 1-78.
[76] P.P.E. de Moor, T.P. Beelen, B.U. Komanschek, L.W. Beck, P. Wagner, M.E. Davis, R.A. van Santen, Imaging the assembly process of the organic-mediated synthesis of a zeolite, Chemistry-A European Journal, 5 (1999) 2083-2088.
[77] B.J. Schoeman, Analysis of the nucleation and growth of TPA-silicalite-1 at elevated temperatures with the emphasis on colloidal stability, Microporous and Mesoporous Materials, 22 (1998) 9-22.
[78] 張馨方, 以二次生長法合成 MFI 薄膜探討表面型態與氣體滲透之研究, 中興大學環境工程學系所學位論文, (2010) 1-119.
[79] E. Bayrakdar, T. Gürkaynak Altınçekiç, M. Ö ksüzömer, Effects of PVP on the preparation of nanosized Al $_2O_3$ supported Ni catalysts by polyol method for catalytic partial oxidation of methane, Fuel Processing Technology, 110 (2013) 167-175.
[80] H. Cheng, J. Ma, Z. Zhao, L. Qi, Hydrothermal preparation of uniform nanosize rutile and anatase particles, Chemistry of Materials, 7 (1995) 663-671.
[81] N. Daud, B. Hameed, Decolorization of Acid Red 1 by Fenton-like process using rice husk ash-based catalyst, Journal of hazardous materials, 176 (2010) 938-944.
[82] 黃柄樺, 以可見光光觸媒對揮發性有機物之光催化研究, 中興大學環境工程學系所學位論文, (2008) 1-132.
[83] 鄭智鴻, 量身訂做的二氧化鈦光觸媒之合成及應用, 成功大學化學工程學系學位論文, (2006) 1-75.
[84] 林淑君, ZnWO4-TiO2 複合式光觸媒對亞甲基藍處理之研究, 屏東科技大學環境工程與科學系所學位論文, (2011).
[85] 杜怡君、張毓娟、翁乙壬、蘇怡帆、陳世毓、梁哲銘、葉巧雯、吳信璋、卓育泯, 磁性基本特性及磁性材料應用, 國立台灣大學化學系.
[86] O. Carp, C.L. Huisman, A. Reller, Photoinduced reactivity of titanium dioxide, Progress in solid state chemistry, 32 (2004) 33-177.
[87] C.J. Brinker, G.W. Scherer, Sol–gel science, 1990, New York, Academic Press., (1990).
[88] C. Hoogendam, J. Peters, R. Tuinier, A. De Keizer, M. Cohen Stuart, B. Bijsterbosch, Effective viscosity of polymer solutions: relation to the determination of the depletion thickness and thickness of the adsorbed layer of cellulose derivatives, Journal of colloid and interface science, 207 (1998) 309-316.

[89] P.S. Tin, T.S. Chung, Y. Liu, R. Wang, S.L. Liu, K.P. Pramoda, Effects of cross-linking modification on gas separation performance of Matrimid membranes, Journal of Membrane Science, 225 (2003) 77-90.
[90] L.M. Robeson, The upper bound revisited, Journal of Membrane Science, 320 (2008) 390-400.
[91] K.E. Strawhecker, S.K. Kumar, J.F. Douglas, A. Karim, The critical role of solvent evaporation on the roughness of spin-cast polymer films, Macromolecules, 34 (2001) 4669-4672.

Journal of Membrane Science 453 (2014) 603–613

Contents lists available at ScienceDirect

Journal of Membrane Science

journal homepage: www.elsevier.com/locate/memsci

Improving the mechanical strength and gas separation performance of CMS membranes by simply sintering treatment of α-Al_2O_3 support

Ming-Yen Wey [a], Hui-Hsin Tseng [b,c,*], Chian-kai Chiang [b,c]

[a] Department of Environmental Engineering, National Chung Hsing University, No. 250, Guoguang Road, South District, Taichung City, Taiwan, ROC
[b] School of Occupational Safety and Health, Chung Shan Medical University, No.110, Sec. 1, Jianguo N. Road, Taichung City, Taiwan, ROC
[c] Department of Occupational Medicine, Chung Shan Medical University Hospital, No.110, Sec. 1, Jianguo N. Road, Taichung City, Taiwan, ROC

ARTICLE INFO

Article history:
Received 5 September 2013
Received in revised form
25 October 2013
Accepted 22 November 2013
Available online 11 December 2013

Keywords:
Carbon membrane
Gas separation
Mechanical strength
Substrate
Sintering

ABSTRACT

Asymmetrical thin carbon molecular sieving (CMS) membranes exhibiting good mechanical strength and high separation performance were prepared by changing the physical properties of α-Al_2O_3 substrates. The physical properties of the substrates, such as pore size, pore volume and surface roughness, significantly influence the penetrability of polymer solution and were systematically modified by sintering temperature, heating rate and dwell time. The tetradecahedral shape of the substrate achieved at the sintering temperature of 1400 °C was found to be suitable for the prepared CMS membranes, which exhibited a H_2 permeability of 1300 Barrer with H_2/CH_4 and CO_2/CH_4 selectivities of 174.16 and 56.44, respectively. To optimize the substrate structure to provide a cost-effective and highly productive method for the deposition of brittle CMS membranes, this proposed procedure can be used to improve the mechanical strength of the supported membrane for enhanced manipulation.

1. Introduction

Due to the demand for gas separation and purification technologies [1–6], inorganic membranes, such as zeolites [7–9], carbon molecular sieving (CMS) membranes [10–12], and metallic Pd membranes, have progressively grown in prominence. These materials have molecular sieve structures, which have applications in hydrogen purification, carbon capture and oxygen/nitrogen separations.

CMS membranes are fabricated using an amorphous carbon matrix that derived from polymer precursor. These membranes exhibit hydrophobicity and thermostability and are resistant to corrosion from planar molecules (e.g., ethylene, formaldehyde, and benzene). The pore structure of CMS membranes consists of micro and ultramicro pores, which can improve diffusibility and ensure high selectivity, respectively [11,13,14]. However, the primary disadvantage that impedes their commercialization is their brittleness, which requires careful handling [15].

CMS membranes can be divided into symmetric and asymmetric types according to their structure or shape. The symmetric types generally have insufficient mechanical strength to meet the various demands for high productivity and efficiency in industrial applications [16]. In comparison, the asymmetric-type membranes typically consist of a support layer, a top layer, and/or intermediate layers, which are beneficial for producing thin, selective carbon layers [17–19] and allow excellent separation performance and long term operation [20,21]. Haar and Verweij [22] proposed that the mechanical stability of the deposited layers strongly depends on the properties of the substrate and should meet the following requirements: (1) a narrow pore size distribution, (2) the ability to withstand the operation temperature, (3) similar thermal and chemical expansion properties as the top layer, (4) a permeation mechanism that is independent of the mass transport resistance, and (5) sufficient mechanical strength. At present, numerous researchers have used different substrates to prepare CMS membranes, such as stainless steel, carbon substrate, and ceramic substrate. However, the effect of substrate properties on the mechanical stability and separation performance of CMS membranes have not been sufficiently discussed.

Several researchers are making efforts to estimate the influences of substrate properties, such as surface roughness and pore size distribution, on the polymer and metallic membrane fields. Hamad et al. [20] used porous polyethersulfone (PES) as a substrate to prepare polyphenylene oxide (PPO)/PES asymmetric polymer membranes. The greater surface roughness of the substrate caused the bottom of the selective layer to be closely conglutinated with the substrate, thereby improving the selectivity of the selective layer. Wei at al. [23] coated a polymeric membrane onto a ceramic substrate to overcome the expansion

* Corresponding author at: Department of Occupational Medicine, Chung Shan Medical University Hospital, No.110, Sec. 1, Jianguo N. Road, Taichung City, Taiwan, ROC. Tel.: +886 4 2473 0022; fax: +886 4 2324 8194.
E-mail address: hhtseng@csmu.edu.tw (H.-H. Tseng).

0376-7388/$ - see front matter © 2013 Elsevier B.V. All rights reserved.
http://dx.doi.org/10.1016/j.memsci.2013.11.039

phenomena. The expansion was limited using a cross-linking process, which strengthened the adhesion between the separation layer and the ceramic substrate, especially when the surface roughness of the ceramic substrate is greater. Huber et al. [24] explored the O_2/N_2 separation performance by polymer plasma deposition onto the alumina substrate. These researchers studied the effect of pore size distribution in the substrate and found that evenly distributed pore sizes led to enhanced carriers. Moreover, the even distribution of pore sizes enabled the membrane to completely cover the pores of the substrate during deposition. In combination with the above-mentioned results, the pore size distribution of the substrate is conducive to the formation of a thin, continuous and defect-free selective layer.

To strengthen the mechanical stability of CMS membranes, porous materials, such as alumina, are typically used as a substrate for membrane fabrication. According to previous work in our lab, when an alumina substrate with relatively large pore sizes was used, the polymer precursor easily penetrated into the substrate. Dense and defect-free carbon membranes were not easily obtained, as this process required several coatings to form a defect-free top layer. However, when an alumina substrate with relatively small pore sizes was used, the polymer precursors could not easily penetrate into the substrate, and the marginal adaptability between the top layer and the substrate was reduced, resulting in a decrease of the membrane selectivity. Therefore, when using alumina as the carbon substrate, an appropriate pore size distribution is essential to the construction of the asymmetric carbon membrane, allowing high permeability and selectivity to be obtained through a simple preparation process. Lin et al. [25] have studied and compared the effects of α- and γ-Al_2O_3 support on the separation performances of CMS membranes. The Al_2O_3 support possessing a smaller pore size and smoother surface might be helpful for forming a thinner and better quality of the membrane, due to the reduce of thermal expansion mismatch between the carbonizing layer and the alumina support during pyrolysis. However, the effect of pore size distribution of Al_2O_3 supports on the separation performance was not evaluated.

The pore structure of the alumina is mainly controlled by sintering conditions, such as sintering temperature, heating rate, and soaking time, which affects the particle arrangement and pore size distribution. Wang et al. [26] have evaluated the effect of sintering conditions on particle arrangement and pore size distribution of micro-sized alumina. The results indicated that after the sintering treatment, the alumina particles were coarser, and the pores became larger during the early stage. As the temperature increased to 1400 °C, the alumina particles were transformed to a vermicular shape (also known as a tetradecahedral shape). This structure was relatively loose, and the total pore volume was increased. When the temperature rose to 1500 °C, the alumina particles gradually became denser, resulting in a significant reduction in the total pore volume. The pore structure completely collapsed above 1600 °C.

To optimize the substrate structure, we modified the porous structure and surface roughness of the α-Al_2O_3 substrate by controlling the sintering conditions, including sintering temperature, heating rate, and soaking time. To prevent the gas transport resistance within the alumina substrate from increasing due to sintering at high temperatures, the sintering temperature was maintained below 1600 °C.

2. Experimental

2.1. Pretreatment of α-Al_2O_3 substrates

The green disk-shaped nanoceramic α-Al_2O_3 substrates with approximately 23-mm diameter and 1.4-mm thickness were purchased from Ganya Fine Ceramics Co., Taiwan. These green substrates were prepared by compressing α-Al_2O_3 powder (purity > 99.5, Japan) with particle sizes ranging from 0.1 to 2 μm. The surface morphology and X-ray diffraction pattern are shown in Fig. 1. These substrates were sintered in air in the 1100–1400 °C temperature range with a dwelling time of 2–3 h and a ramping rate of 1–10 °C/min. The sintered substrates are hereafter referred to as substrate SX–Y–Z, where X, Y, and Z are the sintering temperature, ramping rate, and dwelling time, respectively. In the course of the experiment, the substrate sintering temperature was kept below 1500 °C to prevent an increased substrate resistance to mass transfer, a result of the sintering process which results in an increased density that impacts the overall mass transfer behavior of the membrane.

2.2. Preparation of CMS membrane

The asymmetric CMS membrane was prepared by a spin-coating method previously described [27]. A 10% polyetherimide (PEI) solution was spin-coated at 1000 rpm for 20 s on a substrate surface. The coated supporting polymer film was left overnight at ambient temperature for solvent evaporation, which was followed by curing in a vacuum oven at 240 °C for 6 h at a heating rate of 5 °C/min. The film was subsequently heated to 600 °C at a rate of 5 °C/min and held at that temperature for 2 h. Subsequently, the membranes were slowly cooled to room temperature and were stored in a desiccator containing silica gel. Prior to aging decay, within 24 h, the membranes were subjected to a gas permeance test. Hereafter, the resultant CMS membranes are renamed by replacing the "S" in the original name of the corresponding substrate with an "M". For example, the carbon membrane fabricated with an S1100-1-2 substrate is designated as M1100-1-2.

2.3. Characterization of substrates and CMS membranes

The porous structures were measured using N_2 sorption at −196 °C with a PMI automated Brunauer–Emmett–Teller (BET) sorptometer (201AEL). The crystalline structure were recorded by X-ray diffraction (XRD) using a PW1830 X-ray powder diffractometer (Philips) with a Cu-K_α source ($\lambda = 1.5418$ Å) in a wide Bragg angle range ($20^\circ \le 2\theta \le 70^\circ$) with a 2°/min scanning rate. The surface roughness was measured by atomic force microscopy in the non-contact mode using a C26 Dualscope/Rasterscope scanner (DME, Denmark). The surface morphology and cross-sectional images were examined by field-emission scanning electron microscopy (FE-SEM; JSM 5600). The mechanical strength was measured by biaxial pressure mode.

2.4. Gas permeation test

The gas permeance experiments were performed using the steady-state gases H_2, CO_2, O_2, N_2, and CH_4 at room temperature (25 ± 2 °C). The permeate side of the membrane was degassed in a vacuum before testing, whereas a pressure of 2 atm was applied on the feed side. The gas permeance was calculated from the slope (dP/dt) of the plot of pressure (P) versus time (t) using the following equation:

$$\text{Permeability}, Q = \left(\frac{dP}{dt}\right) \times \frac{VT_0}{A\Delta P} \times \frac{L}{TP_0} \quad (1)$$

where dP/dt is the rate of pressure increase at steady state, V is the downstream gas permeation volume (in cm^3), A is the membrane area (in cm^2), ΔP is the differential pressure across the membrane, L is the membrane thickness (in cm), P_0 is 76 cm Hg, T_0 is 273 K, and T is the measured temperature (in K).

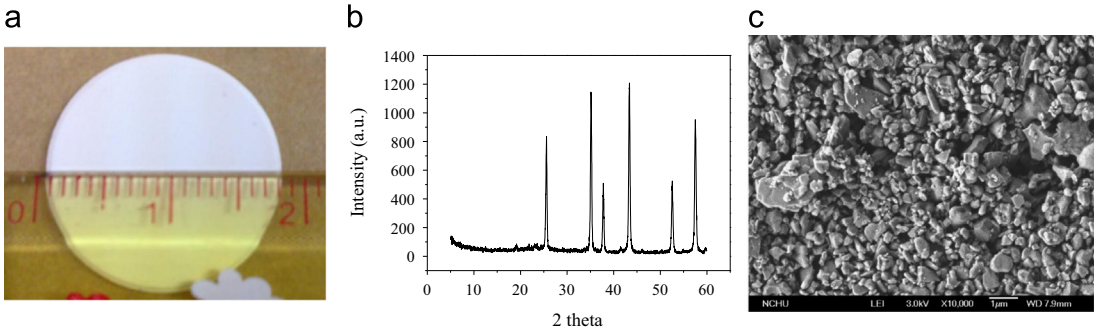

Fig. 1. (a) Surface morphology, (b) X-ray diffraction pattern, and (c) FE-SEM images of green disk-shaped α-Al_2O_3 supports. (For interpretation of the references to color in this figure legend, the reader is referred to the web version of this article.)

The ideal selectivity coefficient of pure gas A/B ($\alpha_{A/B}$) is defined as the ratio of the permeability of A to that of B:

$$\alpha_{A/B} = \frac{Q_A}{Q_B} \quad (2)$$

The average values and standard deviation were determined from six samples of two batches.

3. Results and discussion

3.1. Effect of the sintering conditions on the chemical-physical properties of the substrates

3.1.1. Crystal phase

The influence of the different sintering parameters on the crystal phase and crystal size of the alumina substrate is shown in Fig. 2 and Table 1. The crystal size, calculated by the diffraction patterns (use different sintering temperatures as examples) and Schere's formula, indicated that there was no significant change in the crystal phase and size of the alumina. Each substrate had a crystal size range of 34.1–38.0 nm and exhibited no change between different sintering conditions because the α-Al_2O_3 powder used for the spindles had already been subjected to a high temperature sintering process at 1600 °C. This temperature was higher than the sintering temperatures used in this study. Therefore, the crystal phase and size did not change significantly under different sintering conditions.

3.1.2. Pore structure

Table 1 shows the influence of the different sintering parameters on the specific surface area, average pore radius and pore volume of the substrates. It was found that as the sintering temperature increased from 1100 °C to 1400 °C, the specific surface area of the α-Al_2O_3 substrates decreased from 5.9 to 1.6 m^2/g. The average pore size increased from 78.63 to 107.40 Å. The pore volume decreased from 0.0116 to 0.0043 cm^3/g. The overall pore structure indicated an apparent loss as the sintering temperature increased. As shown in Fig. 3(a), the difference of pore volume was most significant for pore sizes between 15 and 40 Å. These observations indicate that the high sintering temperature results in a higher diffusion coefficient and thus accelerates the sintering of alumina substrates [27]. Based on the sintering theory model proposed by Ashby [28], the curvature around the neck of the alumina particles during the early stage of sintering and the high temperatures enabled the particles to diffuse. As a result, the contact surface between the alumina particles was slowly transformed into a neck shape during the early stage of sintering. At this stage, the pore shrank but remained in the open state. The same tendency is observed from past research [28]. As the

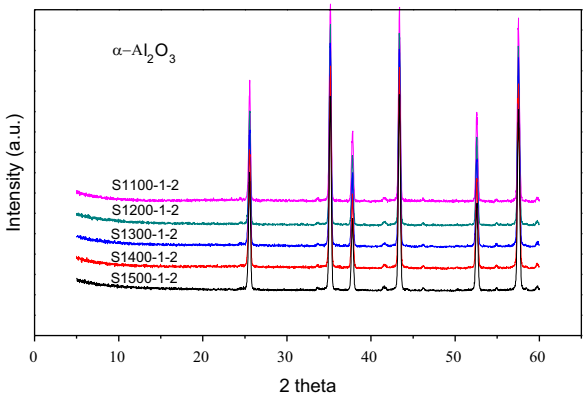

Fig. 2. X-ray diffraction pattern of α-Al_2O_3 supports sintered at different temperatures.

sintering temperature continued to rise to 1500 °C, all sintering diffusion mechanisms continued to occur. During this stage, interparticle pores developed on the edges and corners of the grains, making the movement of the grain boundary unfavorable. Therefore, at this stage, the grain growth was less obvious. The pore structure slowly disintegrated and gradually became smooth in shape. In addition, the grain was transformed into a 14-sided columnar body. The particles were fast-growing and tended to be dense (as shown in Table 1, the pore structure could not be measured by an analyzer). This phenomenon can be clearly observed in the FE-SEM images in Fig. 4, which demonstrate that the alumina particles diffused into larger particles. The contact surface of the particles increased significantly, resulting in decreases of the specific surface area and the overall pore volume.

The influence of the sintering heating rate on the pore structure of alumina was also significant. As shown in Table 1 and Fig. 3(b), when the heating rate was reduced from 10 °C/min to 1 °C/min, the specific surface area was clearly observed to decrease. In addition, the average pore diameter increased, and the pore volume decreased. This trend is also observed when the sintering temperature is increased. This phenomenon could be explained in that the slow heating rate helped the alumina particle transform into a tetradecahedral shape, resulting in the apparent loss of the pore structure. This result was consistent with the FE-SEM image. Fig. 4(d) and (f)–(h) shows that the particle size increased when the heating rate was decreased.

The influence of the dwell time on the pore structure and pore size distribution of the alumina substrate is shown in Table 1 and Fig. 3(c). When the dwell time increased from 2 to 3 h, there was no significant difference in the specific surface area, pore volume and pore diameter distribution. It is possible that the selected

Table 1
Effect of sintering conditions on chemical-physical properties of α-Al_2O_3 supports.

Code	Crystal size (nm)	S_{BET} (m^2/g)	D_{pore} (Å)	V_{total} (cm^3/g)	BJH adsorption cumulative pore volume of pores between 13.5 and 1000 Å (cm^3/g)		
					V_{micro}	V_{meso}	V_{macro}
S1100-1-2	34.1	5.9	78.63	0.0116	0.0021	0.0082	0.0011
S1200-1-2	35.9	4.3	76.54	0.0084	0.0017	0.0058	0.0008
S1300-1-2	35.9	3.1	80.16	0.0061	0.0011	0.0044	0.0005
S1400-1-2	37.5	1.6	107.40	0.0043	0.0005	0.0033	0.0003
S1500-1-2	38.0	N.D.	N.D.	N.D.	N.D.	N.D.	N.D.
S1400-2-2	36.8	4.3	74.22	0.0080	0.0011	0.0063	0.0005
S1400-5-2	36.3	5.2	66.48	0.0087	0.0012	0.0062	0.0005
S1400-10-2	36.5	5.2	66.00	0.0086	0.0012	0.0068	0.0005
S1400-2-3	36.0	4.3	74.10	0.0080	0.0011	0.0062	0.0005

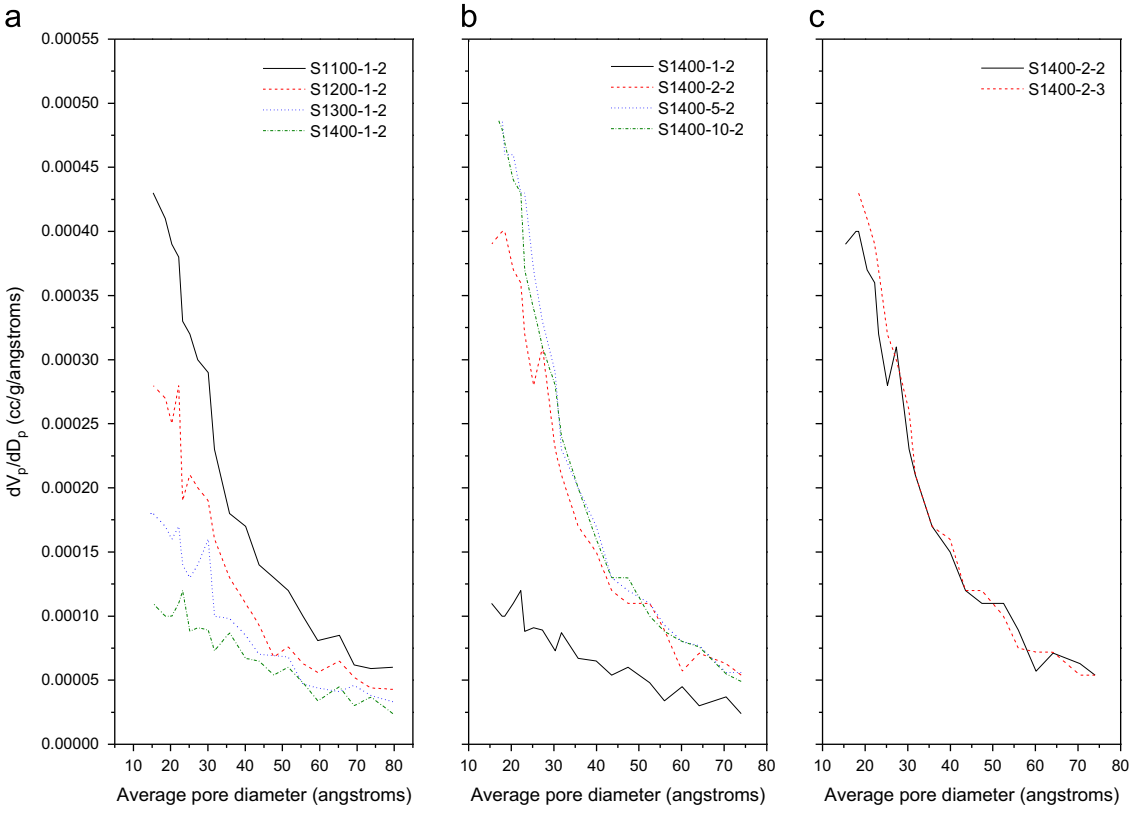

Fig. 3. Effects of (a) sintering temperature, (b) heating rate, and (c) dwell time on the pore size distribution of α-Al_2O_3 substrates.

dwell times were sufficiently similar for the influence of the dwell time on the pore structure not to be observable.

3.1.3. True density and volume shrinkage

Fig. 5 shows the substrate volume shrinkage of as a function of sintering temperature. It was observed that the substrate volume shrinkage increased as the sintering temperature increased from 0.55% (1100 °C) to 16.55% (1500 °C). Under the different sintering temperatures, the volume shrinkage rate can be divided into two stages: (1) first, as the temperature increased from 1100 to 1400 °C, higher shrinkage rate was exhibited due to particle coarsening; (2) second, as the temperature increased from 1400 to 1500 °C, a lower shrinkage rate was observed due to the green body densification.

3.1.4. Surface roughness

Fig. 6 shows the AFM images of the alumina substrates treated under different sintering conditions. When the sintering temperature of the substrate increased from 1100 to 1500 °C, the surface roughness coefficient (Ra) of the substrate increased from 38.8 to 103.0 nm. The increased surface roughness could be a result of alumina particle coarsening and densification, causing the surface roughness coefficient to increase as the sintering temperature increased.

With the sintering temperature fixed at 1400 °C and the heating rate reduced from 10 to 2 °C/min, the surface roughness coefficient of the substrate decreased from 67.6 to 42.8 nm. The slow heating rate provided the alumina particles with enough heat energy to transform into a tetradecahedral structure. Therefore, the substrate surface became relatively homogeneous when the heating rate was decreased. However, when the heating rate was further decreased to 1 °C/min, the surface roughness coefficient increased from 42.8 to 69.7 nm because the relative surface roughness became heterogeneous when the alumina density increased. Table 2 summarizes similar results obtained from different dwell time conditions. When the sintering temperature and heating rate were fixed at 1400 °C and 2 °C/min, respectively,

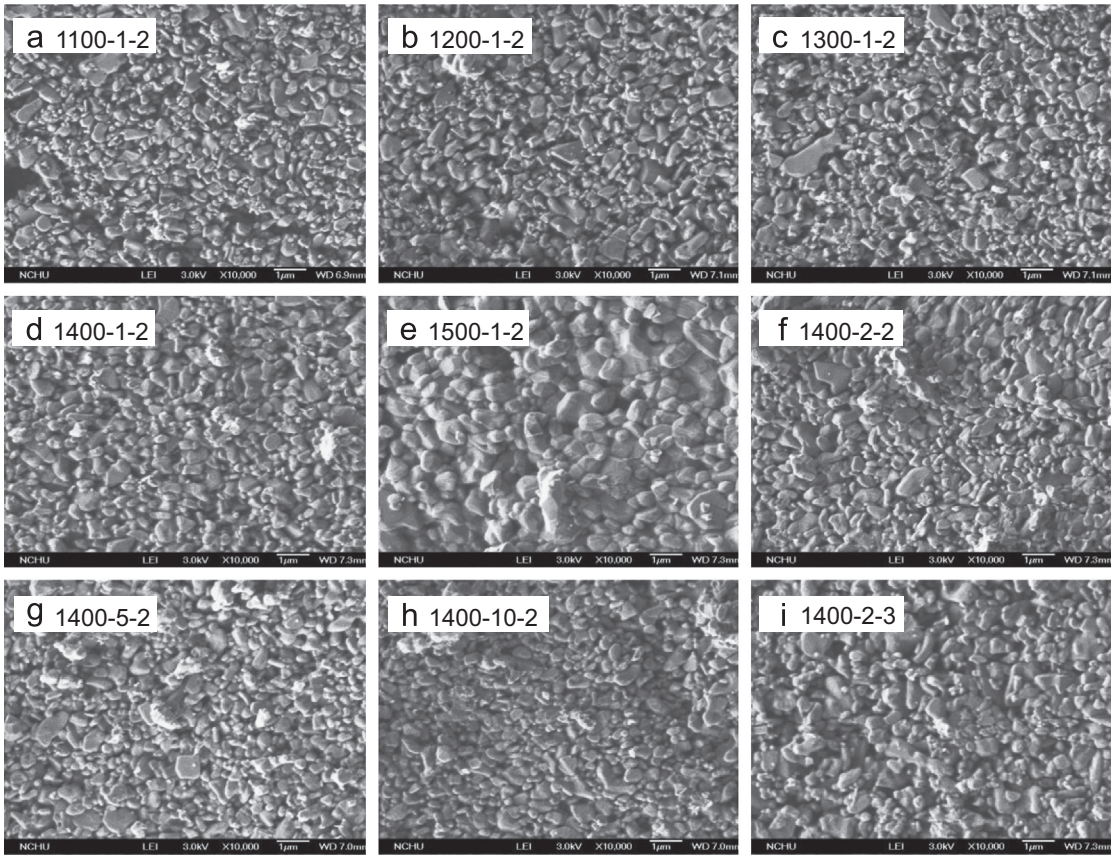

Fig. 4. FE-SEM images of α-Al_2O_3 substrates treated under different sintering conditions.

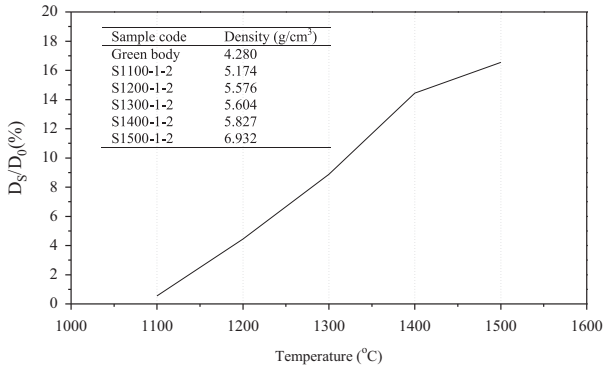

Fig. 5. Volume shrinkage of substrates as a function of sintering temperature.

the surface roughness coefficient increased from 53.1 to 75.5 nm when the dwell time increased from 2 to 3 h. A relatively extended dwell time increased the degree of coarsening for the alumina particles, making the surface of the substrate relatively heterogeneous and thereby enhancing the surface roughness coefficient.

The XRD, BET, FE-SEM and AFM results are integrated in a schematic diagram in Fig. 7 to exhibit the change in the alumina substrate structure with respect to sintering temperature. The particle sintering behavior can be divided into three heating stages: (1) from ambient to 1300 °C, the alumina particles coarsened and were subsequently restacked, leading to a reduced pore volume and increased surface roughness. (2) When the temperature was elevated to 1400 °C, the alumina particles started to change to the tetradecahedral shape and increased in density. Consequently, the pore volume decreased. The surface roughness continued to increase due to tetradecahedral particle aggregation. (3) When the temperature rose to 1500 °C, the alumina particles became very dense, resulting in a notably low substrate pore volume. The surface roughness was also relatively heterogeneous. Therefore, a series of phenomena associated with the increased sintering temperature (including particle growth, coarsening and densification) was the main reason for the increase in the surface roughness and decrease in the pore volume.

3.2. *The characterization of the α-Al_2O_3 supported CMS membrane*

3.2.1. *The morphology and d-spacing of the carbon matrix*

The FE-SEM microphotographs of CMS membranes supported on different α-Al_2O_3 substrates are shown in Fig. 8. It can be observed that these surface images show a smooth, almost defect-free morphology (Fig. 8(a1)–(i1)). Carbon layers with dense matrix structures were sequentially deposited on the α-Al_2O_3 substrates, even under different sintering conditions. Furthermore, good adherence between the top layer and the alumina substrate was observed. The thickness of the PEI-derived carbon layers approximately measured 2.9–5.6 μm (as shown in Table 3). The highest thickness (5.550 μm) of the CMS layer was obtained from the M1500-1-2 membrane.

The d-spacing of carbon membranes refers to the interlayer distance of the carbon matrix and can also be considered to be the pore size relevant for the transport of gas molecules through the carbon membranes. As indicated in Table 2, the change in the d-spacing of the carbon membranes showed a bimodal trend when the sintering temperature of the substrate was increased from 1100 °C to 1500 °C. The d-spacing values of M1200-1-2 and M1400-1-2 were larger than that of other membranes. This phenomenon was significantly different than other trends: with increasing sintering temperature, reduced specific surface area

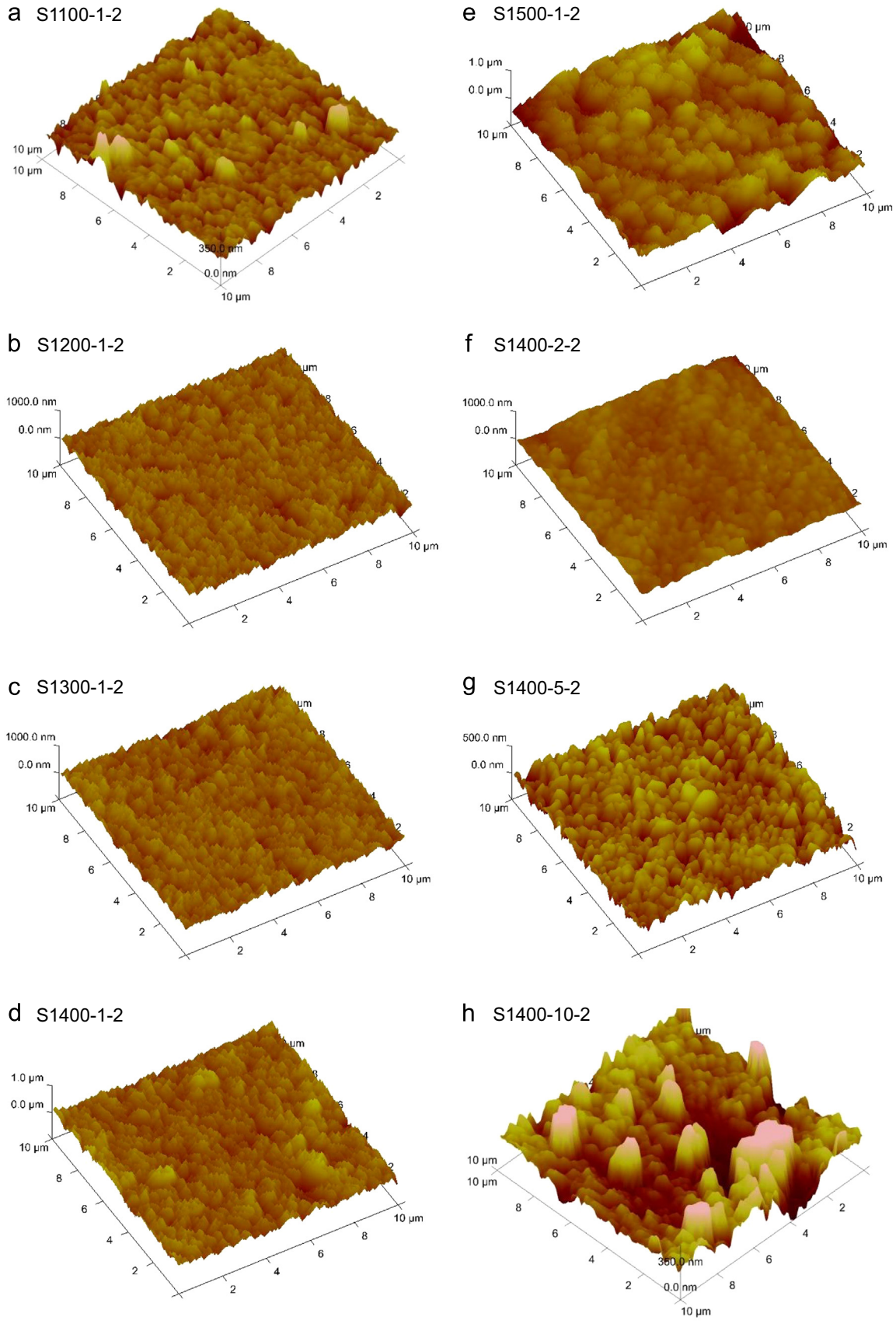

Fig. 6. AFM images of α-Al_2O_3 substrates treated under different sintering conditions.

and total pore volume or increased average pore size and surface roughness were observed, as described above for the alumina substrate. Note that this finding cannot be explained by random occurrence because the permeability through these membranes are strongly correlated with the d-spacing value (see Section 3.3). Several effects could be responsible for the observed bimodal-type

d-spacing value. Because d-spacing value is the distance between the stacked carbon matrix layers, it directly affects by the physical properties of the alumina substrate. Therefore, it can be inferred that the trends observed in the d-spacing values are caused by the combined effects of both pore structure and surface roughness of α-Al_2O_3 substrates. Theoretically, the interlayer distance of the carbon matrix was formed from the gap generated after pyrolysis when the aromatic compounds were irregularly stacked on the polymer precursor-coated substrate, thereby determining by the pore structure and the surface roughness of the substrate. Generally speaking, when the pore sizes of the substrate are larger, the casting dope more readily penetrates into the pores of the substrate during the coating process. The casting dope is deposited not only on the surface but also within the pores, resulting in a strong mechanical interlock (see. Section 3.2.2.) with the substrate, which leads to larger d-spacing values. In contrast, with smaller pores, casting dope less readily penetrates into the substrate, resulting in a relatively thick membrane and relatively smaller d-spacing values (e.g., M1500-1-2). The surface roughness also exerts significant influence on the d-spacing values. When the substrate surface is rougher, the folding of the polymer chains is more irregular and prominent, resulting in a larger interlayer distance after carbonization. Therefore, it is expected that the d-spacing values exhibit a bimodal trend due to the combined effects of the reduced substrate pore structure and the increased surface roughness.

The above assumptions can be verified by the results obtained from the substrates treated with different dwell times and heating rates. As indicated in Table 2, the surface roughness of the alumina substrate can be increased by controlling the dwell time while maintaining a constant pore structure. The d-spacing also increases with increasing roughness when the pore structure remains unchanged. For heating rates in the range of 2–10 °C/min, the pore structure, surface roughness and d-spacing all decrease when the heating rate is reduced. Therefore, a decrease in the pore structure also decreases the d-spacing.

3.2.2. *Mechanical strength*

Fig. 9 shows the mechanical strength measured by the bi-axial method. The average strength of 185 N is high enough when compared with that of conventional alumina ceramics. It was

Table 2
d-Spacing, surface roughness, and membrane thickness of CMS membranes supported on various α-Al_2O_3 supports.

Sample code	Membrane thickness (μm)	d-Spacing (Å)	Ra of support (nm)	Ra of membranes (nm)
M1100-1-2	4.237	4.47	38.8	55.3
M1200-1-2	4.219	4.51	57.2	73.6
M1300-1-2	3.722	4.32	60.4	48.3
M1400-1-2	4.144	4.64	69.7	64.2
M1500-1-2	5.550	4.02	103.0	123.0
M1400-2-2	4.800	4.32	42.8	44.4
M1400-5-2	4.500	4.62	61.0	92.0
M1400-10-2	4.313	4.76	67.6	107.0
M1400-2-3	2.981	4.64	59.4	52.9

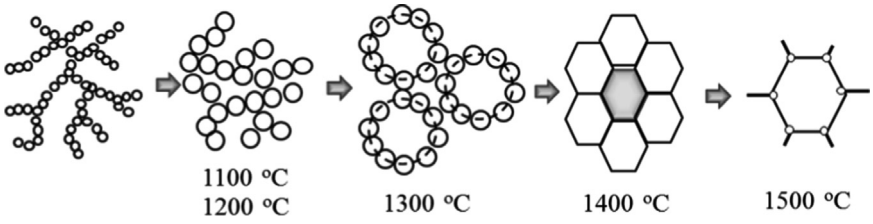

Fig. 7. Schematic of the changing in the alumina substrate structure with respect to sintering temperature (adapted from ref [27]).

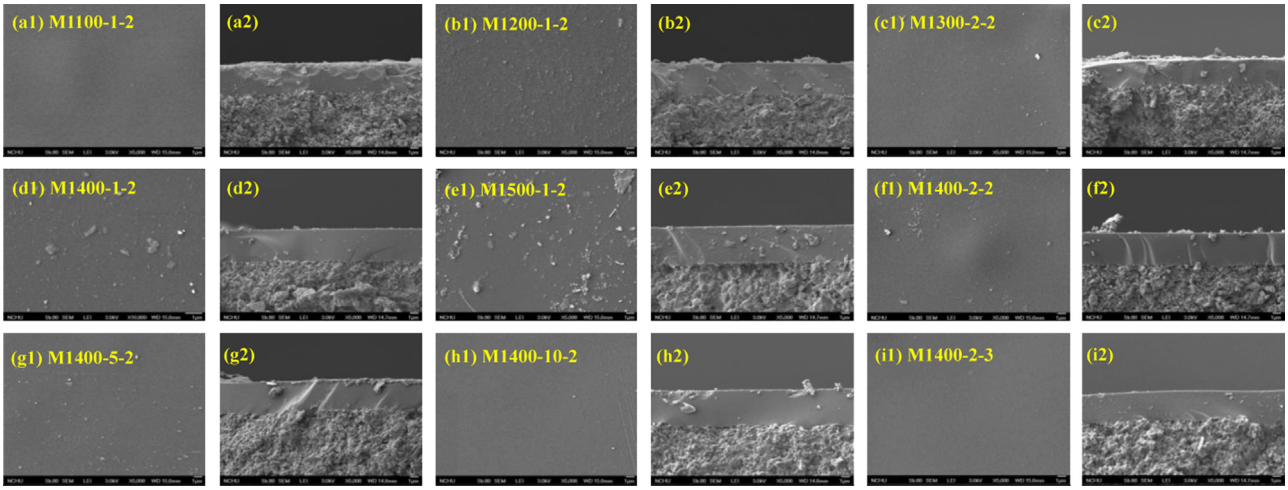

Fig. 8. FE-SEM images of (1) surface view and (2) cross-sectional view of CMS membranes supported on various γ-Al_2O_3 substrates.

found that the strength of M1400-2-3 was higher than the other three membranes. This could be explained by average pore size, that it is resulted from the effect of sintering pretreatment, i.e., a suitable sintering treatment is required in the improving the mechanical strength of α-Al_2O_3 supported CMS membranes.

3.3. Gas separation performance

Fig. 10 and Table 3 present the effects of substrate properties on the performance of the CMS membranes based on the pure gas permeation rate and permselectivity for the gas pairs of H_2/CH_4, CO_2/CH_4, and O_2/N_2 against (a) sintering temperature, (b) heating rate, and (c) dwell time, respectively. As shown in Fig. 10, it can be observed that the gas permeability increased with the gas kinetic diameter in the following order: $H_2 > CO_2 > O_2 > N_2 > CH_4$. This observation is consistent with the mechanisms of molecular sieving.

The effect of the substrate sintering temperature on the gas permeability is shown in Fig. 10(a). Based on the estimated membrane thicknesses given in Table 2, the hydrogen permeabilities at 25 °C are 2112.2, 2304.38, 385.71, 1532.34, and 102.67 Barrer for membranes M1100-1-2, M1200-1-2, M1300-1-2, M1400-1-2, and M1500-1-2, respectively. It seems that the trend in the gas permeability was consistent correlated with the d-spacing value, where the gas permeability increased as the d-spacing increased, and the gas permeability decreased as the d-spacing decreased. Previously study also indicated that a similar trend was observed when the d-spacing value was changed [29]. The gas diffusion path increased with increasing d-spacing, which results in high permeability. The effects of the sintering heating rate and dwell time of the substrate on the gas permeability are shown in Fig. 10(b) and (c). These figures also show that the gas permeability increased as the d-spacing increased.

The gas pair selectivities of CMS membranes supported on substrates treated with different sintering temperatures are indicated in Table 3. Comparison of the selectivity of CMS membrane with sintering temperature indicates increases as high as 11.3 times in the H_2/CH_4 separation factor for the membrane supported on the S1400-1-2 substrate compared to that on the S1100-1-2 substrate. The observed increases in permselectivity are significantly larger than those expected from other sintering temperatures; similar results were also observed for the gas pairs CO_2/CH_4 (20.6 times) and O_2/N_2 (4.7 times). The sintering of α-Al_2O_3 substrates at the high temperature of 1400 °C appears to be a contributing factor to the increases in the selectivities of the CMS membranes.

The hypothetical path of a gas molecule permeating through the carbon film on the sintered substrate is depicted in Fig. 11. The route has three identifiable regions: the carbon film on the surface, the carbon matrix in contact with alumina (i.e., carbon matrix penetration into the substrate, see Fig. 12), and the pore of substrate. As mentioned above, the influence of sintering is expected to be primarily centered around the carbon matrix in the first two regions. The resistance model is utilized to assess the effect of the penetration of the carbon matrix into the pores of the

Table 3
Gas pair selectivity of CMS membranes supported on α-Al_2O_3 substrates treated with different sintering conditions.

Sample code	Selectivity		
	H_2/CH_4	O_2/N_2	CO_2/CH_4
M1100-1-2	5.94 ± 1.27	1.15 ± 0.16	1.51 ± 0.48
M1200-1-2	5.06 ± 1.76	1 ± 0.04	1.4 ± 0.38
M1300-1-2	17.05 ± 3.44	2.38 ± 0.55	5.21 ± 0.65
M1400-1-2	67.31 ± 4.61	5.41 ± 0.46	31.08 ± 10.05
M1500-1-2	9.05 ± 6.20	1.51 ± 1.12	1.86 ± 1.40
M1400-2-2	174.16 ± 39.05	8.05 ± 0.81	56.44 ± 8.9
M1400-5-2	89.32 ± 6.41	6.73 ± 1.43	28.63 ± 3.64
M1400-10-2	57.66 ± 18.20	5.12 ± 0.96	18.39 ± 2.79
M1400-2-3	76.35 ± 14.21	5.73 ± 0.50	25.44 ± 3.66

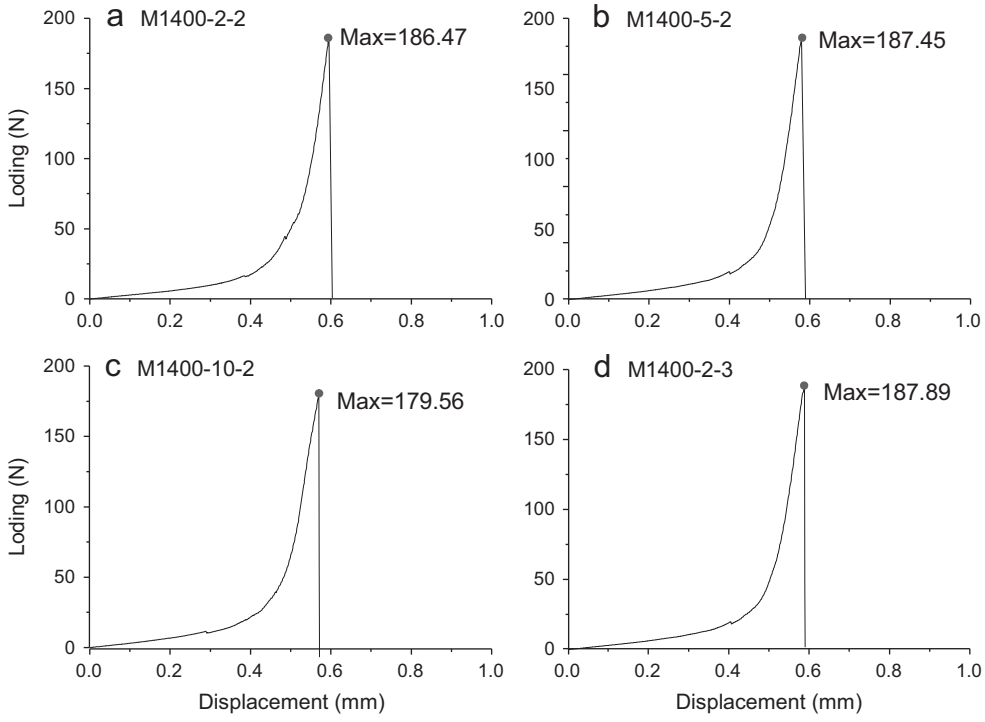

Fig. 9. Mechanical strength of CMS membrane supported on various supports.

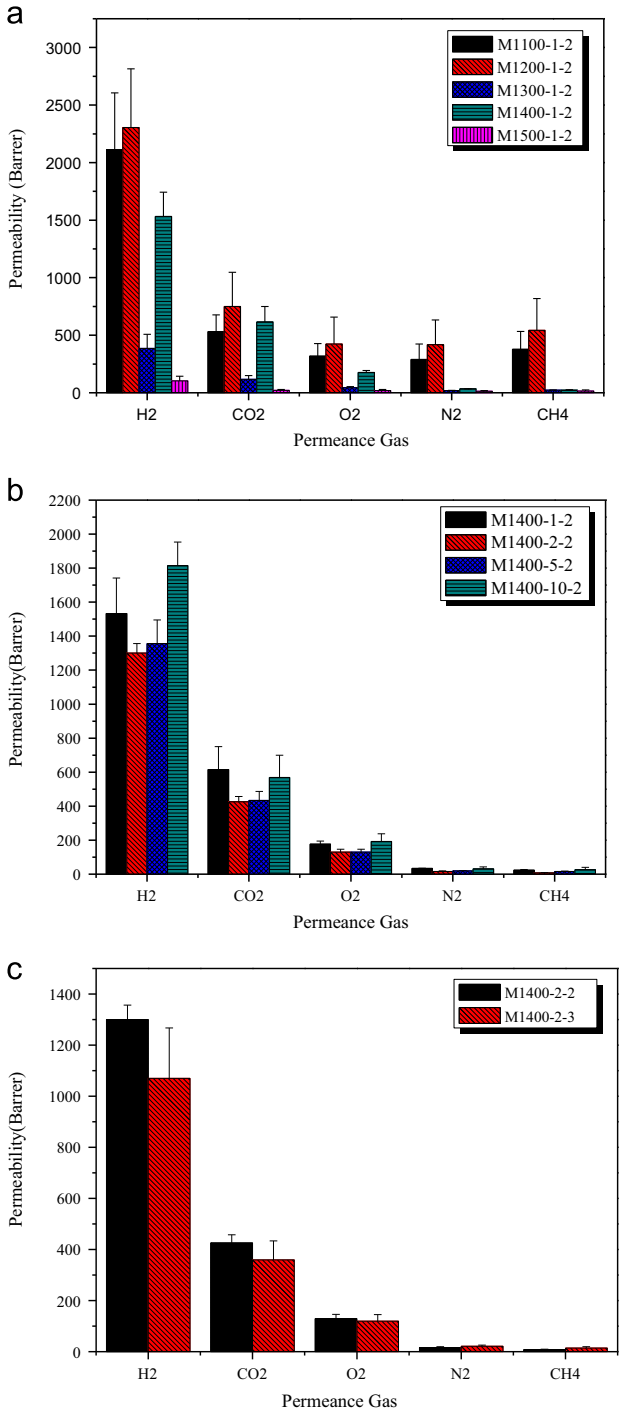

Fig. 10. Gas permeability of CMS membranes supported on α-Al_2O_3 substrates treated with different (a) sintering temperatures, (b) heating rates, and (c) dwell times.

different substrates on the overall performance of the supported membranes [20,30]. The overall resistances of the supported CMS membranes are defined by the following equations:

$$R_T = R_1 + R_2 + R_3 \tag{3}$$

$$\frac{\ell_T}{P_T} = \frac{\ell_1}{P_1} + \frac{\ell_2}{P_2} + \frac{\ell_3}{P_3} \tag{4}$$

where ℓ is the thickness of carbon layers, P is the permeability, and the suffixes 1, 2, and 3 of ℓ and P are the permeance routes. The resistance of the substrate, ℓ_3/P_3, is assumed to be negligible because the treated substrate still retains a fairly high flux P_3 value, indicating insignificant resistance to gas flow (no observable significant difference was recorded for the gas flux prior to and after sintering). Therefore, the overall resistance of the supported CMS membrane is integrated with the resistance of the carbon film on the surface and the resistance of the carbon film penetration into the substrate. Therefore, based on Eq. (4), a reduction of the thickness of the surface film should further increase the overall selectivity of the supported membrane. This effect was verified by Moaddeb and Koros [30]. They systematically reduced the thickness of the polymer membrane by changing the concentration of the casting dope. As the amount of the deposited polymer was reduced, the separation factor of the membrane increased. However, for the supported membrane, the actual effective thickness, $\ell_1+\ell_2$, is not precisely known due to the penetration of carbon matrix into the pores of the substrate. The sintering of the α-Al_2O_3 substrates increased the average pore size but also reduced the pore volume inside the pores; therefore, even a small amount of polymer could enter the substrate pores. Table 2 presents the "apparent thickness" of film on the surface, as measured from the FE-SEM images of the cross sections of the supported membranes. The results indicated that the apparent thickness was decreased when the sintering temperature increased to 1300 °C, and subsequently increased by 1500 °C. In contrast with the pore size and pore volume illustrated in Table 1, the larger pore size was helpful for polymer penetration into the pores, but the penetrating amount of polymer was restricted by the total pore volume, Therefore, the smallest thickness was obtained from M1300-1-2 due to its larger pore size but not the smallest pore volume. The penetrated carbon matrix is in contact with α-Al_2O_3 particles to increase mechanical interlocking, which has a higher permselectivity than the surface carbon membrane. So a reduced surface film thickness will increase the contribution from the more selective composite layer. It was for this reason that the selectivity of the membranes initially increased with sintering temperature followed by a decrease in value.

For practical application, an increase in selectivity accompanied by an unapparent loss in permeability is expected. However, the M1400-1-2 membrane exhibits the highest selectivity, but a loss in permeability was still observed. Even considering these values of gas permeability, the separation performances of the CMS membrane supported on S1400-1-2 substrates are improved by raising

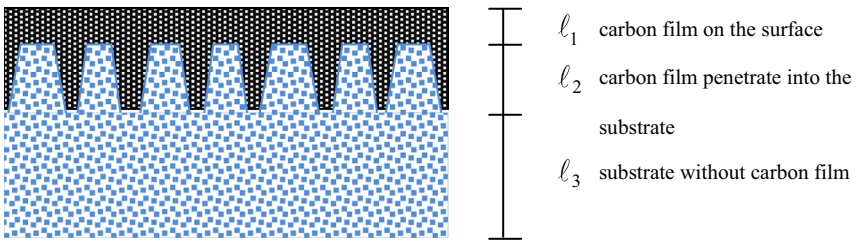

Fig. 11. The hypothetic path of a gas molecule permeating through the carbon film on the sintered substrate.

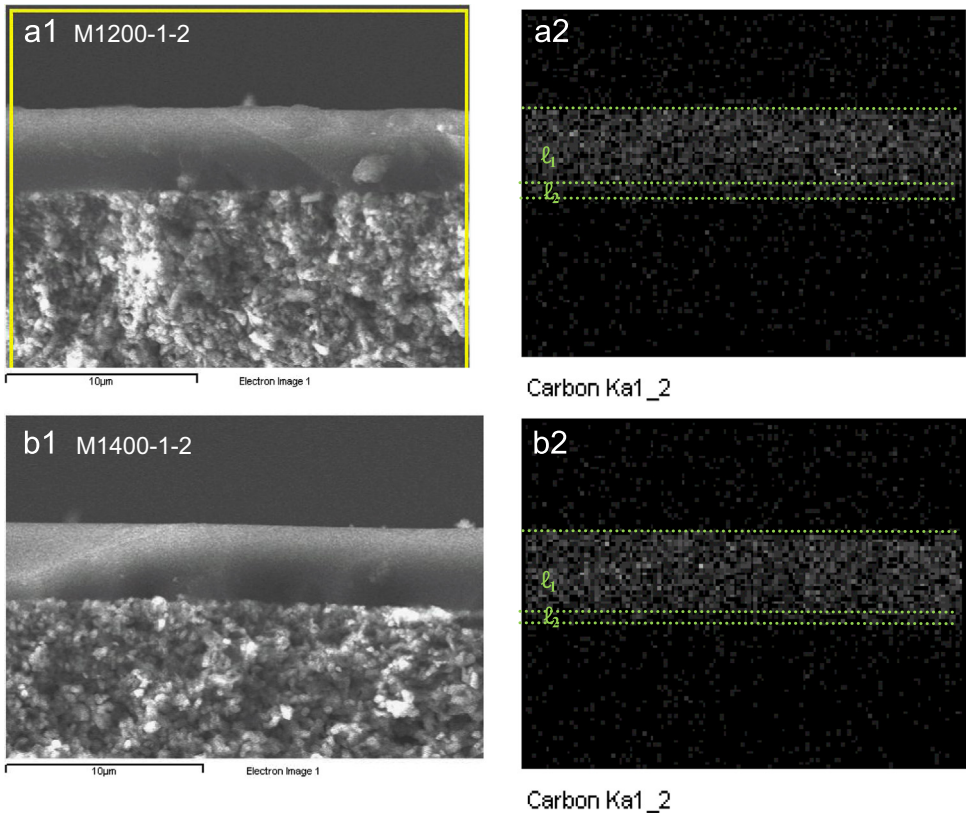

Fig. 12. (1) FE SEM photographs and (2) EDS maps of (matrix distributions in CMS composit membranes: (a) MI200-2 and (b) MI400-1-2.

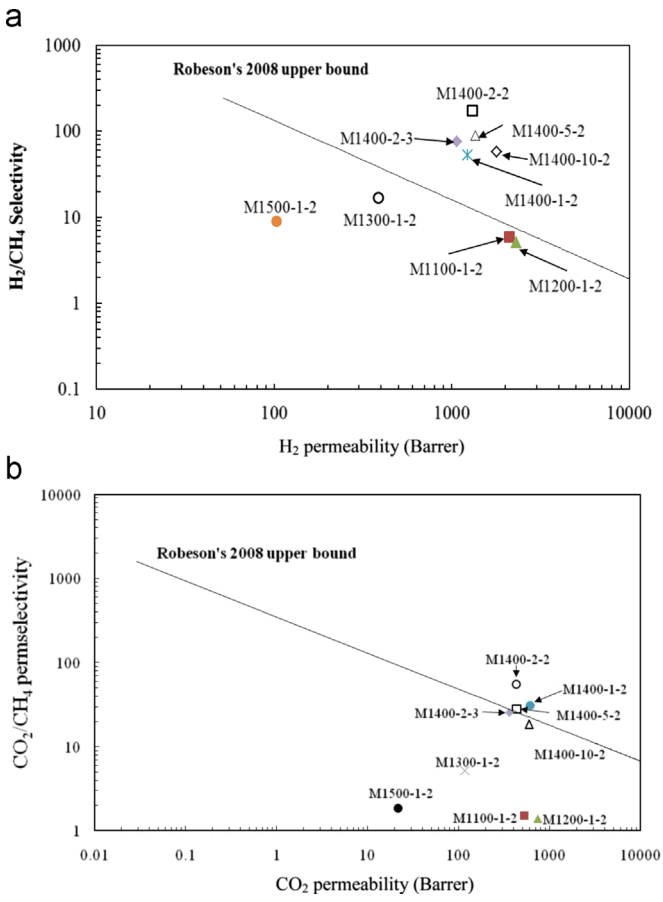

Fig. 13. Gas separation performance of CMS membrane compared with Robeson's 2008 upper bound: (a) H_2/CH_4 and (b) CO_2/CH_4.

the sintering temperature surpassing the 2008 Robeson's line [31] (as shown in Fig. 13).

Fig. 10(b) and (c), and Table 3 show the effects of heating rate and dwell time of α-Al_2O_3 substrates on gas permeability and selectivity. As shown in Fig. 10(b), the H_2 permeability gradually decreased from 1796.89 to 1300.3 Barrer, while the selectivity of H_2/CH_4 increased from 57.66 to 174.16 with a decreasing heating rate of 10–2 °C/min, due to the stacked, increased packing density of the carbon matrix (i.e., low d-spacing values) and the thick carbon film. Similar results were also observed in other gases and gas pair separation performances. Additionally, these observations also surpassed the 2008 Robeson's line [31] (as shown in Fig. 13).

Using the upper-bound relationship proposed by Robeson (2008) [31], this study selected membranes with high gas permeability and high selectivity. The comparison results are shown in Fig. 13. Among the membranes prepared using different sintering conditions, it was found that the carbon membranes supported by carrier bodies at sintering temperatures of 1400 °C showed the best permeability and selectivity performance for H_2/CH_4 and surpassed the upper-bound line. Similarly, only the M1400-1-2, M1400-2-2 and M1400-5-2 membranes were found to surpass the upper-bound line of CO_2/CH_4. Based on the above results, this study found that the M1400-2-2 membrane exhibited a high permeability and selectivity performance. Moreover, this membrane surpassed the upper-bound lines for the H_2/CH_4 and CO_2/CH_4 gas pairs proposed by Robeson (2008) [31], which was suitable for H_2 purification and CO_2 capture.

The perm-selectivities of selected CMS membranes derived from PEI precursor are summarized and compared with the present work in Table 4. The H_2 and/or CO_2 separation performances of the present membranes are impressive compared with other membranes reported in the literature, indicating the advantage of optimizing the substrate structure by altering sintering conditions. Optimization can simplify the coating-pyrolysis cycles into a single cycle to avoid a complex and high-energy demanding

Table 4
The perm-selectivities of CMS membranes from the literature compared with the present work.

Precursor/support	Preparation conditions	$P(H_2)$ (Barrer)	$P(CO_2)$ (Barrer)	H_2/CH_4	CO_2/CH_4	Reference
PEI/carbon	–	–	38	–	31.0	[32]
PEI/α-Al_2O_3	Post-treatment with self-assisted deposition carbon segment	811.6	512.5	136.3	86.1	[33]
PEI/α-Al_2O_3	Concentration of casting dope and pyrolysis temperature	198	50	46	11	[2]
PEI/α-Al_2O_3	Incorporation of SBA-15 mesoporous silica	667.5	222.5	75	25	[34]
PEI/α-Al_2O_3	Substrate structure	1200	458	84	33	[35]
PEI/α-Al_2O_3	Modified the support structure with sintering treatment	1300.3	426.1	174.2	56.4	This work

process and to improve the productivity of defect-free carbon membranes.

4. Conclusion

The optimum substrate structures for CMS membranes deposition were evaluated with various α-Al_2O_3 substrates. In this study, nanoceramics α-Al_2O_3, which has the pore size in the nanolevel was used as the supporting materials. As shown in the content and Table 1, the Dpore of the supports sintered at different temperatures are between 50 and 110 Å (5–11 nm), which is substantially smaller than the pore size of around 100–200 nm for the α-alumina supports used in other reported work. Due to the specific property of the alpha-alumina used in this work, the influence of support structure can be systematically studied. The physical properties, such as pore size distribution, total pore volume and surface roughness of α-Al_2O_3 substrates, were changed under different sintering conditions. As the sintering temperature increased, the pore structure of α-Al_2O_3 substrate was diminished, and the surface became rougher. When the sintering temperature reached 1500 °C, a densified pore structure was observed. The tetradecahedral shape of the substrate was achieved at the sintering temperature of 1400 °C, which was found to be suitable for the preparation of defect-free and high performance H_2- or CO_2-separation CMS membranes; additionally, decreasing the heating rate and dwell time were also benefit for increasing the permselectivity without significantly changed in permeability.

Acknowledgments

The authors would like to gratefully acknowledge the financial support provided by the NSC program (NSC 100-2221-E-040-004-MY3).

References

[1] G.Q. Lu, J.C. Diniz da Costa, M. Duke, S. Giessler, R. Socolow, R.H. Williams, T. Kreutz, Inorganic membranes for hydrogen production and purification: a critical review and perspective, J. Colloid Interface Sci. 314 (2007) 589–603.
[2] A.K. Itta, H.H. Tseng, Hydrogen separation performance of CMS membranes derived from the imide-functional group of two similar types of precursors, Int. J. Hydrog. Energy 36 (2011) 8645–8657.
[3] M. Bikshapathi, A. Sharma, N. Verma, Preparation of carbon molecular sieves from carbon micro and nanofibers for sequestration of CO_2, Chem. Eng. Res. Des. 89 (2011) 1737–1746.
[4] A. Brunetti, F. Scura, G. Barbieri, E. Drioli, Membrane technologies for CO_2 separation, J. Membr. Sci. 359 (2010) 115–125.
[5] C.W. Jones, W.J. Koros, Characterization of ultramicroporous carbon membranes with humidified feeds, Ind. Eng. Chem. Res. 34 (1995) 158–163.
[6] V.C. Geiszler, W.J. Koros, Effects of polyimide pyrolysis conditions on carbon molecular sieve membrane properties, Ind. Eng. Chem. Res. 35 (1996) 2999–3003.
[7] M.J. Muñoz-Aguado, M. Gregorkiewitz, Preparation of silica-based microporous inorganic gas separation membranes, J. Membr. Sci. 111 (1996) 7–18.
[8] X. Xu, Y. Bao, C. Song, W. Yang, J. Liu, L. Lin, Synthesis, characterization and single gas permeation properties of NaA zeolite membrane, J. Membr. Sci. 249 (2005) 51–64.
[9] J.C. Poshusta, R.D. Noble, J.L. Falconer, Temperature and pressure effects on CO_2 and CH_4 permeation through MFI zeolite membranes, J. Membr. Sci. 160 (1999) 115–125.
[10] P. Tin, T. Chung, Y. Liu, R. Wang, Separation of CO_2/CH_4 through carbon molecular sieve membranes derived from P84 polyimide, Carbon 42 (2004) 3123–3131.
[11] M. Kiyono, P.J. Williams, W.J. Koros, Effect of polymer precursors on carbon molecular sieve structure and separation performance properties, Carbon 48 (2010) 4432–4441.
[12] M.C. Campo, F.D. Magalhães, A. Mendes, Carbon molecular sieve membranes from cellophane paper, J. Membr. Sci. 350 (2010) 180–188.
[13] T. Kyotani, Control of pore structure in carbon, Carbon 38 (2000) 269–286.
[14] M. Kiyono, P.J. Williams, W.J. Koros, Effect of pyrolysis atmosphere on separation performance of carbon molecular sieve membranes, J. Membr. Sci. 359 (2010) 2–10.
[15] C. Song, T. Wang, H. Jiang, X. Wang, Y. Cao, J. Qin, Gas separation performance of C/CMS membranes derived from poly/furfuryl alcohol (PFA) with different chemical structure, J. Membr. Sci. 361 (2010) 22–27.
[16] A.F. Ismail, L.I.B. David, A review on the latest development of carbon membranes for gas separation, J. Membr. Sci. 193 (2001) 1–18.
[17] M.E. Rezac, W.J. Koros, Preparation of polymer–ceramic composite membranes with thin defect-free separating layers, J. Appl. Polym. Sci 46 (1992) 1927–1938.
[18] U. Beuscher, C.H. Gooding, The influence of the porous support layer of composite membranes on the separation of binary gas mixtures, J. Membr. Sci. 152 (1999) 99–116.
[19] X. Ding, Y. Cao, H. Zhao, L. Wang, Q. Yuan, Fabrication of high performance matrimid/polysulfone dual-layer hollow fiber membranes for O_2/N_2 separation, J. Membr. Sci. 323 (2008) 352–361.
[20] F. Hamad, K.C. Khulbe, T. Matsuura, Comparison of gas separation performance and morphology of homogeneous and composite PPO membranes, J. Membr. Sci. 256 (2005) 29–37.
[21] W. Yoshida, Y. Cohen, Ceramic-supported polymer membranes for pervaporation of binary organic/organic mixtures, J. Membr. Sci. 213 (2003) 145–157.
[22] L.M. van der Haar, H. Verweij, Homogeneous porous perovskite supports for thin dense oxygen separation membranes, J. Membr. Sci. 180 (2000) 147–155.
[23] W. Wei, G. Qin, H. Hu, L. You, G. Chen, Preparation of supported carbon molecular sieve membrane from novolac phenol–formaldehyde resin, J. Membr. Sci. 303 (2007) 80–85.
[24] F. Huber, J. Springer, M. Muhler, Plasma Polymer Membranes from Hexafluoroethane/Hydrogen Mixtures for Separation of Oxygen and Nitrogen, J. Appl. Polym. Sci. 63 (1997) 1517–1526.
[25] X. Ma, B.K. Lin, X. Wei, J. Kniep, Y.S. Lin, Gamma-alumina supported carbon molecular sieve membrane for propylene/propane separation, Ind. Eng. Chem. Res. 52 (2013) 4297–4305.
[26] Y. Wang, Observation of α-Al_2O_3 Powder Sintering Behaviors, Department of Resources Engineering, National Cheng Kung University, Taiwan, 2002.
[27] Q. Hong, N. Shufeng, J. Xiaoluo, X. Nanping, Enhanced performance of a macroporous ceramic support for nanofiltration by using α-Al_2O_3 with narrow size distribution, Ceram. Int. 39 (2013) 2463–2471.
[28] M. Ashby, A first report on sintering diagrams, Acta Metall. 22 (1974) 275–289.
[29] A.C. Lua, J. Su, Effects of carbonisation on pore evolution and gas permeation properties of carbon membranes from Kapton polyimide, Carbon 44 (2006) 2964–2972.
[30] M. Moaddeb, W.J. Koros, Effects of colloidal silica incorporation on oxygen/nitrogen separation properties of ceramic-supported 6FDA-IPDA thin films, J. Membr. Sci. 111 (1996) 283–290.
[31] L.M. Robeson, The upper bound revisited, J. Membr. Sci. 320 (2008) 390–400.
[32] A.B. Fuertes, T.A. Centeno, Carbon molecular sieve membranes from polyetherimide, Micro. Meso. Mater. 26 (1998) 23–26.
[33] H.H. Tseng, A.K. Itta, Modification of carbon molecular sieve membrane structure by self-assisted deposition carbon segment for gas separation, J. Membr. Sci. 389 (2012) 223–233.
[34] H.H. Tseng, P.T. Shiu, Y.S. Lin, Effect of mesoporous silica modification on the structure.of hybrid carbon membrane for hydrogen separation, Int. J. Hydrog. Energy 36 (2011) 15352–15363.
[35] H.H. Tseng, K. Shih, P.T. Shiu, M.Y. Wey, Influence of support structure on the permeation behavior of polyetherimide-derived carbon molecular sieve composite membrane, J. Membr. Sci. 405-406 (2012) 250–260.

Journal of Membrane Science 446 (2013) 220–229

Contents lists available at ScienceDirect

Journal of Membrane Science

journal homepage: www.elsevier.com/locate/memsci

Effect of MFI zeolite intermediate layers on gas separation performance of carbon molecular sieve (CMS) membranes

Ming-Yen Wey [a], Hui-Hsin Tseng [b,c,*], Chian-kai Chiang [b,c]

[a] Department of Environmental Engineering, National Chung Hsing University, No. 250, Guoguang Rd., South Dist., Taichung City, Taiwan, ROC
[b] School of Occupational Safety and Health, Chung Shan Medical University, No. 110, Sec. 1, Jianguo N. Rd., Taichung City, Taiwan, ROC
[c] Department of Occupational Medicine, Chung Shan Medical University Hospital, No. 110, Sec. 1, Jianguo N. Rd., Taichung City, Taiwan, ROC

ARTICLE INFO

Article history:
Received 8 March 2013
Received in revised form
24 June 2013
Accepted 25 June 2013
Available online 2 July 2013

Keywords:
Gas separation
Carbon membrane
Support
MFI zeolite
Molecular sieve

ABSTRACT

To strengthen interfacial adhesion between selective carbon molecular sieve (CMS) layers and α-Al_2O_3 substrates, mordenite framework inverted (MFI)-type intermediate layers were synthesized to reduce pore sizes and improve chemical characteristics of underlying substrates and consequently facilitate formation of CMS layers. MFI-type zeolite intermediate layers were prepared on α-Al_2O_3 substrates via secondary growth of seeds to form polycrystalline zeolite layers with *a*-oriented crystallites. These crystallites increased cross-link strength between separation layers as well as gas pair separation performance. When a porous substrate was treated with silica seeds and covered with an MFI intermediate layer, CMS selectivity for H_2/CH_4 increased to 260.9 with permeability towards H_2 of 2224 Barrer. These modifications improved the mechanical stability of CMS layers and will assist in their commercialization.

1. Introduction

Porous carbon molecular sieve (CMS) membranes are highly promising materials for gas separation because their rigid and uniform structure are suitable for severe application conditions such as high-temperature corrosive environments. CMS membranes feature thin selective layers that are fabricated from ultramicroporous carbon matrices with pore diameters (<7 Å) near the size of gas molecules. Thin selective CMS layers are typically prepared on macroporous inorganic supports [1–4] to enhance membrane mechanical stability. Supported configurations allow CMS membranes to simultaneously operate under high pressure conditions and maintain high permeability and selectivity with ultrathin selective layers.

Primary issues related to commercialization of supported CMS membranes, separation performance and structural stability [5,6], usually depend on carbon structure and interfacial adhesion between selective layers and inorganic substrates. The dependence of carbon structure on polymer precursors and pyrolysis conditions has been investigated intensively [7–13]. Therefore, interfacial adhesion between soft/flexible polymeric membranes and rigid inorganic substrates continues to be a major issue.

Several studies have been dedicated to improving structural stability of composite membranes by strengthening interfacial adhesion [14–19]. Mendes et al. [15] developed single deep coat methods to produce leak free CMS membrane supported in alumina. Dipping was performed by vacuum assisted dip coating, where the precursor solution penetrates into the openings beneath the surface of the support. Mardilovich [16] has proposed that smooth supports with nanometer-sized pores are essential for preparing ultrathin Pd composite membranes because larger pore apertures interfere with preparing pinhole-free membranes. However, smoother surfaces may weaken adhesion and decrease physical strength of supported membranes [17]. Wei et al. [18,19] investigated effects of ZrO_2/Al_2O_3 ceramic substrate roughness as well as casting solution viscosity on interfacial adhesive strength of polydimethylsiloxane (PDMS) polymer composite membranes on ZrO_2/Al_2O_3 zeolite supports. Their results indicated that rougher supports and lower solution viscosities increased interfacial adhesive strength. Adhesion of separation layers to ceramic substrates relies on adsorption, chemical bonding, and mechanical interlocking, which are controlled by surface energy, hydrogen bonding, and enchased structures, respectively [18,19]. Generally, enchased structures form when polymer solutions penetrate substrate pores and polymeric layers interlock with substrates [19]. Therefore, decreasing penetrable pore diameters and strengthening hydrogen bonding by modifying substrate structure benefit supported membrane preparation.

However, there are few published studies about substrate surface modification for CMS membrane fabrication. Studies

* Corresponding author at: School of Occupational Safety and Health, Chung Shan Medical University, No.110, Sec. 1, Jianguo N. Rd., Taichung City, Taiwan, ROC. Tel.: +886 4 2473 0022; fax: +886 4 2324 8194.
E-mail address: hhtseng@csmu.edu.tw (H.-H. Tseng).

0376-7388/$ - see front matter © 2013 Published by Elsevier B.V.
http://dx.doi.org/10.1016/j.memsci.2013.06.051

primarily focus on novel preparation methods for porous substrates [20], applications such as nanofiltration [21], or zeolite, metal, and polymer membrane preparation techniques [22–24]. Qi et al. [20] doped macroporous Al_2O_3 substrates with TiO_2 to form Al_2TiO_5 composites with greater mechanical strength and excellent corrosion resistance. Huang and Dittmeyer [23] used yttria-stabilized zirconia (YSZ) layers to modify porous support surface roughness for palladium membrane preparation. With these YSZ layers, thinner membranes were formed without compromising membrane integrity. However, forming membranes on YSZ layers improved selectivity but decreased hydrogen permeability. Therefore, intermediate layers are necessary to reduce substrate pore diameters and strengthen hydrogen bonding with selective layers.

Mordenite framework inverted (MFI)-type zeolites possess silanol groups and well-defined micropores that facilitate cross-linking with polymer precursors and gas permeation [25,26]. In this study, we proposed a strategy to use MFI silica intermediate layers to modify α-Al_2O_3 substrates. The substrate pore sizes were decreased by silica zeolite seeding and secondary growth of MFI layers. Moreover, deposition of MFI intermediate layers provides more OH groups to increase α-Al_2O_3 substrate polarity. Consequently, MFI intermediate layers enhance and facilitate CMS layer formation. Effects of substrate pore size on gas separation performance were also investigated. Information about effects of physicochemical substrate properties, such as pore size, surface roughness, and chemical composition, on mechanical interlocking and chemical bonding with additional layers is valuable information for CMS membrane module fabrication.

2. Experimental

2.1. Materials

Tetraethyl orthosilicate (TEOS), tetrapropylammonium hydroxide (TPAOH), cetyltrimethylammonium bromide (CTAB), and NaOH were obtained from Sigma Aldrich Co. (USA) and used as precursors to synthesize MFI intermediate layers. Pure polymer precursor, polyethyleneimine (PEI, repeat unit MW = 592 g/mol), was purchased from Sigma Aldrich Co. (USA), and *N*-methyl-2-pyrrolidone (NMP) solvent was purchased from Mallinckrodt Chemicals Co. (USA) and used without further purification. Alumina disks were purchased from Ganya Fine Ceramics Co. (Taiwan), pressed with α-Al_2O_3 powder to a thickness of ca. 1.4 mm and a diameter of 23 mm, and used as bare support material. For pure gas tests, H_2, CO_2, O_2, N_2, and CH_4 gases with purity greater than 99.999% were used.

2.2. Preparation of macroporous α-Al_2O_3 supports and MFI intermediate layers

Porous α-Al_2O_3 supports with different pore size distributions were prepared to evaluate pore size effects on MFI/α-Al_2O_3 support quality. Bare supports were dried overnight and sintered in air over a temperature range from 1100 to 1400 °C with a 2 °C/min ramping rate and a 2 h dwell time. Sintered supports were coded as S1100, S1200, S1300, and S1400, and were prepared with the following average pore sizes: 65.16, 70.63, 69.88, and 74.22 Å, respectively (see Table 1).

MFI intermediate layers were deposited on α-Al_2O_3 supports via vacuum seeding and secondary growth. Microcrystalline silica seeds were synthesized using a solution growth method [25,26]. The molar ratio 1 TEOS: 0.4 TPAOH: 40 H_2O, which produces cubic pore structures in MFI [27], was used to prepare MFI intermediate layers in this study. Reagents TPAOH and TEOS were dissolved in deionized water and reacted overnight at 100 °C for 24 h. The silica seeds were filtered, washed, and dried overnight. Silica seeds were dispersed ultrasonically in alcohol to form homogeneous solutions that were used to coat α-Al_2O_3 supports with a vacuum pump. These pre-seeded Si/α-Al_2O_3 supports were calcined at 400 °C for 4 h and coded as S-MFI-1, e.g., S1300-MFI-1.

Pre-seeded S-MFI-1 supports were further immersed in a mixture of silica species with molar ratio 1 TEOS: 0.025 TAPOH: 0.25 NaOH: 200 H_2O. A second hydrothermal reaction was performed at 110 °C for 48 h. After this synthesis, MFI/α-Al_2O_3 supports were washed with distilled water, dried overnight, and calcined at 600 °C for 4 h. These MFI/α-Al_2O_3 supports with secondary growth were coded as S-MFI-2, e.g., S1300-MFI-2.

Table 1
Pore structure of α-Al_2O_3, S-MFI-1, and S-MFI-2 supports.

Support code	S_{BET} (m^2/g)	D_{pore} (Å)	BJH adsorption cumulative pore volume of pores between 3.5 and 1000 Å radius (cm^3/g)			
			V_{total}	V_{micro}	V_{meso}	V_{macro}
S1100	8.0	65.16	0.0131	0.0026	0.0096	0.0008
S1100-MFI-1	5.6	74.41	0.0105	0.0020	0.0074	0.0010
S1100-MFI-2	9.0	137.92	0.0311	0.0029	0.0253	0.0027
S1200	6.4	70.63	0.0115	0.0021	0.0084	0.0008
S1200-MFI-1	4.2	80.46	0.0086	0.0016	0.0060	0.0009
S1200-MFI-2	2.6	170.64	0.0372	0.0050	0.0310	0.0010
S1300	6.9	69.88	0.0122	0.0020	0.0094	0.0006
S1300-MFI-1	3.6	82.20	0.0074	0.0012	0.0053	0.0007
S1300-MFI-2	4.9	70.90	0.0087	0.0017	0.0061	0.0007
S1400	4.3	74.22	0.0080	0.0011	0.0063	0.0005
S1400-MFI-1	6.1	61.13	0.0094	0.0012	0.0075	0.0005
S1400-MFI-2	5.1	70.24	0.0091	0.0014	0.0070	0.0005

2.3. Preparation of PEI-derived composite CMS membranes

Supported CMS membranes were prepared by spin coating. Solutions of 10% PEI were used to coat α-Al_2O_3 and MFI/α-Al_2O_3 supports while spinning at 1000 rpm for 20 s. Coated supports were stored overnight at room temperature to allow solvent to evaporate. Dried films were cured in a vacuum at 240 °C for 6 h with a rate of 5 °C/min. Films were pyrolyzed to 600 °C at a rate of 5 °C/min, and the final temperature was maintained for 2 h. Subsequently, CMS membranes were slowly cooled to room temperature, stored in a desiccator containing silica gel, and tested for permeance within 24 h to avoid aging effects. These CMS membranes were coded by replacing "S" in the original name of the corresponding support with "M". For example, the carbon membrane fabricated on an S1100-MFI-1 support was designated M1100-MFI-1. However, polymer films were weakly attached to S1100-MFI-2 and S1200-MFI-2 support surfaces when these supports were covered by large amounts of densely packed MFI as the intermediate layer. These weakly attached films might be due to support properties, such as pore size distribution and porosity (see Table 1). Thus, M1100-MFI-2 and M1200-MFI-2 membranes were not tested for gas permeation in this study.

2.4. Characterization of supports and CMS membranes

Support pore structure was measured using N_2 sorption at −196 °C with an automated Brunauer–Emmett–Teller (BET) sorptometer (201AEL). Crystal structure of supports and CMS membranes was recorded by X-ray diffraction (XRD) using a PW1830 X-ray powder diffractometer (Philips) with a Cu-K_α source ($\lambda = 1.5418$ Å) and a wide Bragg angle range ($20° \le 2\theta \le 70°$) with a 2°/min scanning rate. Chemical structure was monitored by Fourier transform infrared spectroscopy (FTIR) from 400 to 4000 cm^{-1} in attenuated total reflectance (ATR) mode. Surface roughness was measured by atomic force microscopy in non-contact mode using a C26 Dualscope/Rasterscope scanner (Denmark). Surface morphology and cross-sectional

images of CMS/MFI/α-Al_2O_3 composite membranes were examined by field-emission scanning electron microscopy (FE-SEM; JSM 5600).

2.5. Gas permeance measurements

A standard vacuum time-lag method was used to measure the single-gas (H_2, CO_2, O_2, N_2, and CH_4) permeabilities at room temperature (25 °C). The permeate side of a membrane was degassed under a vacuum before testing, and a pressure of 2 atm was applied on the feed side of the membrane. Gas permeance was calculated from the slope (dP/dt) of the plot of pressure (P) versus time (t) using the following equation:

$$\text{Permeability, } Q = \left(\frac{dP}{dt}\right) \times \frac{VT_0}{A\Delta P} \times \frac{L}{TP_0} \quad (1)$$

where dP/dt is the steady state rate of pressure increase, V is the downstream gas permeation volume (cm^3), A is the membrane area (cm^2), ΔP is the pressure difference between the sides of the membrane, L is the membrane thickness (cm), P_0 is 76 cm Hg, T_0 is 273 K, and T is the temperature (K).

The ideal selectivity coefficient for pure gases A/B ($\alpha_{A/B}$) is defined as the ratio of the permeabilities towards A and B, which can be expressed by Eq. (2):

$$\alpha_{A/B} = \frac{Q_A}{Q_B} \quad (2)$$

Average values and standard deviations were determined from six samples of two batches.

3. Results and discussion

3.1. MFI/α-Al_2O_3 support structures

Surface images of intermediate layers synthesized on various supports are presented in Fig. 1. As shown in Fig. 1(1a)–(1d), after seeding, support surfaces were covered loosely with silica seeds with diameters ~1 μm (see Fig. 1(2a)–(2d)). Images of MFI-2 intermediate layers are shown in Fig. 1(3a)–(3d). These intermediate layers are polycrystalline zeolite layers with particle sizes of ca. 5 μm × 3 μm × 2 μm (L × W × H).

Fig. 2 shows XRD patterns of α-Al_2O_3, S-MFI-1, and S-MFI-2 supports where X-ray reflections correspond to ordered mesoporous cubic MFI structures. As shown in Fig. 2(a), weak diffraction peaks were observed for 2θ ranges from 8° to 10° and from 23° to 25°. After secondary growth, these peaks became stronger and indicated the presence of (1 0 1), (2 0 0), (5 0 1), (3 0 0), and (1 3 3) crystal planes of MFI-type structures [28]. The two largest peaks detected at 2θ values of 8.856° and 7.906° were due to (2 0 0) and (1 0 1) crystal planes, respectively. This result implies that MFI intermediate layers consisted primarily of a-oriented and some (h 0 h)-oriented MFI-type zeolite crystallites (Fig. 3) [28].

Porous structures of α-Al_2O_3 supports before and after modification were analyzed with N_2 adsorption techniques. As shown in Table 1, total pore volumes of MFI-1 modified S1100, S1200, and S1300 supports decreased after silica seeds were deposited on α-Al_2O_3 support surfaces, assuming porosity loss rates of 19.84%, 25.22%, and 39.34%, respectively. The percent porosity loss increased as the total volume of micropores and mesopores decreased. Porosity reduction may be attributed to plugging by silica seeds deposited in support pores.

The particle size and pore size distribution of silica seeds synthesized in this study using a solution growth method was shown in Fig. 4. The particle size was ranged from nanoscale to microscale with a main size of ca. 1 μm. Therefore, it can be deduced that, the smaller (nanoscale) silica seeds were deposited into the pore structure of α-Al_2O_3 supports via vacuum system during the seeding process. Dispersion of silica seeds was further confirmed by cross-sectional energy-dispersive X-ray spectroscopy (EDS) mapping analysis (Fig. 5 (1a)–(3a)). These images indicated that silica seeds packed more densely in pores in S1100, S1200, and S1300 than S1400 (Fig. 4(4a)). Cross-sectional EDS analysis of MFI-2 modified supports confirmed these observations (Fig. 5(5a)–(6a)), indicating that intermediate MFI layers entered pores in α-Al_2O_3 supports via secondary growth. These results suggested that silica seeds and MFI densely packed in micropores and mesopores and near throats of large micropores in α-Al_2O_3 supports. Seed particles agglomerated on alumina support surfaces and in pores during vacuum suction seeding.

However, as shown in Table 1, the pore volume of MFI-1 modified S1100, S1200 and S1300 supports shows only slightly

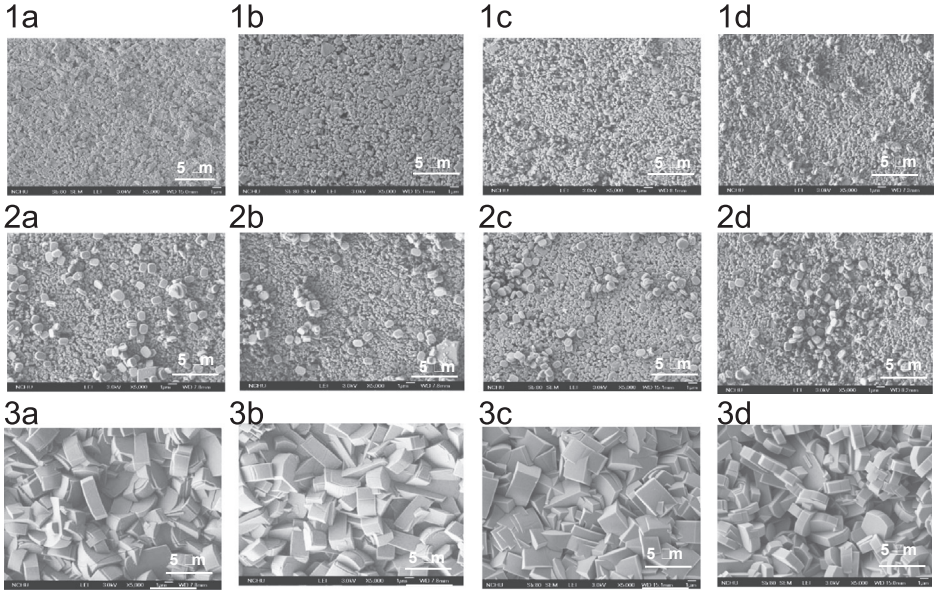

Fig. 1. FE-SEM images of (1) α-Al_2O_3, (2) S-MFI-1, and (3) S-MFI-2 substrates. (1a) S1100, (1b) S1200, (1c) S1300, (1d) S1400, (2a) S1100-MFI-1, (2b) S1200-MFI-1, (2c) S1300-MFI-1, (2d) S1400-MFI-1, (3a) S1100-MFI-2, (3b) S1200-MFI-2, (3c) S1300-MFI-2 and (3d) S1400-MFI-2.

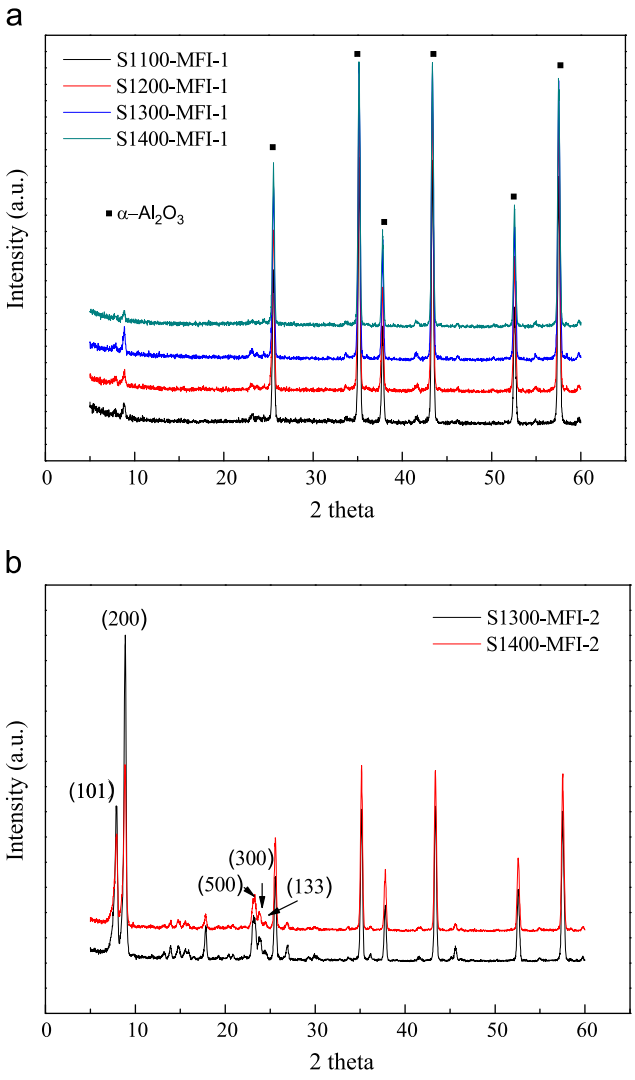

Fig. 2. XRD diffraction patterns of (a) S-MFI-1 and (b) S-MFI-2 supports.

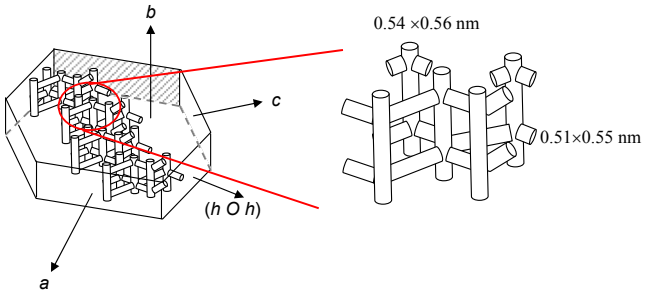

Fig. 3. Crystal shape and pore structure of an MFI-type zeolite [28].

lower than that of original supports. The smaller reduction was due to the volume contribution of silica seeds. Fig. 4(b) shows the pore size distribution of silica seeds. The silica seeds have bimodal pores, in the mesopore and macropore regions, with a marrow distribution and two large peaks at 2.2 and 5.8 nm. The pore volumes of micropore and mesopore for silica seed were estimated to 0.1708 and 0.1213 cm^3/g, respectively. Therefore, although the pore throat of support was blocked with seeds, the pore volume shows slightly lower than that of original support.

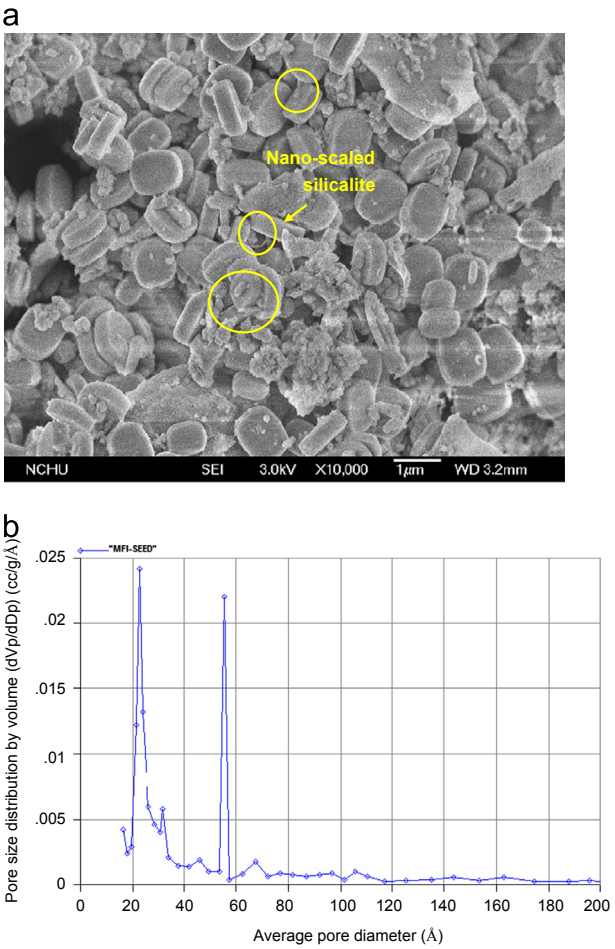

Fig. 4. (a) FE-SEM image and (b) pore size distribution of silica seeds synthesized in this study via solution growth method.

3.2. *Interactions between PEI polymer films and MFI/α-Al_2O_3 supports*

Changes in PEI film chemical structure before and after coating surfaces of different Si/Al supports were correlated with ATR-FTIR analysis. As shown in Fig. 6, the presence of crystalline MFI was confirmed by the triplet peak of Si–O–Si, Si–O, and MFI stretching vibrations with maximum values at approximately 1066, 800, and 547 cm^{-1}, respectively. Highlighted regions represent characteristic PEI bands. Infrared absorption at 1775, 1717, and 1353 cm^{-1} corresponds to the asymmetric stretch of C═O, the symmetric stretch of C═O, and the –C–N–C– stretching band of the amide group, respectively. These spectroscopic results are consistent with previous reports [29]. There is a qualitative difference in the functional group band intensity for pristine PEI and composite PEI/MFI/α-Al_2O_3. Peak intensities were weaker for PEI coatings on S-MFI-1 and S-MFI-2 surfaces, and the MFI triplet peak was weaker as well.

These results indicate that PEI films self-assemble when coordinate bonds form between Si^{3+}(Si–O) and N (from –NH bonds in membrane structures) [30]. The proposed self-assembly mechanism, shown in Fig. 7, involves formation of H-bonds between carbonyl and surface hydroxyl groups of the zeolite. Consequently, when PEI polymer film coats the surface of an MFI/α-Al_2O_3 support, the amount of PEI bound to the substrate surface increases with the number of hydroxyl groups from the second thermohydrolysis reaction.

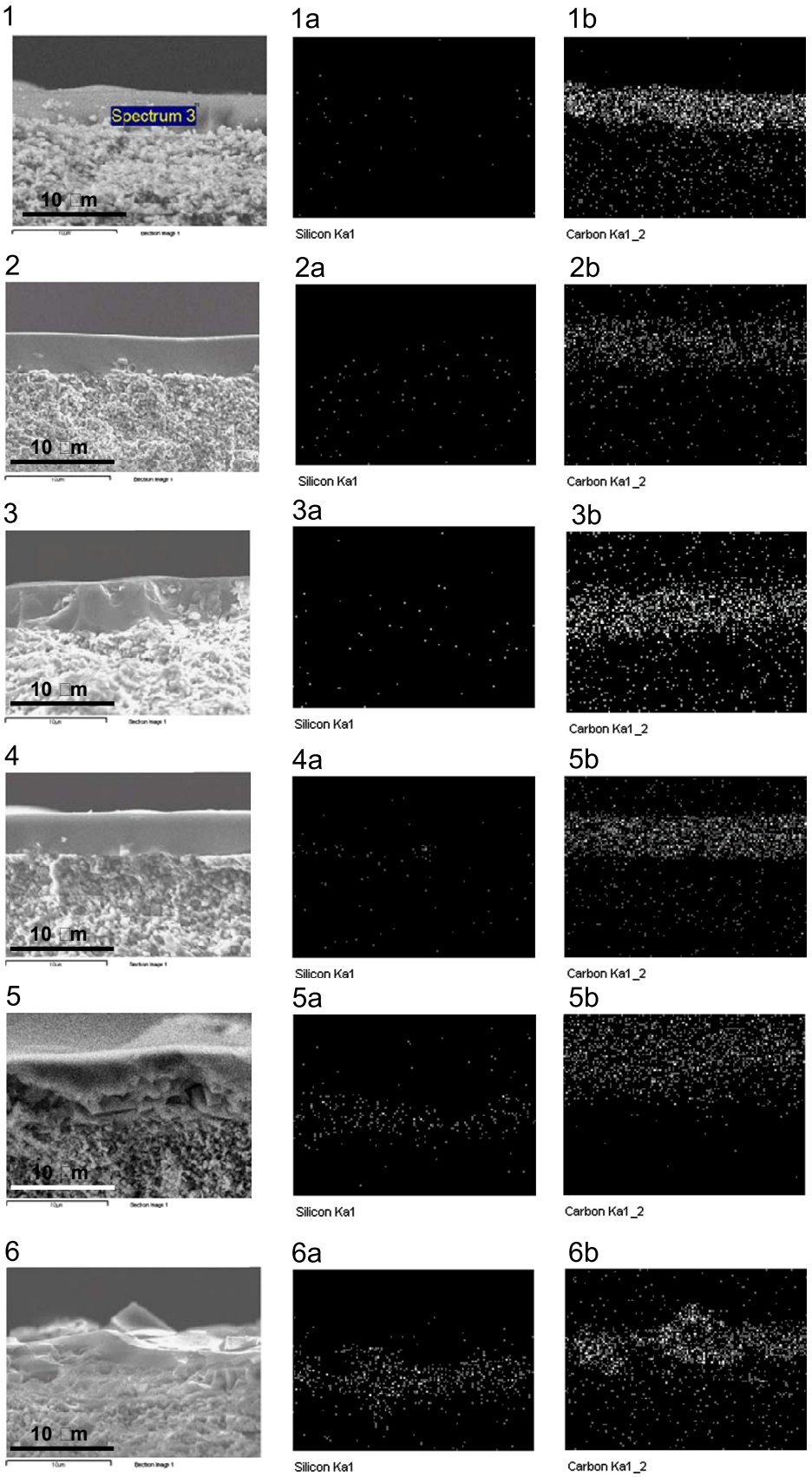

Fig. 5. FE-SEM photographs and EDS maps of (a) Si and (b) C matrix distributions in CMS composite membranes. (1) M1100-MFI-1, (2) M1200-MFI-1, (3) M1300-MFI-1, (4) M1400-MFI-1, (5) M1300-MFI-2 and (6) M1400-MFI-2.

3.3. Gas permeation performance of CMS/MFI/α-Al_2O_3 membranes

Steady state single gas permeation studies were performed on CMS/MFI/α-Al_2O_3 composite membranes to examine the influence of MFI intermediate layers. After supports were modified with silica seeds, selectivity of S-MFI-1 supported membranes increased. As shown in Tables 2 and 3, CMS membranes supported by S1100-MFI-1, S1200-MFI-1, and S1300-MFI-1 substrates demonstrated greater gas pair selectivity. For example, H_2/CH_4 selectivity increased from 32.31 for M1100 to 260.96 for M1100-MFI-1, an eightfold increase, and CO_2/CH_4 selectivity for M1100-MFI-1 was 5.77 times greater than for M1100, but permeability was ca. 40% lower. Opposite trends were observed for S1400 where CMS selectivity decreased and permeability, especially for CO_2 and O_2, increased after the support was modified with silica seeds. For example, CO_2 permeability increased from 345.2 for M1400 to 614.2 for M1400-MFI-1. These results indicated that pore structures of original α-Al_2O_3 substrates significantly influenced surface modification efficacy.

After silica seeds grew into MFI-type zeolites, gas permeability of CMS membranes supported on S-MFI-2 substrates increased. For example, the permeability towards H_2 of M1300-MFI-2 and M1400-MFI-2 increased from 1192 to 3067 Barrer and from 1267 to 1948 Barrer, respectively. However, some discrepant results are observed in Table 3 including contradictory results for M1300 and M1400 gas

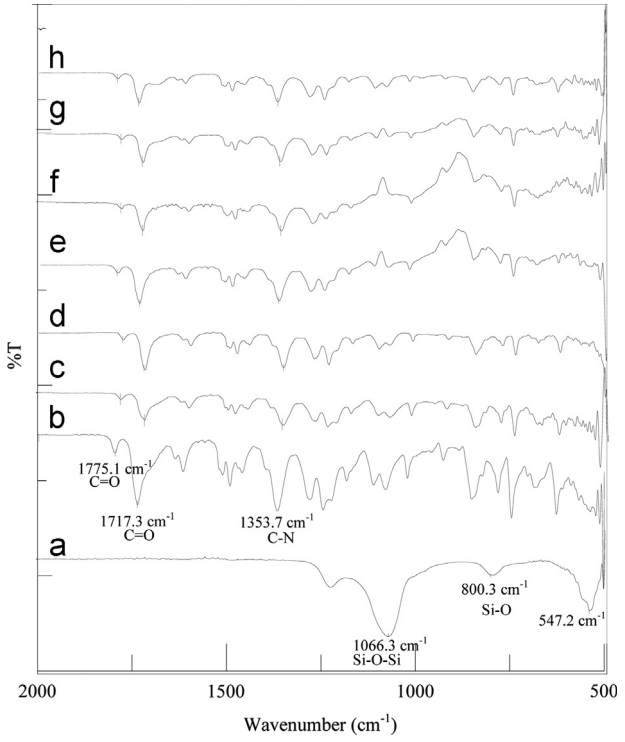

Fig. 6. FTIR spectra of (a) MFI powder, (b) pure PEI polymer film, and PEI films on various substrates: (c) S1100-MFI-1, (d) S1200-MFI-1, (e) S1300-MFI-1, (f) S1300-MFI-2, (g) S1400-MFI-1, and (h) S1400-MFI-2.

Table 2
Permeability of CMS membranes supported on various substrates.

CMS membrane	Permeability (Barrer)				
	H_2	CO_2	O_2	N_2	CH_4
M1100	3503 ± 298	1371 ± 158	411 ± 75	113 ± 43	130 ± 61
M1100-MFI-1	2224 ± 190	631 ± 64	168 ± 34	18 ± 3	9 ± 1
M1200	2653 ± 188	995 ± 151	295 ± 57	61 ± 19	62 ± 20
M1200-MFI-1	1502 ± 136	611 ± 30	167 ± 13	23 ± 1.0	13 ± 0.4
M1300	1192 ± 321	434 ± 97	123 ± 31	13 ± 0.4	8 ± 3
M1300-MFI-1	1298 ± 325	361 ± 112	90 ± 31	10 ± 3	5 ± 2
M1300-MFI-2	3067 ± 177	1202 ± 146	378 ± 11	75 ± 21	84 ± 27
M1400	1267 ± 76	345 ± 91	116 ± 12	17 ± 1	16 ± 5
M1400-MFI-1	1346 ± 190	614 ± 87	185 ± 33	26 ± 5	17 ± 1
M1400-MFI-2	1948 ± 236	744 ± 79	221 ± 15	25 ± 1	16 ± 1

Table 3
Selectivity of CMS membranes supported on various substrates.

CMS membrane	Selectivity			
	H_2/CH_4	H_2/N_2	O_2/N_2	CO_2/CH_4
M1100	32 ± 17	34 ± 13	4 ± 1.9	13 ± 8
M1100-MFI-1	261 ± 51	127 ± 20	10 ± 0.9	74 ± 14
M1200	471 ± 20	48 ± 20	5 ± 2	17 ± 6
M1200-MFI-1	120 ± 14	66 ± 8	7 ± 0.56	49 ± 4
M1300	147 ± 36	89 ± 21	9 ± 2	54 ± 10
M1300-MFI-1	252 ± 43	134 ± 11	9 ± 2	69 ± 7
M1300-MFI-2	40 ± 16	43 ± 14	5 ± 2	15 ± 5
M1400	115 ± 54	75 ± 3	7 ± 1	22 ± 31
M1400-MFI-1	77 ± 4	53 ± 5	7 ± 0.9	35 ± 2
M1400-MFI-2	121 ± 25	78 ± 12	9 ± 0.7	46 ± 9

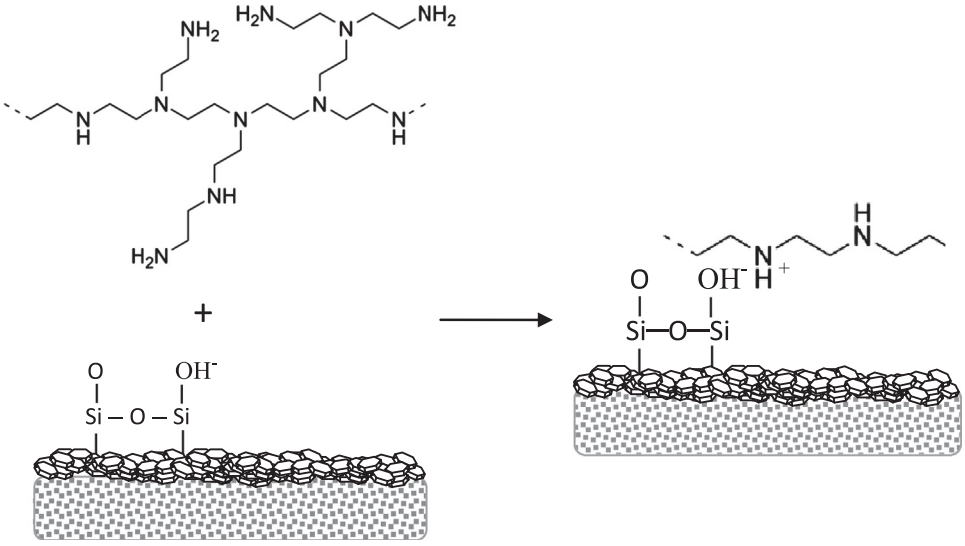

Fig. 7. Schematic of PEI crosslinking with an MFI-type zeolite intermediate layer.

selectivity. The H_2/CH_4 gas pair selectivity of the M1300-MFI-2 membrane (40) was 73% lower that the M1300 membrane (1 4 7). The opposite trend was observed for the H_2/CH_4 gas pair selectivity of the M1400-MFI-2 membrane (1 2 1), which was slightly higher than the M1400 membrane selectivity (1 1 5). These gas selectivity results implied that the MFI-2 intermediate layer increased permeability and improved selectivity of CMS membranes on S-1400 supports with relatively small pore volumes/sizes.

To investigate changes in separation performance caused by MFI intermediate layers and CMS layers, single gas permeation performance of the CO_2/CH_4 gas pair was assessed for S-MFI-2 and α-Al_2O_3 supports. Pure gas transport through porous supports occurs by viscous flow and Knudsen diffusion [24]. Therefore, the Knudsen selectivity was calculated for comparison purposes. As shown in Table 4, observed CO_2/CH_4 selectivity values for all substrates were somewhat lower than predictions of Knudsen selectivity. Experimental values for the S1400-MFI-2 substrate were closer than the S1300-MFI-2 support results to the Knudsen ratio. These observations suggested that pore sizes in MFI intermediate layers in S1300-MFI-2 or S1400-MFI-2 were sufficiently large and did not significantly influence transport mechanisms.

As shown in XRD spectra, S-MFI-2 supports contained *a*- and (*h* 0 *h*)-oriented crystallites. Lai et al. [31] investigated permeation properties through *b*-, *c*-, *a*/*b* (mixed)-, and (*h* 0 *h*)-oriented zeolite membranes. Their results indicated that permeation and separation of xylene isomers were unaffected by *a*-oriented membrane layers because MFI zeolites did not have pores parallel to the *a*-axis to achieve molecular-sieve effect (as shown in Fig. 3). Therefore, in this study, gas transport through S-MFI-2 supports occurred according to the viscous flow mechanism instead of a molecular-sieve mechanism. This result was also observed for diffusion of relatively small gas molecules, such as CO_2, O_2, N_2, and CH_4, in zeolite membranes [24,32]. Therefore, we conclude that improvement in separation performance after modification with MFI-type zeolite intermediate layers was primarily due to carbon selective layers. Thus, there is particular interest in characterization of pore formation and pore structure of CMS membranes after modifying α-Al_2O_3 supports with silica seeds and MFI zeolite layers.

3.4. Characterization of CMS/MFI/α-Al_2O_3 membranes

As discussed in Section 3.2, polymer chains are cross-linked to modified supports to form bonds with Si–O groups in silica seeds or MFI zeolites. Thus, these polymers can become more rigid than bulk polymer chains [30]. Consequently, polymer bonding produces a small increase in CMS membrane density. The degree of packing in ultramicroporous carbon structures and interplanar distances can be obtained from average *d*-spacing values [1]. As illustrated in Table 5, a decrease in *d*-spacing was observed in all membranes supported on S-MFI-1 supports except S1400-MFI-1. (The *d*-spacing of membranes supported on S-MFI-2 substrates was not detected due to interruption of MFI crystalline diffraction peaks.) Results indicated that interplanar carbon layer distances decreased after seeding silica intermediate layers, suggesting that formation of cross-linked separation layers with silica seeds increased the degree of packing in ultramicroporous carbon matrices. Therefore, chemical bonding between polymer films and intermediate layers is a key parameter that influences gas separation selectivity.

Carbon layer packing depends on the strength of cross-linked separation layers and the topology of polymer chains piled on intermediate layer surfaces. Neatly stacked polymer chains produce a tighter structure because of interfacial piling. Therefore, support roughness and pore structure are two additional main parameters that determine interplanar distances of carbon layers. To investigate the effect of roughness on *d*-spacing, α-Al_2O_3 support roughness was measured before and after modification using a surface roughness analyzer, and results were presented as the quadratic mean value, Rq. As shown in Table 5, the surface roughness of every α-Al_2O_3 support increased after modification with silica seeds or an MFI intermediate layer. The roughness of S-MFI-2 supports was much higher than for S-MFI-1 supports, suggesting that larger silica seeds and MFI crystallites growth produced rougher supports. In general, rougher supports produced larger *d*-spacing and higher permeability [33]. For example, the permeability towards hydrogen of M1400 increased slightly from 1267 to 1346 Barrer after it was modified with silica seeds

Table 4
Selectivity and permeability of various supports towards the testing gases.

Support	Permeability (GPU)					Selectivity			
	H_2	CO_2	O_2	N_2	CH_4	H_2/CH_4	CO_2/CH_4	O_2/N_2	H_2/CO_2
S1200-MFI-1	7052	4317	4171	4463	5026	1.4	0.9	0.9	1.6
S1200-MFI-2	7814	4516	3825	4184	4751	1.6	0.9	0.9	1.7
S1300-MFI-1	6483	3251	2777	3086	3640	1.8	0.9	0.9	2.0
S1300-MFI-2	157	43	456	50	625	0.3	0.1	9.2	3.6
S1400-MFI-1	3657	1603	1642	1871	2464	1.5	0.7	0.9	2.3
S1400-MFI-2	9893	11,592	13,333	14,965	13,569	0.7	0.9	0.9	0.9
Knudsen separation factor						2.8	0.6	0.7	3.3

Table 5
Surface roughness, *d*-spacing, and thickness of CMS membranes supported on different substrates.

Membrane Code	Rq of support (nm)	Rq of membrane (nm)	*d*-spacing (Å)	Thickness (μm)
M1100	28.9	6.5	3.99	3.994
M1100-MFI-1	145.0	24.6	3.88	4.519
M1200	38.1	3.6	3.93	4.05
M1200-MFI-1	212.0	18.9	3.89	4.969
M1300	39.5	4.9	3.82	2.794
M1300-MFI-1	270.0	14.8	3.61	3.975
M1300-MFI-2	339.0	52.0	N.D.	4.987
M1400	53.1	10.9	4.04	3.188
M1400-MFI-1	209.0	15.2	4.08	4.106
M1400-MFI-2	342.0	64.1	N.D.	4.837

because the support configuration transferred to the carbon selective layer and formed a porous carbon layer [34]. However, *d*-spacing values of S-MFI-1 supported membranes decreased with increased roughness (Table 5), except for the S1400-MFI-1 support. Therefore, support pore volume is another dominant factor. Consequently, CMS layer morphology was analyzed.

As previously mentioned, pore volumes (especially micropore and mesopore volumes) of α-Al_2O_3 supports decreased after modification with silica seeds because of pore throat blockage, which prevented coating solutions from penetrating supports. The influence of support pore volume on formation of dense carbon membranes was evaluated on the basis of surface morphologies of CMS membranes formed on α-Al_2O_3, S-MFI-1, and S-MFI-2 supports with the same carbon membrane preparation procedure. Carbon layers were pyrolyzed from 10% PEI cast film. All support surfaces were completely covered with carbon film layers, as shown in FE-SEM images in Fig. 8(a). The as-synthesized surfaces had excellent morphologies, which were continuously well attached to supports without surface cracks or defects. However, membranes on bare substrates (Fig. 8(b)) were not completely covered with carbon. The roughness and pore volume of the bare α-Al_2O_3 substrate was too large for the deposition of a thin polymer film on its surface and the formation of a carbon layer because the polymer solution tends to penetrate the pores of the support. Therefore, the pretreatment conditions used in this study (including sintering temperature, soaking time, heating rate, seeding silica seeds, and secondary growth into an MFI zeolite film) were appropriate to reduce support pore volume and maintain carbon/MFI/α-Al_2O_3 composite membrane integrity. Furthermore, comparison of different membranes (Table 5) showed that carbon layer thickness varied with surface roughness and total support pore volume. For M1100, M1200, M1300, and M1400 membranes, carbon layer thickness increased after seeding and secondary growth of MFI intermediate layers. Support roughness similarly increased, while pore volumes and diameters decreased due to blockage by silica seeds (except for S1400 support). For example, surface roughness of S1100 increased fivefold, from 28.9 to 145 μm, after seeding with silica. Roughness of other supports increased approximately four- to sevenfold but was too large for the given carbon layer. However, a continuous defect-free carbon membrane formed on the rougher supports. In general, the separation layer thickness should be larger than the support roughness to completely cover the support surface. However, in this study, the carbon membranes were thinner than the support roughness. These observations demonstrated that intermolecular interactions existed between polymer casting solutions and intermediate layers. Rougher MFI-1 and MFI-2 intermediate layers limited fluid flow and permeability, thereby preventing polymer solution from penetrating the porous substrate and interlocking with the intermediate layer. Thus, the casting solution remained on the support surface. Mechanical interlocking between rough supports and polymer films determine the carbon separation layer attachment [18] because additional contact improves adhesion of the carbon membrane to the support. Consequently, the carbon layer thickness increased while the interplanar distance decreased with increased support roughness when pore volumes, especially micropore and mesopore volumes, were reduced. Beyond this observation, selectivity increased with decreasing permeate flux for M1100-MFI-1, M1200-MFI-1, and M1300-MFI-1 membranes compared with their unmodified counterparts.

Carbon membranes supported on MFI-2 supports showed gradually increasing permeability for all permeate gases. Further, compared to M1300-MFI-2 membrane, the M1400-MFI-2 membrane also showed slightly increasing selectivity simultaneously. These observations could be attributed to properties of porous supports, including pore size distribution. After sintering, the porosity of S1400 shifted to a smaller pore size distribution than S1300. Therefore, fewer silica seeds were introduced into pores in the S1400 support, and fewer MFI crystallites were implanted onto and within S1400-MFI-2 supports. Pore channels that were not blocked by silica seeds allowed casting solution to penetrate and interlock with α-Al_2O_3 support (Fig. 8(l)), which obstructed permeance of large gas molecules and slightly increased membrane gas pair selectivity.

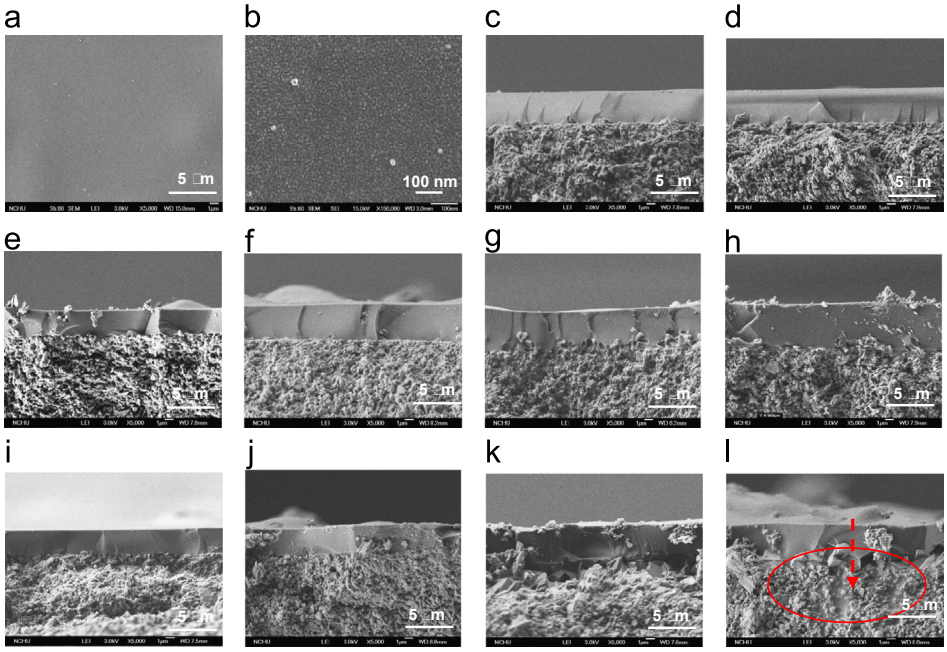

Fig. 8. FE-SEM images of surfaces and cross-sections of CSM membranes supported on different supports. (a) Membrane supported on sintered support, (b) Membrane supported on bare support, (c) M1100, (d) M1200, (e) M1300, (f) M1400, (g) M1100-MFI-1, (h) M1200-MFI-1, (i) M1300-MFI-1, (j) M1400-MFI-1, (k) M1300-MFI-2 and (l) M1400-MFI-2.

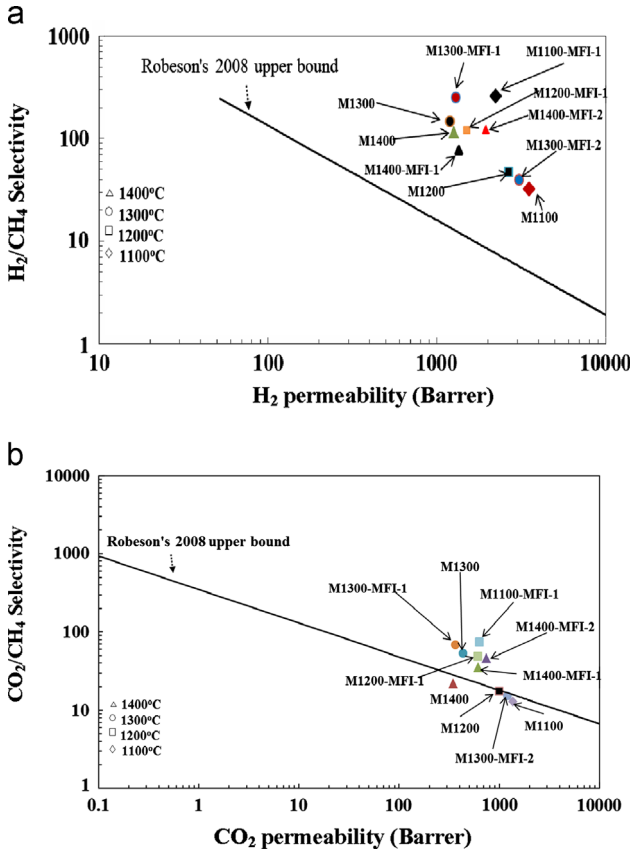

Fig. 9. Permselectivity of CMS membranes supported on various supports compared with Robeson's 2008 upper bound [34]: (a) H_2/CH_4 and (b) CO_2/CH_4.

Finally, as shown in Fig. 9(a), the performance of all membranes, and especially MFI-1 modified membranes, surpassed the upper bound proposed by Robeson [35]. The M1100-MFI-1 membrane displayed the highest separation performance compared with the original α-Al_2O_3- and other S-MFI-1 supported membranes. The M1100-MFI-1 membrane achieved high permeability towards H_2 of 2224 Barrer and CO_2 of 631 Barrer, with H_2/CH_4 and CO_2/CH_4 selectivity of 261 and 74, respectively, as shown by the longest straight distance from the line proposed by Robeson in 2008 [35] in Fig. 9(a) and (b). This attractive gas separation performance strongly demonstrates that silica seeds are beneficial to CMS membranes when α-Al_2O_3 supports have relatively large pore volumes/sizes.

4. Conclusions

In this study, α-Al_2O_3 supports with different pore size distributions and pore volumes were modified with MFI-type zeolites via secondary growth of silica seeds. These seeds were deposited on or in pores of α-Al_2O_3 supports. The seeds produced continuous MFI-zeolite layers on support surfaces, which functioned as intermediate layers that altered support surface characteristics. Pore structure, roughness, and chemical characteristics of α-Al_2O_3 supports were modified. Interactions between supported carbon layers became stronger because of chemical cross-linking and interlocking. Membranes supported on supports with relatively large pore volumes only showed increased selectivity after seeding with silica. By contrast, membranes on supports with smaller pore volumes showed increased permeability and selectivity after secondary growth of MFI-zeolite films. Supports with larger pore volumes were blocked by seeds, which prevented casting solution from penetrating the support, thereby decreasing its permeability. Supports with smaller pores that were not blocked by silica seeds formed strong interlocking interactions with casting solution, thereby increasing permeability and selectivity. The permeation and separation performance of membranes supported on modified supports were significantly affected by pore volume and pore size distribution of the support. These modifications improved the mechanical stability of CMS layers and superior performance, which will assist in their commercialization.

Acknowledgments

The authors gratefully acknowledge financial support from an NSC program (NSC 100-2221-E-040-004-MY3).

References

[1] A.F. Ismail, Basic aspects of polymeric and inorganic membrane preparation, in: E Drioli, L Giorno (Eds.), Comprehensive Membrane Science and Engineering, Elsevier, Japan, 2010, pp. 275–290.
[2] W. Wei, G. Qin, H. Hu, L. You, G. Chen, Preparation of supported carbon molecular sieve membrane from novolac phenol-formaldehyde resin, J. Membr. Sci. 303 (2007) 80–85.
[3] A.B. Fuertes, T.A. Centeno, Preparation of supported asymmetric carbon molecular sieve membranes, J. Membr. Sci. 144 (1998) 105–111.
[4] M.T. Ravanchi, T. Kaghazchi, A. Kargari, Application of membrane separation processes in petrochemical industry: a review, Desalination 235 (2009) 199–244.
[5] P. Bernardo, E. Drioli, G. Golemme, Membrane gas separation: a review/state of the art, Ind. Eng. Chem. Res. 48 (2009) 4638–4663.
[6] A.F. Ismail, L.I.B. David, A review on the latest development of carbon membranes for gas separation, J. Membr. Sci. 193 (2001) 1–18.
[7] M. Kiyono, P.J. Williams, W.J. Koros, Effect of pyrolysis atmosphere on separation performance of carbon molecular sieve membranes, J. Membr. Sci. 359 (2010) 2–10.
[8] H.H. Tseng, I.A. Kumar, Modification of carbon molecular sieve membrane structure by self-assisted deposition carbon segment for gas separation, J. Membr. Sci. 389 (2012) 223–233.
[9] H.H. Tseng, P.T. Shiu, Y.S. Lin, Effect of mesoporous silica modification on the structure of hybrid carbon membrane for hydrogen separation, Int. J. Hydrogen Energy 36 (2011) 15352–15363.
[10] I.A. Kumar, H.H. Tseng, Hydrogen separation performance of CMS membranes derived from the imide-functional group of two similar types of precursors, Int. J. Hydrogen Energy 36 (2011) 8645–8657.
[11] M. Kiyono, P.J. Williams, W.J. Koros, Effect of polymer precursors on carbon molecular sieve structure and separation performance properties, Carbon 48 (2010) 4432–4441.
[12] I.A. Kumar, H.H. Tseng, M.Y. Wey, Effect of dry/wet-phase inversion method on fabricating polyetherimide-derived CMS membrane for H_2/N_2 separation, Int. J. Hydrogen Energy 35 (2010) 1650–1658.
[13] H.H. Tseng, I.A. Kumar, T.H. Weng, C.Y. Lu, M.Y. Wey, Preparation and characterization of carbon molecular sieve membranes for gas separation application: the effect of incorporated multi-walled carbon nanotube, Desalination 240 (2009) 40–45.
[14] R. Saha, W.D. Nix, Effects of the substrate on the determination of thin film mechanical properties by nanoindentation, Acta. Mater. 50 (2002) 23–38.
[15] M. Teixeira, M.C. Campo, D.A.P. Tanaka, M.A.L. Tanco, C. Magen, A. Mendes, Composite phenolic resin-based carbon molecular sieve membranes for gas separation, Carbon 49 (2011) 4348–4358.
[16] I.P. Mardilovich, E. Engwall, Y.H. Ma, Dependence of hydrogen flux on the pore size and plating surface topology of asymmetric Pd-porous stainless steel membranes, Desalination 144 (2002) 85–89.
[17] Y. Huang, R. Dittmeyer, Preparation and characterization of composite palladium membranes on sinter–metal supports with a ceramic barrier against intermetallic diffusion, J. Membr. Sci. 282 (2006) 296–310.
[18] W. Wei, S. Xia, G. Liu, X. Gu, W. Jin, N. Xu, Interfacial adhesion between polymer separation layer and ceramic support for composite membrane, AIChE J. 56 (2010) 1584–1592.
[19] G. Liu, W. Wei, H. Wu, X. Dong, M. Jiang, W. Jin, Polymer/ceramic composite membrane and their application in pervaporation process, Chin. J. Chem. Eng. 20 (2012) 62–70.
[20] H. Qi, Y. Fan, W. Xing, L. Winnubst, Effect of TiO_2 doping on the characteristics of macroporous Al_2O_3/TiO_2 membrane supports, J. Eur. Ceram. Soc. 30 (2010) 1317–1325.
[21] L.I. Gaiye, Q.I. Hong, F.A.N. Yiqun, X.U. Nanping, Toughening macroporous alumina membrane supports with YSZ powders, Ceram. Int. 35 (2009) 1641–1646.

[22] H. Qi, S. Niu, X. Jiang, N. Xu, Enhanced performance of a macroporous ceramic support for nanofiltration by using α-Al_2O_3 with narrow size distribution, Ceram. Int. 39 (2013) 2463–2471.
[23] Y. Huang, R. Dittmeyer, Preparation of thin palladium membranes on a porous support with rough surface, J. Membr. Sci. 302 (2007) 160–170.
[24] P. Kumar, J. Ida, S. Kim, V.V. Guliants, J.Y.S. Lin, Ordered mespoourous membranes: effects of support and surfactant removal conditions on membrane quality, J. Membr. Sci. 279 (2006) 539–547.
[25] T. Bein, Synthesis and applications of molecular sieve layers and membrane, Chem. Mater. 8 (1996) 1636–1653.
[26] Q.Y. Zhao, J.Q. Wang, N.B. Chu, X.Y. Yin, J.H. Yang, C.L. Kong, et al., Preparation of high-permeance MFI membrane with the modified secondary growth method on the macroporous alpha-alumina tubular support, J. Membr. Sci. 320 (2008) 303–309.
[27] H.F. Chang, Fabrication and characterization of MFI zeolite membranes by secondary growth method for gas separation (Master thesis), National Chung Hsing University, Taiwan, 2010.
[28] Y. Hasegawa, T. Ikeda, T. Nagase, Y. Kiyozumi, T. Hanaoka, F. Mizukami, Preparation and characterization of silicaite-1 membranes prepared by secondary growth of seeds with different crystal sizes, J. Membr. Sci. 208 (2006) 397–405.
[29] P.S. Tin, T.S. Chung, Y. Liu, R. Wang, S.L. Liu, K.P. Pramoda, Effects of cross-linking modification on gas separation performance of Matrimid membranes, J. Membr. Sci. 225 (2003) 77–90.
[30] T.S. Chung, L.Y. Jiang, Y. Li, S. Kulprathipanja, Mixed matrix membranes (MMMs) comprising organic polymers with dispersed inorganic fillers for gas separation, Prog. Polym. Sci. 32 (2007) 483–507.
[31] Z. Lai, G. Bonilla, I. Diaz, J.G. Nery, K. Sujaoti, M.A. Amat, et al., Microstructural optimization of a zeolite membrane for organic vapor separation, Science 300 (2003) 456–460.
[32] M.P. Bernal, J.C.M. Menéndez, J. Santamaría, Separation of CO_2/N_2 mixtures using MFI-type zeolite membranes, AIChE J. 50 (2004) 127–135.
[33] H. Kaczmarek, H. Chaberska, The influence of solvent residue, support type and UV-irradiation on surface morphology of poly(methyl acrylate) films studied by Atomic Force Microscopy, Polym. Test. 27 (2008) 736–742.
[34] T.A. Peters, C.H.S. Poeth, N.E. Benes, H.C.W.M. Buijs, F.F. Vercauteren, J.T.F. Keurentjes, Ceramic-supported thin PVA pervaporation membranes combining high flux and high selectivity; contradicting the flux-selectivity paradigm, J. Membr. Sci. 276 (2006) 42–50.
[35] L.M. Robeson, The upper bound revisited, J. Membr. Sci. 320 (2008) 390–400.

Journal of Membrane Science 405–406 (2012) 250–260

Contents lists available at SciVerse ScienceDirect

Journal of Membrane Science

journal homepage: www.elsevier.com/locate/memsci

Influence of support structure on the permeation behavior of polyetherimide-derived carbon molecular sieve composite membrane

Hui-Hsin Tseng[a,b], Kaimin Shih[c], Pei-Ting Shiu[d], Ming-Yen Wey[d,*]

[a] School of Occupational Safety and Health, Chung Shan Medical University, Taichung 402, Taiwan, ROC
[b] Department of Occupational Medicine, Chung Shan Medical University Hospital, Taichung 402, Taiwan, ROC
[c] Department of Civil Engineering, Hong Kong University, Haking Wong Building, HKU, Hong Kong
[d] Department of Environmental Engineering, National Chung Hsing University, Taichung 402, Taiwan, ROC

ARTICLE INFO

Article history:
Received 16 December 2011
Received in revised form 13 February 2012
Accepted 7 March 2012
Available online 14 March 2012

Keywords:
Ceramic support
Sintering condition
Carbon molecular sieve
Gas separation
Microstructure

ABSTRACT

Polyetherimide (PEI) was used as polymeric precursor to prepare selective carbon molecular sieve (CMS) layer supported by a porous Al_2O_3 ceramic disk. The effects of the porous structure and surface roughness of the ceramic support on the interfacial adhesion and texture of the PEI/Al_2O_3-derived composite CMS membrane were investigated by modulating the sintering temperature and holding time. When the surface roughness of the ceramic support increased, the pore size and its distribution of the selective CMS layer were found to have shifted to the larger one and its roughness increased from the top to the bottom surface. This structure resulted in high permeability and low selectivity. Our results indicate that the porous structure of the ceramic support also played an important role in dominating the pore size and its distribution of the selective CMS layer, which influences the gas separation performance.

1. Introduction

Inorganic membranes, such as silica [1,2], zeolite [2,3], and carbon molecular sieve (CMS) membranes [4–6], have received much attention as advance materials in the gas separation technology due to their superior gas permeation performance and thermal and chemical stability. Among these membranes, only the CMS membrane has an amorphous construction, which consists of micrometer-to-submicrometer porous channel. Kiyono et al. [5,7] stated that the pore structure in a CMS membrane can be described as a "slit-like" structure with an idealized bimodal pore distribution. These pores include continuous smaller porous channel of 4–6 Å sub-micropores, connected to 6–20 Å micropores, where the micropores can improve the diffusibility of the gas in the membrane and the sub-micropores can ensure high membrane selectivity. This bimodal structure enables the CMS membrane to possess superior properties for the separation of smaller gas molecules with similar dimensions (for example, H_2, CO_2, O_2, and N_2). Two main factors, namely, selecting the polymer precursors [8–10] and controlling the pyrolysis conditions [11–13], are usually evaluated for production of porous CMS membrane for the control of the microstructure of porous CMS membrane to attain certain microporosity in the molecular dimension. Moreover, due to low mechanical strength, the CMS membrane typically uses porous materials (like alumina) as support layers, forming a complete and defect-free carbon membrane, as well as increasing the mechanical strength of the membrane. However, based on our operation experience, the gas permeation and selection behaviors of the CMS membrane are obviously affected by the support microstructure, because the support structure will influence the microstructure of CMS selective layer.

From the interfacial behavior viewpoint, the support structure and its surface roughness also play important roles in determining the pore size distribution of the composite membranes [14]. Wei et al. [15] coated the polymeric membrane on the surface of an inorganic ceramic substrate to overcome the deformation caused by swelling and studied the effect of roughness on the ceramic substrate. The results indicated that when the polymeric membrane was completely coated on the substrate surface, no deformation occurred. The authors further controlled the polishing duration to obtain different levels of substrate surface roughness and evaluated its influence on adhesion. Their results indicated that polishing reduced the number of ceramic surface flaws and improved interfacial adhesion, and the mechanical strength of the polymer/ceramic composite membrane accordingly increased.

* Corresponding author at: National Chung Hsing University, Department of Environmental Engineering, 250 Kuo Kuang Rd., Taichung 402, Taiwan, ROC.
Tel.: +886 4 22852455; fax: +886 4 22862587.
E-mail address: mywey@dragon.nchu.edu.tw (M.-Y. Wey).

0376-7388/$ – see front matter © 2012 Elsevier B.V. All rights reserved.
doi:10.1016/j.memsci.2012.03.014

Wei et al. [16] also stated that the surface roughness of the support is an important factor in preparing a defect-free membrane because the defects of the substrate will be transferred to the top separation layer. They applied a coat of alcohol solution of novolac phenol–formaldehyde resin on a porous resin support from the same material. The crack on the composite CMS membrane was dramatically reduced because the top layer and the support had similar constriction during carbonization.

Hamad et al. [17] further addressed the influence of pore penetration by covering the support with polymeric doping solution. They used porous polyethersulfone (PES) polymers as substrates to prepare polyphenylene oxide (PPO)/PES asymmetric membranes and compared the difference in gas permeation behaviors with a symmetric (pure PPO) one. The results indicated that the gas leakage through the interstitial void space was minimized due to the densification and compaction of the polymer adjacent to the support membrane interface, and the selectivity was enhanced as a direct result of the solvent evaporation from the substrate into the air. The surface of the substrate swelled, followed by shrinkage, resulting in a compressive force that worked at the bottom of the coating film.

Huber et al. [18] also studied the effect of pore size distribution of support materials and found that evenly distributed pore sizes led to better support. Moreover, the even distribution of the pore size enabled the membrane to cover completely the pores of the substrate during deposition.

The structure of the Al_2O_3 ceramic is mainly dominated by the sintering parameters, such as sintering temperature and dwell time, which affect the particle movements attributed to full density, grain coarsening, and pore closing [19]. As the temperature increases to over 1000 °C, rapid densification with limited grain growth first occurred, followed by rapid grain growth with little densification at higher temperature [19,20]. However, when the temperature rises to 1500 °C, the structure becomes dense, resulting in significant reduction in the pore volume [20]. In the current paper, the effect of the Al_2O_3 support structure on the microstructure of CMS selective layer is explored to optimize its performance and the applied process conditions. The porous structure and the surface roughness of the ceramic support were modulated by controlling the sintering temperature and the dwell time. In the course of the experiment, the sintering temperature of the support was varied from 900 °C to 1200 °C to prevent the mass transfer resistance through the support layer from densification behavior of the sintered body and the corresponding effects on the overall mass transfer behavior of the membrane.

2. Experimental

2.1. Materials

The pure polymer precursor PEI (Mw. of repeated unit = 592 g/mol) was purchased from Aldrich Co., U.S. The structure of this polymer is shown in Fig. 1. The N-methyl-2-pyrolidone (NMP) solvent was purchased from Mallinckrodt Chemicals Co., U.S., and was used without further purification. The alumina disk, with an average pore size of 0.14 μm, a thickness of 1.4 mm, and a diameter of 23 mm, was purchased from Ganya Fine Ceramics Co., Taiwan, and was used as bare support.

2.2. Preparation

Batches of five obtained bare disk supports were first heat-treated in air at 800 °C for 2 h to remove the agglutinant. Then, these samples were sintered at four different temperatures, namely, 900, 1000, 1100, and 1200 °C in air for 1 and 2 h in a tube furnace (Thermolyne, F59348, U.S.). The resulting supports were kept in a dry oven before use.

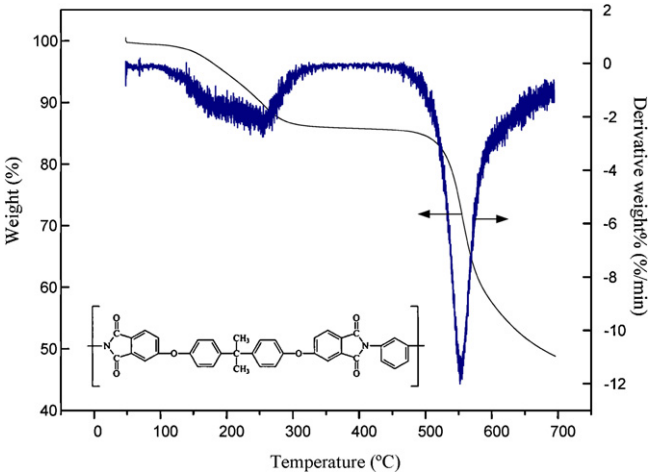

Fig. 1. Chemical structure and TGA and DTA curves of the PEI polymer.

The PEI/ceramic composite CMS membranes were prepared using the conventional spin coating method, similar to that in our previous study [8,21]. A 10% PEI coating solution was prepared by dissolving it in NMP and continuously stirring in the temperature range of 60–80 °C for 12 h. Subsequently, the solution was degassed in a vacuum system to avoid the existence of gas bubbles. The PEI solution was coated on the surface of the Al_2O_3 support using spin coating technique. After drying at room temperature for 24 h, the polymer/ceramic composite membrane was formed. Subsequently, the polymer membrane was characterized by thermogravimetric analyzer (TGA) to determine the pyrolysis temperature program. As shown in Fig. 1, the pyrolysis takes place in two stages: (a) the first decomposition step occurs between 150 and 250 °C and it may due to the removing of excess solvent. The weight loss is around 15%; (b) in the second stage, hydrocarbon releases occur and is thought to create a three-dimensional porous network. The weight loss ceases at a temperature of around 650 °C. Therefore, the composite polymer membranes were first cured at 240 °C for 6 h (heating rate: 5 °C/min). Then, the membranes were pyrolyzed at 600 °C under a vacuum system (heating rate: 5 °C/min) maintained at this final temperature for 2 h. Finally, all the CMS membranes were kept in a moisture buster to isolate them from moisture and dust before use.

2.3. Characterization

The textural property of the support was measured using N_2 sorption at −196 °C with a PMI Automated BET Sorptometer (201AEL). The X-ray diffractograms (XRDs) of all support sintering at different temperatures and their derived composite CMS membrane were recorded at room temperature with Cu Kα source (λ = 1.5418 Å) using X-ray powder diffractometer (PW1830, Philips) in a wide range of Bragg angle ($20° \le 2\theta \le 70°$) with a 2°/min scanning rate. The surface roughness was acquired using noncontact-mode atomic force microscopy (AFM) with a Dualscope/Rasterscope C26, DME, Denmark scanner. The mean roughness (Ra) of the captured surface was calculated based on the following equation: $Ra = (1/L_xL_y)\int_0^{L_x}\int_0^{L_y}|f(x,y)|\,dx\,dy$, where $f(x, y)$ is the surface relative to the center plane and L_x and L_y are the dimensions of the surface. The center plane is the plane where the volumes above and below it are equal. The surface morphology and cross-sectional images of the PEI/ceramic-derived composite CMS membranes were examined using field emission scanning electron microscope [(FE-SEM), JSM 5600].

2.4. Evaluation of performance

The gas permeance performance of the composite CMS membrane was investigated using the standard vacuum time-lag method [22,23] through different gases at 25 °C and a feed pressure of 2 atm, which were similar to those in our previous study [8,21]. The gases included the following: H_2 (2.8 Å), CO_2 (3.3 Å), O_2 (3.46 Å), N_2 (3.64 Å), and CH_4 (3.8 Å) (the values in parentheses correspond to the kinetic diameter of each gas). Before the permeation test, the composite membranes were masked using impermeable aluminum tape with a predetermined area (3.14 cm^2), and epoxy sealant was then carefully applied at the interface between the tape and the membranes to prevent any gas leak. The composite membrane was attached to a permeation cell (25 mm disk filters, Millipore, U.S.) and was degassed by exposing both sides of the membrane to vacuum for 6 h. After degassing, high-purity penetrant, supplied from the compressed gas cylinders, was introduced into the upstream side of the membrane. The variation in the downstream pressure was recorded using a pressure transducer and digital equipment connected to a computer. The permeability coefficient P was expressed in Barrer (1 Barrer = 1×10^{-10} cm^3 (STP) cm cm^{-2} s^{-1} $cmHg^{-1}$), calculated by the following equation:

$$P = \frac{dp}{dt}\left(\frac{V \cdot T_0 \cdot L}{P_0 \cdot T \cdot \Delta p \cdot A}\right) \quad (1)$$

where V is the calibrated downstream volume (cm^3), dp/dt is the steady-state pressure rise rate, Δp is the membrane side pressure difference (cmHg), A is the membrane area (cm^2), L is the membrane thickness (cm), T is the measured temperature (K), and P_0 and T_0 are the standard pressure (76 cmHg) and temperature (273 K), respectively. The ideal selectivity for gas A to gas B is defined as

$$\alpha_{A/B} = \frac{P_A}{P_B} \quad (2)$$

The average value and standard deviation were determined from six samples of two batches.

Table 1
The effect of sintering parameters on the crystal size of the Al_2O_3 supports.

Support code	Crystal size (nm)	Support code	Crystal size (nm)
S900-1	40.3 ± 1.09	S900-2	49.3 ± 0.92
S1000-1	44.9 ± 1.31	S1000-2	39.8 ± 0.17
S1100-1	51.1 ± 0.24	S1100-2	45.3 ± 0.23
S1200-1	56.2 ± 0.83	S1200-2	52.7 ± 1.19

The data were calculated base on the three times measurement results.

3. Results and discussion

3.1. Characterization of Al_2O_3 support

3.1.1. XRD analysis

The α-Al_2O_3 support was characterized using XRD, BET, SEM, and AFM to evaluate their potential as membrane supports. Based on the results of XRD patterns (not shown here, the XRD pattern depends neither on temperautre nor on holding duration), all the alumina supports are of a pure phase with no other phase detected in the scanning range, which indicates good homogeneity and crystallization of the samples. The alumina phase was identified using appropriate standard diffraction patterns (JCPDS 46-1212), and the results indicated that all the reflection peaks showed the occurrence of crystalline α-Al_2O_3 phase.

The crystal size of the different Al_2O_3 supports estimated by the Scherrer formula from XRD data are given in Table 1. The influence of sintering temperature (900–1200 °C) was studied while maintaining the dwell-time duration. For the 1 h dwell time, the support sintered at 900 °C had a crystal size of approximately 40.3 nm. When the sintering temperature increased, the crystal size progressively increased, reaching 56.2 nm for the support sintered at 1200 °C. Shirsath also obtained similar result in his literature report [24]. However, similar upward trend was not observed for the 2-h-dwell time-treated samples.

The influence of dwell times (1 and 2 h) on the crystal size is also shown in Table 1. At 900 °C, the crystal size regularly increases with the increase in dwell time from 40.3 nm to 49.3 nm. When the sintering temperature increases to 1200 °C, the crystal size slightly decreases with the increase in the dwell time. This result indicates that prolongation of dwell time at higher sintering temperature does not significantly promote the growth of crystal lattice when

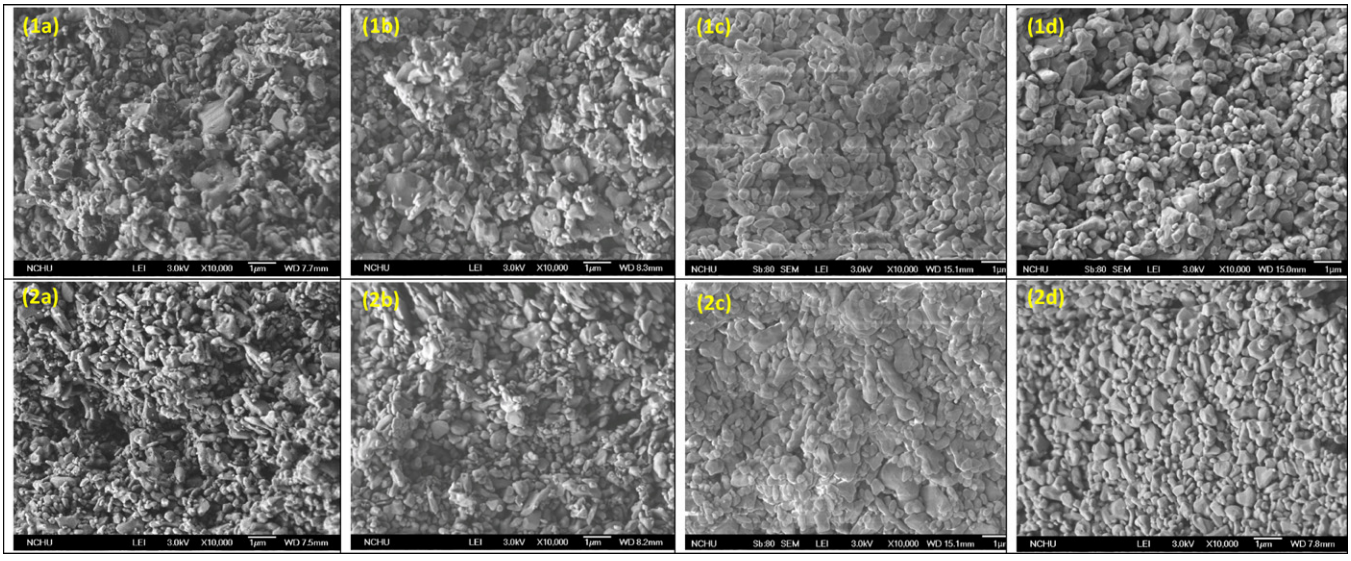

Fig. 2. FE-SEM micrographs of the surface view of Al_2O_3 support sintered at different dwell times: (1) 1 h and (2) 2 h, and different temperatures: (a) 900 °C, (b) 1000 °C, (c) 1100 °C, and (d) 1200 °C.

the Al_2O_3 support is sintered at the temperature range from 1000 °C to 1200 °C. Conclusion can be made that the increases in the sintering temperature and the dwell time are not significantly in altering the crystal size of Al_2O_3, and the crystal size of Al_2O_3 were ranged from 40 to 56 nm.

3.1.2. FE-SEM analysis

The alumina support used in the current work is the green disk obtained by pressing the α-Al_2O_3 grain under higher pressure. To improve the bonding energy between particles, the size distribution of the α-Al_2O_3 grain was divided into two groups; the fine grains ranged from 0.2 μm to 0.5 μm, and the coarse grain ranged from 1 μm to 1.5 μm. Therefore, some pores appeared in the internal structure of the green disks (as shown in Fig. 2). Using the previously mentioned sintering process, the alumina grain undergoes growth or densification, which changes the microstructure of the alumina and simultaneously improves the mechanical strength of the support.

Fig. 2 shows the FE-SEM micrographs of the Al_2O_3 support sintered at different conditions. Most of the particles appear oval in shape, and some coarse grains are present. As the sintering temperature increases to 1200 °C, the microstructures of the support become denser than those sintered at low temperature under the same dwell time; the support sintering at 1200 °C shows a significantly increasing particle size, which results in a dense sintering body. On the other hand, the support sintered at the same temperature but at different dwell time did not show any change in surface texture.

Sagar et al. also indicated that sintering generally decreases the lattice defects and cause coalescence of crystallites, resulting in increase of the average size of the nanoparticles [24]. In general, the mass transport diffuses along the grain boundaries and through the lattice of the grains during sintering, resulting in the increase of grain size and production of neck growth [25,26], that is, growth of the grain size.

3.1.3. BET analysis

The influence of different sintering conditions on the reduction of macropore, mesopore, and micropore volumes of the α-Al_2O_3 support were evaluated through N_2 adsorption/desorption isotherm. The analytic results are shown in Fig. 3. All the macropore [Fig. 3(a)], mesopore [Fig. 3(b)], and micropore [Fig. 3(c)] volumes of the Al_2O_3 support show a downward trend with the rise in sintering temperature. When the sintering temperature increases from 1100 °C to 1200 °C, a turning point appears in the temperature–pore volume curve. Further, the extent of reduction of the pore volume for the 2 h dwell time is larger than that for the 1 h dwell time. The considerable reduction in the pore volume can be attributed to densification after the sintering temperature reaches over 1100 °C. Immediately after the growth of crystalline size, the neck grows to a value such that rearrangement of the grains subsequently occurs [27]. Thus, presumption can be made that porosity reaches a certain value where rearrangement of the grains can occur when the sintering temperature increases to 1200 °C.

Fig. 4 shows the shrinkage percentages of the support sintered at different conditions. The shrinkage percentage is defined as $(1-(H/H_0))\times 100\%$, where H is the thickness of the support after sintering and H_0 is the thickness of the green disk. The shrinkage percentages of the support directly increase with sintering temperature, and they dramatically increase at temperatures higher than 1000 and 1100 °C, which suggest that the ceramic has lost its original high porosity. This rapid change is attributed to the gradual growth of grain and the subsequent collapse of the pores. As a result, supports with bigger shrinkage percentages have dense microstructures.

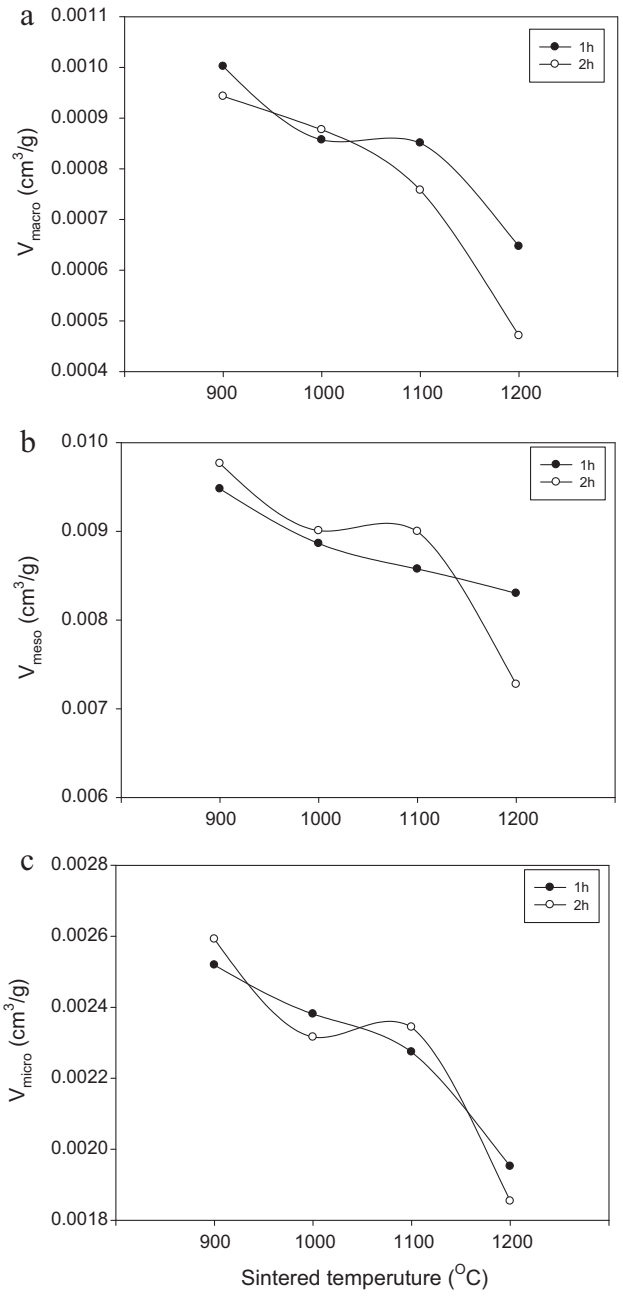

Fig. 3. Influence of sintering conditions on the development of (a) macropore, (b) mesopore, and (c) micropore volumes.

3.1.4. Surface roughness

To explore the influence of grain growth on the surface roughness coefficient (*Ra*) of the support, AFM was employed in the current study. As shown in Fig. 5, when the sintering temperature rises from 900 °C to 1000 °C, the surface roughness of the support shows a clear upward trend, with *Ra* increasing from 50.0 nm to 116.6 nm. Fig. 5(1b) shows some bigger nodules present at the surface of the support sintered at 1000 °C. However, when the temperature increases from 1000 °C to 1200 °C [Fig. 5(1d)], the grains are orderly arranged on the surface of the support, and the surface becomes smoother, resulting in the drop of *Ra* from 116.5 nm to 55.0 nm.

By integrating the XRD, BET, AFM and SEM results, the alumina grain size and the microstructure of the support are shown to be dominated by the sintering temperature, as shown in the

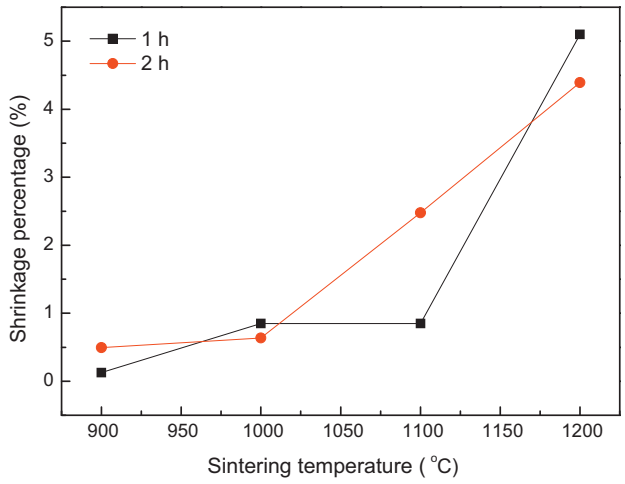

Fig. 4. Shrinkage percentages of Al_2O_3 support sintered at different conditions.

schematic diagram of Fig. 6. The variation in the microstructure that depends on the sintering temperature can be divided into three types, namely, (1) crystal growth, (2) neck growth, and (3) rearrangement of grain. When the sintering temperature rose from 900 °C to 1000 °C, the crystal size increased, leading to grain coarseness and resulting in the increase of the surface roughness and decrease in the pore volume. When the sintering temperature increased to 1100 °C, neck growth occurred though surface diffusion between grains. Generally, the increase in average size of the grains is always accompanied by the disappearance of some grains, usually the smaller ones [28]. The neck growth, therefore, resulted in the diminishing of the roughness between coarse and fine grains. When the sintering temperature rose to 1200 °C, the rearrangement of the grains produced a dense structure, favoring the shrinkable pores due to the compressed grain growth behaviors. Such an increase also resulted in averaging of the grain size and decrease in the surface roughness of the carrier. Therefore, the movements of the crystal/grain have different features at each stage attributed to grain coarsening, pore closing, and full density, which will influence the gas permeation behavior through the support materials.

3.2. Gas permeation behavior of the support

The gas permeability and selectivity of the Al_2O_3 supports were evaluated based on pure gases with different molecular weights and dimensions to predict the transport mechanism. These gases are as follows: H_2 (2 g/mol, 2.8 Å), CO_2 (44 g/mol, 3.3 Å), O_2 (32 g/mol, 3.46 Å), N_2 (28 g/mol, 3.64 Å), and CH_4 (16 g/mol, 3.8 Å) (the values in the parentheses show the molecular weights and kinetic diameters, respectively). Fig. 7 shows the permeability as a function of the root of the reciprocal of the molecular weight of each gas $[(1/M)^{1/2}]$. The results showed a high gas permeability, which decreased with the increase in the sintering temperature and dwell time. Further, Fig. 7 shows that the permeabilities of these five gases decreased with the increase in the gas molecular weights. Compared with the theoretical selectivity of the Knudsen diffusion mechanism, only a few results of the gas selectivity (such as O_2/N_2 and CO_2/CH_4) are similar to the Knudsen selectivity value. The rest are all lower than the theoretical selectivity (Table 2), which indicated that gas transport through the different Al_2O_3 supports occurred according to the Knudsen mechanism

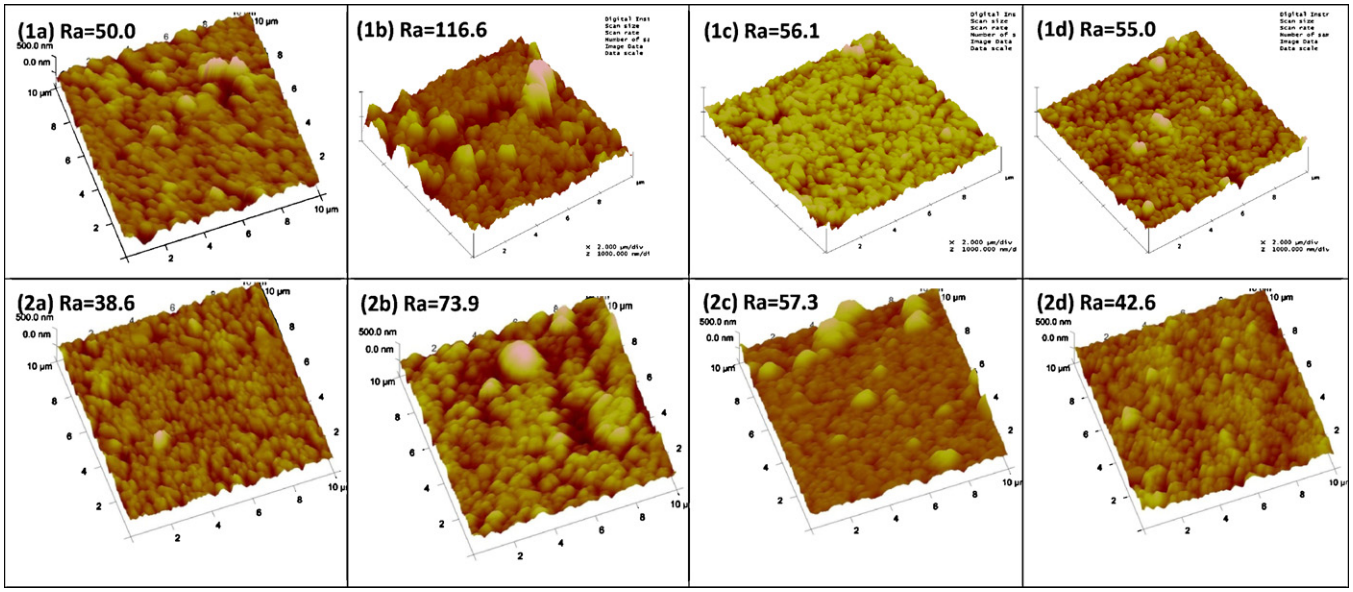

Fig. 5. AFM images of Al_2O_3 support sintered at different dwell times: (1) 1 h and (2) 2 h, and different temperatures (a) 900 °C, (b) 1000 °C, (c) 1100 °C, and (d) 1200 °C.

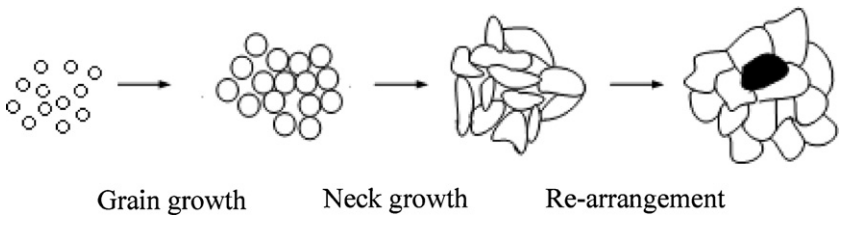

Fig. 6. Grain growth, neck growth, and grain rearrangement of Al_2O_3 support as a function of the sintering temperature.

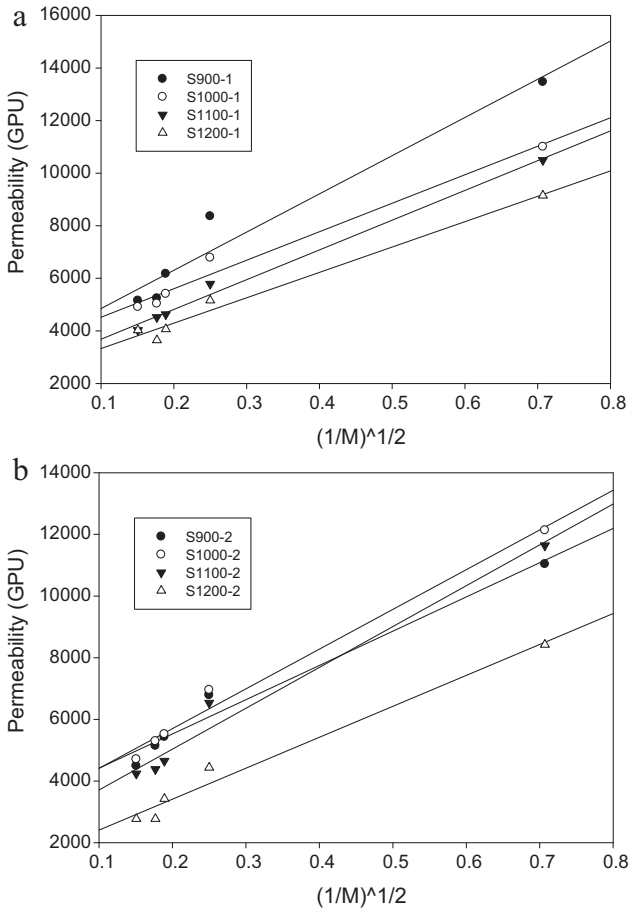

Fig. 7. Gas permeability through Al_2O_3 support sintered at different dwell times: (a) 1 h and (b) 2 h as a function of Knudsen transport mechanism (*M*: molecular weights of the gases).

and/or the Poiseuille flow [16]. Thus, the microstruc1ture of Al_2O_3 supports is significantly reduced by the sintering treatment, and the pores have a size bigger than that of the mean free path of gas molecules.

3.3. Gas permselectivity of composite CMS membrane

Figs. 8 and 9 show the influence of the microstructure of Al_2O_3 support on the permeability and selectivity of the composite CMS membrane. Fig. 8 shows that the gas permeability through the membrane correlated with the kinetic diameter, instead of the molecular weight of the gas molecules, and decreased as the kinetic diameter increased. These results indicated that the microstructures of the CMS selective layer are in molecular dimensions, which allowed the separation of gases by the molecular sieve mechanism.

Further, Fig. 8 shows that when the sintering temperature of the support rises from 900 °C to 1000 °C, the permeability of all gases increased; for example, the permeability of H_2 increased from 1203 Barrer to 2291.1 Barrer and that of CH_4 increased from 15.1 Barrer to 240.8 Barrer. Meanwhile, as the sintering temperature rose from 1000 °C to 1200 °C, the permeability decreased; that of H_2 dropped from 2291.1 Barrer to 1014.7 Barrer and that of CH_4 dropped from 240.8 Barrer to 23.2 Barrer. The separation efficiency clearly indicates that an increase in the gas permeability is accompanied by a decrease in the selectivity for all gases when the sintering temperature rises to 1000 °C, as shown in Fig. 9. When the temperature rose again to 1200 °C, the gas permeability decreased, and an increase in selectivity can be found. For the permselectivity of the composite CMS membrane pretreated at different sintering conditions, especially at different temperature under the same dwell time, in spite of the existence of the change of permeability, the influence of sintering temperature is dominant.

The dependence of permeation temperature on gas permeability of the composite CMS membrane supported by different Al_2O_3 supports is shown in Fig. 10 with an Arrhenius plot. For H_2 and CO_2 gases, the gas permeabilities increases with permeation temperature, indicating that the gas transport mechanism takes place according to an activated process, as expected in a molecular sieving membrane [29]. Consequently, the apparent activation energies (indicated in the figure) calculated by the Arrhenius equation increase with the kinetic diameter of H_2 and CO_2 penetrant gases. CMS1000-1 is found to have lower apparent activation energies for H_2 and CO_2 penetrant gases, indicating that the gas molecules require considerably less energy to penetrate through CMS1000-1. However, the variation of CH_4 permeance with temperature exhibits a decrease with temperature increased while through the CMS1000-1, CMS1100-1, and CMS1200-1 membranes, and the values of the apparent activation energy depends neither on the *d*-spacing nor on the permeability of composite CMS membranes (see Section 3.4). It is well known that the permeabilities of adsorbable gases (condensation temperature H_2 = 60 K, CO_2 = 195 K, and CH_4 = 149 K) is mainly determined by the solubility term (a thermodynamic factor, dependent on the Lennard–Jones potential) [23]. Therefore, this behavior is typical of systems where gas adsorption on the membrane occurs and as a consequence the CH_4 transport through membrane takes places as a combination of gas diffusion and superficial diffusion at a temperature around 25–110 °C.

Table 2
Selectivity of Al_2O_3 support sintered at different conditions.

Support code	Ideal selectivity				
	H_2/CH_4	H_2/N_2	O_2/N_2	CO_2/CH_4	H_2/CO_2
S900-1	1.6	2.2	0.8	0.6	2.6
S1000-1	1.6	2.0	0.9	0.7	2.2
S1100-1	1.8	2.3	1.0	0.7	2.6
S1200-1	1.8	2.2	0.9	0.8	2.3
S900-2	1.6	2.0	0.9	0.7	2.5
S1000-2	1.7	2.2	1.0	0.7	2.6
S1100-2	1.8	2.5	0.9	0.6	2.7
S1200-2	1.9	2.5	0.8	0.6	3.0
Knudsen selectivity[a]	2.83	3.74	0.94	0.77	4.69

[a] The selectivity was predicted from Knudsen transport mechanism by the following equation: $\alpha_{AB} = \sqrt{M_B/M_A}$.

3.4. Microstructure of the carbon membrane

The gas permeation results indicate that the support structure has the effect of predominantly improving the gas permselectivity due to the enhancement of gas diffusivity. These results are consistent with the variation of the surface roughness of Al_2O_3 supports sintered at different conditions. Comparing with the surface roughness illustrated in Fig. 5, it clearly indicated that as the surface roughness of Al_2O_3 support increased, the permeability increased and the selectivity decreased; while the roughness decreased, the permeability decreased and the selectivity increased. This result suggests that enhanced permeability or selectivity is most likely inherent to the surface roughness of Al_2O_3 supporting layer. Therefore, in this section, the influence of the Al_2O_3 support roughness on the preparation of defect-free carbon membranes is first discussed.

Fig. 11 shows the typical SEM microphotographs of the composite CMS membranes. The composite CMS membranes with different microstructure supports have no significant differences

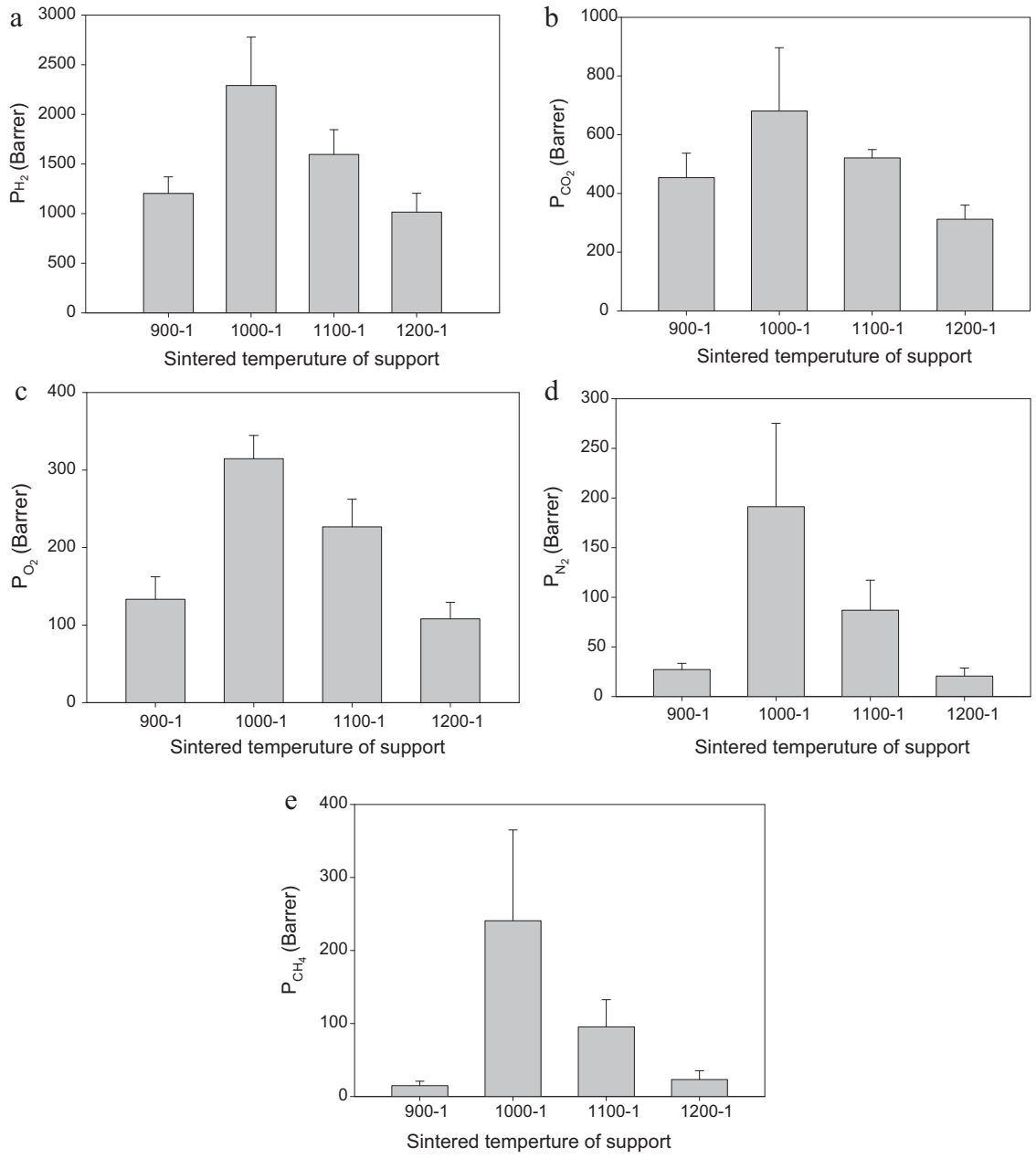

Fig. 8. Influence of microstructure of Al_2O_3 supports on gas permeability through composite CMS membranes: (a) H_2, (b) CO_2, (c) O_2, (d) N_2, and (e) CH_4.

in the surface and cross-sectional views of the carbon selective layer (the CMS1200-1 is considered as an example). Further, the images also indicate that the surfaces of the different supports are all completely covered with carbon selective layer, which was continuous and crack-free. This result suggests that the thickness of the precursor polymer thin film is bigger than the roughness of the Al_2O_3 support (*Ra* is from 38.6 nm to 116.6 nm); therefore, after pyrolysis treatment, the carbon selective layer can completely cover the support surface, and a defect-free film is formed.

Further, the thicknesses of carbon selective layers also increased with the increase in roughness. Table 2 shows that as the roughness of the Al_2O_3 support increases from 50.0 nm to 116.6 nm, the carbon layer thickness increases from 2.737 μm to 4.350 μm. In contrast, as the roughness decreases, the thickness also decreases. This phenomenon can be explained by the following:

Wei et al. [15] quantified the interfacial adhesion among polymer/ceramic supports for composite membrane and indicated that the mechanical interlocking and the interfacial chemical bonds were the two key factors responsible for interfacial adhesion. The additional contact area between the rough ceramic support and the polymer separation layer gave rise to higher interfacial adhesion. As a result, increasing the surface roughness improved the interfacial adhesion between the polymer/ceramic supports interface. Therefore, deduction can be made that during the spin coating process, the polymer doping solution may have sprayed out when the support with smoother surface was used and then leave small amount of polymer precursor on it. Further, the Wenzel [30] model indicated that the hydrophilicity of a wettable solid is strengthened with the increase in roughness, preventing the doping solution to penetrate easily into the pore volume of Al_2O_3 supports due to the repulsive interaction between the polar Al_2O_3 and non-polar PEI/NMP doping solutions. Therefore, a large amount of doping solution is left on the surface of the Al_2O_3 support, hence enlarging the thickness of the carbon layer. As a consequence, the membrane

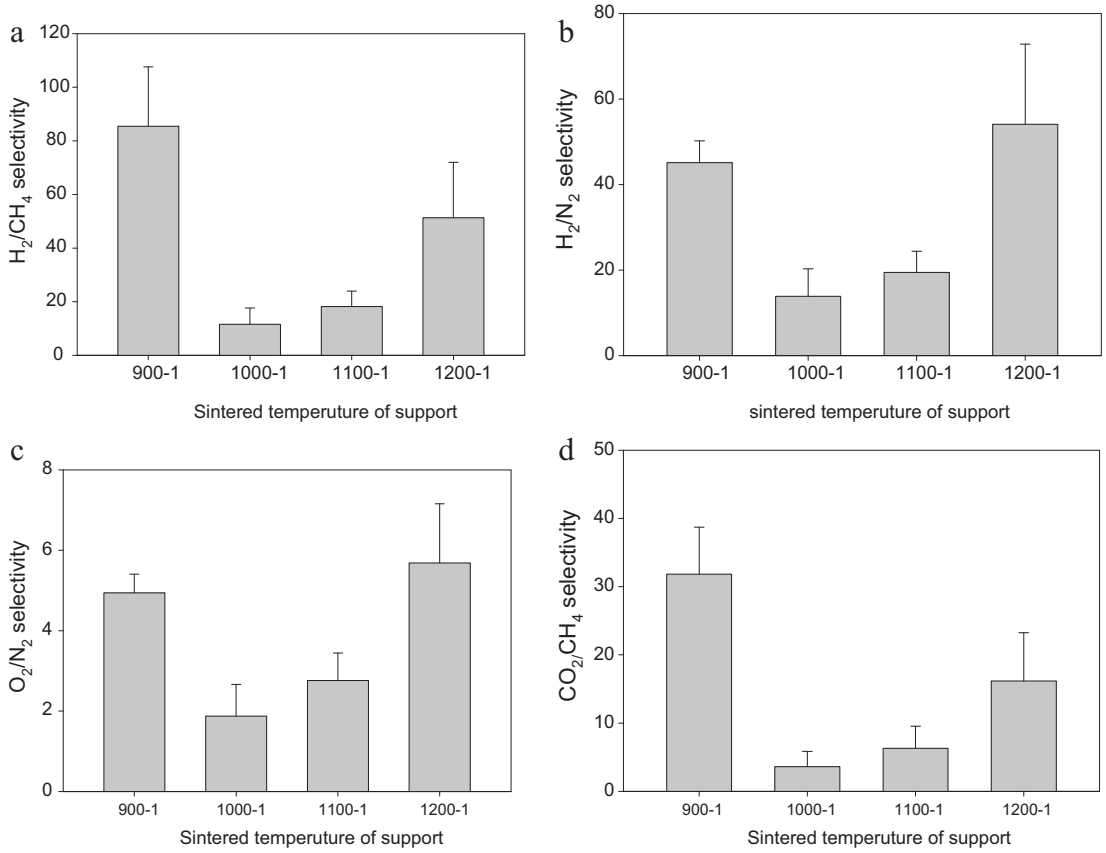

Fig. 9. Influence of microstructure of Al_2O_3 supports on gas selectivity through composite CMS membranes: (a) H_2/CH_4, (b) H_2/N_2, (c) O_2/N_2, and (d) CO_2/CH_4.

thickness reaches the maximum when the roughness of the Al_2O_3 support approaches 116.6 nm.

The formation process of the carbon selective layer was comprehensively investigated in previous studies [7,31,32]. The microstructure of the CMS membrane was piled out with polymer chain. The pore mouth, often referred to as an ultramicropore (<10 Å), is the distance between atoms in neighboring planes [22]. In the current study, PEI was used as the polymer precursor, and its chemical structure is shown in Fig. 1. PEI is a linear chain with plastic property, which is favorable for the preparation of a nonporous dense layer. Such property enables the PEI to melt during pyrolysis and effectively eliminates the pinhole in the dense layer. Table 3 shows the *d*-spacing (d_{002}) values of all composite CMS membranes providing the interlayer distance of the carbon membranes. The interlayer distance can be considered as a pore for the gas molecule transport through the carbon membranes. The composite CMS membranes gave broad XRD patterns, and the average *d*-spacing values for CMS900-1 and CMS1000-1 increased from 4.10 Å to 4.27 Å and consequently decreased to 3.90 Å for CMS1200-1, consistent with the results of the surface roughness of Al_2O_3 supports as discussed earlier. The results indicate that the microstructure of CMS1000-1 is bigger than the others and is less orderly and tightly arranged. The height fluctuation of the support surface nodule causes the polymer chain to be arrayed irregularly due to the rough surface of S1000-1, suggesting that effective transport of gas molecules through the microstructure can be obtained in CMS1000-1. On the contrary, the low surface roughness reduces the number of support surface flaws and improves the tight piling up of the polymer chain. Therefore, the large membrane thickness and *d*-spacing were both contributed to the high permeability and low selectivity.

3.5. Gas permeation properties of the alumina-supported CMS membranes

Fig. 12 shows the trade-off relationship between the H_2 permeability and the H_2/CH_4 selectivity for various composite CMS membranes with the reference data at around 298 K [33,34]. All the CMS membranes supporting on different Al_2O_3 substrates prepared in the current study exhibited an excellent performance

Table 3
Surface roughness, thickness and *d*-spacing of carbon layer supporting on various Al_2O_3 supports with different sintering treatment.

Membrane code	Ra of bottom surface (nm)	Ra of top surface (nm)	Carbon layer thickness ((m)	*d*-Spacing (Å)
CMS900-1	50	97.9	2.737	4.10
CMS1000-1	116.6	180	4.350	4.27
CMS1100-1	56.06	34.8	3.450	4.08
CMS1200-1	55	31	3.600	3.90
CMS900-2	38.6	134	1.819	4.07
CMS1000-2	73.9	135.3	3.956	4.22
CMS1100-2	57.3	77.8	3.731	4.20
CMS1200-2	42.6	80.4	2.719	4.15

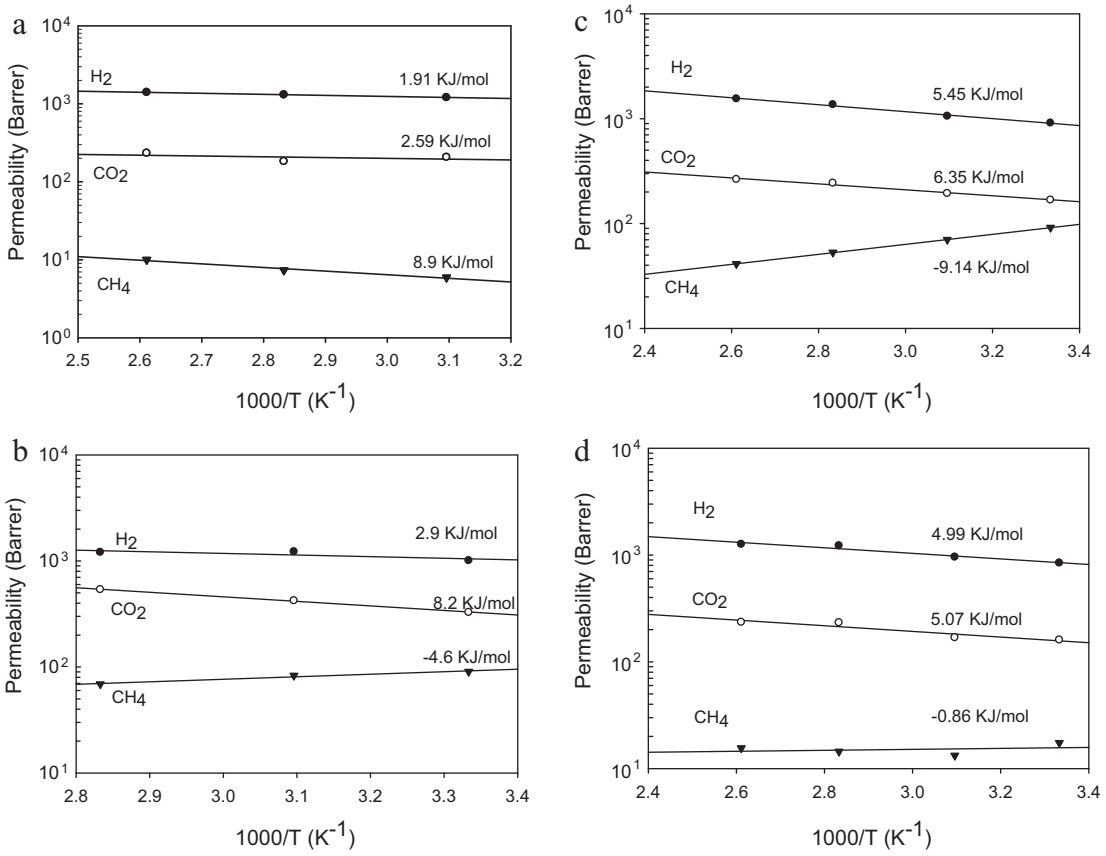

Fig. 10. Variation of gas permeability with temperature in an Arrhenius plot obtained from composite CMS membrane supported on different Al_2O_3 sintered at (a) 900 °C, (b) 1000 °C, (c) 1100 °C, and (d) 1200 °C. The indicated values correspond to the apparent activation energies.

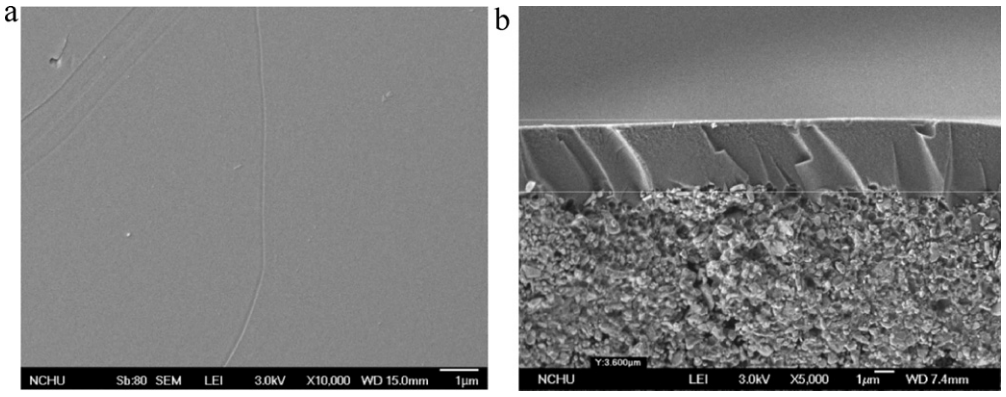

Fig. 11. FE-SEM morphology of CMS1200-1: (a) surface view and (b) cross-sectional images.

Table 4
Performance comparison of CMS membranes prepared in this work with those in the literature.

CMSM/support	Pyrolysis temperature (°C)	Test temperature (°C)	$P(CO_2)$ (Barrer[a])	CO_2/CH_4	Reference
PEI/Al_2O_3	600	27	1046	27.6	This work
PEI/carbon	800	25	–	25	[35]
PEI/ceramic tube	600	25	31	61	[36]
Polyimide/porous graphite	550	25	18	37.4	[37]
polyimide/silicon wafer	600	35	1032	38	[38]
Polyimide/Al_2O_3	500	25	8	100	[39]

[a] 1 Barrer = 10^{-10} cm^3 (STP) cm cm^{-2} s^{-1} cmHg.

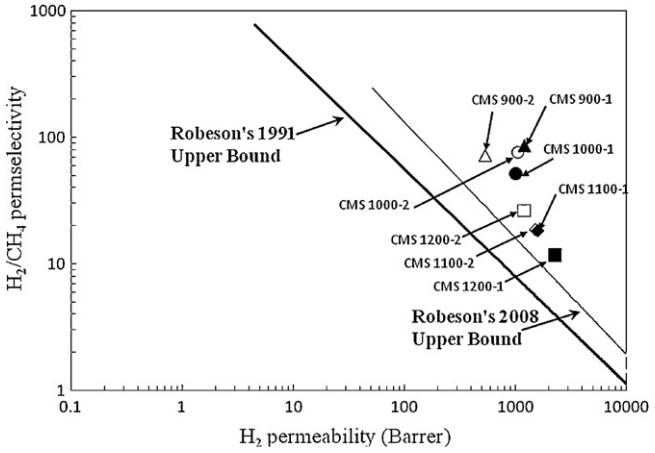

Fig. 12. Trade-off relationship between the H_2 permeability and the H_2/CH_4 selectivity for various CMS composite membranes compared with the reference data at approximately 295 K.

comparable with that of the upper bound of the conventional polymer membranes. The permeability and selectivity of carbon membranes from the literature are shown in Table 4 for comparison with the present work [35–39]. Although the selectivity of the present membrane is not impressive compared with other membranes in the literature, the merit of using Al_2O_3 support with different microstructures is clear because the selectivity of the present membrane was significantly influence by the microstructure of support layer and the reproducibility of defect-free carbon membranes was improved.

4. Conclusions

The microstructure of Al_2O_3 substrate controlled by different sintering conditions has been shown to influence significantly on the gas permeability of supporting carbon layer. In previous permeation models, the influence of the support layer on gas separation has often been neglected or overly simplified due to the high velocities inside the support [40]. The transport mechanism of gas molecules in the porous support is a combination of the Knudsen and Poiseuille flows, which offers a smaller or negligible resistance to gas molecules. However, in the present work, the results indicated that the performance of PEI/Al_2O_3-derived composite CMS membrane is strongly influenced by the support structure because of its different surface roughness and hydrophilicity will result in different microstrucutre of CMS selective layer. The height fluctuation of the support surface nodule causes the polymer chain to be arrayed irregularly and results in large *d*-spacing values of CMS selective layer, which suggests that effective transport of gas molecules through the microstructure can be obtained. Although the selectivity of the present membrane is not impressive compared with other membranes in the literature, the further study to improve the selectivity of CMS membranes is being conducted based on this concept.

References

[1] M.J. Muñoz-Aguado, M. Gregorkiewitz, Preparation of silica-based microporous inorganic gas separation membranes, J. Membr. Sci. 111 (1996) 7–18.
[2] J.C. Poshusta, R.D. Noble, J.L. Falconer, Temperature and pressure effects on CO_2 and CH_4 permeation through MFI zeolite membranes, J. Membr. Sci. 160 (1999) 115–125.
[3] X. Xu, Y. Bao, C. Song, W. Yang, J. Liu, L. Lin, Synthesis, characterization and single gas permeation properties of NaA zeolite membrane, J. Membr. Sci. 249 (2005) 51–64.
[4] P.S. Tin, T.S. Chung, Y. Liu, R. Wang, Separation of CO_2/CH_4 through carbon molecular sieve membranes derived from P84 polyimide, Carbon 42 (2004) 3123–3131.
[5] M. Kiyono, P.J. Williams, W.J. Koros, Effect of polymer precursors on carbon molecular sieve structure and separation performance properties, Carbon 48 (2010) 4432–4441.
[6] M. Campo, F. Magalhães, A. Mendes, Carbon molecular sieve membranes from cellophane paper, J. Membr. Sci. 350 (2010) 180–188.
[7] M. Kiyono, P.J. Williams, W.J. Koros, Effect of pyrolysis atmosphere on separation performance of carbon molecular sieve membranes, J. Membr. Sci. 359 (2010) 2–10.
[8] A.K. Itta, H.H. Tseng, Hydrogen separation performance of CMS membranes derived from the imide-functional group of two similar types of precursors, Int. J. Hydrogen Energy (2011) 8645–8657.
[9] H.J. Lee, M. Yoshimune, H. Suda, K. Haraya, Gas permeation properties of poly(2,6-dimethyl-1,4-phenylene oxide) (PPO) derived carbon membranes prepared on a tubular ceramic support, J. Membr. Sci. 279 (2006) 372–379.
[10] C.J. Anderson, S.J. Pas, G. Arora, S.E. Kentish, A.J. Hill, S.I. Sandler, G.W. Stevens, Effect of pyrolysis temperature and operating temperature on the performance of nanoporous carbon membranes, J. Membr. Sci. 322 (2008) 19–27.
[11] V.C. Geiszler, W.J. Koros, Effects of polyimide pyrolysis conditions on carbon molecular sieve membrane properties, Ind. Eng. Chem. Res. 35 (1996) 2999–3003.
[12] H. Hatori, H. Takagi, Y. Yamada, Gas separation properties of molecular sieving carbon membranes with nanopore channels, Carbon 42 (2004) 1169–1173.
[13] M. Yoshimune, I. Fujiwara, K. Haraya, Carbon molecular sieve membranes derived from trimethylsilyl substituted poly(phenylene oxide) for gas separation, Carbon 45 (2007) 553–560.
[14] A. Clarke, Coating on a rough surface, AIChE J. 48 (2002) 2149–2156.
[15] W. Wei, S. Xia, G. Liu, X. Gu, W. Jin, N. Xu, Interfacial adhesion between polymer separation layer and ceramic support for composite membrane, AIChE J. 56 (2010) 1584–1592.
[16] W. Wei, G. Qin, H. Hu, L. You, G. Chen, Preparation of supported carbon molecular sieve membrane from novolac phenol–formaldehyde resin, J. Membr. Sci. 303 (2007) 80–85.
[17] F. Hamad, K. Khulbe, T. Matsuura, Comparison of gas separation performance and morphology of homogeneous and composite PPO membranes, J. Membr. Sci. 256 (2005) 29–37.
[18] F. Huber, J. Springer, M. Muhler, Plasma polymer membranes from hexafluoroethane/hydrogen mixtures for separation of oxygen and nitrogen, J. Appl. Polym. Sci. 63 (1997) 1517–1526.
[19] A.F. Ismail, K. Li, M. Reyes, M. Miguel, From polymer precursorss to hollow fiber carbon and ceramic membranes, Membr. Sci. Technol. 13 (2008) 81–119.
[20] E. Levänen, T. Mäntylä, Effect of sintering temperature on functional properties of alumina membranes, J. Eur. Ceram. Soc. 22 (2002) 613–623.
[21] H.H. Tseng, P.T. Shiu, Y.S. Lin, Effect of mesoporous silica modification on the structure of hybrid carbon membrane for hydrogen separation, Int. J. Hydrogen Energy (2011) 15352–15363.
[22] S.W. Rutherford, D.D. Do, Review of time lag permeation technique as a method for characterisation of porous media and membranes, Adsorption 3 (1997) 283–312.
[23] H.B. Park, C.H. Jung, Y.K. Kim, S.Y. Nam, S.Y. Lee, Y.M. Lee, Pyrolytic carbon membranes containing silica derived from poly(imide siloxane): the effect of siloxane chain length on gas transport behavior and a study on the separation of mixed gases, J. Membr. Sci. 235 (2004) 87–98.
[24] S.E. Shirsath, R. Kadam, A.S. Gaikwad, A. Ghasemi, A. Morisako, Effect of sintering temperature and the particle size on the structural and magnetic properties of nanocrystalline $Li_{0.5}Fe_{2.5}O_4$, J. Magn. Magn. Mater. 323 (2011) 3104–3108.
[25] J.S. Reed, Principles of Ceramic Processing, Second ed., John Wiley & Sons, New York, 1995.
[26] J.G. Santanach, A. Weibel, C. Estrournès, Q. Yang, Ch. Laurent, A. Peigney, Spark plasma sintering of alumina: study of parameters, formal sintering analysis and hypotheses on the mechanism(s) involved in densification and grain growth, Acta Mater. 59 (2011) 1400–1408.
[27] L. Tan, X. Gu, L. Yang, L. Zhang, C. Wang, N. Xu, Influence of sintering condition on crystal structure microstructure, and oxygen permeability of perovskite-related type $Ba_{0.8}Sr_{0.2}Co_{0.8}Fe_{0.2}O_3$-[delta] membranes, Sep. Purif. Technol. 32 (2003) 307–312.
[28] A.F. Ismail, K. Li, From polymeric precursors to hollow fiber carbon and ceramic membranes, Membr. Sci. Technol. 13 (2008) 81–119.
[29] H. Suda, K. Haraya, Carbon molecular sieve membranes: preparation, characterization, and gas permeation properties, Am. Chem. Soc., Chapter 20 (2000) 295–313.
[30] R.N. Wenzel, Resistance of solid surfaces to wetting by water, Ind. Eng. Chem. 28 (1936) 988–994.
[31] K. Takashi, Control of pore structure in carbon, Carbon 38 (2000) 269–286.
[32] H.C. Foley, Carbogenic molecular sieves: synthesis, properties and applications, Micropor. Mater. 4 (1995) 407–433.
[33] L.M. Robeson, Correlation of separation factor versus permeability for polymeric membranes, J. Membr. Sci. 62 (1991) 165–185.
[34] L.M. Robeson, The upper bound revisited, J. Membr. Sci. 320 (2008) 390–400.

[35] A.B. Fuertes, T.A. Centeno, Carbon molecular sieve membranes from polyetherimide, Micropor. Mesopor. Mater. 26 (1998) 23–26.
[36] M.G. Sedigh, L. Xu, T.T. Tsotsis, M. Sahimi, Transport and morphological characteristics of polyetherimide-based carbon molecular sieve membranes, Ind. Eng. Chem. Res. 38 (1999) 3367–3380.
[37] A.B. Fuertes, T.A. Centeno, Preparation of supported asymmetric carbon molecular sieve membranes, J. Membr. Sci. 144 (1998) 105–111.
[38] L. Shao, T.S. Chung, G. Wensley, S.H. Goh, K.P. Pramoda, Casting solvent effects on morphologies, gas transport properties of a novel 6FDA/PMDA-TMMDA copolyimide membrane and its derived carbon membranes, J. Membr. Sci. 244 (2004) 77–87.
[39] J. Hayashi, H. Mizuta, M. Yamamoto, K. Kusakabe, S. Morooka, S.H. Suh, Separation of ethane/ethylene and propane/propylene systems with a carbonized BPDA-pp′ODA polyimide membrane, Ind. Eng. Chem. Res. 35 (1996) 4176–4181.
[40] C.Y. Pan, Gas separation by high-flux, asymmetric hollow-fiber membrane, AIChE J. 32 (1986) 2020–2027.

附件五

科技部補助專題研究計畫出席國際學術會議心得報告

日期：103 年 10 月 10 日

計畫編號	MOST　100－2221－E－040－004－MY3		
計畫名稱	基材物化特性對碳分子篩選薄膜之孔洞結構及氣體分選能力之影響		
出國人員 姓名	曾惠馨	服務機構 及職稱	中山醫學大學/職業安全衛生系暨研究所/教授
會議時間	103 年 07 月 20 日 至 103 年 07 月 26 日	會議地點	中國蘇州
會議名稱	(中文) 第十屆國際薄膜及薄膜程序研討會 (英文) The 10th International Congress on Membranes and Membrane Process (ICOM2014)		
發表題目	1. Po-Yu Cheng, Ching-Ting Wang, **Hui-Hsin Tseng***, Ming-Yen Wey, The effect of support roughness and dope viscosity on the separation performance of CMS membrane, International Congress on Membrane and Membrane Processes (ICOM2014) July 20-25, 2014, Suzhou, China. 2. Hao-wei Chuang, **Hui-Hsin Tseng***, Kuo-Liang Chuang, Ming-Yen Wey, The effect of SBA-15 on composite PPO membrane for gas separation, International Congress on Membrane and Membrane Processes (ICOM2014) July 20-25, 2014, Suzhou, China. Nanjing Tech University. 3. Kuo-Liang Chuang, **Hui-Hsin Tseng**, Ming-Yen Wey*, Preparation and characterization of PDMS-silica membrane by non-toxic green sol–gel method for gas separation, International Congress on Membrane and Membrane Processes (ICOM2014) July 20-25, 2014, Suzhou, China.		

一、參加會議經過

本次參與 2014 年在中國舉辦的第十屆薄膜與薄膜程序國際研討會(ICOM2014)，帶領兩位研究生於 7 月 20 日抵達中國蘇州，預計於研討會議開始前先安置個人行李並確認會議場地與行程的規劃，同時也利用時間讓欲上台口頭報告之研究生有時間練習與演練，以求上台報告之穩定。此次會議地點於蘇州太湖國際會議中心所舉辦，於 7 月 20 日下午開始註冊報到，約莫 18:00 為大會開幕晚宴，在餐會中很榮幸能夠與來至中原大學的薄膜中心各位教授同桌。7 月 21 日早上開始是 Opening Ceremony，由主辦單位這一次主要由南京工業大學 (Nanjing Tech University)的 Dr. Zhenyu Chu 和 Dr. Gongping Liu 為主要的統籌。接著就是兩位著名的學者進行 Plenary Session，分別是 William J. Koros (USA)、Yiqun Fan (China)。這次報告有關以低能源密集性的薄膜途徑用於氣體分離技術和無機膜的產業流程。無機薄膜對於氣體分離和水處理上的技術與產業的現況。二氧化碳的捕捉技術仍然是世界發展的重要目標，碳

捕捉與封存技術中的薄膜技術實際應用於燃燒前與燃燒後的碳捕捉探討，可以瞭解在實際應用上，需要克服的問題，以及實際需要處理的混合氣體成分和操作環境需求與希望能夠達到的目的，這對於未來研究上給予很多的資料，目前也在有些先進國家，也已開始進行實廠的捕捉膜廠測試，和 Integrated Gasification Combined Cycle(IGCC)上的應用。本次大會領域與議題大致可分為：(1)薄膜發展(薄膜材料、薄膜合成、薄膜改植與薄膜特性)、(2)氣體分離(薄膜種類、二氧化碳捕捉技術、氣體分離程序)、(3)特殊性薄膜(陶瓷薄膜、炭薄膜、金屬薄膜、沸石薄膜、MOFs 薄膜、SRNF 與 OSN 博膜)、(4)UF/MF 薄膜程序、(5)氣體滲透蒸發薄膜、(6)模式與計算、(7)膜反應器設計與元件和(8)混合基材薄膜、(9)薄膜積垢和(10)應答型/生物性薄膜等十大類。除了各個 Session 外，會場內有設置多間廠商，也看到並了解現在產業界薄膜材料的趨向和膜組的建立。

帶領的博士班學生-莊國良，在 7/21、7/23 共報告兩篇目前的研究結果；而碩士班學生-鄭博育，在 7/24 報告一篇目前的研究結果。Prof. Li、Prof. Golemme、Prof.Yan Huang 給予兩位學生研究上的建議。在會議結束後，在主辦單位的協助下，特地準備了當地的特色料理，讓與會的各位同仁一同品嘗當地特是佳餚，在晚上的餐會中，很有幸和幾位研究學者同桌，也和來至新加坡國立大學薄膜中心的首席負責人-鍾台生老師，同時也是該校與美國麻省理工學院聯盟的董事，因此也乘此機會和鐘老師交流，談論研究經歷與對於薄膜的改質與應用技術上在未來的發展趨勢。

7 月 24 日，早上八點去聆聽來至德國的 Prof. Favre，主要講述近年來碳捕捉程序所要克服之重點與目標，在碳捕捉程序，若要達到實場化，必須考慮其經濟性與碳捕捉後之應用性，了解氣體分離程序在實廠使用實需要考慮的東西。而今晚大會也特別準備晚宴，請來當地的京劇表演。7 月 25 日，最後一天是安排專家學者的演講。也很幸運能聽到鍾院士，他是致力於新加坡海水淡化的研究，因為新加坡缺水，必須和鄰近的國家購買水源，因此勢必需要突破現階段的狀態，找到解決水源之問題，因此在他的研究之下，新加坡也已經有了初步的海水淡化工程，但仍然有進步改進的空間，如何達到大量處理與高效率的淡化程序，也勢必為重要的課題。在演講結束後，各國的專家學者，也報告了近幾年的研討會動向與新訊息，本人也期待參與下一次的國際研討會議，能吸收到更多新知，提供後續實驗室能有新創新研究。

二、與會心得

首先很感謝國科會給予經費上之補助，能夠減少出國報告之負擔。本次前往中國蘇州參加國際性學術研討會，不僅是針對不同領域做相關之見習參訪之外，對於如何前往參與研討會的事前安排諸如食衣住行等也是一種生活技能上的學習，期望政府等相關單位能持續推動國內研究人才出國參加國際研討會之政策，以增進國內學者之國際觀。

三、發表論文全文或摘要

Preparation and characterization of PDMS-silica membrane by non-toxic green sol–gel method for gas separation

Guo-Liang Zhuang[1], Ming-Yen Wey[1,]*, Hui-Hsin Tseng[2, 3]

[1]*Department of Environmental Engineering, National Chung Hsing University, Taichung 402, Taiwan, ROC*
[2]*School of Occupational Safety and Health, Chung Shan Medical University, Taichung 402, Taiwan, ROC*
[3]*Department of Occupational Medicine, Chung Shan Medical University Hospital, Taichung 402, Taiwan, ROC*

*mywey@dragon.nchu.edu.tw (M.-Y. Wey)

Polydimethylsiloane (PDMS)-silica composite membrane was fabricated with an inorganic precursor, (tetraethoxysilane, TEOS) and an organic precursor PDMS through green sol–gel chemistry and were used to recover hydrogen by gas separation process. In the present study, the preparation conditions of the PDMS-silica composite membrane which had great effects on the gas separation performance were evaluated through a hybridization model of TEOS weight ratios and curing processes (temperature and time) schematically. The characteristics of the composite membranes were investigated via atomic force microscopy (AFM) and total reflection Fourier transform infrared (FTIR) spectroscopy PDMS-silica for coating were obtained with TEOS weight ratios from 9.4 to 15.8wt. %. As the TEOS weight ratio was increased, the H_2 permeability and H_2/CO_2 selectivity were improved. At a feed pressure of 2 atm, the H_2 permeability of 432.3 GPU and H_2/CO_2 selectivity of 3.35 was obtained by the following preparation conditions: TEOS weight ratio 15.8 wt. %, curing time 12 h and curing temperature 75 °C.

References

1. S. Li, F. Qin, P. Qin, M.N. Karim and T. Tan, *Green Chem.*, 15,2180 (2013).

2. K.P. Ramaiah, D. Satyasri, S. Sridhar and A. Krishnaiah,*J. Hazard. Mater.*, 261, 362 (2013).

The effect of SBA-15oncomposite PPOmembrane for gasseparation

Hao-wei Chuang[1], Hui-Hsin Tseng[2,3,]*, Kuo-Liang Chuang[1], Ming-Yen Wey[1]

[1] *Department of Environmental Engineering, National Chung-Hsing University, Taichung 402, Taiwan, ROC*
[2] *School of Occupational Safety and Health, Chung Shan Medical University, Taichung 402, Taiwan, ROC*
[3]*Department of Occupational Medicine, Chung Shan Medical University Hospital, Taichung 402, Taiwan, ROC*

*hhtseng@csmu.edu.tw (Hui-Hsin Tseng)

Currently, membrane technology has been widely investigated for gas separation. To overcome the trade-off relationship between gas permeability and selectivity [1], the multilayer composite membrane by coating the mesoporous silicates(SBA-15)-incorporated PPO polymer on the surface of the carbon-selective intermediate layer was study in the present work. The introduction of the carbon-selective layer into the composite membrane can improve the gas selectivity without losing permeability [2].

Characteristic of SBA-15 has been studied in composite membrane including its sharp, particle loadings and particle sizes. Morphological studies showed that the newly developed spherical SBA-15 is benefiting for dispersion and improving the interfacial contact between the PPO polymer and the spherical SBA-15.The roughness of the surface of membrane had high relationship to particle loadings, and it increased significantly at high loading(10 – 30 wt. %).At the same time, the different loadings and particle size of SBA-15 filler let the crystallinity of PPO decreased as well as increase the gas permeability. All the results indicated that the spherical SBA-15 filler exhibit higher permeability and selectivity simultaneously than net PPO membranes.

Reference

1. M.A. Aroon, A.F. Ismail, T. Matsuura, M.M. Montazer-Rahmati, Sep. Purif. Technol.,**75**(2010)
2.T.H. Weng, H.H. Tseng, M.Y. Wey, J. Hydrogen Energy,**35**(2010)

Effect the roughness of supporting layer and viscosity of polymer solution on carbon molecular sieve membrane fabrication and gas separation

Po-Yu Cheng[1],Ching-Ting Wang[2,3] , Hui-Hsin Tseng[2,,3,*], Ming-Yen Wey[1]

[1]*School of Environmental Engineering, National Chung Hsing University, Taichung 402, Taiwan, ROC*
[2] *School of Occupational Safety and Health, Chung Shan Medical University, Taichung 402, Taiwan, ROC*
[3]*Department of Occupational Safety and Health, Chung Shan Medical University, Taichung 402, Taiwan, ROC*

*hhtseng@csmu.edu.tw (Hui-Hsin Tseng)

To enhance the mechanical stability, CMS membrane is usually supported at porous material to form an asymmetric membrane. This membrane can be usually prepared by carbonization of polymeric material, such as polyetherimide (PEI) and use porous Al_2O_3 ceramic disk as supporting material. However, the adhesion of CMS layer on the surface of Al2O3 support is always playing a significantly role on the separation performance and mainly influenced by the surface roughness of the support. [1]

In this study, we used the TiO_2 served as an intermediate layer between the CMS layer and the Al_2O_3 support to strong the mechanical interlocking between them. Further, we also discussed the viscosity of casting solution and surface roughness of Al2O3 supporting materials.

The results indicated that the TiO_2 layer dominated the adhesion between the separation layer and the porous ceramic support. The gas permeability decreased after polishing because the Al_2O_3 surface became smoother and then decreased the interaction between the CMS layer and Al_2O_3 support. The viscosity of casting solution was adjusted by heating to 10, 30, and 50℃. The viscosity of polymer solution increased with decreasing of the heating temperature and led the gas permeability increased.

References

1. H.H. Tseng, K. Shih, P.T. Shiu, M.Y. Wey, J. Membr. Sci., 405–406, 250 (2012).

四、建議

希望研討會可以設計一些不管是當地文化或是相關企業的參訪項目，使我們更瞭解這個國家與實場上的製造流程與應用。如國內舉辦國際研討會時能有類似安排，以便讓國際學者更瞭解臺灣，則可真正達到學術外交的目的。

本團隊近十年積極從事薄膜研發及其於環境工程之應用，並努力與國際知名實驗室、學術單位進行交流，如台灣中原薄膜中心、新加坡大學鍾台生院士研究單位、捷克皇家學院化工及基礎程序研究中心 Dr. Petr，希望能進而發展國際合作計畫。非常感謝科技部於研究經費之支持。

五、攜回資料名稱及內容

此次攜回資料共計有：出席證、大會手冊、論文集(USB)、與會者大合照、商展廠商資料等。

六、其他

科技部補助計畫衍生研發成果推廣資料表

日期:2014/10/30

科技部補助計畫	計畫名稱: 基材物化特性對碳分子篩選薄膜之孔洞結構及氣體分選能力之影響
	計畫主持人: 曾惠馨
	計畫編號: 100-2221-E-040-004-MY3　　學門領域: 環境工程

無研發成果推廣資料

100 年度專題研究計畫研究成果彙整表

計畫主持人：曾惠馨	計畫編號：100-2221-E-040-004-MY3
計畫名稱：基材物化特性對碳分子篩選薄膜之孔洞結構及氣體分選能力之影響	

成果項目			量化			單位	備註（質化說明：如數個計畫共同成果、成果列為該期刊之封面故事...等）
			實際已達成數（被接受或已發表）	預期總達成數(含實際已達成數)	本計畫實際貢獻百分比		
國內	論文著作	期刊論文	0	0	100%	篇	
		研究報告/技術報告	0	1	100%		獲2015年化工年會特輯邀稿，出版無機薄膜技術及其應用，該特質將於2015年10月出刊。
		研討會論文	5	5	100%		
		專書	0	0	100%		
	專利	申請中件數	0	1	100%	件	
		已獲得件數	0	0	100%		
	技術移轉	件數	0	0	100%	件	
		權利金	0	0	100%	千元	
	參與計畫人力（本國籍）	碩士生	2	2	100%	人次	
		博士生	0	0	100%		
		博士後研究員	0	0	100%		
		專任助理	0	0	100%		
國外	論文著作	期刊論文	3	5	100%	篇	本計畫研究成果目前已發表三篇 SCI 期刊論文，並獲刊登於 Journal of Membrane Science，該期刊 I.F.=4.093；Ranking=7/133=5.26%。
		研究報告/技術報告	0	0	100%		
		研討會論文	5	5	100%		
		專書	0	0	100%	章/本	
	專利	申請中件數	0	0	100%	件	
		已獲得件數	0	0	100%		
	技術移轉	件數	0	0	100%	件	
		權利金	0	0	100%	千元	
	參與計畫人力（外國籍）	碩士生	0	0	100%	人次	
		博士生	0	0	100%		
		博士後研究員	0	0	100%		
		專任助理	0	0	100%		

其他成果 (無法以量化表達之成果如辦理學術活動、獲得獎項、重要國際合作、研究成果國際影響力及其他協助產業技術發展之具體效益事項等，請以文字敘述填列。)	入選臺灣第一屆 ’’ Scopus 青年科學家獎” Environmental Science 學科領域初選

	成果項目	量化	名稱或內容性質簡述
科教處計畫加填項目	測驗工具(含質性與量性)	0	
	課程/模組	0	
	電腦及網路系統或工具	0	
	教材	0	
	舉辦之活動/競賽	0	
	研討會/工作坊	0	
	電子報、網站	0	
	計畫成果推廣之參與（閱聽）人數	0	

科技部補助專題研究計畫成果報告自評表

請就研究內容與原計畫相符程度、達成預期目標情況、研究成果之學術或應用價值（簡要敘述成果所代表之意義、價值、影響或進一步發展之可能性）、是否適合在學術期刊發表或申請專利、主要發現或其他有關價值等，作一綜合評估。

1. 請就研究內容與原計畫相符程度、達成預期目標情況作一綜合評估

■達成目標

□未達成目標（請說明，以 100 字為限）

□實驗失敗

□因故實驗中斷

□其他原因

說明：

2. 研究成果在學術期刊發表或申請專利等情形：

論文：■已發表 □未發表之文稿 □撰寫中 □無

專利：□已獲得 ■申請中 □無

技轉：□已技轉 □洽談中 ■無

其他：(以 100 字為限)

(1) SCI 期刊論文：本研究第一年與部分第二年研究成果已相繼發表於 Journal of Membrane Science 期刊 (SCI，I.F.=4.093； Ranking=7/133=5.26%) 共 2 篇，另有 2 篇準備中。

(2) 研討會論文：計畫三年研究成果分別發表於 AMS7、AMS8、2012 環工年會、2012、2013、2014 環境保護與奈米科技學術研討會、ICOM2014 與 ICIM2014 研討會等，共 8 篇。

3. 請依學術成就、技術創新、社會影響等方面，評估研究成果之學術或應用價值（簡要敘述成果所代表之意義、價值、影響或進一步發展之可能性）（以 500 字為限）

為因應溫室效應所衍生的氣候變遷，各國紛紛投入膜技術來控制二氧化碳的排放減量。其中，碳分子篩選薄膜(carbon molecular sieving membrane) 因具有耐高壓、高溫及化學安定等特性，而成為最具發展潛力的分離膜之一。

碳分子篩選薄膜係由非晶相之碳結構所組成，當碳基質之層間距接近氣體分子動力尺寸時，如 H2（2.8 Å）、CO2（3.2 Å）、O2（3.46 Å）、N2（3.64 Å）及 CH4（3.8 Å），即可經由分子篩選機制，達到氣體分離的目的；相較於高分子膜或其它無機薄膜，碳分子篩選薄膜因具有微孔與次微孔的雙峰孔徑分佈，因此更能同時兼具高滲透率與高選擇率。唯機械強度及老化問題延緩其商業化時程。

長期以來，該領域以氧化鋁為基材增強其機械強度，且因不具有質傳阻力而忽略擔體材料的影響。

本計畫設計合成一系列具「不同網絡結構及不同親合性之基材」，可改變碳基質堆砌結構，在不影響層間距值的情形下，同時提升有效孔徑分佈的孔隙率及機械強度，而能大幅地提升滲透分選性能。其中具代表性的 MFI/Al2O3 基材，能有效提升 CO2 滲透率達 630 Barrer 以上、CO2/CH4 選擇率達 74、H2/CH4 選擇率達 261，為目前已發表之碳分子篩選薄膜中的最佳性能，同時也大幅超越高分子薄膜的表現水平。此項結果可避免複雜的製備程序，受到國際相關領域的矚目，對於推進碳分子篩選薄膜於潔淨能源的實際應用具有突破性貢獻。